Inertial Particle Dynamics in the Turbulent/Non-Turbulent Interface

Amélie Ferran

To cite this version:

Amélie Ferran. Inertial Particle Dynamics in the Turbulent/Non-Turbulent Interface. Fluid mechanics [physics.class-ph]. Université Grenoble Alpes [2020-..], 2023. English. ⟨NNT : 2023GRALI102⟩. ⟨tel-04850255⟩

HAL Id: tel-04850255
https://theses.hal.science/tel-04850255v1

Submitted on 20 Dec 2024

THÈSE

Pour obtenir le grade de

DOCTEUR DE L'UNIVERSITÉ GRENOBLE ALPES

École doctorale : I-MEP2 - Ingénierie - Matériaux, Mécanique, Environnement, Energétique, Procédés, Production

Spécialité : MEP - Mécanique des fluides Energétique, Procédés

Unité de recherche : Laboratoire LEGI : Laboratoire des Ecoulements Géophysiques et Industriels

Dynamique des particules d'inertie dans une interface turbulente/non-turbulente

Inertial Particle Dynamics in the Turbulent/Non-Turbulent Interface

Présentée par :

Amélie FERRAN

Direction de thèse :

Martín OBLIGADO PROFESSEUR DES UNIVERSITES, Centrale Lille Institut, LMFL	Directeur de thèse
Alberto ALISEDA FULL PROFESSOR, University of Washington	Co-Directeur de thèse
Nathanaël MACHICOANE CHARGE DE RECHERCHE, CNRS, LEGI	Co-Encadrant de thèse

Rapporteurs :

Mickaël BOURGOIN
DIRECTEUR DE RECHERCHE, CNRS, ENS de Lyon

Philippe CLAUDIN
DIRECTEUR DE RECHERCHE, CNRS, PMMH

Thèse soutenue publiquement le **18 décembre 2023**, devant le jury composé de :

Martín OBLIGADO PROFESSEUR DES UNIVERSITES, Centrale Lille Institut, LMFL	Directeur de thèse
Mickaël BOURGOIN DIRECTEUR DE RECHERCHE, CNRS, ENS de Lyon	Rapporteur
Philippe CLAUDIN DIRECTEUR DE RECHERCHE, CNRS, PMMH	Rapporteur
Henda DJERIDI PROFESSEURE DES UNIVERSITES, Grenoble INP, LEGI	Présidente
Aurore NASO DIRECTRICE DE RECHERCHE, CNRS, LMFA	Examinateur
Alain CARTELLIER DIRECTEUR DE RECHERCHE EMERITE, CNRS, LEGI	Examinateur

UNIVERSITÉ GRENOBLE ALPES

ÉCOLE DOCTORALE I-MEP2

Ingénierie - Matériaux, Mécanique, Environnement, Energétique, Procédés, Production

THÈSE

pour obtenir le titre de

Docteur en sciences

de l'Université Grenoble Alpes

Mention : MEP - MÉCANIQUE DES FLUIDES, ENERGÉTIQUE, PROCÉDÉS

Présentée et soutenue par

Amélie FERRAN

Dynamique des particules d'inertie dans une interface turbulente/non-turbulente

Thèse dirigée par Martín OBLIGADO et
codirigée par Alberto ALISEDA et Nathanaël MACHICOANE

préparée au laboratoire LEGI
Laboratoire des Ecoulements Géophysiques et Industriels

soutenue le 18 décembre 2023

Jury :

Rapporteurs :	Mickaël BOURGOIN	-	Directeur de recherche, ENS de Lyon
	Philippe CLAUDIN	-	Directeur de recherche, PMMH
Présidente :	Henda DJERIDI	-	Professeure des Universités, LEGI
Examinatrice :	Aurore NASO	-	Directrice de recherche, LMFA
Examinateur :	Alain CARTELLIER	-	Directeur de recherche émérite, LEGI
Directeur :	Martín OBLIGADO	-	Professeur des Universités, LMFL
Co-Directeur :	Alberto ALISEDA	-	Professeur étranger, University of Washington

– Pour mon frère.

Acknowledgements

First and foremost, I would like to express my gratitude to Philippe Claudin and Mickaël Bourgoin, the reviewers of this thesis, for accepting considering my work and evaluating my manuscript on short notice. I would also like to thank the other members of the jury for honoring this work: Henda Djeridi, Aurore Naso, and Alain Cartellier.

I would like to extend my thanks to all the members of the instrumentation team, the mechanical team, and the computer support service. In particular, I want to express my gratitude to Laure Vignal for her constant assistance in setting up the lasers and generously sharing her knowledge during the experiments in Grenoble. Additionally, I would like to thank Sinan and Vincent for their help with the experimental setup during the initial stages of my PhD.

I will always be grateful for this work opportunity and the ones who made it possible. Nathanaël Machicoane, I would like to thank for your help and advice on how to do a PhD, especially at the early stages of it during the pandemic time. I would also like to mention Nicolas Mordant, without whom this thesis wouldn't have been able to start. During my stay in the US, I have learned a great deal about the world of experimental fluid dynamics and particle-laden flows under the guidance of Alberto Aliseda. Throughout that time, I appreciated gaining research independence, learning from your experimental skills and your confidence in mine. I also want to thank you, Alberto, for ensuring that my stay in Seattle was also enriching and enjoyable on a personal level. Finally, I would like to express my gratitude to Martín Obligado. Your optimism, creativity, attentive listening and scientific ideas were a real motor of this thesis. Our discussions were always motivating and inspiring, while dissipating any concerns that would arise in my mind of PhD student.

During my thesis, I had the opportunity of visiting the turbulence group at the University of Buenos Aires for a very fruitful collaboration. I want to acknowledge Pablo Mininni for hosting me in the group at UBA and teaching me about direct numerical simulations and the GHOST code. Thank you to Sofía Angriman, Florencia Zapata and Pablo Cobelli and for all the great work we did together; I also learned a lot by collaborating with you. While I was in the US, I also had the pleasure to visit Bayo's group in Portland several times. I would like to thank all of Portland's crew for their friendliness; each of my visits was very fun and enjoyable.

In Grenoble, I would like to extend my thanks to many PhD students and Post-docs of LEGI, for all the great moments we have shared together. Among them, I would like to mention Ivan, Costanza, Oliver, Xavier, Luis, Umair, Mohammad, Felix, Benjamin, Quentin, Helder, Neda, Maria Rita, Pablo, Sevan, Anastasia, Arman, Claudine, Alicia, Géraldine, Cruz, Yael, Arash, Remi, Santanu, Wessel ... and more. I am grateful to Yann Mezui for providing many advices in the matter of both what to do and not to do during a PhD. I also want to express my gratitude to Daniel Mora Paiba for the time he dedicated explaining me his work. This thesis would have been the same without the significant scientific contributions that he has made beforehand (including building a wind tunnel). Finally, I would like to acknowledge Sarah Smith, who has not only been a kind labmate, but also a travel buddy and a great friend throughout this transcontinental PhD journey.

In Seattle, I was also lucky to have amazing labmates. I would like to thank Laurel, Maria, Angela, Erin, Sari and Marissa for their daily support, constant assistance, and empowering presence. Being around you made my stay much more comfortable and enjoyable. In Alberto's lab, I wish to express my gratitude to Kee Onn Fong and Mike Barbour for their help with the experiments and generously sharing their experimental knowledge with me. I am very grateful to Ryan McGinty and Sari Barczay for offering to share their home in Seattle with me, and for their kindness and generosity as roommates. I also would like to extend my gratitude to all my Ballard friends, Abhi, Abhi, Rishi, Kevin, Aaron, Donnie, Hector, Brenda, Andy and Fanette (also in that category). Thank you to everyone for all the truly memorable moments that we've shared, for your generosity, friendliness, and warm welcome since my very first week in Seattle.

Enfin, je voudrais aussi remercier mes amis de Toulouse pour continuer d'être présents et pour leur joie de vivre. J'ai grandement apprécié chacune de nos retrouvailles. Merci aussi à Philippe Dominique d'avoir pris le temps de relire ma thèse et d'en corriger les erreurs. Finalement, je tiens à exprimer ma gratitude envers ma famille: mes parents, mon frère, grands-parents, cousins, tantes et oncles. Merci à toutes les personnes impliquées dans la confection du pot de thèse. Je tiens particulièrement à remercier mes parents pour leur dévouement à mon égard lors des derniers mois précédant la soutenance. Plus généralement, j'apprécie leur confiance en moi et leur soutien dans la poursuite de mes rêves.

Abstract

Many environmental phenomena involve inertial particles advected in an inhomogeneous turbulent flow. Over the last decades, various studies have focused on the simplified case of homogeneous and isotropic turbulence. Nevertheless, most relevant applications feature non-homogeneous turbulence with a turbulent/non-turbulent interface. This thesis aims to study the motion of small, heavy inertial particles advected by a turbulent/non-turbulent interface. The thesis is divided into three main parts.

In a first part, we present a method to analyse experimentally single-phase turbulent flows using solely statistics on points where the fluctuating velocity is equal to zero. We demonstrate that voids of zero crossings primarly control the degree of turbulence and the Taylor Reynolds number, Re_λ.

In a second part, we explore the settling velocity modification of inertial particles in homogeneous isotropic turbulence through wind tunnel experiments. Our findings confirm that the settling enhancement decreases significantly with increasing values of the Taylor Reynolds number. Additionally, this study reveals that large-scale structures have a significant impact on the settling rate, even at constant turbulent intensity and Reynolds number.

In the third part, we present wind tunnel experiments on the dynamics of inertial particles advected in a turbulent/non-turbulent interface. Only the high-turbulence side is laden with inertial particles, and we are interested in how their properties change as they travel across the interface, particularly their preferential concentration and settling velocity. Our observations confirm that particles tend to oversample high-energetic events within the mixing layer. Finally, the interface is also associated with an increase in clustering intensity and a stronger enhancement of the settling velocity. The work finishes with preliminary results of particle tracking velocimetry measurements.

Keywords: wind tunnel experiments, inertial particles, turbulent/non-turbulent interface

Résumé en français

Un grand nombre de phénomènes environnementaux sont associés au transport de particules inertielles au sein d'un écoulement turbulent inhomogène. Au cours des dernières décennies, la plupart des études se sont concentrées sur le cas simplifié de la turbulence homogène et isotrope. Néanmoins, beaucoup d'écoulements naturels présentent une turbulence non homogène avec une interface turbulente/non turbulente. Cette thèse vise à étudier le mouvement de petites particules inertielles et denses transportées à travers une interface turbulente/non-turbulente. La thèse est divisée en trois parties principales.

Dans une première partie, nous présentons une méthode permettant d'analyser expérimentalement les écoulements turbulents monophasiques en se basant exclusivement sur des statistiques concernant les zéros de la vitesse fluctuante. Nous démontrons que les espaces vides de zéros contrôlent le niveau de turbulence et la valeur du nombre de Taylor Reynolds, Re_λ.

Dans une seconde partie, nous étudions la modification de la vitesse de chute des particules dans une turbulence homogène et isotrope à l'aide d'expériences en soufflerie. Nous confirmons que l'augmentation de la vitesse de chute diminue significativement avec une augmentation du nombre de Taylor Reynolds. Cette étude dévoile également que les structures de grande échelle ont un effet sur la vitesse de chute, même pour une intensité turbulente et un nombre de Reynolds constants.

Dans une dernière partie, nous présentons des expériences en soufflerie sur la dynamique des particules inertielles transportées dans une interface turbulente/non-turbulente. Les gouttes d'eau sont introduites seulement du côté fortement turbulent de l'interface, et nous analysons comment leur propriétés sont modifiées par la présence de l'interface, en se concentrant plus particulièrement sur leur concentration préférentielle et la modification de leur vitesse de chute. Dans la couche turbulente/non-turbulente, nous confirmons que les particules ont tendance à se concentrer dans les portions du fluides présentant de larges fluctuations turbulentes. Enfin, l'interface est également associée à une concentration préférentielle plus intense et à une forte augmentation de la vitesse de chute. En conclusion de ce travail nous présentons des résultats préliminaires sur des mesures de vélocimétrie par suivi de particules.

Mots clés : expériences en soufflerie, particules d'inertie, interface turbulente/non-turbulente

Contents

List of Figures

List of Tables

Nomenclature

The next list describes several symbols that will be later used within the body of the document.

α	PDPA beam intersection angle [°]
β	PDPA misalignment angle [°]
β	redefined particle-to-fluid density ratio ($\beta = 3/(2\rho_p/\rho_f + 1)$)
$\boldsymbol{a}^p(\boldsymbol{x}, t)$	particle acceleration [m/s]
$\boldsymbol{u}(\boldsymbol{x}, t)$	Eulerian fluid velocity [m/s]
$\boldsymbol{u}(\boldsymbol{x}^p(t), t)$	fluid velocity at the particle position [m/s]
$\boldsymbol{v}^p(\boldsymbol{x}, t)$	particle velocity [m/s]
ΔP	pressure difference of the Pitot tube [Pa]
ΔU	velocity difference across a mixing layer [m/s]
ΔV	velocity difference between the particle settling velocity and the particle terminal velocity [m/s]
ΔZ	distance between two successive zero crossings [m]
δ	PDPA fringe spacing [m]
δ	characteristic width of a mixing layer [m]
η	Kolmogorov lengthscale [m]
η_C	cutoff size of a low-pass filter [m]
$\hat{u}(\omega)$	Fourier transform of the fluid velocity
$\hat{v}^p(\omega)$	Fourier transform of the particle velocity
κ	wavenumber vector [m^{-1}]
κ_1	wavenumber component in the longitudinal direction [m^{-1}]
λ	Taylor microscale [m]
λ	laser wavelength [m]
$\mathscr{C}$	local particle concentration [m^{-1}]
$\mathscr{L}$	integral length scale [m]

$\mathscr{L}_a$	integral length scale from the integration of the autocorrelation function [m]
$\mathscr{L}_{McF}$	integral length scale computed with MacFadden equation [m]
$\mathscr{L}_{voro}$	integral length scale from the Voronoï analysis of the longitudinal fluctuating velocity zero crossings [m]
$\mathscr{V}$	normalised Voronoï cell size
μ	fluid dynamic viscosity [kg.m^{-1}.s^{-1}] (sometimes denoted μ_f)
μ_n	nth central moment
ν	fluid kinematic viscosity [m^2.s^{-1}] (sometimes denoted ν_f)
Ω	rotation rate tensor, $\frac{1}{2}(\nabla \boldsymbol{u} - \nabla \boldsymbol{u}^T)$, [s^{-1}]
$\bar{l}$	length of the signal [m]
ϕ_v	volume fraction
ϕ_{1-2}	phase shift between the two detectors of the PDPA [rad]
$\Pi(\kappa)$	interscale flux of turbulent kinetic energy [m^3.s^{-2}]
ψ	Cobra probe yaw angle [°]
ρ	fluid density [kg.m^{-3}] (sometimes denoted ρ_f)
ρ_p	particle density [kg.m^{-3}]
$\sigma_{\mathscr{V}}$	standard deviation of the Voronoï cell size distribution
σ_{RPP}	standard deviation of a Random Poisson Process distribution
τ_η	Kolmogorov timescale [s]
$\tau_{\mathscr{L}}$	integral time scale [s]
τ_f	fluid characteristic time scale [s]
τ_p	particle relaxation time [s]
θ	Cobra probe pitch angle [°]
ε	mean dissipation rate of turbulent kinetic energy [m^2.s^{-3}]
$\widehat{var}$	local longitudinal velocity variance [m^2/s^2]
a, b, n	King's law coefficients
B	constant of the Rice theorem (or C)

C_1	Kolmogorov universal constant for the one-dimensional spectra
C_ε	(or C) dissipation rate universal constant (from Kolmogorov's theory)
D	diameter of the cylinder [m]
d_p	particle diameter [μm]
$E(\kappa)$	energy-spectrum function [m^3.s^{-2}]
$E_{11}(\kappa_1)$	one-dimensionnal longitudinal energy spectrum [m^3.s^{-2}]
$f(r)$	normalised autocorrelation function
f	volumetric forces [kg.m^{-2}.s^{-2}]
f_C	cutoff frequency of a low-pass filter [s^{-1}]
f_D	Doppler frequency [s^{-1}]
F_s	sampling frequency [s^{-1}]
g	gravitational acceleration [m.s^{-2}]
L_c	cluster size [m] or [m^2]
L_v	void size [m] or [m^2]
M	grid mesh size [m]
m_f	mass of fluid occupied by a particle of diameter d_p [kg]
m_p	particle mass [kg]
N_0	zero crossings frequency [s^{-1}]
n_s	zero crossings density [m^{-1}] or [m^{-3}]
p	pressure [Pa] or [kg.m^{-1}.s^{-2}]
r	radial coordinate or lengthscale [m]
$R_{uu}(\rho)$	normalised longitudinal velocity autocorrelation function
Re	Reynolds number, UL/ν, based on a characteristic velocity scale U and a characteristic lengthscale L of the flow
Re_λ	Taylor-scale Reynolds number ($\lambda u'/\nu$)
Re_G	global Reynolds number based on the boundary conditions (MU_∞/ν)
Re_L	Reynolds number based on the integral length scale of the flow ($\mathscr{L}u'/\nu$)

Ro	Rouse number based on the flow large scales (V_T/u')
$RoSt$	Rouse-Stokes number ($Ro \times St$)
S	strain rate tensor, $\frac{1}{2}(\nabla \boldsymbol{u} + \nabla \boldsymbol{u}^T)$, [s^{-1}]
St	Stokes number based on the Kolmogorov scale (τ_p/τ_η)
$St_{\mathscr{L}}$	Stokes number based on the integral length scale ($\tau_p/\tau_{\mathscr{L}}$)
Sv_η	settling parameter based on the Kolmogorov scale (V_T/u_η)
u'	root mean square of the fluctuating velocity [m/s]
u_η	Kolmogorov velocity scale [m/s]
U_∞	wind tunnel bulk velocity [m/s]
$U_y(\boldsymbol{x}, t)$	Eulerian fluid velocity in the vertical direction [m/s]
U_{perp}	velocity component perpendicular to the hot-wire [m/s]
V_β	velocity bias due to the PDPA misalignment [m/s]
V_S	particle settling velocity [m/s]
V_T	terminal velocity of a particle (settling velocity in a quiescent fluid) [m/s]
x	cartesian coordinate (streamwise direction of the wind tunnel) [m]
Y	width of the wind tunnel [m]
y	cartesian coordinate (vertical direction) [m]
z	cartesian coordinate (spanwise direction) [m]

Introduction 1

Turbulent-particle laden flows have gathered the attention of the scientific community for decades (Boussinesq 1903; Crowe, Chung, and Troutt 1988; Elghobashi 1994; Monchaux, Bourgoin, and Cartellier 2012; Brandt and Coletti 2022). Their inherent complexity poses great challenges to their study, leaving experimentalists, modelers, and numericians to many uncertainties. The large variety of different properties between the particles and the fluid, the vast separation of scales among turbulent motions, and the reciprocal interaction of the dispersed phase with the flow lead to the creation of a multitude of physical mechanisms. As a result, many unknowns in their underlying physics have yet to be understood.

Moreover, their ubiquity in various everyday phenomena and industrial processes makes their understanding valuable across multiple domains. Many natural turbulent particle-laden flows have direct implications on current important societal challenges. For instance, coastal erosion and flood management are affected by the transport of sediments in rivers and seas. The dispersion of aerosols and pollutants in the atmosphere, or microplastics in the ocean, raises concerns about environmental contamination. The accuracy of meteorological models in predicting the formation of rain and the intensity of precipitations is affected by the motion of water droplets or snowflakes in atmospheric turbulence. Last but not least, climate change is affected by marine snow, sea sprays, and cloud properties, all featuring inclusions moving in a turbulent fluid.

Additionally, the majority of these systems exhibit a non-canonical background turbulent flow. Meaning that, in nature, the underlying turbulence is frequently characterized by non-homogeneous anisotropic properties, such as a turbulent interface. A turbulent/non-turbulent interface refers to a portion of the flow that delimits two fluid regions originally at two different turbulent states. These interface layers are omnipresent in the environment; and they can be found, for instance, in the atmosphere at cloud boundaries. Indeed, the interior of cumulus clouds, laden with water droplets is known to be significantly more turbulent than the surrounding unladen flow.

The factors controlling the distribution of cloud droplets and their radiative properties are issues that still require significant attention from the scientific community, with implications for weather forecasting and climate change modeling. The role of small-scale turbulence and dry air entrainment in cumulus clouds is known to play a crucial part in determining their macroscopic properties, influencing aspects such as their lifetime, expansion, precipitation efficiency, and optical properties (Blyth 1993; Shaw 2003). In the context of cloud dynamics, cloud droplets can be modeled as inertial particles, as their trajectories deviate from the paths of fluid parcels, exhibiting rather their own dynamics.

The scope of the present study focuses on small-scale mechanisms that could be relevant for modeling cloud edges. We investigated experimentally inertial particles, being water droplets, advected within a turbulent airflow. The inertial particles are characterized as small, implying their sizes are smaller than the smallest turbulent motions, and heavy, given their significantly higher density compared to the fluid. The concentration of particles is also considered to be in dilute conditions, meaning that the volumetric ratio between the discrete phase and the carrier phase is very low, resulting in no modulation of turbulence by the droplets. Several underlying turbulent flows were generated, each having different properties. We considered both the ideal case of homogeneous isotropic turbulence and scenarios where the carrier phase presents a turbulent interface.

Many topics have to be addressed when dealing with particle-laden flows, and this chapter aims to cover a wide range of them. We will begin by discussing single-phase turbulence, exploring aspects related to the turbulent energy cascade theory, homogeneous isotropic turbulence, turbulent/non-turbulent interfaces, nonequilibrium turbulent cascades, and the characterization of turbulence. The second section focuses on the current knowledge concerning the motion of the dispersed phase, covering topics like the particles equations of motion, the phenomena of preferential concentration and settling velocity modification, and the dispersion of particles in free shear flows.

1.1 Turbulence

It has been 200 years since the Navier-Stokes equations were derived to describe the dynamics of all fluid flows (with Newtonian properties), including turbulent ones. Here we present the conservation of mass and momentum for an incompressible flow of a Newtonian fluid, with $\boldsymbol{u} = \boldsymbol{u}(\boldsymbol{x}, t)$ as the three-dimensional velocity field and all vector quantities indicated in bold font.

$$\rho\Big(\partial_t \boldsymbol{u} + \boldsymbol{u} \cdot \nabla \boldsymbol{u}\Big) = -\nabla p + \mu \Delta \boldsymbol{u} + \boldsymbol{f} \tag{1.1}$$

$$\nabla \cdot \boldsymbol{u} = 0 \tag{1.2}$$

Where ρ is the constant fluid density, μ the dynamic viscosity, p the pressure field and $\boldsymbol{f}$ represents some volumetric forces acting on the flow, for instance gravity. The Navier-Stokes equations inherent nonlinearity, and the non local nature of the pressure term, make them very challenging to solve analytically (Lemarié-Rieusset 2018). Only few exact solutions have been found, often requiring the introduction of unrealistic simplifying assumptions.

One may nondimensionalize equation 1.1 by introducing a characteristic velocity scale U and a characteristic length scale L. The dimensionless counterparts of the equation variables are defined as $\boldsymbol{u}_+ = \boldsymbol{u}/U$, $\boldsymbol{x}_+ = \boldsymbol{x}/L$, $t_+ = tU/L$ and $p_+ = p/(\rho U^2)$. Substituting them in equations 1.1 and 1.2 leads to

$$\partial_{t_+} \boldsymbol{u}_+ + \boldsymbol{u}_+ \cdot \nabla_+ \boldsymbol{u}_+ = -\nabla_+ p_+ + \underbrace{\frac{\nu}{LU}}_{Re^{-1}} \Delta_+ \boldsymbol{u}_+ \tag{1.3}$$

$$\nabla_+ \cdot \boldsymbol{u}_+ = 0 \tag{1.4}$$

The above equation, completely non-dimensional, reveals a dimensionless parameter called the Reynolds number, $Re = UL/\nu$. Introduced for the first time by Osborne Reynolds 1883, this parameter describes the relative importance of inertial forces over viscous forces. An increase in this Reynolds number leads to a decay of the viscous dissipation term, feeding the non-linear term in the left hand side. As a result, the flow becomes turbulent for large Reynolds number, $Re \gg 1$, where predicting the temporal evolution becomes drastically more challenging due to the dominance of the non-linear advection term $(\boldsymbol{u} \cdot \nabla \boldsymbol{u})$.

There is no rigorous mathematical definition of a turbulent flow, as the specific circumstances under which turbulence occurs remain uncertain. A wide variety of turbulent flows exists, featuring substantially different properties, and as a result different authors may give their own definition (Lesieur 2008). Nonetheless, some general features, commonly observed in turbulent flows, can be depicted (Tennekes and Lumley 1972). Turbulent flows are characterized by chaotic fluid motions, presenting a seemingly random behavior and large velocity and vorticity fluctuations. The solution to the Navier-Stokes equations is known to present a high sensitivity to initial conditions (Lorenz 1963), which implies that a small change in the initial data can lead to a considerably different dynamic, rendering the flow unpredictable. Moreover, turbulent flows are highly dissipative, causing enhanced mixing of momentum, heat and mass transfer. Last but not least, they involve a wide range of spatial and temporal scales.

The multiscale nature of turbulence is probably one of the main challenges of its study. Turbulent flows can be visualized as the superposition of many different sized eddies. As the Reynolds number increases, smaller scales become progressively finer, while larger scales grow larger. The distribution and transfer of kinetic energy among these various scales have been the focus of great attention and have led to the most significant phenomenological theory of turbulence.

1.1.1 The turbulent energy cascade

Richardson's energy cascade

The first picture of the turbulent energy cascade was introduced by Richardson 1922. Richardson's idea behind the cascade of energy is that kinetic energy enters the flow through the largest scales of motion. As large eddies become unstable, they break down into successively smaller-sized eddies, transferring progressively their energy into the smallest scales. The energy transfer goes on until the size of turbulent motions becomes so small that viscous dissipation is predominant. The scale at which the energy is initially injected is named the integral length scale, denoted as $\mathscr{L}$. This description of energy dissipation, commonly referred to as the turbulent energy cascade, is well summarized in Richardson's verses, inspired by Jonathan Swift's poem (Tamai 2016).

> *"Big whorls have little whorls,*
> *which feed on their velocity;*
> *And little whorls have lesser whorls,*
> *And so on to viscosity."*

Kolmogorov's phenomenology of turbulence

A more quantitative representation of the energy cascade was proposed by A.N. Kolmogorov in 1941, known as the K41 theory (Kolmogorov 1941). The results provided by Kolmogorov relie on three important hypotheses: the hypothesis of local isotropy and two similarity hypothesis. While this theory provides an excellent foundation for predicting relevant flow statistics, some discrepancies persist between theoretical predictions and experimental values, particularly for higher-order moments. An extension of the K41 theory, with refined similarity hypothesis, was proposed by Kolmogorov and Obukhov in 1962 to account for the internal intermittency at higher orders. Several other models have been proposed to describe this intermittent property of turbulent flows (Frisch 1995). This refined theory, denoted as K62 to distinguish it from K41, will not be adressed in this manuscript.

Kolmogorov's first hypothesis is known as the hypothesis of local isotropy. It assumes that, at sufficiently high Reynolds number, small-scale motions are statistically isotropic, meaning that the three fluctuating velocity components have similar properties. Even if the largest scales exhibit anisotropic behavior, their anisotropic properties are lost during the transfer of energy from large to small scales. The fine-scale motions statistics are then independent of their generation mechanism, boundary conditions and large-scale geometry. As a consequence, the statistics of small-scale motions remain similar across every high Reynolds number flow, establishing them as universal. The term "local isotropy" refers to isotropy of the small scales only.

We may wonder which parameters influence this statistically universal state of small scales. As an answer, Kolmogorov's first similarity hypothesis states that, at sufficiently high Reynolds number, the statistics of small eddies are uniquely and universally determined by the mean energy dissipation rate ε and the kinematic viscosity ν. This can be understood from the two dominant processes at play for these small structures: the transfer of energy from larger scales and the energy loss through viscous dissipation. It assumes that the insertion and removal of kinetic energy within this range occur at the same rate: ε, the mean energy dissipation rate. From dimensional analysis, a characteristic length η, time τ_η, and velocity scale u_η can be estimated using ν and ε.

$$\eta = \left(\frac{\nu^3}{\varepsilon}\right)^{1/4}, \quad \tau_\eta = \left(\frac{\nu}{\varepsilon}\right)^{1/2}, \quad u_\eta = (\nu\varepsilon)^{1/4} \tag{1.5}$$

This characteristic scale η, known as the Kolmogorov scale or dissipative scale, represents the size of the smallest eddies in the flow, below which viscous effects are predominant. Indeed, it can easily be verified that the Reynolds number based on the Kolmogorov velocity and length scale is equal to unity, $\eta u_\eta/\nu = 1$.

An increase in the Reynolds number results in a wider separation between the energy-containing wavenumbers, associated with the integral length $\mathscr{L}$, and the dissipation range wavenumbers, linked to the Kolmogorov scale η. If the Reynolds number is sufficiently high, there exists a range of scales r, corresponding to wavenumbers $\kappa = 2\pi/r$, considerably larger than the Kolmogorov scale η and smaller than $\mathscr{L}$, $\eta \ll r \ll \mathscr{L}$. In this range, the turbulent motions are statistically independent from both the energy-containing eddies and the dissipative eddies. For these wavenumbers, the energy transferred by inertial forces is the dominant process, while viscous dissipation is negligible. That is why this range of scales is known as the "inertial subrange". As a result, the turbulent structures statistics within this subrange depend only on the rate at which energy enters, i.e. on the mean dissipation rate ε. These assumptions lead to Kolmogorov second similarity hypothesis, which states that at a sufficiently high Reynolds number, the motions statistics of sizes r in the range $\eta \ll r \ll \mathscr{L}$ have a universal form, uniquely determined by ε and independent of ν (Pope 2001; Vassilicos 2015).

We may consider the energy spectrum function $E(\kappa)$, which represents how the energy is distributed across the different wavenumbers. The kinetic energy contained in the wavenumber range $[\kappa_a, \kappa_b]$ can be estimated from $\int_{\kappa_a}^{\kappa_b} E(\kappa) d\kappa$. In the inertial subrange, Kolmogorov's second similarity hypothesis predicts by dimensional analysis the form of the energy spectrum function to be:

$$E(\kappa) = C\varepsilon^{2/3}\kappa^{-5/3} \tag{1.6}$$

where C is a universal constant. A compilation of experimental data provided an estimation of the Kolmogorov universal constant C_1 for the one-dimensional longitudinal spectra, given by $E_{11}(\kappa_1) = C_1\varepsilon^{2/3}\kappa_1^{-5/3}$ where κ_1 is the wavenumber component in the longitudinal direction. According to Sreenivasan 1995, $C_1 = 0.52 \pm 0.04$, leading to the universal constant $C = 1.5$ for the three-dimensional energy spectrum function, as both are related by $C_1 = \frac{18}{55}C$ with the hypothesis of local isotropy (Pope 2001).

In a turbulent flow, the energy injected by the large scales is always equal to the one lost through viscous dissipation. Furthermore, Kolmogorov's theory assumes that the rate at which kinetic energy is transferred across a length scale r remains constant through the cascade, from the largest to the smallest scales. In other words, if we consider the interscale flux of turbulent kinetic energy $\Pi(\kappa)$ from wavenumbers smaller to wavenumbers larger than κ, it should be approximately equal to the turbulent dissipation rate for wavenumbers larger than κ, denoted as $\varepsilon(\kappa)$.

$$\Pi(\kappa) \approx \varepsilon(\kappa) \tag{1.7}$$

The relationship above is an expression of the local equilibrium hypothesis, which provides the basis of the Kolmogorov's 1941 similarity hypothesis (Goto and Vassilicos 2016a). In the framework of K41 theory, the energy cascade is said to be in "equilibrium". It is worth noting that, in this context, the term "equilibrium" refers to a scale-by-scale balance between energy injection and dissipation (equation 1.7), and is not used with the same meaning as in thermodynamic equilibrium encountered in statistical physics. While the Richardson-Kolmogorov cascade is still believed to be present in many flows, both experimental evidence and numerical simulations have revealed the existence of fluid regions where expression 1.7 is not valid, and a "nonequilibirium" cascade occurs. We will detail this nonequilibrium turbulence cascade in section 1.1.4.

1.1.2 Homogeneous and isotropic turbulence

Most of the early theoretical work, conducted during the 1930s (Taylor 1935; Karman and Howarth 1938), was performed in the simplified case of homogeneous and isotropic turbulence (HIT). In a homogeneous turbulent flow, the turbulent fluctuating quantities are independent of the spatial position. An even stronger assumption is to assume that the flow is isotropic, which implies that the statistics are invariant under rotations and reflections. It is important to note that a completely homogeneous and isotropic flow is an idealized concept, as no experimental method can perfectly generate this flow (Batchelor 1953). However, it is possible to create a flow with negligible dependence of the statistics on the position and the rotation. For instance, a stream passing through a regular grid of bars have been found to generate a turbulent flow close to homogeneous and isotropic. Indeed, the study of HIT flows has been traditionally conducted in wind tunnels with grid-generated turbulence (Simmons and Salter 1934; Comte-Bellot and Corrsin 1971). Nonetheless, in recent decades, other facilities have been shown to produce turbulent flows close to homogeneous and isotropic conditions: oscillating grids (Murray 1970; Cheng and Law 2001), jet actuators in a turbulence chamber (Hwang and Eaton 2004) or multiple propellers randomly rotating (Zimmermann et al. 2010).

1.1.3 Turbulent/non-turbulent interfaces

Although most of the available data and theoretical advances have been obtained in the ideal case of homogeneous and isotropic turbulence, turbulent motions encountered in nature are usually more complicated. From the sharp edges of atmospheric clouds, the aerodynamics of rigid structures like aircraft and vehicles, the impact zone of a plunging jet to the thermocline in the ocean, most turbulent flows are bounded by a fluid at a different turbulent state. Indeed, all of these flows present an interface layer (turbulent/non-turbulent or turbulent/turbulent interface), separating regions of different turbulent intensities or a turbulent flow with an irrotational flow (da Silva et al. 2014). Among the canonical flows that are widely studied, these interfaces are prevalent at the edges of jets, wakes, mixing layers and boundary layers. Following a comprehensive review by da Silva et al. 2014, we present a summary of our current understanding of the flow dynamics across these turbulent/non-turbulent interfaces.

The first experimental results on a front separating a turbulent flow from a contiguous non-turbulent fluid were conducted by Corrsin and Kistler 1955. They describe this front, separating both flow regions, to be a very thin layer of fluid with irregular motions. They denote this thin fluid region the "laminar superlayer", differing from the well-known laminar sublayer in wall-bounded flow by the fact that it is a randomly moving portion of fluid.

Then, consensus has been found to describe the turbulent interface by two layers: a viscous superlayer (VSL) and a turbulent sublayer (TSL) (Bisset, Hunt, and Rogers 2002; da Silva et al. 2014). As an initially irrotational fluid can gain vorticity only through diffusion, viscous forces must play a central role in a turbulent interface. It is in the viscous superlayer that vorticity is transmitted to the laminar fluid through viscous diffusion (Corrsin and Kistler 1955; Westerweel et al. 2009). In the turbulent sublayer, however, the vorticity profile must match the vorticity values in the viscous superlayer (VSL) and in the turbulent region. A schematic illustrating the different regions in the interface is shown in Figure 1.1.

The flow variable that characterizes the interface position best is vorticity. Indeed, a sharp gradient of vorticity has been observed in various flows, and in some cases, the interface position exhibits a peak in the vorticity profile (Westerweel et al. 2009; da Silva et al. 2014). Therefore, this quantity is frequently used in numerical studies to detect the interface position. A typical procedure involves applying a low vorticity threshold to the field, above which the flow is identified as the turbulent region.

Some debates dealt with determining the most efficient mechanisms for transferring vorticity from the turbulent region to the non-turbulent flow. Several studies have concluded that entrainment is dominated by the penetration of large scale structures into the non turbulent region (engulfment) (Dahm and Dimotakis 1987; Dimotakis 2000). However, vorticity can also be spread due to viscous diffusion processes (nibbling) along the entire interface, since rotation can only be transmitted to the irrotational flow through direct viscous action. For a turbulent jet, ’nibbling turbulence’ has been shown to be the predominant process for exchanging vorticity between the two regions (Westerweel et al. 2005; Westerweel et al. 2009; Mathew and Basu 2002).

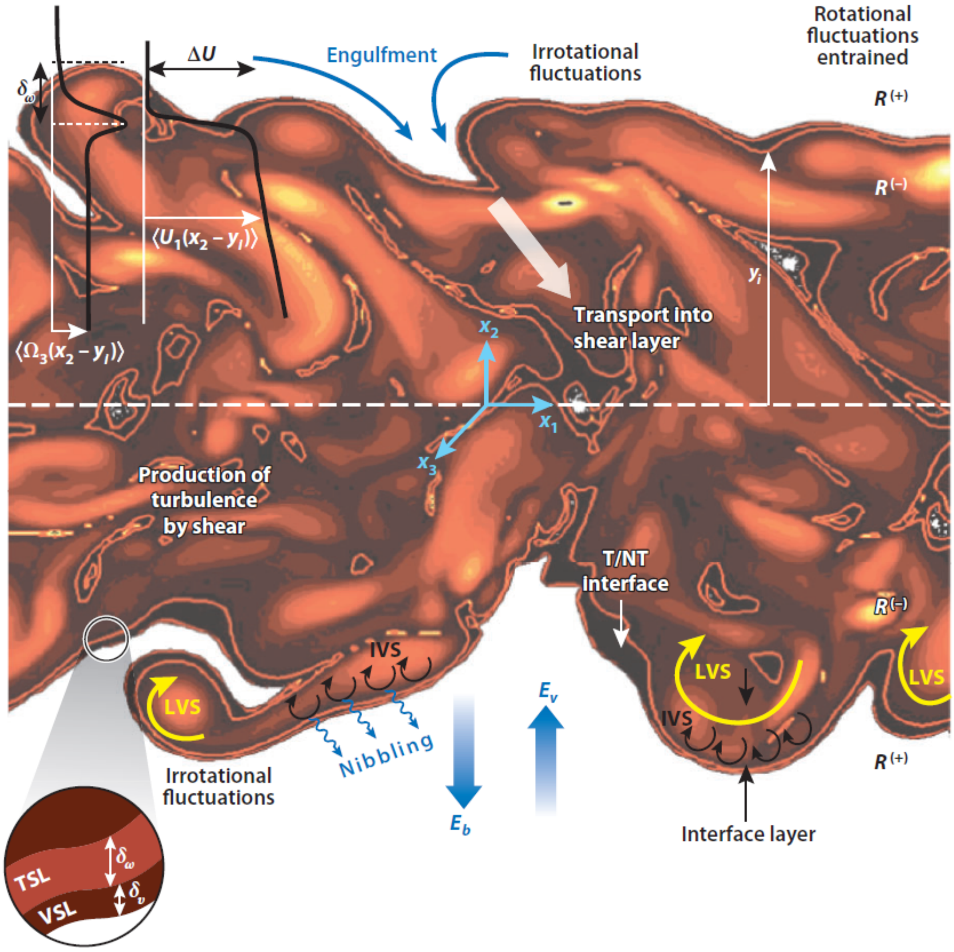

Figure 1.1: Schematic showing the several regions, the length scales and the main physical processes taking place inside a free shear layer. Taken from da Silva et al. 2014.

1.1.4 Non-equilibrium turbulence dissipation law

We recall that when the energy cascade is at an equilibrium state, the rate at which kinetic energy is transferred between scales is the same from the largest to the smallest scales. If we assume the validity of relation 1.7 for the largest scales it infers that, for a wavenumber κ equal to $2\pi/\mathscr{L}$, the interscale flux of kinetic energy $\Pi(2\pi/\mathscr{L})$ can be estimated via the Taylor-Kolmogorov dissipation law (Taylor 1935):

$$\Pi(2\pi/\mathscr{L}) \propto \frac{u'^3}{\mathscr{L}} \tag{1.8}$$

where u' is a characteristic velocity of the large scales. From the above relationship and the assumption 1.7 holding for small κ, it follows that the dissipation rate of turbulent kinetic energy is proportional to $u'^3/\mathscr{L}$.

$$\varepsilon = C_\varepsilon \frac{u'^3}{\mathscr{L}} \tag{1.9}$$

with u' the r.m.s. of the fluctuating velocity, $\mathscr{L}$ the flow integral length scale, and C_ε a constant independent of the Reynolds number at high enough Reynolds number for a set of fixed boundary conditions (Taylor 1935).

However, various studies have found C_ε not to be constant at fixed inlet conditions, but to follow another dissipation scaling (Vassilicos 2015). In that case, the scale by scale equilibrium of the energy cascade expressed by relation 1.7 is no longer valid, and the cascade of energy is said to be 'out of equilibrium', or denoted as a nonequilibrium turbulent cascade. At large enough Reynolds number, the normalized dissipation rate C_ε follows some well documented law, it increases as the local Reynolds number decreases, C_ε varies then as $1/Re_\lambda$, with $Re_\lambda = u'\lambda/\nu$ a local, position dependent, Taylor-scale-based Reynolds number and λ representing the flow Taylor microscale. First experimental evidence of this scaling was found by Seoud and Vassilicos 2007, in the wake of fractal grids in wind tunnel experiments. Later, Valente and Vassilicos 2012 generalized this dissipation scaling for a wider range of flow than fractal grid wakes. Using a global inlet Reynolds number based on the boundary conditions, Re_G, and a local Reynolds number based on some flow lengthscale, they found

$$C_\varepsilon \propto \frac{Re_G}{Re_L} \propto \frac{Re_G^{1/2}}{Re_\lambda} \tag{1.10}$$

in a significant portion of the decay region. Here, Re_L is based on the integral length scale and Re_λ on the Taylor microscale. This nonequilibrium dissipation scaling has also been recovered in direct numerical simulations of unsteady flows (Goto and Vassilicos 2015; Goto and Vassilicos 2016b). Experimental observations of this nonequilibrium turbulent energy cascade have been discussed in some results of this manuscript, particularly in chapter 3.

Even though a wide variety of flows seems to exhibit a nonequilibrium cascade in their decay region, the classic Richardson-Kolmogorov cascade is still believed to be present in various configurations, such as boundary-free flows, forced stationary turbulence in simulations and flows without interfacial layers.

1.1.5 Characterisation of turbulent flows

Integration of the dissipation spectrum

The mean energy dissipation rate ε is commonly estimated in wind tunnel experiments by integration of the dissipation spectra. For homogeneous and isotropic turbulence, the longitudinal fluctuating velocity one-dimensional spectrum $E_{11}(\kappa_1)$ along wavenumber κ_1 is related to ε by

$$\varepsilon = 15\nu \int_0^\infty \kappa_1^2 E_{11}(\kappa_1) d\kappa_1 \tag{1.11}$$

From the estimation of ε we can deduce the values of the Kolmogorov scale η, u_η, τ_η and the Taylor microscale λ. This scale, calculated as $\lambda = \sqrt{15\nu u'^2/\varepsilon}$ with u' the root mean square fluctuating velocity and ν the kinematic viscosity, is the transverse microscale defined for the first time by Taylor 1935.

While the aforementioned method is a common way to estimate ε and λ, another procedure, described in the following section, has been developed to characterize the energy cascade. Both techniques have been employed in this thesis.

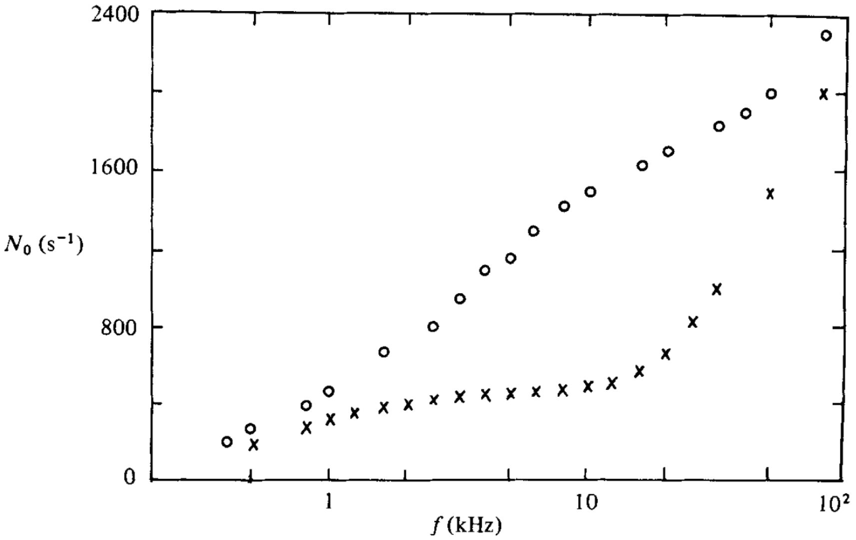

Figure 1.2: The measured zero-crossing frequency N_0 is plotted against the low-pass filter cut-off frequency f, taken from the study of Sreenivasan, Prabhu, and Narasimha 1983. The curve with cross symbols is derived from hot-wire measurements with a reasonably adequate signal-to-noise ratio. N_0 initially increases with f, until it reaches a plateau, from which we can determine the accurate value of N_0. For higher values of f, the number of zero crossings starts to increase linearly again due to white noise in the signal. The signal shown with round symbols has a low signal-to-noise ratio, and as a result no clear plateau can be distinguished.

Using stagnation points

In 1944, Rice 1944 explored the question of how frequently a stationary random process is expecting to cross a particular value (for instance zero) per unit of time. He derived a relation relating the expected rate of occurence of any value of a Gaussian variable with the probability density of the variable and its autocorrelation function. For the expected rate of zero, N_0, of a variable exhibiting a Gaussian probability density, Rice relation becomes:

$$N_0 = \frac{1}{\pi}[-f''(0)]^{1/2} \tag{1.12}$$

with $f(r)$ the normalised autocorrelation function of the signal and $f(0) = 1$. Later on, Liepmann and collaborators (Liepmann, Laufer, and Liepmann 1951; Liepmann, H.W. and M.S. Robinson 1953) were the first to apply the Rice theorem to a turbulent flow velocity signal as a way to determine its Taylor microscale. The Taylor microscale can be related to the behavior of the fluctuating velocity autocorrelation function in the vicinity of zero as $\lambda = [-f''(0)]^{-1/2}$. Using the expression of the Taylor microscale, Rice equation 1.12 can lead to:

$$N_0 = (\pi\lambda)^{-1} \tag{1.13}$$

However, the theorem given by Rice was derived for electrical noise issues and relies on assumptions that are not rigorously true for turbulent flows. It assumes that the velocity signal $u(t)$ and its derivative $\partial u/\partial t$ have Gaussian distributions. It also assumes that these two functions are uncorrelated, thus statistically independent. For turbulent flows, the first assumption is usually true, meaning that the velocity follows a Gaussian probability density but the same cannot be said for the velocity derivative. However, even when these assumptions are not valid, experimental work has shown the Rice theorem to hold for the determination of λ with turbulent signals presenting non-Gaussian distributions (Sreenivasan, Prabhu, and

Narasimha 1983; Mazellier and Vassilicos 2008).

The zero-crossing density can be affected by various factors, such as the dynamic range of the signal, noise, and the instrument's cutoff frequency. In order to accurately resolve the density of zero crossings, one should follow a systematic procedure to determine N_0 (Sreenivasan, Prabhu, and Narasimha 1983; Mora-Paiba 2020). This procedure consists of filtering the acquired velocity signal with a low-pass filter, for instance a fifth order Butterworth filter, at different filter sizes $\eta_C = 2\pi/\kappa$, with κ the wavenumber. The signal has to be previously converted from time to space with the use of Taylor's hypothesis, and the mean velocity has to be subtracted. The zero-crossing density, $N_0(\eta_c)$, (number of times the signal crosses zero divided by the signal length) needs to be evaluated for each filter size. By plotting N_0 against the filter size η_c (see Figure 1.2 for an illustration), a plateau should be observed for low wavenumbers to confirm that N_0 is properly resolved. The Taylor microscale can then be estimated as $\lambda = B(\pi N_0)^{-1}$, with B a constant, different than one, that accounts for the departure from Gaussianity in the velocity derivative.

1.2 Inertial particles

1.2.1 Equation of motion

The equation of motion for a sphere settling under gravity in a stagnant fluid was initially derived by Basset 1888, and then independently by Boussinesq 1903 and Oseen 1910. In this equation, known as the Basset-Boussinesq-Oseen equation, the fluid force acting on the sphere was calculated from the results of an unsteady Stokes flow. Later on, Tchen revisited this equation in an attempt to extend it to unsteady non-uniform flow, more relevant to turbulent flows applications (Tchen 1947). After Tchen's formulation, multiple discussions took place to reach a consensus regarding the terms of the forces exerting on the particle (Corrsin and Lumley 1956; Buevich 1966).

Today, the most accepted form of the equation of motion for small particles in a non-uniform flow is the one derived by Maxey and Riley 1983, and independently by Gatignol 1983. This equation relies on several assumptions. First of all, the particle is assumed to be spherical, rigid, non-deformable and non-rotating. The particle diameter, d_p, is considered small compared to the length scale of the flow variations, ensuring a uniform pressure gradient around the sphere. This equation is valid for low particle Reynolds number Re_p, i.e. $Re_p = d_p|\boldsymbol{v}^p - \boldsymbol{u}|/\nu << 1$ with $|\boldsymbol{v}^p - \boldsymbol{u}|$ the slip velocity where $\boldsymbol{v}^p$ is the particle velocity and $\boldsymbol{u}$ the fluid velocity at the particle's position. For a sphere of diameter d_p and mass m_p, the Maxey Riley equation can be written, at the lowest order in d_p, as:

$$\begin{aligned} m_p \frac{d\boldsymbol{v}^p}{dt} = {} & \underbrace{(m_p - m_f)\boldsymbol{g}}_{\text{Archimedes force}} + \underbrace{3\pi\mu_f d_p \left(\boldsymbol{u} - \boldsymbol{v}^p\right)}_{\text{Stokes drag}} + \underbrace{\frac{1}{2} m_f \frac{d(\boldsymbol{u} - \boldsymbol{v}^p)}{dt}}_{\text{Added mass}} \\ & + \underbrace{m_f \frac{D\boldsymbol{u}}{Dt}}_{\text{Pressure gradient}} + \underbrace{\frac{3}{2} d_p^2 \sqrt{\pi\mu_f\rho_f} \int_0^t \frac{d\left(\boldsymbol{u} - \boldsymbol{v}^p\right)/d\tau}{\sqrt{t-\tau}} d\tau}_{\text{Basset or history term}} \end{aligned} \tag{1.14}$$

where $v^p(t)$ represents the particle velocity and $\boldsymbol{u} = \boldsymbol{u}(\boldsymbol{x}_p(t), t)$ is the undisturbed fluid velocity at the particle's position, m_f the mass of fluid displaced by the sphere, μ_f and ρ_f the dynamic fluid viscosity and density respectively. $D/Dt = (\partial_t + \boldsymbol{u}\nabla)$ denotes the Lagrangian acceleration of the undisturbed flow and $\boldsymbol{g}$ is the gravitational acceleration vector. The different forces acting on the particle are explained in the following by order of appearance:

- The first term is the **Archimedes force**, which is due to gravity and buoyancy. It is uniquely caused by the difference of density between the two phases.
- The second term, **the Stokes drag force**, is due to the relative velocity between the fluid and the particle.
- The following term is the **added mass force**. This force is generated by the resistance of the fluid displaced by the particle during its acceleration/deceleration.
- **The pressure gradient term** is equivalent to the acceleration of a fluid element at the particle position.
- **The history term**, or Basset force, takes into consideration the memory of the particle motion in the carrier fluid up to the instant t. It mainly considers the particle interaction with its own wake.

This equation presents some limitations. It assumes that the sphere is isolated, neglecting particle-particle interactions or interactions with boundaries. Maxey-Riley & Gatignol's equation also introduces second-order corrections in d_p, known as Faxen corrections, to account for the non-uniformity of the fluid flow around the sphere due to finite-size effects. However, they are neglected here as they were shown to be irrelevant for heavy particles much smaller than the dissipative scale ($d_p \ll \eta$) (Calzavarini et al. 2009). In most cases, the Stokes drag term is the dominant force acting on the particle with the assumptions of low Reynolds number and a small diameter. If buoyancy forces are significant, the Maxey-Riley equation results in a balance between the Stokes drag forces and gravitational forces (Maxey 1987).

$$\frac{d\boldsymbol{v}^p}{dt} = \frac{1}{\tau_p}(\boldsymbol{u}(\boldsymbol{x}^p(t), t) - \boldsymbol{v}^p) + \boldsymbol{g} \tag{1.15}$$

where $\tau_p = m_p/(3\pi\mu_f d_p) = (\rho_p/\rho_f)d_p^2/(18\nu_f)$ is the particle relaxation time with a linear Stokes drag.

Equation 1.15 can be scaled with some characteristics flow parameters. If we use the r.m.s. of the velocity fluctuations u', and the Kolmogorov time scale, τ_η, the following dimensionless variables are introduced: $t_+ = t/\tau_\eta$, $\boldsymbol{x}_+ = \boldsymbol{x}/(u'\tau_\eta)$, $\boldsymbol{u}_+ = \boldsymbol{u}/u'$, $\boldsymbol{v}_+^p = \boldsymbol{v}^p/u'$ (Maxey 1987). The resulting equation of motion is

$$\underbrace{\frac{\tau_p}{\tau_\eta}}_{St} \frac{d\boldsymbol{v}_+^p}{dt_+} = (\boldsymbol{u}_+(\boldsymbol{x}_+^p(t_+), t_+) - \boldsymbol{v}_+^p) + \underbrace{\frac{\tau_p g}{u'}}_{Ro} \boldsymbol{e}_y \tag{1.16}$$

Two governing dimensionless parameters appear in the equation above: the Stokes number and the Rouse number. The Stokes, $St = \tau_p/\tau_\eta$, is calculated as the ratio between the particle relaxation time to a characteristic time scale of the flow, often the Kolmogorov time scale. It represents the importance of particle inertia due to its size and density. When the Stokes number is large, the particle cannot respond to the flow variations. Whereas for very low Stokes number, the particle behaves as a tracer, closely following the fluid parcels and responding to the smallest turbulent motions. Interesting phenomena in particles-turbulence interactions occur when St is of the order of unity.

The second dimensionless parameter is the Rouse number, denoted as $Ro = \tau_p g/u'$, and also known as the settling parameter. This parameter is the settling velocity in a stagnant fluid, $V_T = \tau_p g$, normalized by the carrier phase velocity fluctuations u'. It characterizes the competition between gravity and turbulence effects, and is particularly relevant for the settling of inertial particles in a gravitational field. A settling parameter based on the Kolmogorov velocity scale is also frequently used, $Sv_\eta = \tau_p g/u_\eta$ (Good et al. 2014; Berk and C. 2021).

In the simplest case, without gravity, for small and infinitely heavy inertial particles ($\rho_p >> \rho_f$), we can neglect all the forces except the Stokes drag. Equation 1.14 then reduces to:

$$\frac{d\boldsymbol{v}^p}{dt} = \frac{1}{\tau_p}(\boldsymbol{u}(\boldsymbol{x}^p(t), t) - \boldsymbol{v}^p) \tag{1.17}$$

This equation is extensively used in direct numerical simulations (DNS) studies (Squires and Eaton 1991; Wang and Maxey 1993; Bec et al. 2006; Ireland, Bragg, and Collins 2016b). One may take the temporal Fourier transform of equation 1.17 and get:

$$\hat{v}^p(\omega) = \frac{1}{1 + i\omega\tau_p}\hat{u}(\omega) \tag{1.18}$$

where $\hat{v}^p(\omega)$ is the Fourier transform of the particle velocity and $\hat{u}(\omega)$ the Fourier transform of the fluid velocity along the particle trajectory. This equation predicts that particle velocities are low-pass filtered versions of tracers' ones, with a transfer function given by $H = 1/(1 + i\omega\tau_p)$. The cutoff frequency, f_c, of this low-pass filter can be written as a function of the Stokes number $f_c = (2\pi\tau_\eta St)^{-1}$. Equation 1.18 illustrates that, for heavy and large particles, associated with a high Stokes number and a smaller cut-off frequency, the low-pass filtering effect becomes more pronounced. In that case, particle fluctuating velocity exhibit considerably reduced fluctuations compared to the carrier-phase. Conversely, in the limit case of very small Stokes number, particle velocity approaches the fluid, as they respond to the intense small-scale velocity fluctuations. Since this filtering process is attributed to the particle's inertia, it is commonly referred to as "inertial filtering". The filtering property of particles helps to extract information about the large-scale fluid-phase characteristics, and has been extensively used in this thesis to quantify background flow statistics, especially in chapter 5.

Apart from the inertial filtering effect, various interesting phenomena result from the interactions between particles and turbulence. Depending on the parameter range, particles have been shown to preferentially follow distinct flow features (Monchaux, Bourgoin, and Cartellier 2012), to have their settling rate modified compared to the one in a stagnant fluid (Maxey 1987), and to modulate the background turbulent flow (Gore and Crowe 1991; Elghobashi 1994). In the following, we will describe the phenomena of preferential concentration and settling velocity modification, as they are relevant to the range of parameters studied in this thesis.

1.2.2 Preferential concentration of particles in turbulence

One counter-intuitive property of turbulence is that an initially random distribution of particles is not going to be perfectly mixed by the turbulent motions. Instead, particles will tend to agglomerate preferentially in some specific regions of the flow, forming areas with high local particle concentrations, known as clusters, and depleted zones, called voids. This phenomenon is commonly referred to as "preferential concentration" or "inertial clustering", since it is related to the density difference between the particles and the fluid.

The definitions of preferential concentration and particle clustering may vary among authors. These two concepts are close but distinct. The interpretations presented in the following are the ones employed in this thesis. Clustering refers to the inhomogeneous spatial distribution of particles, composed of regions of very high and very low particle concentrations (clusters and voids). On the other hand, preferential concentration suggests that the distribution of particles is correlated with the local flow properties, as particles tend to visit some specific flow regions. To accurately demonstrate the presence of preferential concentration, it is essential to measure both phases and to correlate the local fluid velocity with particle positions.

A considerable amount of work has been accomplished over the last decades regarding the topic of particle clustering. Numerous studies have reported on the clusters' topology with their characteristic sizes (Aliseda et al. 2002; Baker et al. 2017), their fractal-like structures (Sumbekova et al. 2017; Baker et al. 2017; Petersen, Baker, and Coletti 2019) and their lifetime, temporal evolution and decay (Liu et al. 2020). Substantial efforts were made over the last decades to explain preferential concentration, leading to the proposition of various mechanisms. The centrifugation mechanism, for small Stokes number, has been proposed for an extended period (Maxey 1987; Squires and Eaton 1991; Wang and Maxey 1993), and more recently, the sweep-stick mechanism has gained attention for larger St (Chen, Goto, and Vassilicos 2006; Goto and Vassilicos 2008; Coleman and Vassilicos 2009). However, there is no consensus on a mechanism that could be responsible for inertial clustering across all turbulent scales.

Centrifugation mechanism

Early experimental measurements of particle concentration fields have noticed that particles tend to agglomerate in saddle regions between vortices (Lázaro and Lasheras 1989; Crowe, Chung, and Troutt 1988; Longmire and Eaton 1992; Eaton and Fessler 1994). Analytical and computational approaches have also offered useful insights: Maxey 1987 used asymptotic methods to demonstrate that particle inertia causes dense particles to accumulate in regions of low vorticity and high strain rate. The particle velocity, $\boldsymbol{v}^p$, can be expressed as an expansion involving the fluid velocity $\boldsymbol{u}$ and the Kolmogorov scale-based Stokes number, as discussed in Balachandar and Eaton 2010. If we compute the divergence of this expansion, we arrive at the following:

$$\nabla \cdot \boldsymbol{v}^p = -St(1-\beta)\Big(||S||^2 - ||\Omega||^2\Big) \tag{1.19}$$

Here, β represents the redefined particle-to-fluid density ratio, defined as $\beta = 3/(2\rho_p/\rho_f + 1)$, that takes into account added mass and pressure gradient forces. $S = \frac{1}{2}(\nabla \boldsymbol{u} + \nabla \boldsymbol{u}^T)$ and $\Omega = \frac{1}{2}(\nabla \boldsymbol{u} - \nabla \boldsymbol{u}^T)$ are the strain rate tensor and rotation rate tensor, respectively. In the case of heavy particles ($\beta < 1$), the above equation indicates that particles accumulate ($\nabla \cdot \boldsymbol{v}^p < 0$)

in regions where the strain dominates over vorticity ($||S||^2 > ||\Omega||^2$). This is consistent with the classical view that heavy particles tend to be expelled from the center of vortices and accumulate at their edges where the strain rate is important (Squires and Eaton 1991; Eaton and Fessler 1994). This preferential sampling mechanism has constantly been found to be more pronounced when the Stokes number is around unity (Wang and Maxey 1993; Eaton and Fessler 1994; Aliseda et al. 2002). However, it is worth noting that this centrifugation mechanism is related to the small turbulent scales and appears to be in conflict with increasing values of Re_λ, as a single scale cannot fully control the particle dynamics.

Sweep-stick mechanism

To account for the multiscale nature of turbulence and the fractal-like structures of particle voids, Vassilicos and collaborators proposed a mechanism for particle clustering valid in the inertial range (Chen, Goto, and Vassilicos 2006; Goto and Vassilicos 2008; Coleman and Vassilicos 2009). Initially described in two-dimensional simulated turbulence by Chen, Goto, and Vassilicos 2006, this mechanism was later extended to three-dimensional turbulence through direct numerical simulations (Goto and Vassilicos 2008; Coleman and Vassilicos 2009). In the absence of gravity, it suggests that particles are swept by the local fluid velocity to points where the local acceleration equals zero. Particles will then stick to these zero acceleration points.

The sweep-stick is applicable as long as particles have sufficient time to stick to the points of null acceleration. Consequently, the particle relaxation time τ_p must be significantly smaller than the lifetime of zero acceleration points. These zero acceleration points are known to be very persistent, with a lifetime of the order of the integral time scale of turbulence (Goto and Vassilicos 2008). As a result, this phenomenon is valid if $\tau_\eta < \tau_p < \tau_{\mathcal{L}}$. Experimental and numerical studies that have examined both the particle concentration and the fluid acceleration field have produced consistent results with this mechanism (Obligado et al. 2014; Mora et al. 2021a).

Besides their preferential concentration, particles immersed in a turbulent flow may also experience changes in their average settling rate compared to that in a stagnant fluid, $V_T = \tau_p g$. The following section focuses on the current state of knowledge and ongoing discussions regarding the settling velocity modification of inertial particles by turbulence.

1.2.3 Settling of inertial particles in turbulent flows

If we consider the gravitational settling of small heavy inertial particles, Maxey-Riley equation can be reduced to a balance between the Stokes drag and the gravitational forces:

$$\frac{d\boldsymbol{v}^p}{dt} = \frac{1}{\tau_p}(\boldsymbol{u}(\boldsymbol{x}^p(t), t) - \boldsymbol{v}^p) + \boldsymbol{g} \tag{1.20}$$

where $\boldsymbol{x}^p(t), \boldsymbol{v}^p(t)$ are the particle and fluid position, and $\boldsymbol{g} = g\boldsymbol{e}_y$ the gravitational acceleration with $\boldsymbol{e}_y$ directed toward gravity. Equation 1.20 is also frequently employed to account for gravity in particle dynamics in direct numerical simulation studies (Elghobashi 1994;

Balachandar and Eaton 2010; Ireland, Bragg, and Collins 2016a; Tom and Bragg 2019; Falkinhoff et al. 2020). For a statistically stationary system, the ensemble average of equation 1.15 projected in the direction of gravity gives

$$\langle v_y^p(t)\rangle = \langle u_y(\boldsymbol{x}^p(t),t)\rangle + \tau_p g \tag{1.21}$$

since $\langle \dot{v}_y^p(t)\rangle = 0$. The last term introduced in this equation is the particle terminal speed $V_T = \tau_p g$. From 1.21, we can see that the average vertical speed $\langle v_y^p(t)\rangle$ is different from V_T only if $\langle u_y(\boldsymbol{x}^p(t),t)\rangle \neq 0$ (Maxey 1987). If the particle concentration field is uniform, the Lagrangian-averaged fluid velocity $\langle u_y(\boldsymbol{x}^p(t),t)\rangle$ reduces to the Eulerian spatial average, and should be equal to zero in absence of mean vertical flow. Then, the question of whether the particle settling velocity differs from the one in a quiescent fluid depends on the value of the fluid velocity along the particle trajectory, $\langle u_y(\boldsymbol{x}^p(t),t)\rangle$.

If the value of $\langle u_y(\boldsymbol{x}^p(t),t)\rangle$ is greater than zero, then $\langle v_y^p(t)\rangle > V_T$, the particle settling speed is enhanced compared to its velocity in a stagnant fluid. Multiple evidences from both experimental and numerical studies, have demonstrated this effect to happen (Maxey and Corrsin 1986; Maxey 1987; Wang and Maxey 1993; Yang and Lei 1998; Aliseda et al. 2002; Ireland and Collins 2012; Bec, Homann, and Ray 2014; Ireland, Bragg, and Collins 2016b; Rosa et al. 2016; Monchaux and Dejoan 2017; Falkinhoff et al. 2020). Pioneering studies by Maxey and Corrsin 1986 have demonstrated that inertial particles in a simple cellular flow field settle more rapidly than in a stagnant fluid. Subsequent studies of Maxey 1987 and Wang and Maxey 1993 have also reported enhancement in a random Gaussian velocity field and with direct numerical simulations. Most theoretical results and simulations predict an increase in the settling rate with little exceptions (Maxey 1987; Yang and Lei 1998; Monchaux and Dejoan 2017; Tom and Bragg 2019; Tom, Carbone, and Bragg 2022).

On the opposite, if $\langle u_y(\boldsymbol{x}^p(t),t)\rangle < 0$ then $\langle v_y^p(t)\rangle < V_T$, and inertial particles settling is slowed down by turbulence (hindering). Although there are in proportion much less studies exhibiting settling reduction, a non negligible number of experiments and few DNS studies have reported evidences of this effect (Nielsen 1993; Ireland and Collins 2012; Akutina et al. 2020; Mora et al. 2021a).

A couple of studies have reported both types of settling rate modification (Good, Gerashchenko, and Warhaft 2012; Good et al. 2014; Petersen, Baker, and Coletti 2019; Akutina et al. 2020). Settling velocity enhancement is observed to occur at low Stokes and Rouse numbers, reaching a maximum for St and Ro of order unity. The average settling rate then gradually decreases as the Stokes and Rouse numbers increase, until reaching a critical Rouse or Stokes above which hindering of settling velocity becomes the main outcome. As a result, most studies have exhibited bell-shaped curves when plotting the velocity difference ($\langle v_y^p(t)\rangle - V_T$) against the Rouse or Stokes number. However, despite the significant amount of work on the subject, there is still no consensus on a parameter that would drive the transition between hindering and enhancement. The value of this critical Rouse or Stokes number, or any other parameter, that delimit the transition between both effects remains undetermined.

Effect of turbulence on the settling velocity.

One important topic of discussion regarding the settling velocity modification by turbulence concerns the relevant length and time scales that influences this phenomenon. There is a general agreement that the modification of settling velocity by turbulence is a multiscale phenomenon, involving a wide range of spatial and temporal scales. As a result, the choice of a unique flow scale cannot capture the entire dynamic (Yang and Lei 1998; Tom and Bragg 2019).

Yang and Lei 1998 have considered the role of the different scales affecting the settling velocity and proposed a mixed scaling, using both a large-scale velocity u' and a dissipative time scale τ_η. They argued that the small scales are important to the preferential sweeping mechanism, (further information about this mechanism is provided in the next section), since they govern the preferential concentration of particles on the downward side of eddies. However, the large-scale flow structures also play a significant role on the settling velocity, as the drag force on the particles depends mainly on u', associated to the large kinetic eddies. To account for the multiscale nature of turbulence, a recent study by Tom and Bragg 2019 proposed a theoretical analysis predicting that the range of scales contributing to the settling velocity modification depends upon the Stokes number. They demonstrate that $\langle v_y^p(t)\rangle$ is impacted by increasingly larger flow length scales with a monotonic increase in the Stokes number. Finally, a dimensionless parameter considering multiple turbulent scales that has gained a growing interest is the Rouse-Stokes number $RoSt$ (Ghosh et al. 2005; Good et al. 2014; Petersen, Baker, and Coletti 2019; Mora et al. 2021b). This Rouse-Stokes number, $RoSt = (V_T\tau_p)/(u'\tau_\eta)$, can also be expressed as the ratio between a particle characteristic distance and the Taylor microscale λ, $RoSt = \sqrt{15}(V_T\tau_p)/\lambda$.

Concerning the effect of the scale separation or the turbulent fluctuations, there is not a trivial dependence between the value of the turbulent Reynolds number Re_λ and the settling velocity modification $(\langle v_y^p(t)\rangle - V_T)$. Depending on the range of Reynolds number investigated, some studies have reported that the enhancement seems to increase with Re_λ (Nielsen 1993; Yang and Lei 1998; Bec, Homann, and Ray 2014; Rosa et al. 2016; Wang, Lam, and Lu 2018), while others show signs of an opposite trend (Akutina et al. 2020; Mora et al. 2021b). Overall, observations suggest that the dependence of the maximum enhancement on the Reynolds number is likely to be non-monotonic (Mora et al. 2021b; Yang and Shy 2021). The transition between enhancement and hindering, i.e., the so-called critical Stokes and Rouse numbers, also exhibits a non-trivial dependence with the carrier flow Reynolds number (Mora et al. 2021b). No simple scaling has been identified to describe either the peak of the settling velocity modification in the bell-shaped curves or the critical parameter delimiting the transition between enhancement and hindering.

Mechanisms of the settling velocity modification

Since turbulence has been shown to produce opposite effects on the settling velocity (hindering and enhancement) depending on the particle inertia and carrier phase properties, no single mechanism can be valid for the entire range of Stokes and Rouse number. Conversely, multiple mechanisms have been proposed, each valid for different ranges of nondimensional parameters. Among the various propositions, the preferential sweeping and the sweep-stick mechanism can be used to explain enhancement, while the loitering effect or non-linear drag can offer an explanation to hindering. Only the mechanisms relevant for small and heavy particles are described in this thesis since for light particles, for instance air bubbles in water, other phenomena may take place.

Preferential sweeping mechanism

In the same study mentioning the centrifugation mechanism, Maxey 1987 presented a detailed theoretical analysis for heavy particles with $St \ll 1$ to explain the enhancement of particle settling speed. He described the existence of a bias in the particles' trajectories toward regions of high strain and low vorticity due to their inertia, creating a net effect on their settling velocity. This mechanism explains that, owing to their high density, heavy particles are expelled outside of turbulent vortices and are carried along their edges. When combined with gravity forces, they tend to oversample the downward sides of eddies, where the fluid is moving on average in the direction of gravity.

Wang and Maxey 1993 confirmed the results from 1987 with direct numerical simulations of homogeneous and isotropic turbulence. They named this effect the preferential sweeping mechanism for the first time, also known as fast-tracking effect, and noticed that it is more pronounced when $St \approx 1$. The preferential sweeping mechanism has later been approved by various experimental and numerical studies (Aliseda et al. 2002; Good et al. 2014; Rosa et al. 2016; Monchaux and Dejoan 2017; Petersen, Baker, and Coletti 2019). To accurately demonstrate the presence of preferential sweeping experimentally, it is necessary to correlate the particle positions with the local flow statistics. Indeed, particle concentration fields have been shown to correlate much more with downward fluid motions than with high strain regions (Petersen, Baker, and Coletti 2019).

Recently, Tom and Bragg 2019 have extended the preferential sweeping mechanism proposed by Maxey 1987 to Stokes number larger than one. As mentioned earlier, this multiscale preferential sweeping mechanism provides insights into the role of the different scales contributing to the particle settling modification.

Sweep-stick

While the sweep-stick mechanism was originally described to explain particle clustering, it can be adapted to account for the presence of gravity. The arguments presented in Goto and Vassilicos 2008 suggest that when gravity is included in the equation of motion, inertial particles should stick to points where the acceleration field is equal to the gravity acceleration, i.e. $\boldsymbol{a} = \boldsymbol{g}$ (Hascoët and Vassilicos 2007). Falkinhoff et al. 2020 expanded the work on this mechanism by observing that particles tend to rather sample regions of low fluid accelerations.

Loitering

The main mechanism available to explain a reduced settling rate is the loitering mechanism (Nielsen 1993), which appears to be predominant for large Rouse and Stokes number. Particles that are too large to be preferentially swept by vortices tend to traverse both upward and downward moving regions of the flow with equal probability. However, rapidly falling particles spend more time crossing upward moving regions due to the larger slip velocity between them and the fluid, resulting in a higher instantaneous drag. The overall effect on the settling velocity is then expecting to result in a global decrease of the settling velocity. To highlight this loitering effect, Good et al. 2014 conducted direct numerical simulations in which particle trajectories were artificially confined to vertical paths to prevent preferential sweeping. They observed a reduction in particle settling in their simulations, and similar findings were presented in the study by Rosa et al. 2016, both attributing it to the loitering effect.

Non-linear drag

One topic of discussion deals with the influence of nonlinear drag effects that could arise for large particles, when the particulate Reynolds number is greater than one ($Re_p > 1$). DNS studies have recovered hindering of the settling velocity for large Rouse numbers by applying a non-linear drag to the particles (Wang and Maxey 1993; Good et al. 2014). However, other studies did not observe such reduction in settling velocity (Rosa et al. 2016).

1.2.4 Dynamics of inertial particles in inhomogeneous turbulence

Interestingly, most of the early work on the influence of turbulent structures over a particle concentration field was provided by studying particles in free shear flows (Eaton and Fessler 1994; Crowe, Chung, and Troutt 1988). Indeed, those early studies provided compelling experimental evidence of the preferential concentration phenomenom (Monchaux, Bourgoin, and Cartellier 2012). Free shear flows, such as mixing layers, jets and wakes, are governed by large-scale organized structures. The regularity of these large structures creates the perfect environment to understand how particles interact with turbulent eddies. Some simple observations emerged from these early studies: particles are avoiding vortex cores and concentrate at the edges of vortices. These observations served as a fundation for describing basic mechanisms that occur across various flows.

In the following, we will discuss the main experimental findings on particle-turbulence interactions within planar mixing layers and jets. We will also describe the up to date experimental work that was undertaken to study particles in a shear-less turbulent/non-turbulent interface.

Plane mixing layers

The seminal study by Brown and Roshko 1974 demonstrated that turbulent plane shear layers feature a regular series of quasi-two dimensionnal large-scale vortices. Early two-phase flow experiments with mixing layers mainly focused on the dispersion of inertial particles (Kamalu et al. 1988; Lázaro and Lasheras 1989; Lázaro and Lasheras 1992). They revealed that heavy particles can disperse more effectively than fluid parcels within an intermediate range of Stokes number, while for very low Stokes numbers, particles disperse at the same rate as the carrier phase. Simultaneous visualization of both the flow and the particulate phase of particle-laden mixing layers revealed that vortex core are devoided of particles, while particles cluster in thin rings surrounding the large vortices (Lázaro and Lasheras 1989). Additionally, larger particles are shown to be flung outside the layer, resulting in a non-uniform droplet size distribution (Lázaro and Lasheras 1989). Numerical simulations of particle-laden mixing layers corroborated the experimental observations on particle dispersion (Crowe, Gore, and Troutt 1985; Chein and Chung 1988). In most studies, the fluid time scale used to characterize particle inertia is based on the properties of the mixing layer, that is to say ΔU the velocity difference across the layer and δ the characteristic width of the vortices, $\tau_f = \delta/\Delta U$. It results in a large-scale local Stokes number that varies with streamwise position as the layer grows along the longitudinal coordinate.

Jets

The near field of a jet can be thought of as an axisymmetric mixing layer, where the flow is dominated by mostly two-dimensional large vortex rings. Results from jet studies present qualitatively the same particle behavior and mechanisms as mixing layer studies. Indeed, the particles' lateral dispersion have been found to be larger than that of fluid parcels for a Stokes number around unity (Chung and Troutt 1988). The spanwise coherent vortices are described to be responsible for the large variations in particle concentration and their lateral dispersion. The outcome revealed by jet studies that probably differs the most from mixing layers analysis is the formation of particle clusters in high strain regions between the vortex rings (Longmire and Eaton 1992; Eaton and Fessler 1994).

Shearless turbulent/non-turbulent interface

One interesting case of study is a turbulent interface between a turbulent flow and an irrotational region moving at the same uniform speed. This ideal flow offers the possibility to study the dynamics and propagation of a turbulence front without any turbulent energy production caused by a mean shear. Although numerous numerical studies have investigated this specific flow (Befeno and Schiestel 2007; Ireland and Collins 2012; Fathali and Deshiri 2016; Elsinga and da Silva 2019), this configuration has proven to be more challenging to create experimentally (Corrsin and Kistler 1955; Veeravalli and Warhaft 1989). Nevertheless, Warhaft and collaborators have managed to create such a shearless turbulent/non-turbulent interface in a wind tunnel facility (Veeravalli and Warhaft 1989; Gerashchenko, Good, and Warhaft 2011; Good, Gerashchenko, and Warhaft 2012; Gerashchenko and Warhaft 2013). In their original experiments, Veeravalli and Warhaft 1989 used a parallel bar grid (or a perforated plate) with variable grid spacing (or different hole sizes) across the cross-sectional area, while conserving the same mean blockage to obtain an homogeneous mean velocity. For the particle-laden turbulent interface experiment, an active grid was employed in the particle-laden high-turbulence region, while damping screens were used in the unladen, low-turbulence region to compensate for the pressure drop and homogenize the mean field (Gerashchenko, Good, and Warhaft 2011; Good, Gerashchenko, and Warhaft 2012). The dynamics of inertial particles entrained into an adjacent flow was examined for two different mixing regions: a turbulent/non-turbulent interface and turbulent/turbulent interface.

In the case of the turbulent/non-turbulent interface, both carrier phase velocity and particle velocity exhibited strong non-Gaussian distributions. This deviation from Gaussianity is attributed to large-scale intermittent "bursts" coming from the high-turbulence side and penetrating the adjacent laminar flow. The droplets small-scale statistics are similar inside the bursts and within the homogeneous isotropic region. Indeed, particles transported by these large-scale eddies conserve their size distribution and acceleration statistics. The radial distribution functions of the droplets positions revealed both large-scale preferential concentration due to the intermittent entrainment process and dissipative-scale clustering caused by particle inertia.

Conclusion

In conclusion, it is widely accepted that, in various flows, preferential concentration is most pronounced when the Stokes number is around unity. However the appropriate time scale to estimate this Stokes number has to be related to the vortex motions that actually preferentially concentrate the particles (Eaton and Fessler 1994). In most turbulent flows, vortical structures have a wide range of scales and particles may be concentrated by different sized eddies depending on their diameter, and thus their Stokes number. The problem becomes even more complex if the background flow is a mixing region between two turbulent flows with different inertial range characteristics and scale separations. For instance, the interface between a fully developed turbulent flow and a laminar flow or two co-flows featuring different large scale structures. Although there is a multitude of studies on the dispersion of inertial particles in free shear flows and homogeneous isotropic turbulence, there is a scarce number of experimental research regarding the impact on inertial particle dynamics when they travel from a highly turbulent environment into a less turbulent region.

Despite the insight brought by previous studies, there are still some fundamental questions that remain unanswered regarding the dynamics of inertial particles in such flows. Do they cluster similarly as in homogeneous turbulence ? In other words, if the interface is governed by large scale energetic eddies will the dissipative scales of turbulence still impact inertial particle clustering as in homogeneous isotropic turbulence ? Which scale of turbulence has the most impact on their concentration distribution ? How is the inertial particle settling velocity affected by the turbulent motions while they travel across the mixing layer ?

1.3 Thesis overview

In order to answer the previous issues, two experimental campaigns were conducted in two different experimental facilities, in LEGI (Laboratoire des Ecoulements Géophysiques et Industriels) and in the Department of mechanical Engineering of the University of Washington. The dynamics of heavy, sub-Kolmogorov inertial particles was examined in both homogeneous and isotropic turbulence and in a turbulent interface, using both Eulerian and Lagrangian experimental techniques.

A description of the two experimental facilities and the measurement techniques used are presented in chapter 2. The main results of this thesis are organized in three main parts.

- The first part of this thesis, chapter 3, examines new methods to characterize the turbulent carrier phase. This first work introduces a method to compute single-phase turbulent flows Reynolds number from the zero-crossings of the longitudinal velocity fluctuations. Previously, the Rice theorem and the MacFadden equation were applied to a turbulent flow signal to estimate both the Taylor microscale and the integral length scale, respectively. By combining both formulas, an expression can be deduced to determine the flow Reynolds number using solely statistics of the fluctuating velocity zero-crossings. The relation was tested with hot-wire anemometry measurements in

three different turbulent flows, an active-grid, a passive grid and a planar wake (taken in LEGI and LMFL). From that expression, we can see that the Reynolds number is mainly related to the zero-crossings voids statistics. By means of uni-dimensional Voronoï tesselations, we studied clusters and voids of zero crossings. We found that both zero-crossings voids and clusters average size are proportional to the Reynolds number.
This work was extended by the study in Appendix A, which presents an attempt to apply the Rice theorem to two-phase, three-dimensional flows. This study utilizes datasets from direct numerical simulations of both single-phase and two-phase flows, employing a random forcing to generate homogeneous and isotropic turbulence at five different turbulent Reynolds number. For the dispersed phase, both tracers and inertial particles were integrated in the simulations, using a minimal model of heavy, point particles for the inertial case. A three-dimensional Eulerian particle velocity field was reconstructed by interpolation of their Lagrangian velocities. We then attempted to apply the generalized Rice theorem to the stagnation points positions of the single-phase and particle-phase velocity field. We confirm that, for the carrier phase, the Taylor length scale is proportional to the average distance between stagnation points. However, for the two-phase flow simulations, the Rice theorem cannot be applied to estimate the Taylor microscale due to the intense stagnation points clustering.

- Chapter 4 focuses on examining the settling velocity of heavy, sub-Kolmogorov water droplets in wind tunnel grid-generated turbulence. This experimental study was conducted in the LEGI wind tunnel, where turbulence can be produced with three different grid configurations. The various grids allow us to cover a wide range of turbulence conditions and Taylor Reynolds number Re_λ. We observe that settling enhancement decreases significantly with the Taylor-Reynolds number thanks to this wide range of flow parameters. The influence of the large scale forcing was also investigated as the different grids allow us to study cases with fixed Re_λ and turbulent intensity but significantly different integral length scale. This study shows that for the range of parameters studied (Stokes number, Rouse number and volume fraction), the large scale structures have a significant impact on the settling rate. Smaller large scales in the flow are associated with higher enhancement of the settling velocity.
- Chapter 5 presents the work conducted in Alberto Aliseda's wind tunnel, at the University of Washington. The dynamics of dense, sub-Kolmogorov water droplets were investigated in a wind tunnel inhomogeneous turbulent flow. In this wind tunnel, turbulence is generated using a passive grid, supporting 81 independent gas/liquid sprays for droplets atomization. These air atomizers, contributing significantly to the mean velocity and fluctuations, can be activated independently to vary the turbulent intensity across the cross-section. Particles are exclusively introduced into the high-turbulence region, and our primary interest is about studying their entrainment within the adjacent, particle-free air flow. We observe that particle velocities distributions are not Gaussian across the interface and that particle clustering and settling velocity are enhanced in the mixing region. Moreover, conditional statistics on particle velocities and mean number densities show that particles oversample high-energetic events of the flow. This confirms previous studies, stating that they are transported into the low turbulence side by large-scale "bursts".
- The final chapter of this thesis gives a brief description of the Particle Tracking Velocimetry campaign conducted in Seattle during the summer of 2023. While this

study is still ongoing, we present preliminary results for homogeneous isotropic turbulence.

Experimental methods

2

2.1 Experimental facilities

As discussed in chapter 1, two different experimental facilities were used in this thesis. A first set of experiments were conducted in the Lespinard wind tunnel in LEGI (laboratoire des Ecoulements Geophysiques et Industriels) in Grenoble, France. Another series of experiments was then carried out with the Chibchacum wind tunnel at the Mechanical Engineering Department of the University of Washington, Seattle. A description of both facilities is provided in the following sections.

2.1.1 Experimental setup in LEGI, France

The Lespinard wind tunnel, built in the late 1960s, is still a very well designed, versatile and extensively used facility (Lespinard 1968). It is a closed circuit wind tunnel with a 4 m-long test section and a cross sectional area of 0.75m × 0.75m. A sketch of the wind tunnel test section is provided in Figure 2.1(a). The entire facility is composed of two counter rotating fans, a settling chamber and a convergent section with a contraction coefficient of 12 upstream of the test section. The total equipment measures 16.0 m long, 5.0 m high and 2.6 m wide. Great care in the design was taken to ensure a uniform mean velocity profile. The mean streamwise velocity can be varied over the range $U_\infty \in [2 - 45]$m/s.

One advantage of the wind tunnel in LEGI is the possibility to modify the wind tunnel's turbulent intensity with a wide range of different inlet conditions. For an empty test section, the flow is completely laminar with a turbulent intensity below 0.2%. A moderate turbulent flow can be generated with the use of a passive grid, allowing to get a Taylor-based Reynolds number in the range $Re_\lambda \in [30 - 100]$. An illustration of the passive grid used in LEGI can be found in Figure 2.1(c). With the use of an active grid (see picture in Figure 2.1(b)), the Taylor-based Reynolds number can reach higher values, up to a couple of hundred.

Another interesting feature of the Lespinard wind tunnel is the possibility to study particle-laden flow with the injection of water droplets. A rack of 36 droplet injectors can be positioned right downstream the turbulence generative grid to distribute the water drops uniformly across the cross-section. Water flow rate and air flow rate achievable in this facility gives values of volume fraction, ratio between the liquid and air volumetric flow rate ϕ_v, of the order of $10^{-6} - 10^{-5}$.

2.1.2 Experimental setup at the University of Washington, USA

The facility in the Multiphase and Cardiovascular flow lab in Seattle is an open-loop wind tunnel with a 4.0m long test section and a 1.0m × 1.0m constant cross-sectional area. This wind tunnel has previously been characterized and used in former experimental studies (Bateson

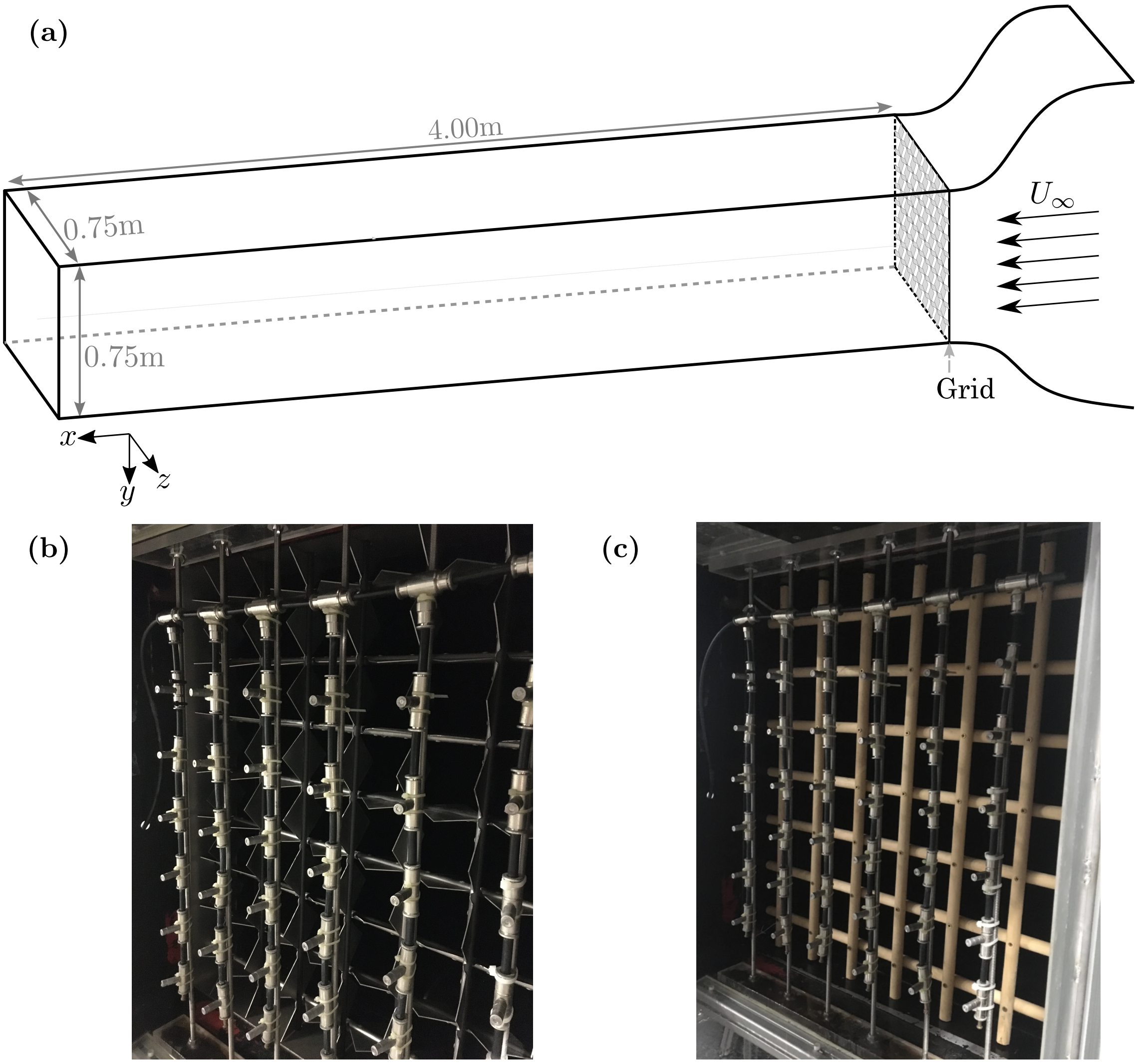

Figure 2.1: The experimental facility of the Lespinard wind tunnel with the different grids available. (a) Schema of the Lespinard wind tunnel in LEGI. (b) The active grid in open configuration (with the blades minimizing blockage and the axis remaining static). (c) The regular passive grid.

and Aliseda 2012; Huck et al. 2018). The test section walls are made of acrylic panels, allowing full optical access. The free-stream velocity is generated using a rack of 25 PC fans. Before entering the test section, the airflow passes over a passive grid made of 9 × 9 aluminium tubes, forming a square mesh with a mesh size M of 10 cm. An illustration of the facility can be found in Figure 2.2(a).

An important characteristic of this wind tunnel is the possibility to study turbulent flow laden with water droplets thanks to an adequately designed atomization system. Indeed the passive grid serves two purposes: it generates homogeneous and isotropic turbulence in the test section and it supports the water droplet injection system. For the injection of droplets, 81 atomizers are positioned at each intersection between a horizontal and a vertical grid bar. Each injector consists of an air jet impacting a water jet at a significant angle, resulting in the liquid atomization and the formation of a dense spray of micrometer-sized droplets. Injectors water and air supply lines are placed inside the tubing of the passive grid axes. To create a uniform distribution of droplets, each injector has to receive the exact same flow rate. However, the height difference in the grid can create pressure losses between the top

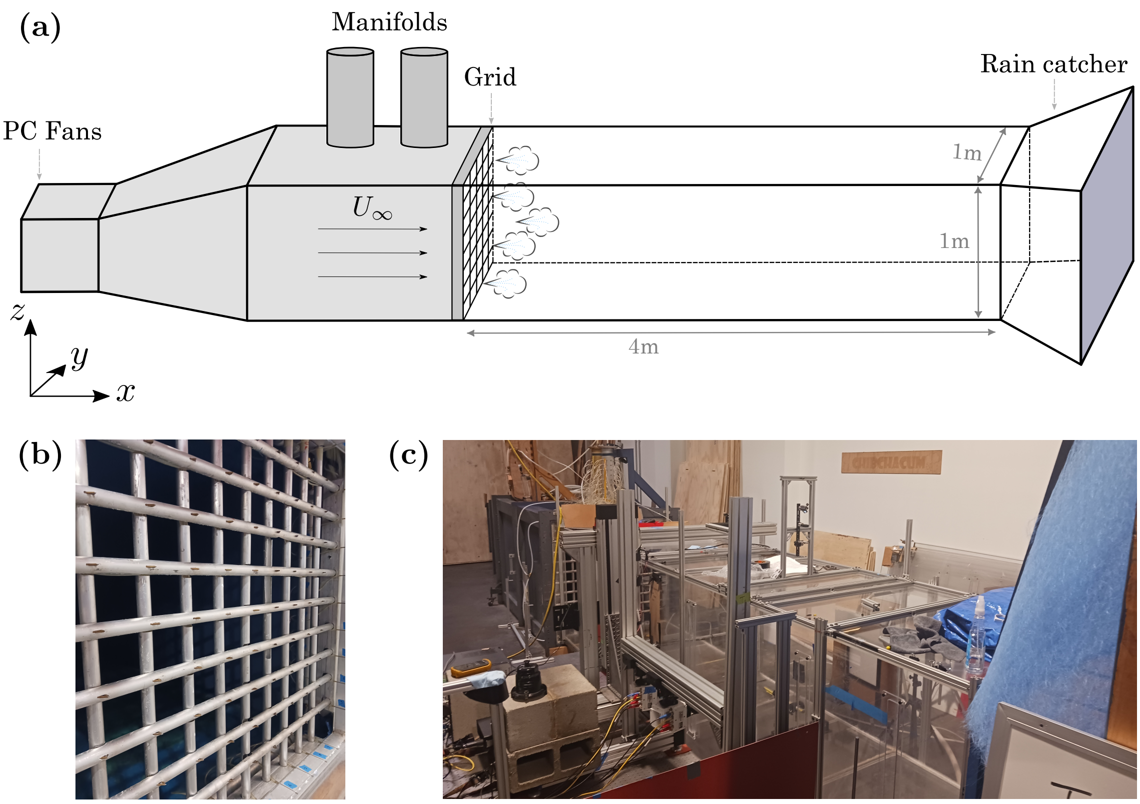

Figure 2.2: The experimental facility at the University of Washington. (a) Schema of the wind tunnel with the PC fans, the air and water manifolds and the passive grid. (b) Image of the passive grid with the droplet delivery system. (c) Picture of the experimental facility.

and bottom injectors. To circumvent this problem, microtubings are installed in the manifold outlets to produce a pressure drop compensating for the hydrostatic pressure difference. Droplet size distribution and volume fraction can be controlled by varying the water and air flow rate independently.

The air jets from the atomizers generate a significant momentum to the main airflow, contributing significantly to the mean velocity and background turbulence intensity. With this facility, it is possible to activate the water and air supply for each droplet injector independently. Given the substantial contribution of the atomizers to the degree of turbulence, it is possible to create a gradient of turbulent intensity by deactivating a portion of them. For instance by turning off only the atomizers situated on one side of the cross sectional area a turbulent interface may be created.

2.1.3 Wind tunnels comparison

As a conclusion, table 2.1 recapitulates the main characteristics of both facilities.

Table 2.1: Experimental facilities in both laboratories.

	Facility	Test section [m^3]	Velocity range [m/s]	Passive grid	Active grid	Droplet injection control
LEGI	closed-circuit	$0.75 \times 0.75 \times 4.0$	$2 - 45$	yes	yes	no
UW	open-circuit	$1.0 \times 1.0 \times 4.0$	$1 - 5$	yes	no	yes

2.2 Measurement techniques

Several experimental techniques were used in this thesis to measure fluid velocity in single-phase flow (hot-wire anemometry, cobra probe) and particle statistics in two-phase flow (Phase Doppler Particle Analyser, Particle Tracking Velocimetry). An explanation of each experimental instrument is given in the following sections.

2.2.1 Hot-Wire Anemometry

Hot-wire anemometry is a commonly used technique to measure fluid velocity in turbulent flows (Comte-Bellot 1976). It consists of a thin heated wire immersed in the flow and positioned perpendicular to the velocity component to be measured (see illustration in Figure 2.3). Since the wire is maintained at a higher temperature than the flow, a heat transfer will occur between the flow and the wire. The fluid is then acting as a cooler and the energy transmitted from the wire into the flow is function of the fluid velocity.

In the case of constant temperature anemometry (CTA), the wire temperature and resistance are kept constant. To compensate the loss of heat in the wire, the current passing through the wire is adjusted by an electrical circuit with a Wheatstone bridge. The voltage E proportional to the current is then function of the velocity component perpendicular to the wire $U_\perp$. The fast response of the wire to the surrounding fluid makes it very useful to sample flows with rapid velocity variations with a high temporal resolution.

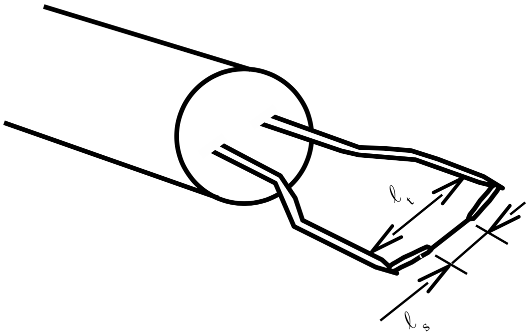

Figure 2.3: Example of a hot-wire probe. The wire is oriented perpendicular to the velocity component to be measured.

A semi-empirical correlation, known as King's Law, gives the relation between the measured voltage and the fluid velocity:

$$E^2 = a + bU_\perp^n \tag{2.1}$$

The constants a, b, n depend upon the working temperature, properties of the wire, cable and support system. Since those parameters can vary with time, it is necessary to estimate them for each series of measurements. In both wind tunnel, the calibration was conducted with a Pitot tube and a differential pressure sensor. For each calibration, we recorded the mean streamwise velocity using the Pitot tube and the mean voltage given by the hot-wire. These measurements were taken for different wind tunnel inlet velocities to determine the values of a, b and n, with n ranging between 0.4 and 0.5. The ambient temperature should remain constant during both the calibration and the series of measurements.

In LEGI, the Pitot tube was placed in the convergent section to measure the bulk inlet velocity coming into the tunnel, U_∞. The Pitot tube pressure difference, ΔP, was recorded with a manometer and Bernouilli's relationship was used to compute U_∞ from ΔP. To account for the velocity acceleration when the air stream is exiting the convergent section, a contraction coefficient $Corr = 1.18$ was taken into consideration. In the end, $U_\infty = Corr \times \sqrt{\frac{2\Delta P}{\rho}}$, where ρ is the fluid density, estimated each day with the ambient pressure and temperature and the law of ideal gases.

At the University of Washington, the Pitot tube was placed adjacent to the hot-wire. A differential pressure transducer, connected to the Pitot, measured a pressure difference ranging from 0 Pa to 25 Pa, corresponding to a change in current ranging from 4 to 20 mA. An electrical circuit was created to convert the current change into a voltage variation, which was acquired with a data acquisition card. The Pitot tube had been previously calibrated with a flow controller, capable of creating a flow with a known flow rate, to establish the conversion between voltage changes and velocity variations. The hot-wire was then calibrated, in the centerline, by varying both the wind tunnel fans and the atomizers' air flow rate, with the use of the previously calibrated Pitot tube.

2.2.2 Cobra probe

The Cobra Probe is a multi-hole pressure probe that provides all three velocity components. This probe (Series 100 Cobra Probe, Turbulent Flow Instrument TFI, Melbourne, Australia) functions as a three-dimensional Pitot tube capable of measuring flow within a ±45° angle cone. It gives access to the three velocity components u, v and w, as illustrated in Figure 2.4. In other words, it allows us to determine the velocity magnitude V, as well as the pitch angle θ and yaw angle ψ (see Figure 2.4(b)). The probe can measure streamwise velocity in a range from $2\,\mathrm{m/s}$ to $100\,\mathrm{m/s}$ with a sampling frequency up to 1250 Hz. The probe's sampling frequency is limited by its finite size. Having a sensing area of $4\mathrm{mm}^2$, it introduces spatial filtering, limiting its ability to sample frequencies as high as the hot-wire. Since turbulent fluctuations can reach higher frequencies, the probe filters out the smallest scales of turbulence (Obligado et al. 2022). When the Cobra Probe head aligns perfectly with the incoming flow direction, the velocity components in the y and z directions, as well as the mean pitch and yaw angles, average to zero.

2.2.3 Phase Doppler Particle Analyzer (PDPA)

Since the Phase Doppler Particle Analyser is an instrument that has been extensively used throughout this thesis, we provide a detailed description of this measurement technique.

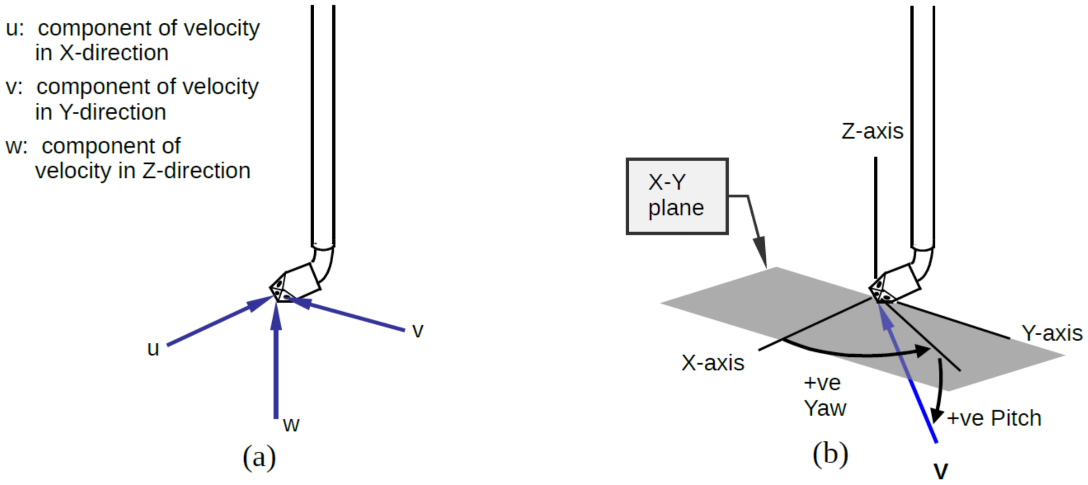

Figure 2.4: (a) Flow axis system with respect to the Probe head. (b) Positive flow pitch and yaw angle. Taken from *Getting Started Series 100 Cobra Probe User Manual*.

Principle of the technique

Phase Doppler Particle Anemometry is a non-intruise optical technique allowing simultaneous Eulerian measurement of particles' diameter and velocity (Bachalo 1980; Bachalo and Houser 1984). The principle of the method is as follows. A monochromatic laser beam is split into two coherent and identical light beams with different optical paths. An optical lens in the transmitter (device emitting the laser) focuses the two beams. Their intersection creates an interference pattern of parallel fringes, as illustrated in Figure 2.5. The beams crossover position defines the measurement volume, which is typically of the order of . The spacing between two consecutive fringes, δ, is determined by the beam intersection angle, α, and the laser wavelength λ following this relation:

$$\delta = \frac{\lambda}{2\sin(\alpha/2)} \tag{2.2}$$

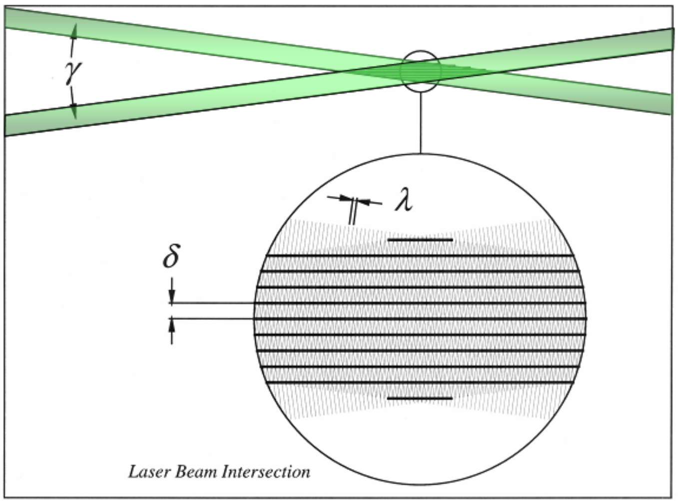

Figure 2.5: Schematic showing the laser beam intersection and the interference fringe pattern created at the sample volume. Taken from *PDI-200 MD User Manual*.

When a water droplet crosses the interference pattern, it refracts and reflects the light intensity in every direction (see Figure 2.6). The interference fringes scattered by the particle generate a light signal that fluctuates in intensity with a frequency related to the particle's velocity and the fringe spacing. This signal, called a Doppler burst signal, is detected by a photo-detector in the receiver. The particle velocity v^p is proportional to the Doppler signal frequency, f_D, and the fringe spacing, δ:

$$v^p = f_D \delta \tag{2.3}$$

The angle between the transmitter and the receiver must be carefully chosen to have a single predominant scattering mechanism. For water droplets in air, the most commonly used scattering mode is refraction. Typically, this means that the optimum angle between the receiver and the incident light axis is 30°. Indeed, off-axis angles of detection have been shown to be more efficient than on-axis scattered light detection and can be employed with a higher particle number density (Bachalo 1980). With this technique, only one particle can be detected in the measurement volume at a time. The receiver aperture limits the detection of light scattered within the sample volume, preventing droplets crossing the beams outside of the sample volume to introduce noise into the signal.

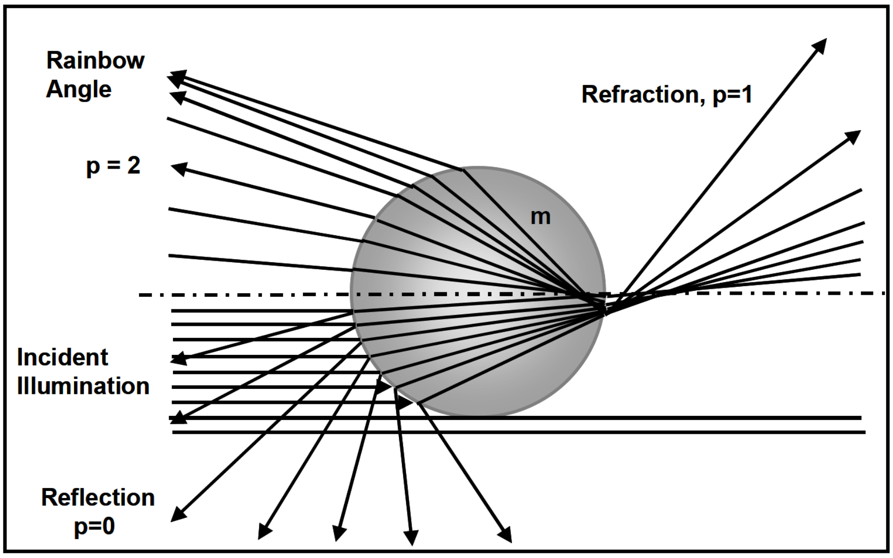

Figure 2.6: Diagram showing the scattering of incident light rays on a spherical drop. Taken from *PDI-200 MD User Manual.*

If the interference pattern is static, two droplets crossing the measurement volume with same velocity but opposite directions will produce the exact same Doppler signal. To determine the sign of the particle velocity, the solution is to introduce a frequency shift to one of the two beams using a Bragg cell. Typically, a frequency shift of 40 MHz is added to the raw Doppler signal frequency.

Figure 2.7 presents a typical Doppler burst signal. This signal is composed of a high frequency Doppler component superimposed on a low-frequency pedestal part due to the Gaussian light intensity across the measurement volume. A series of different filters is applied to the Doppler signal: a high pass filter to remove the pedestal component and a low pass filter to remove the very high frequency noise.

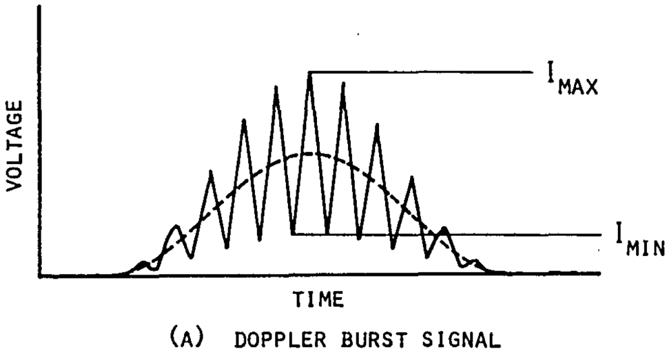

Figure 2.7: Typical Doppler burst signal showing the Doppler and pedestal component. Sketch taken from Bachalo 1980

This technique allows simultaneous measurement of multiple velocity components. In practice, to sample particles' velocities in two different directions, two distinct laser beams with different wavelengths are necessary. Their interference fringe patterns are made orthogonal to each other, and each of them is employed to measure particles' speed in their plane of intersection, perpendicular to their fringes.

The previous description forms the foundation of any laser Doppler velocimetry (LDV) system. The Phase Doppler Particle Analysis (PDPA) technique developed by Bachalo and Houser 1984 allows for the measurement of particle diameters in addition to velocity. Water droplets act as small spherical lenses when interacting with a light beam. They magnify the light fringes with a magnification proportionate to their sizes. Thus, light rays emerging from the spherical droplet will have varying optical path lengths depending on the size of the sphere. The idea introduced by Bachalo and Houser 1984 involves the use of multiple photo-detectors positioned within the receiver at known spatial separation. The phase shift, denoted as ϕ_{1-2}, between a pair of collected Doppler signals is related to the physical distance between the two detectors, the scattering mode, the fringe spacing and the particle radius. ϕ_{1-2} has been shown experimentally to be linearly proportional to the droplet diameter d_p, as shown in Figure 2.8(b) (Bachalo and Houser 1984).

$$\phi_{1-2} \propto \pi \delta^{-1} d_p \tag{2.4}$$

In principle, two detectors are sufficient to determine the particle diameter. However, three detectors are necessary to ensure unambiguous measurements. This arises from the fact that phase shifts can only be measured within the range of 0 to 2π, limiting the range of measurable diameters. For instance, if a large droplet produces a phase shift greater than 2π, an error in the diameter determination could occur. A third detector will identify the correct diameter among several options with a 2π phase difference (see Figure 2.8(a)). The physical distance between two detectors controls the measurable size range and sensitivity. One pair of photodetectors provides a broad range of measurable diameters, while the second pair enhances measurement accuracy.

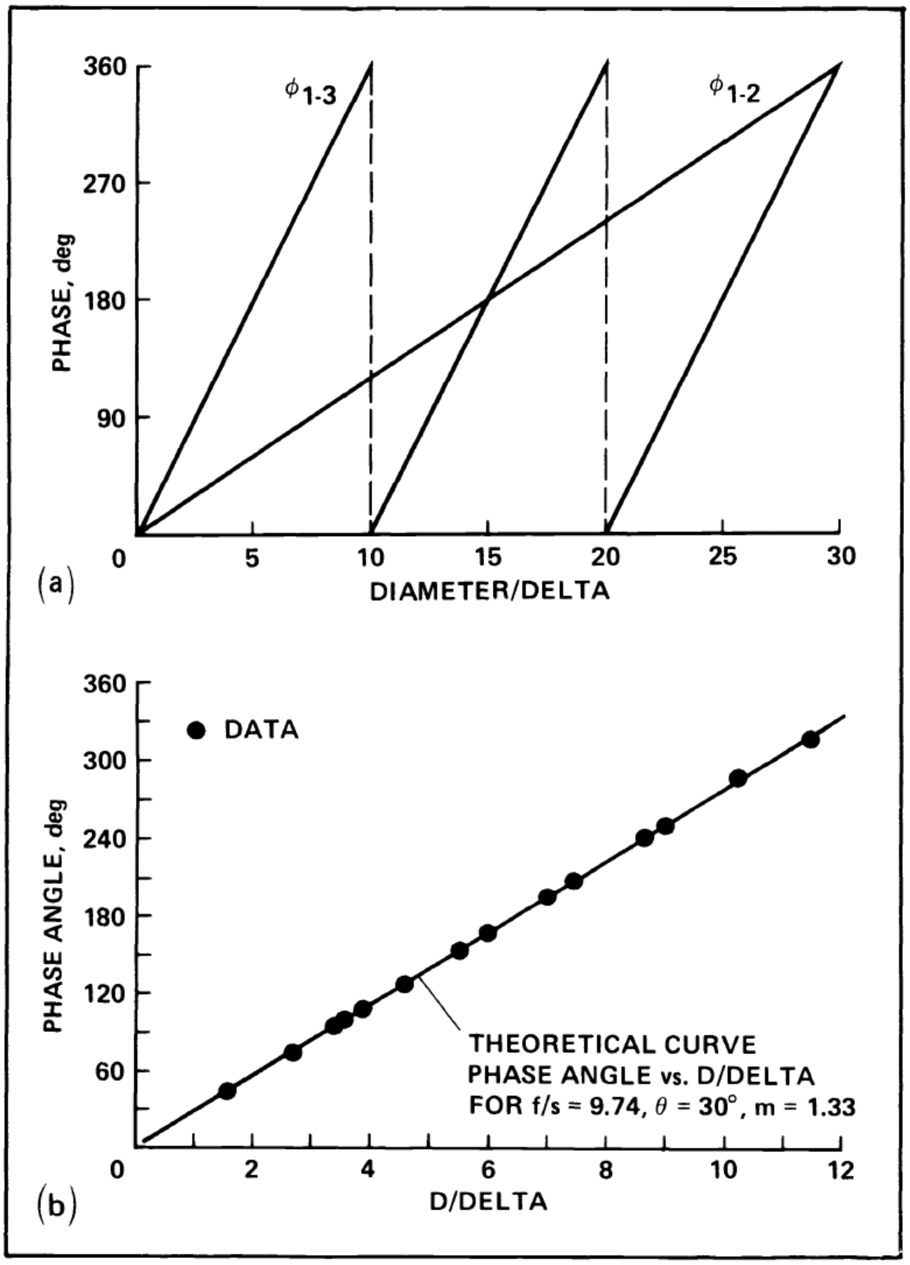

Figure 2.8: Theoretical prediction showing the phase variation with the dimensionless drop size: (a) relationship for three detectors and (b) comparisons with experiment. Taken from Bachalo and Houser 1984.

PDPA setup and parameters

Optical setup in LEGI:

The PDPA system at LEGI is a PDI-200MD (Artium Technologies), capable of measuring two velocity components. The receiver was positioned at an off-axis angle of 30 degree relative to the incident light axis at the opposite side of the wind tunnel, to measure forward scattering. The transmitter emits two solid-state lasers, one green at a 532 nm wavelength and one blue with a 473 nm wavelength. The 532 nm beam is set up to simultaneously measure the particle's vertical velocity and diameter, while the blue beam is oriented to measure the horizontal velocity. PDPA measurements were taken in non-coincident mode, i.e. horizontal and vertical velocities were recorded independently, since the coincident mode can significantly reduce the validation rate. Both transmitter and receiver had a similar focal length of 500 mm. This enabled us to record the vertical velocity component with a resolution of 1 mm/s. This PDPA configuration allows us to detect particles with diameters ranging from 1.5 µm to 150 µm. Depending on the water flow rate and wind tunnel inlet velocity, the measurement sampling rate varied from 20 Hz to 4800 Hz with an average of 1030 Hz and 580 Hz for the streamwise and vertical velocities, respectively.

Optical setup at the University of Washington:

The PDPA system used at the University of Washington was manufactured by TSI Incorporated. Two velocity components were captured as well. A green laser beam with a 515 nm wavelength was used to measure the horizontal component, while the vertical velocity was recorded with a 488 nm blue beam. The PDPA transmitter was positioned facing the right wall of the wind tunnel. The PDPA receiver was placed above the tunnel at a 61 degree angle from the beam direction due to experimental constraints. As the receiver looks into the wind tunnel at an angle, it creates a problem with the refraction of light as it passes through the top of the wind tunnel. To address this issue, two triangular acrylic prisms were attached to both sides of the test section's upper wall. A thin layer of glycerol, with a similar refractive index as acrylic, was added between the acrylic prisms and the wall to minimize light scattering. The emitter has a focal length of 500 mm, allowing measurements to be taken approximately at the centerline of the test section, while the receiver's focal length is 750 mm. Both transmitter and receiver were attached to the same traverse system, allowing them to be displaced simultaneously in the spanwise direction without losing their alignment.

Table 2.2: Parameters for the PDPA setups in both laboratories.

	Transmitter focal length [mm]	Receiver focal length [mm]	Collection angle [°]	Beam expander ratio	Beam diameter [mm]	δ [μm]
LEGI	500	500	30	1.0	1.05	4.33
UW	500	750	61	2.0	3.54	X

PDPA misalignment angle

Even if the best precautions are taken during the device installation, a small angle may be present between the PDPA axes and the wind tunnel axes. This deviation angle can induce a significant bias on the measurement of the particle settling velocity. In wind tunnel experiments, the particle streamwise velocity is at least an order of magnitude larger than the vertical component. As a result, the projection of the horizontal component on a misaligned vertical axis will add a bias into the measured vertical velocity.

We call β the angle of deviation between the PDPA axes and the wind tunnel axes. Here, V_{XPDPA} and V_{YPDPA} are, respectively, the streamwise and vertical components of the velocity measured by the instrument while V_{XWT} and V_{YWT} are the exact particle velocity components in the wind tunnel coordinate system. The vertical velocity due to the horizontal component projection, V_β, is then estimated as $V_\beta = \langle U \rangle \sin(\beta)$, with $\langle U \rangle$ the mean horizontal velocity

(Mora et al. 2021b). The angle-corrected velocity is as follows:

$$V_{YWT} = V_{YPDPA} - \underbrace{\langle U \rangle \sin(\beta)}_{V_\beta} \tag{2.5}$$

The measurement error, V_β, remains constant for all particles velocity measurements under fixed experimental conditions. In order to compute V_β, we estimated the misalignment angle β with olive oil droplets velocity measurements. Olive oil droplets, characterized by small diameters and low volume fraction, enable us to get samples in the tracer limit, where the vertical velocity is extremely small and equal to the Stokes velocity $V_{YWT} = V_T$. Using the empirical formula from Schiller & Nauman (Clift, Grace, and Weber 1978) to estimate V_T, and assuming that the mean centreline velocity is purely streamwise, the misalignment between the PDPA and gravity was estimated.

In LEGI, the settling velocity of olive oil droplets were collected for different free stream velocities in a flow as laminar as possible, i.e. in absence of grids. With several free stream velocities, a least-squares polynomial fit on the values of $\langle V_{YPDPA} \rangle$ and $\langle U \rangle$ can be performed to estimate $\sin(\beta)$. The angle β was calculated to be equal to $\beta = 1.5° \pm 0.3°$.

In Seattle, we attempted to correct for the settling velocity in a similar way. However, the olive oil atomizer was creating a very large momentum in the flow, preventing us from assuming the olive oil droplets as tracer particles.

2.3 Particle Tracking Velocimetry

Since Particle Tracking Velocimetry measurements were conducted with the Seattle wind tunnel, a brief description of this technique is provided here.

Particle Tracking Velocimetry (PTV) is a non-intrusive optical measurement technique that consists in tracking the movement of particles in a flow field. When the particles are tracers, they can serve to estimate the fluid velocity from a Lagrangian perspective. PTV is also applicable to track inertial particles, allowing us to obtain statistics on their positions, velocities, and accelerations, as long as that their properties make them easily trackable. In the case of water droplets within an air flow, a laser light source is employed to illuminate the fluid in the region of interest.

Characterising the energy cascade using the zero-crossings of the longitudinal velocity fluctuations

3

This chapter focuses on characterizing experimentally single-phase turbulent flows, using hot-wire data taken in the LEGI wind tunnel and in Lille laboratory (LMFL). It presents a new method to estimate the carrier flow Reynolds number and introduces the work published in the article:

Ferran, A., Aliseda, A. & Obligado, M. Characterising the energy cascade using the zero-crossings of the longitudinal velocity fluctuations. Exp Fluids 64, 176 (2023).

To properly study the effect of turbulence on particles, it is essential to accurately characterize the carrier phase. However, in some cases, turbulent flows can be challenging to characterize, especially when dealing with statistically unsteady flows or when an appropriate calibration can be difficult to perform, such as in field experiments or two-phase flow studies. For certain flows, the integral length scale can be difficult to determine by integration of the autocorrelation function if the latter does not cross zero. This is the case with some active-grid-generated turbulence in triple random mode, for which various studies have proposed new procedures to overcome the problem (Puga and Larue 2017; Mora and Obligado 2020). Recently, a study by Mora and Obligado 2020 introduced two new methods for estimating this integral length scale, by examining how frequently the longitudinal fluctuating velocity crosses zero. On one hand, the integral length scale $\mathscr{L}$ was found to be related to the variance of the distance between two consecutive zero crossings using an equation from McFadden 1958. On the other hand, the integral length scale has been found to be linked to the clustering properties of the longitudinal velocity zero-crossings, where this scales seems to correspond to the low-pass filtering scale for which the zero crossings are uncorrelated. Regarding the turbulent Taylor microscale, it has been known for an extended period of time that it can be estimated from the zero-crossings frequency using the Rice theorem (Rice 1944; Liepmann, Laufer, and Liepmann 1951; Liepmann, H.W. and M.S. Robinson 1953; Sreenivasan, Prabhu, and Narasimha 1983).

The present study builds upon the findings of Mora and Obligado 2020 and the applicability of the Rice theorem to turbulence. The MacFadden and Rice equations were applied to single-phase hot-wire anemometry measurements to estimate the integral length scale and the Taylor microscale, respectively. By combining both equations, we propose a new estimation of the Reynolds number based solely on the longitudinal velocity zero-crossings statistics. In the experimental datasets, both a balanced Kolmogorov energy cascade (with $C_\varepsilon \approx const$) and a nonequilibrium turbulent cascade ($C_\varepsilon \neq const$) are present, and we demonstrate that the new method is valid for both energy dissipation scalings. Following the idea presented in Mora and Obligado 2020, new insights on the cascade are brought by applying Voronoï tesselations to the zero-crossings detection. In this study, we show that the Reynolds number value is mostly governed by the voids statistics. Thus, a one-dimensional analysis of clusters and voids properties is carried out by means of Voronoï tesselations. Since the turbulent scale separation is observed to be primarily driven by zero-crossing voids, we determine that the Reynolds number is a linear function of the average sizes of zero-crossings voids and clusters.

Experiments in Fluids (2023) 64:176
https://doi.org/10.1007/s00348-023-03722-8

RESEARCH ARTICLE

Characterising the energy cascade using the zero-crossings of the longitudinal velocity fluctuations

Amélie Ferran[1,2] · **Alberto Aliseda**[2] · **Martin Obligado**[1]

Received: 2 June 2023 / Revised: 22 August 2023 / Accepted: 2 October 2023

Abstract

It is well known that the zero-crossings of the longitudinal velocity fluctuations can be used to estimate the Taylor length scale of turbulence via the Rice theorem. Furthermore, it has recently been shown that they can also be used to compute the turbulence integral length scale. We show how these two findings can be combined to study single-point statistics in turbulent flows. As these parameters are shaped by particular averaged properties of the turbulence cascade, they can be used to deduce some aspects of it. This approach is advantageous, as it makes possible the characterisation of turbulent flows in extremely challenging situations, i.e., statistically unsteady flows or conditions when adequate instrument calibration cannot be maintained. Using experimental data for a wide range of Taylor-scale-based Reynolds numbers from different flows (passive- and active-grid-generated turbulence and planar turbulent wakes), we show how, by solely using the zero-crossings of the longitudinal velocity fluctuations, some aspects of the energy cascade can be studied. Furthermore, using Voronoï tessellations, we study zero-crossing clustering properties. In particular, we discuss how its clusters and voids are related to the separation of scales in turbulent flows.

1 Introduction

The study of turbulent flows based on the properties of the fluctuating velocity zero-crossings is fundamentally important and has many environmental applications. This quantity is defined as the set of positions where the streamwise fluctuating velocity (defined as $u(x) = U(x) - \langle U(x) \rangle$, where $U(x)$ is the streamwise velocity and x the streamwise coordinate) is equal to zero. Some relevant situations where the zero-crossings of $u(x)$ have been studied include atmospheric (Akinlabi et al. 2019; Huang et al. 2021), grid-generated (Mora et al. 2019), free-shear (Mazellier and Vassilicos 2008) and two-phase (Mora et al. 2019; Ferran et al. 2022) turbulence.

Several studies have shown how the zero-crossings of $u(x)$ are linked to important characteristics of turbulent flows. For instance, the zero-crossing density n_s can provide an estimate of the Taylor microscale λ (Liepmann and Robinson 1953; Sreenivasan et al. 1983; Mazellier and Vassilicos 2008; Mora et al. 2019). Liepmann and Robinson (1953) were the first to apply Rice theorem (Rice 1945) to turbulent flows and proved that λ is proportional to the inverse of the zero-crossing density, i.e.,

$$n_s^{-1} = \langle \Delta Z \rangle = C\pi\lambda, \tag{1}$$

where ΔZ is the distance between consecutive zeros Z, and C a constant, of order unity, that takes into account the non-Gaussianity of the velocity derivative (where $C = 1$ for a Gaussian process with a Gaussian derivative).

More recently, McFadden equation (McFadden 1958) has been applied to a turbulent signal for an estimation of the flow longitudinal integral length scale $\mathcal{L}$, using the variance and the mean zero-crossing distance (Mora and Obligado 2020). By assuming that the distances between zero-crossings are statistically independent and, once more, a Gaussian process with a Gaussian derivative, McFadden equation relates the integral length scale with the variance and the average of the distances between zero-crossings ΔZ,

---

✉ Martin Obligado
Martin.Obligado@univ-grenoble-alpes.fr

Amélie Ferran
amelie.ferran1@univ-grenoble-alpes.fr

Alberto Aliseda
aaliseda@uw.edu

[1] Université Grenoble Alpes, CNRS, Grenoble-INP, LEGI, F-38000 Grenoble, France

[2] Department of Mechanical Engineering, University of Washington, Seattle, USA

$$\mathcal{L}_{\mathrm{McF}} = \frac{\pi}{4}\frac{\mathrm{Var}(\Delta Z)}{\langle \Delta Z \rangle}. \tag{2}$$

The integral length scale $\mathcal{L}_{\mathrm{McF}}$ obtained in this way is labelled using the subscript 'McF' to differentiate it from values of $\mathcal{L}$ that are obtained using other methods (such as the autocorrelation, see next section).

McFadden equation and Rice theorem have been tested in previous works (see Mora et al. (2019); Zheng et al. (2021) and references therein). Nevertheless, the possibilities that arise from combining Rice theorem and McFadden equation have not been explored yet. For instance, by combining them, an expression relating the distance between zero-crossings and the ratio of turbulent flow scales can be inferred:

$$\frac{\mathcal{L}_{\mathrm{McF}}}{\lambda} \sim \frac{\pi^2}{4}\frac{\mathrm{Var}(\Delta Z)}{\langle \Delta Z \rangle^2}. \tag{3}$$

While this expression neglects intermittency in the turbulent flow, it is a first-order approximation of the scale separation $\mathcal{L}/\lambda$. Moreover, while the above relations are derived for homogeneous isotropic turbulence (HIT), they have been found to hold in several other flows, such as boundary layers, jets and wakes (Sreenivasan et al. 1983; Mazellier and Vassilicos 2008; Mora and Obligado 2020).

Consequently, equation 3 quantifies the ratio of turbulent scales by using solely the position of zero-crossings. This is a very important quantity in turbulent flows, as the separation of scales is related to the number of degrees of freedom in the flow. Furthermore, it can also be related to certain aspects of the energy cascade (Vassilicos 2015). Indeed, within Kolmogorov phenomenology, a well-known relation for HIT is,

$$\mathcal{L}/\lambda = \frac{C_\varepsilon}{15}\mathrm{Re}_\lambda, \tag{4}$$

where Re_λ is the Reynolds number based on λ. This is a kinematic result that follows from the definitions of C_ε, the dissipation constant and λ. The former can be deduced from the scaling $\varepsilon = C_\varepsilon u'^3/\mathcal{L}$, where ε is the dissipation rate of turbulent kinetic energy and u' the rms value of $u(x)$. On the other hand, the Taylor scale is related to ε via $\varepsilon = 15\nu u'^2/\lambda^2$ (with ν the fluid kinematic viscosity).

Within the Kolmogorov equilibrium theory, C_ε is expected to be constant for a given set of boundary conditions (Taylor 1935). In this phenomenology, it is assumed that the small-scale motions evolve much faster than the timescale of the overall turbulence evolution. In consequence, the rate at which the flow's kinetic energy crosses a length scale r is the same across all the scales within the inertial range. This results in a balance between the interscale energy flux and the energy dissipation rate ε, allowing to deduce the expressions $\varepsilon = C_\varepsilon u'^3/\mathcal{L}$ and equation 4 (a more thorough discussion on this topics can be found in Vassilicos (2015)). Therefore, in this framework, an energy cascade where the interscale energy flux and ε are not equal, can be considered as out of equilibrium.

Moreover, it has been recently reported that the scaling $C_\varepsilon = cst.$ is also present in flows that are not fully within Kolmogorov's equilibrium. It is also consistent with a balanced non-equilibrium cascade (Goto and Vassilicos 2016) and with the presence of non-equilibrium in the large scales of the inertial range, as the increment r increases away from λ (Obligado and Vassilicos 2019; Meldi and Vassilicos 2021; Steiros 2022; Bos and Rubinstein 2017). To simplify the discussion about the different energy cascades consistent with $C_\varepsilon = cst.$, that remains out of the scope of the present work, from now on, we will refer to these scalings as 'standard' dissipation scalings.

Furthermore, it has been found that some flows do not follow standard scalings, but rather evolve following the so-called non-equilibrium energy cascade (see Valente and Vassilicos (2012); Vassilicos (2015) for further details). In this case, C_ε is no longer a constant. Given the discussion above, this implies that the Kolmogorov equilibrium does not hold in these flows. Indeed, the dissipation constant is found to be proportional to the ratio $\mathrm{Re}_G^{1/2}/\mathrm{Re}_\lambda$, where Re_G is a Reynolds number that depends on the inlet conditions, defined here as $\mathrm{Re}_G = MU_\infty/\nu$, where M is the grid spacing (or the diameter of the wake generator), and U_∞ is the inlet velocity. Such new scalings imply that the separation of scales follows:

$$\mathcal{L}/\lambda \sim \sqrt{\mathrm{Re}_G} \tag{5}$$

and is therefore independent of Re_λ at fixed Re_G.

This discussion shows how some scalings of statistics deriving from averaged properties of the energy cascade can be characterised by using solely the zero-crossings of $u(x)$. While equations 4 and 5 do not give a full description of the cascade (nor can even discriminate between different ones in the case of $C_\varepsilon = cst.$), they do provide valuable information about how the interscale energy transfer relates to the turbulence dissipation rate. Furthermore, this framework opens the possibility of giving a complete description of the single-point statistics of a turbulent flow with only this measurement. Additionally, it provides a robust tool to study turbulent flows in challenging conditions, as zero-crossings tend to be accessible in field experiments, where calibration may be noisy or drifting, and even in two-phase flows (Mora et al. 2019).

In this study, we aim to describe some particular averaged properties of the turbulent energy cascade by using solely zero-crossings. We analyze experimental hot-wire anemometry (HWA) data in several turbulent flows: passive/active grid-generated turbulence and in a planar wake. In our dataset, both equilibrium and non-equilibrium scalings are observed, including transitions from one state to the other.

It has already been noticed by Smith et al. (2008) that the existence of multiple scales in a Gaussian process influences the clustering properties of zero-crossings. In consequence, the multiscale nature of turbulence would be expected to be related with the clustering properties of the zero-crossings of the fluctuating velocity. For instance, a characteristic length scale derived from the voids, that is to say, regions of the flow depleted from zero crossings, has already been reported (Mazellier and Vassilicos 2008). It was shown that this length scale, characterising the non-uniformity in the spatial distribution of zero-crossings, evolves as $\lambda \mathrm{Re}_\lambda^{1/3}$. Therefore, we report on the preferential concentration of zero-crossings by means of Voronoï tessellations. This tool has been extensively used to characterise clustering in single- and two-phase turbulent flows (Monchaux et al. 2010; Mora et al. 2021). In our dataset, mean cluster and void lengths are shown to be approximately proportional to Re_λ, in both Kolmogorov and non-equilibrium energy cascades.

2 Methodology

Turbulent flows generated by an active grid, a cylinder (Lespinard tunnel at LEGI lab) and a passive grid (Boundary Layer Wind Tunnel from the Laboratoire de Mécanique des Fluides de Lille) are analysed. Streamwise profiles of the streamwise velocity $U(x)$ were taken along the wind tunnel centerline by means of hot-wire anemometry (HWA). The measurements downstream of the two grids have already been published in previous studies (Mora et al. 2019; Steiros 2022).

The Lespinard wind tunnel at LEGI is a large wind tunnel with a 4 m-long measurement section, and a 0.75×0.75 m^2 square cross section. The planar wake was created by a cylinder spanning horizontally the tunnel cross-sectional area with a diameter $D = 4$ cm. Measurements are at centreline of the cylinder and between $20D$ and $70D$ downstream in the wake. The inlet velocities U_∞ tested were 5.4, 8.5 and 12.4 m/s, resulting in Reynolds numbers Re_G based on $D = 14000,\ 23000,\ 33000$.

The active grid, installed at the same facility as the cylinder, is made of 16 rotating axes (eight horizontal and eight vertical) with a $M = 10$ cm mesh size. Each axis is driven independently with a stepper motor whose rotation rate and direction can be changed dynamically. The grid is operated in the so-called triple-random mode, where the motors were driven with random rotation rates and directions, which were changed randomly in time. This mode is known to generate HIT with moderate-to-high Re_λ. Measurements were made at the center of the test section, covering the streamwise range $4.5 - 32.5M$. Only one inlet velocity U_∞ was tested, $U_\infty = 6.7$ m/s, corresponding to a Reynolds number based on M of $\mathrm{Re}_G = 45 \times 10^3$.

The LML Boundary Layer Wind Tunnel has a $20m$-long measurement section and a 2 m × 1 m cross section. The passive grid is planar, with rod diameters of 15 mm and a mesh size equal to $M = 91$ mm. Measurements reported in this work were taken at streamwise positions spanning from 3.3 to $40M$. The grid generated a tunnel blockage of 30%. Three different U_∞ were tested: 4, 5 and 7 m/s (corresponding to Re_G of 24000, 30000 and 43000, respectively). As for the active grid, all measurements were conducted along the centerline of the test section.

For each measurement, it was verified that the Kolmogorov length scale was well resolved, by having at least $(2\pi/\langle U\rangle)f_s\eta = 1$, with f_s the sampling frequency, $\langle U\rangle$ the mean velocity and η the size of the smallest eddies (Kolmogorov scale). For the passive grid and the planar wake, only measurements with a turbulent intensity $(u'/\langle U\rangle)$ below 18% and downstream of the peak in turbulence intensity are reported. For the active grid case, velocity fluctuations are much higher $(u'/\langle U\rangle \in [0.15 - 0.42])$, and the turbulent intensity is above 18% for most downstream positions. Active grid measurements are still considered in this study but the use of Taylor hypothesis with such high fluctuations is a source or uncertainty, and the results should be taken with care. On the figures, and consistently with other works on this device (Mora et al. (2019); Sinhuber et al. (2015)), only measurements with a turbulent intensity lower than 25% are highlighted.

The dissipation rate of turbulent kinetic energy ε was computed via integration of the dissipation spectrum $\varepsilon = \int 15\nu\kappa^2 E_{11}(\kappa_1)d\kappa_1$, where $E_{11}(\kappa_1)$ is the one-dimensional power spectrum of the longitudinal velocity fluctuations, with κ_1 the respective wavenumber and ν is the kinematic viscosity. The conversion from the time to the spatial domain for the HWA signal was always made using Taylor's hypothesis. From the turbulent kinetic energy dissipation rate, the Kolmogorov length scale $(\eta = (\nu^3/\varepsilon)^{1/4})$ and the Taylor microscale $(\lambda = \sqrt{15\nu u'^2/\varepsilon})$ were calculated. The Taylor Reynolds number based on λ is defined as $\mathrm{Re}_\lambda = u'\lambda/\nu$. The integral length scale $\mathcal{L}$ was computed via the streamwise velocity autocorrelation function R_{uu}. For all cases, it was estimated as $\mathcal{L} = \int_0^{r_0} R_{uu}dr$, where r_0 is the smallest value at which $R_{uu} = e^{-1}$, and r is estimated, once more, via Taylor's hypothesis. The main turbulence parameters for each dataset are listed in Table 1.

The profiles of Re_λ versus the normalised streamwise distance are shown in Fig. 1 for the three different turbulent flows. The streamwise distance was normalised by the grid mesh size M for passive/active grid and by the cylinder's

Table 1 Turbulence parameters computed from hot-wire anemometry measurements

Parameters	Passive grid	Active grid	Planar wake
Re_λ	70–177	592–956	148–360
$u'/\langle u\rangle$ (%)	2.7–15.8%	15–42%	5.6–17.5%
ε ($\mathrm{m^2s^{-3}}$)	0.04–74.0	2.8–82.7	0.7–44.4
η (μm)	82–549	80–186	93–268
λ (mm)	2.1–9.0	4.8–8.9	3.4–6.4
$\mathcal{L}$ (cm)	1.1–2.6	8.2–10.6	2.1–3.3

u' is the rms of the streamwise velocity fluctuations, $\mathrm{Re}_\lambda = u'\lambda/\nu$ the Taylor–Reynolds number and $\varepsilon = 15\nu u'^2/\lambda^2$ the dissipation rate of turbulent kinetic energy. $\eta = (\nu^3/\varepsilon)^{1/4}$, $\lambda = \sqrt{15\nu u'^2/\varepsilon}$ and $\mathcal{L} = \int_0^{r_0} R_{uu} dr$ are the Kolmogorov length scale, the Taylor microscale and the integral length scale, respectively

diameter D for the planar wake. For the passive grid and the planar wake (panels (a) and (c)), different colors correspond to different inlet Reynolds number Re_G. In the wake of the passive grid, measurements in the near and far field required a different support system. Therefore, some discontinuities are present in the profiles of Fig. 1a. A small discontinuity is also present in the profile downstream the planar wake with the highest inlet Reynolds number. This is due to measurements being taken in different days, with slightly different ambient conditions that results in the small jump observed (of about 8% difference in Re_λ).

Estimating the integral length scale from the autocorrelation function can sometimes be delicate if this function does not cross zero (Mora and Obligado 2020; Puga and LaRue 2017). We provide the autocorrelation function for our three datasets in Fig. 2 (passive grid in panel (a), active grid in panel (b) and planar wake in panel (c)). As discussed above, the shape of the autocorrelation functions reported in Fig. 2 allows to estimate the integral length scale from their integration. The ratios between the integral length scale estimated from the autocorrelation function and the length scale from MacFadden equation $\mathcal{L}_{\mathrm{McF}} = (\pi/4)\mathrm{Var}(\Delta Z)\langle\Delta Z\rangle^{-1}$ are

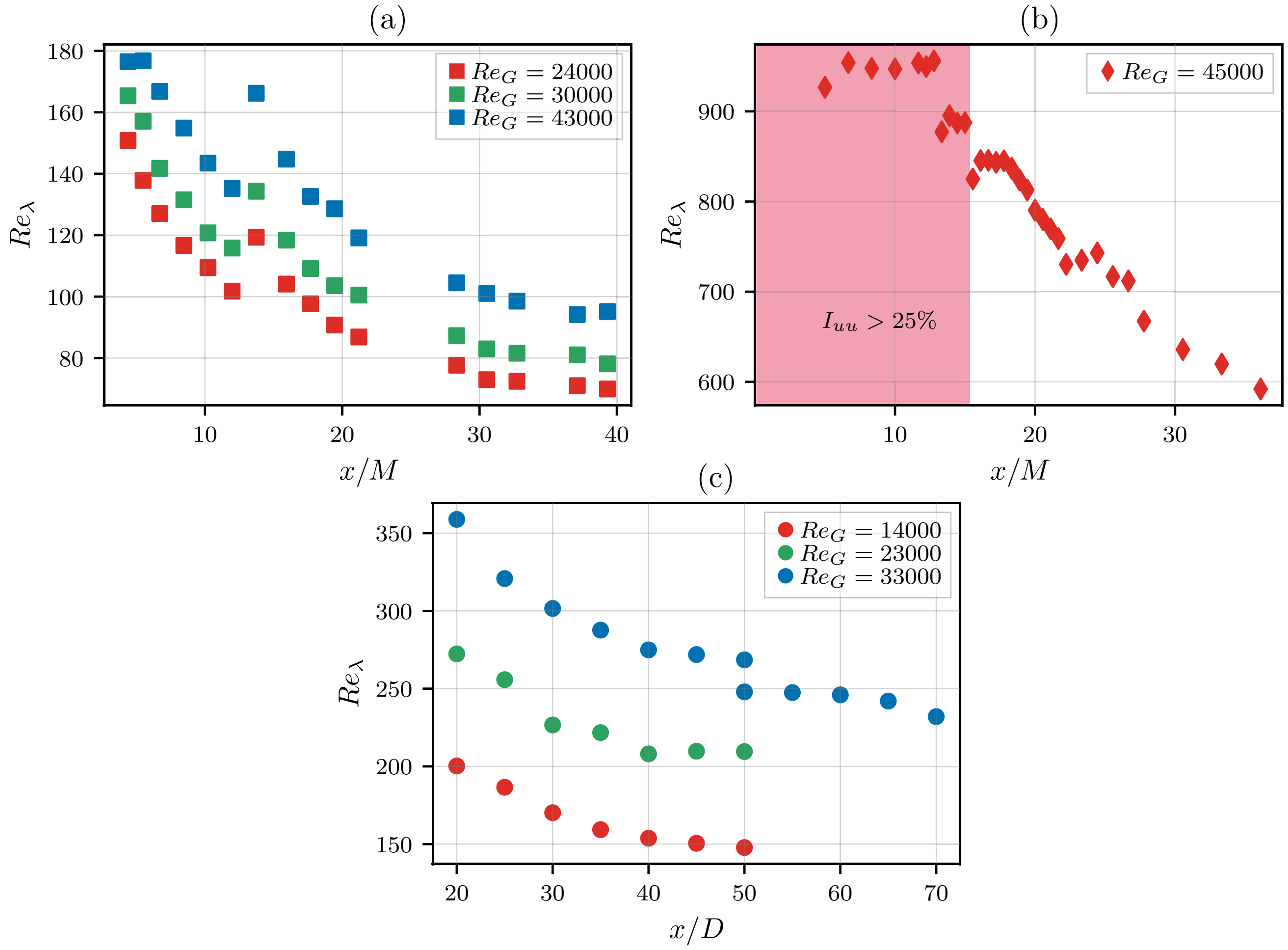

Fig. 1 Taylor-scale-based Reynolds number Re_λ versus the normalised streamwise distance x/D, x/M for the three different datasets: **a** passive grid data, **b** active grid and **c** the planar wake. For panels (**a**) and (**c**) different colors correspond to three different inlet Reynolds number Re_G

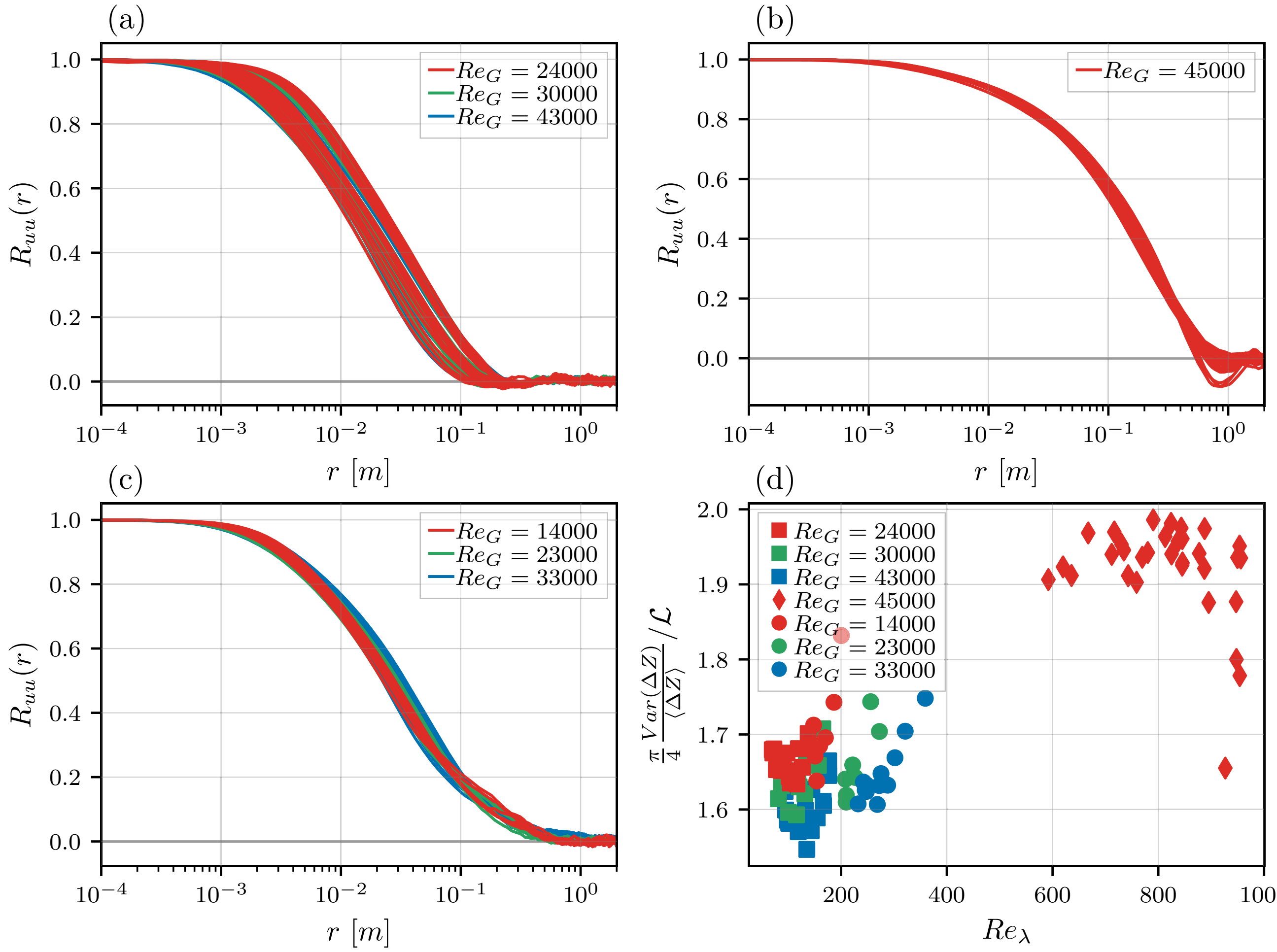

Fig. 2 Autocorrelation functions R_{uu} for the passive grid (**a**), active grid (**b**) and planar wake (**c**). Each curve corresponds to a different downstream distance and different colors correspond to different inlet Reynolds numbers Re_G. **d** Ratios between the integral length scale using MacFadden equation $(\pi/4)\mathrm{Var}(\Delta Z)\langle\Delta Z\rangle^{-1}$ and the integral length scale from the integration of the autocorrelation

also shown in Fig. 2d. The ratios found have similar trends to those reported in Mora and Obligado (2020).

The number of zero-crossings is obtained by counting the number of times the Eulerian fluctuating velocity ($u = U - \langle U\rangle$) is equal to zero. The fluctuating velocity was transposed from time to space using Taylor's frozen turbulence hypothesis. To verify that the temporal resolution is sufficient to resolve all zero-crossings, the following filtering process was used (Sreenivasan et al. 1983; Mazellier and Vassilicos 2008; Mora and Obligado 2020): The signal was low-pass filtered with different filter sizes $\eta_c = 2\pi/\kappa$ (where κ is the cutoff wave number) using a fifth-order Butterworth filter. η_c, the filter size, is not to be confused with the Kolmogorov length scale η. We define ΔZ as the distance between two consecutive zero-crossings and n_s the zero-crossing density (number of crossings normalised by the signal length). By construction, n_s is the inverse of the average distance between zeros $\langle\Delta Z\rangle$, $n_s\langle\Delta Z\rangle = n_s\bar{l} = 1$.

The zero-crossing density was estimated for the unfiltered signal and for different filter sizes. Figure 3 shows the zero-crossing density normalised by the average distance between zeros for the unfiltered signal $n_s\bar{l}$ against $1/\eta_c$. The three panels of Fig. 3 correspond to the passive grid, active grid and planar wake from left to right. Each curve in Fig. 3 comes from a different downstream distance. The number of zero-crossings first increases when the cutoff wavenumber increases until reaching a plateau where the filter size has no more influence on n_s. A plateau is found for all turbulent flows presented in this study (Fig. 3), which ensures that the signal temporal resolution is adequate to capture all zero-crossings and therefore the Rice theorem can be applied. The high fluctuations at the large scale (i.e. small $1/\eta_c$) of Fig. 3a and b are caused by an overly small cutoff frequency of the low pass filter. For such cutoff frequencies, the filter presents some

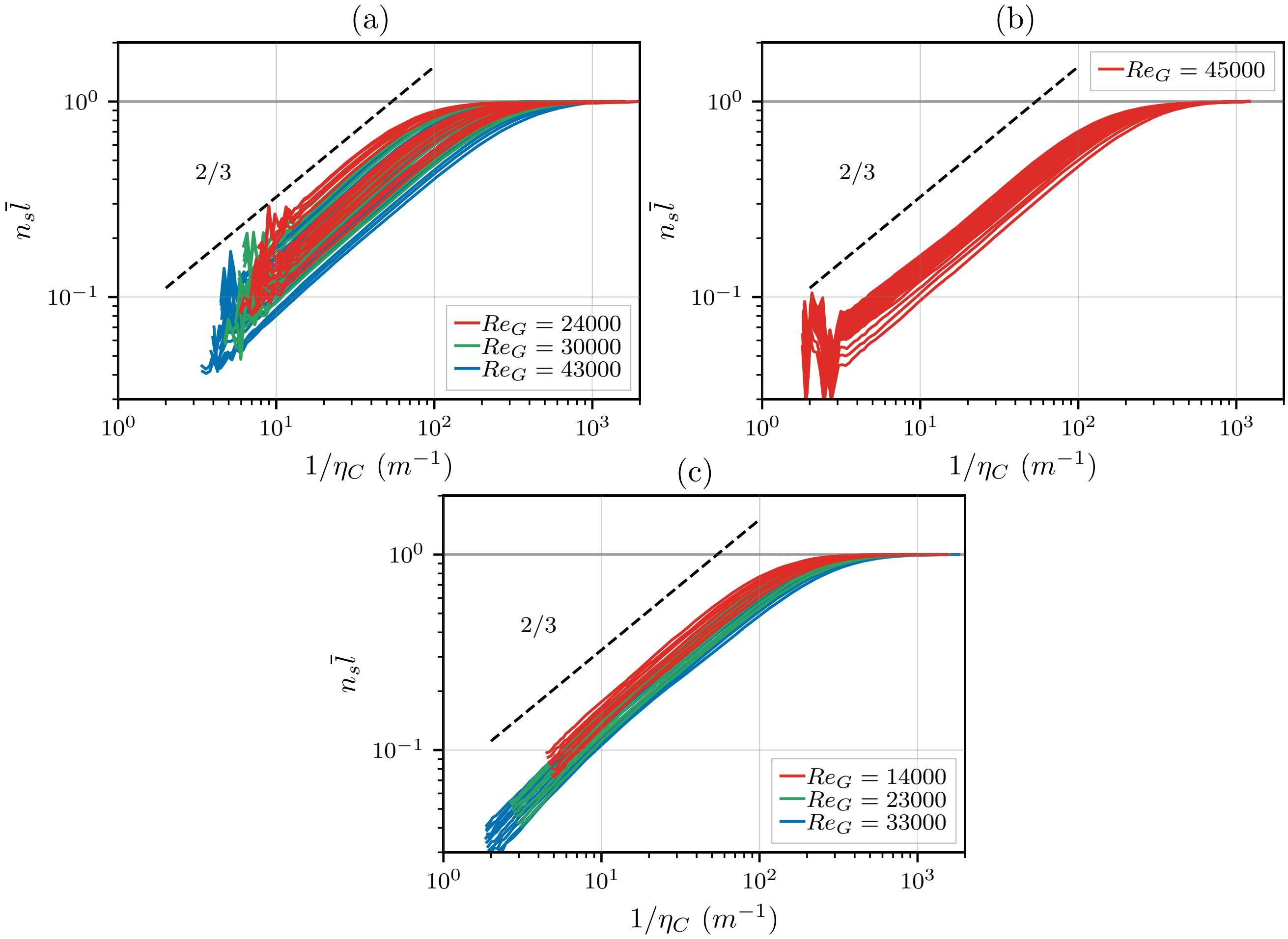

Fig. 3 Normalised zero crossing density $n_s\bar{l}$ against the filter size $1/\eta_c$ for the three different datasets: **a** passive grid data, **b** active grid and **c** the planar wake. The 2/3 power law is shown in dashed line. Each curve corresponds to a different downstream distance and different colors correspond to different inlet Reynolds numbers Re_G

inaccuracies in its application and the filtered signal may not be properly converged. However, those fluctuations do not impact the rest of the analysis since the zero-crossing density was estimated with the values from the plateaux.

3 Results

3.1 Characterisation of the energy cascade using standard techniques

We will first study properties resulting from the energy cascade using standard techniques: an integral scale $\mathcal{L}$ estimated using the autocorrelation function and a kinetic energy dissipation ε computed by means of the dissipation spectra. The evolution of C_ε with $1/\mathrm{Re}_\lambda$ for all flows considered is shown in Fig. 4 (where a consistent trend with $\mathcal{L}/\lambda$ can be seen in Fig. 5).

As already reported in Mora et al. (2019), standard dissipation scalings are observed in the active grid flow, where C_ε is approximately constant for the entire streamwise range studied (Fig. 5b).

For the passive grid and planar wake, $C_\varepsilon = cst$, does not hold. Indeed, for panels (a) and (c), C_ε is proportional to $1/\mathrm{Re}_\lambda$ at large Re_λ, and thus follow the scaling of non-equilibrium turbulence (Valente and Vassilicos 2012; Vassilicos 2015). Since at further downstream distances C_ε reaches a plateau and a standard scaling is observed, this behavior is consistent with the transition from non-equilibrium to standard scalings observed in fractal and regular grids (Valente and Vassilicos 2012). In the planar wake, mostly non-equilibrium turbulence is observed as

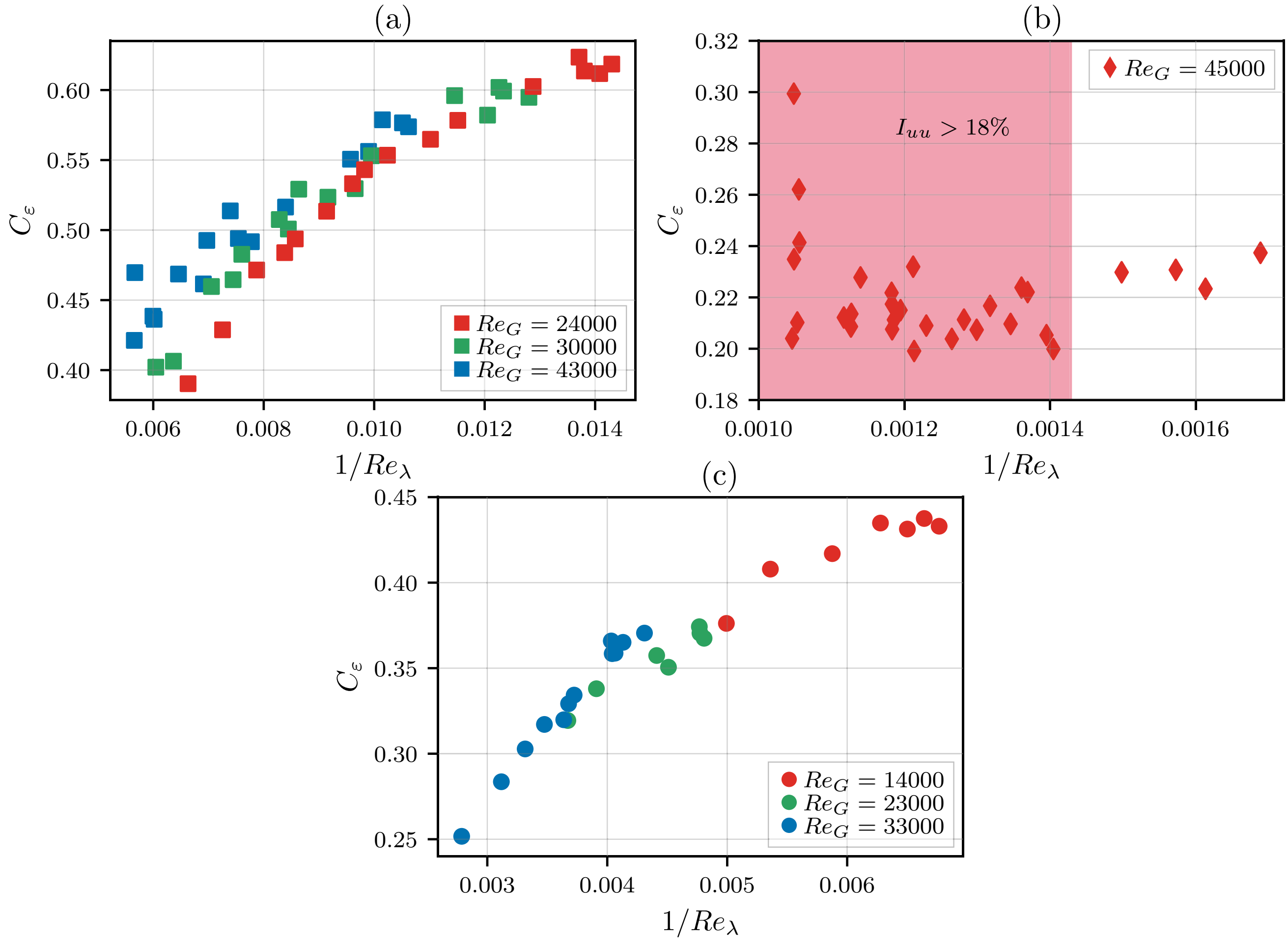

Fig. 4 Normalised energy dissipation C_ε versus $1/\mathrm{Re}_\lambda$. Passive grid data are displayed in panel (**a**), active grid data in panel (**b**) and the planar wake in panel (**c**). For panels (**a**) and (**c**), different colors correspond to three different inlet Reynolds number Re_G

only the profile with the lowest Re_G presents a plateau with $C_\varepsilon = cst$.

Therefore, our dataset presents properties deriving from different types of energy cascade, including transitions between them. In the next section, we will verify that equation 3 can capture all these features.

3.2 Characterisation of the energy cascade using the distance between zero-crossings

As discussed in detail in Sect. 1, equation 3 gives the ratio of turbulent scales using solely the position of zero-crossings. We will therefore compare results obtained with standard methods in the previous section with estimations from zero-crossings: $\mathcal{L}_{\mathrm{McF}}$ estimated from equation 2 and λ using Rice theorem (equation 1).

The left column of Fig. 5 presents the ratio of length scales $\mathcal{L}/\lambda$ calculated using the turbulent dissipation spectrum and the autocorrelation function. It is compared for each turbulent flow (passive grid, active grid and planar wake) to the quantity $\frac{\pi^2}{4}\frac{\mathrm{Var}(\Delta Z)}{\langle \Delta Z\rangle^2}$ (right column). The first row displays both quantities for the passive grid dataset, the middle row shows the active grid and the bottom row contains the planar wake measurements. The results from equation 3 are very similar to the more classical way to compute the length scale ratio, and this is valid for the different turbulent flows. Furthermore, the absolute values of the ratios are similar, with small differences that depend on the nature of the flow. The ratios between the left and right column are around 0.66 for the three different turbulent flows. A study on the origin of that ratio, that could be related to the intermittency of each flow and the threshold used to integrate the structure function, is left for future works.

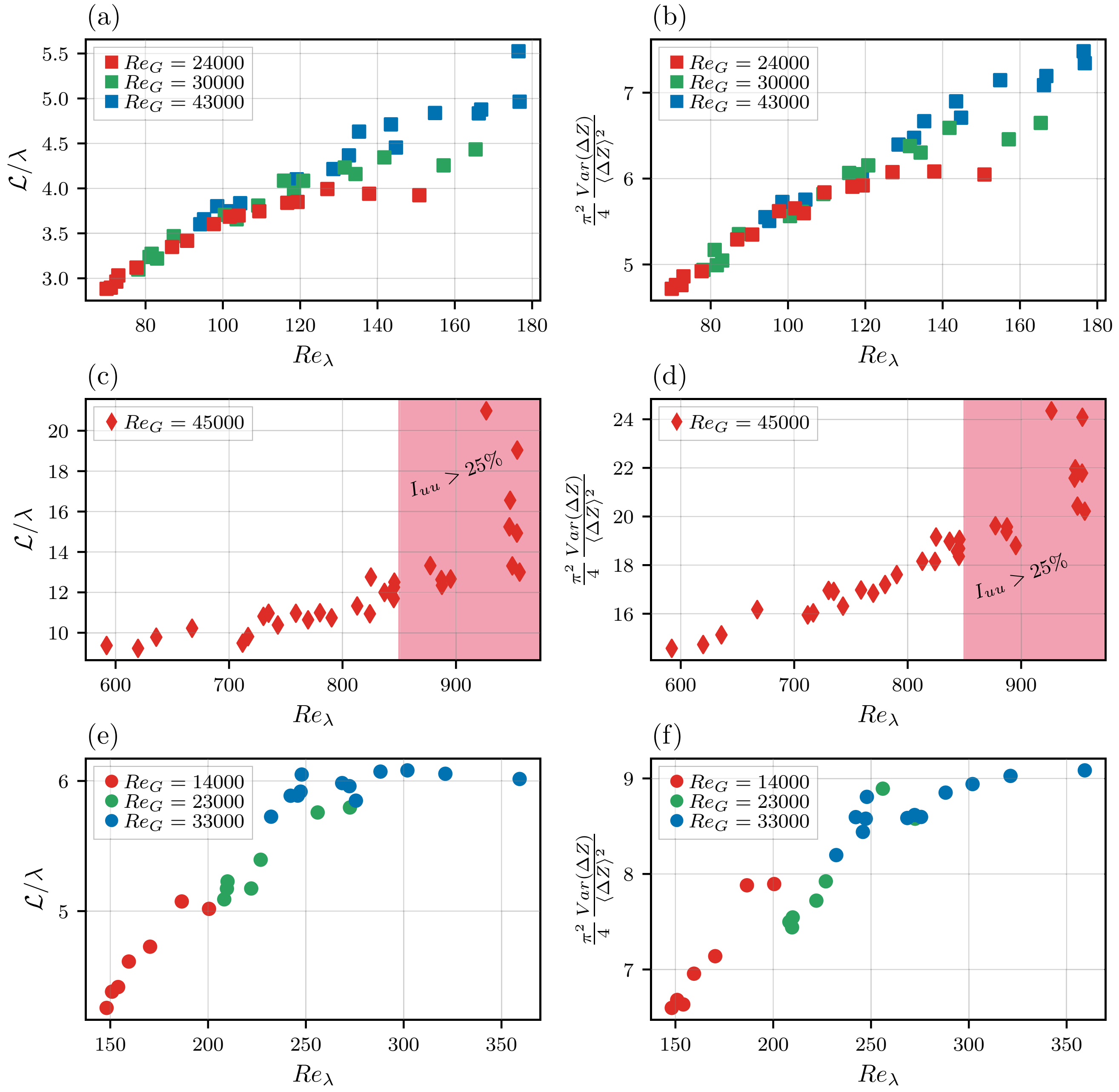

Fig. 5 Left panels (**a**, **c**, **e**) present $\mathcal{L}/\lambda$ against the Taylor Reynolds number Re_λ for the three different wakes. Right panels (**b**, **d**, **f**): the quantity $\frac{\pi^2}{4}\frac{\mathrm{Var}(\Delta Z)}{\langle \Delta Z\rangle^2}$ is plotted against Re_λ for the same measurements. Passive grid data are displayed in the two top panels (**a**, **b**), active grid measurements in panels (**c**) and (**d**) and data from planar wake measurements are shown in the bottom panels (**e**, **f**). For the passive grid and the planar wake, different colors represent different wind tunnel inlet velocities

The transition between standard and non-equilibrium regions is also captured by equation 3 for the regular grid and the planar wake. Similar to Valente and Vassilicos (2012), we observe that $\mathcal{L}/\lambda$ is ≈ const in the out of equilibrium region close to the cylinder and the passive grid, while further downstream, the standard scaling is observed: $\mathrm{Re}_\lambda \sim \mathcal{L}/\lambda$, which is consistent with $C_\varepsilon \approx$ const. For the active grid, similar to Fig. 4, only the standard dissipation scaling is observed.

In conclusion, the results in this section confirm that averaged properties related to the energy cascade can be characterised using the zero-crossings of $u(x)$. In the next section, we will focus on the structure of the zero-crossings distribution and how it can be used for further characterization of the turbulence.

3.3 Voronoï analysis

Since larger distances between zeros contribute more to the variance of ΔZ, $\mathrm{Var}(\Delta Z)$ is mainly controlled by zero-crossing voids. Thus, according to equation 3, the Taylor Reynolds number and the energy cascade are also impacted by voids of zero-crossings. In order to analyze the presence of voids and clusters of zeros in the signal, Voronoï tesselations were used in this study [Ferenc and Néda (2007); Monchaux et al. (2010)]. A Voronoï cell is defined as the portion of the signal closer to one zero than to any other. The Voronoï cell length L_{voro} is computed similar to Mora and Obligado (2020): L_{voro} is given by $L_{\mathrm{voro}} = 1/2(\Delta Z_R + \Delta Z_L)$ where $\Delta Z_R = |Z_p - Z_R|$, $\Delta Z_L = |Z_p - Z_L|$ with Z_L and Z_R the left and right neighbors positions of a zero-crossing situated at Z_p. From this definition, it follows that the average distance between zero-crossings is equal to the average Voronoï cell length $\langle \Delta Z \rangle = \langle L_{\mathrm{voro}} \rangle$.

Figure 6 shows the probability density function (PDF) of the normalised Voronoï cell length $\mathcal{V} = L_{\mathrm{voro}}/\langle L_{\mathrm{voro}} \rangle$. The PDF of the distance between zero-crossings (which is almost equivalent to the PDF of zero-crossings Voronoï cell sizes) have already been presented in the literature (Sreenivasan et al. 1983; Sreenivasan and Bershadskii 2006; Mora and Obligado 2020). The PDF of a random Poisson process (RPP) and a $-5/3$ power law are also displayed in dashed line. As the PDF of the Voronoï cell length intersects the PDF of a RPP twice, it suggests the presence of preferential concentration (Monchaux et al. 2010). Below and above the two intersections with the RPP, the Voronoï cell length probability is higher than for a random process suggesting the presence of more probable clustered regions and regions depleted of zero-crossings. With an increase in Re_λ the PDF of zero-crossings deviates from the random process more,

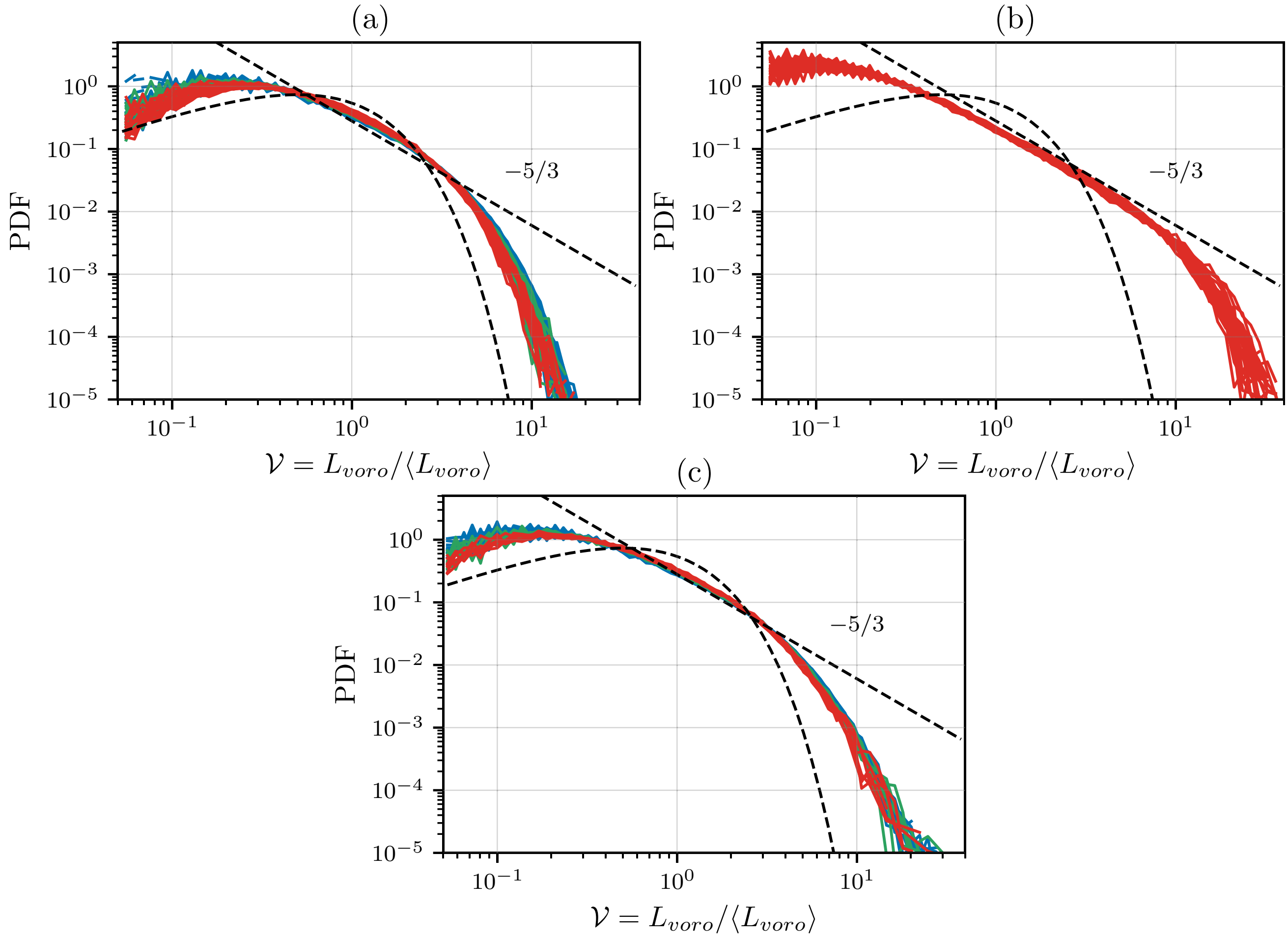

Fig. 6 PDF of the normalised Voronoï length $\mathcal{V} = L_{\mathrm{voro}}/\langle L_{\mathrm{voro}} \rangle$. **a** Passive grid, **b** active grid and **c** planar wake. In the figures, the PDF of a random Poisson process (RPP) and the power law with a $-5/3$ exponent are shown in dashed lines as a reference

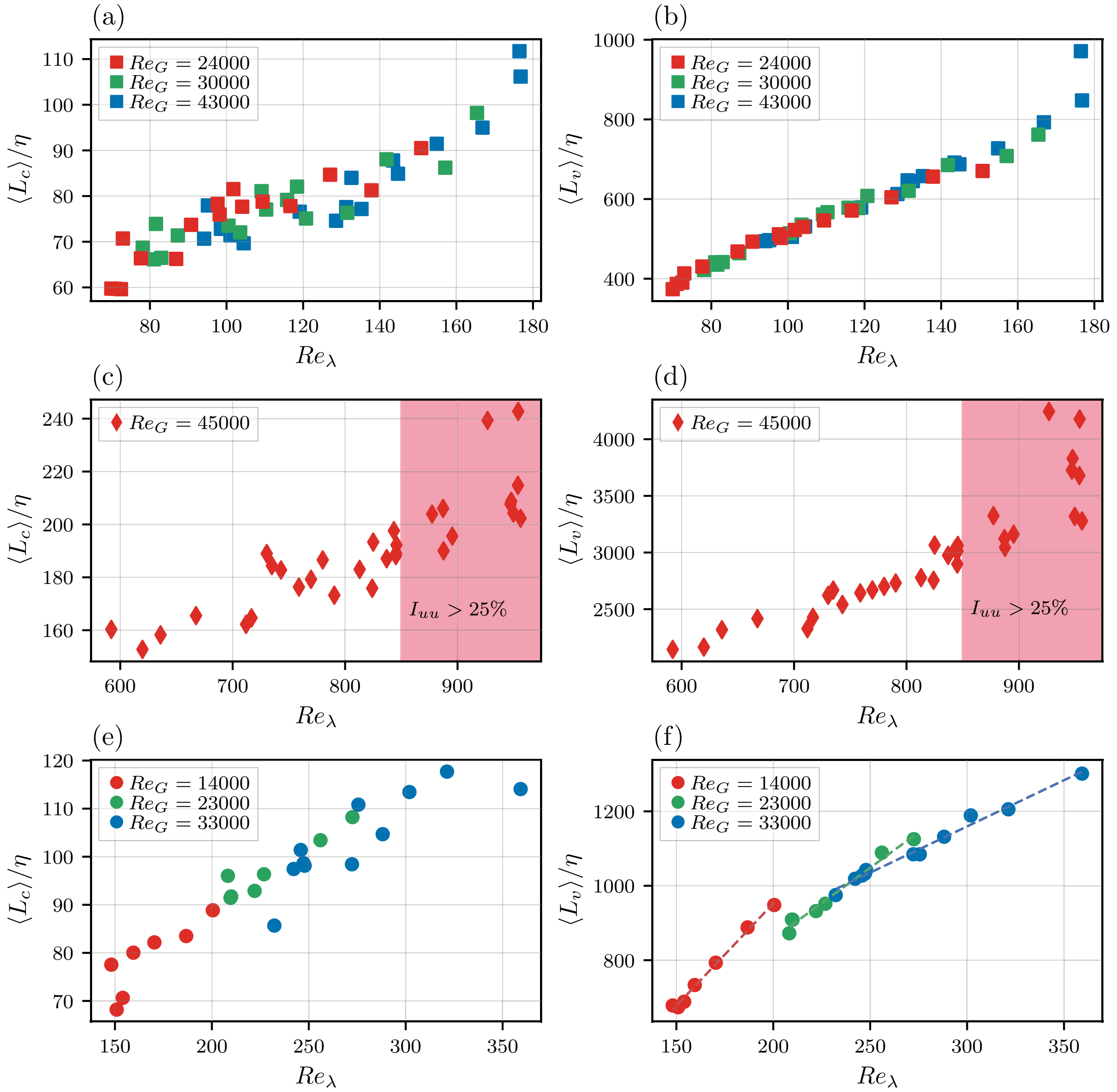

Fig. 7 The mean clusters $\langle L_c \rangle$ and voids lengths $\langle L_v \rangle$ normalised by the Kolmogorov length scale η against the Taylor Reynolds number Re_λ. The mean normalised cluster lengths $\langle L_c \rangle/\eta$ are presented in the left panels, whereas the mean normalised void lengths $\langle L_v \rangle/\eta$ are shown on the right. Passive grid data are displayed in the two top panels (**a**, **b**), active grid measurements in panels (**c**) and (**d**) and data from planar wake measurements are shown in the bottom panels (**e**, **f**). Similar to the previous figures, different colors correspond to different inlet Reynolds numbers

and the range where the PDF is consistent with a $-5/3$ power law behavior widens (consistently with Mora and Obligado (2020)). This is also consistent with Sreenivasan and Bershadskii (2006), which show that there is an increasing tendency to cluster with increasing Re_λ or Mora et al. (2021) for which the standard deviation of the normalised Voronoï cell σ_ν increases with Re_λ.

In Voronoï tessellations, clusters are defined as groups of connected cells with lengths smaller than the first intersection with the RPP. Small Voronoï length cell corresponds to high local concentration. Similarly, voids are defined as a group of connected cells with a length larger than the second intersection. In the present work, at least two cells smaller than the threshold (or larger than the second threshold) have

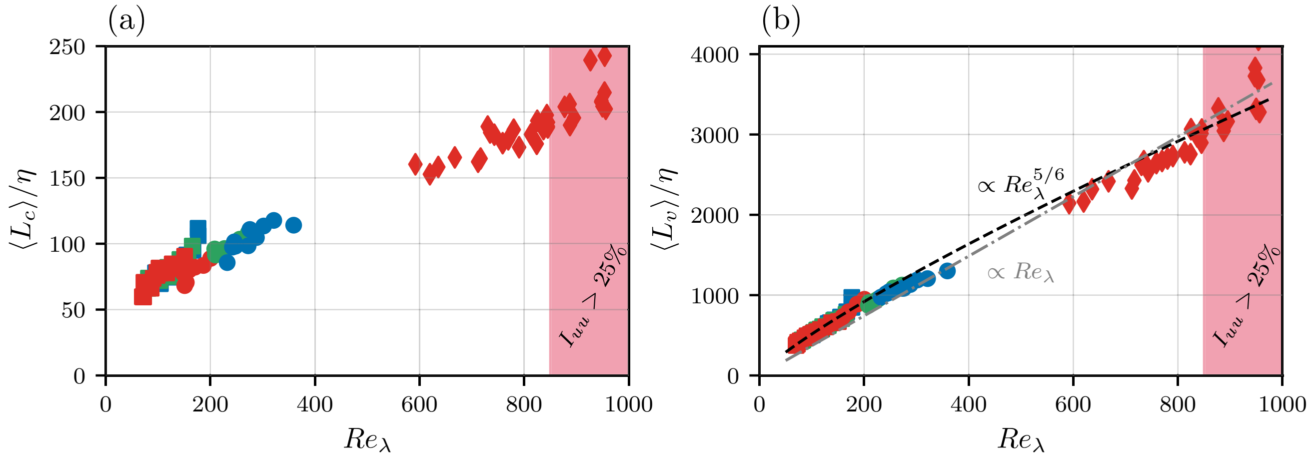

Fig. 8 Mean clusters $\langle L_c \rangle$ (panel (**a**)) and voids lengths $\langle L_v \rangle$ (panel (**b**)) normalised by the Kolmogorov length scale η against the Taylor Reynolds number Re_λ for the three different flows. Similar to the previous figures, different colors correspond to different inlet Reynolds numbers. Different symbols correspond to different wakes: rectangles for the passive grid, diamonds for the active grid and round symbols for the planar wake. Fit to the data with the scalings $\propto \mathrm{Re}_\lambda$ and $\propto \mathrm{Re}_\lambda^{5/6}$ are shown in panel (**b**) in gray and black dashed lines, respectively

to be connected to constitute a cluster (or a void). The cluster length L_c and void length L_v are computed by adding the length of each cell included in the cluster/void.

Figure 7 presents the mean cluster length (left column) and void length (right column) normalised by the Kolmogorov scale ($\langle L_c \rangle/\eta$ and $\langle L_v \rangle/\eta$). The passive grid, active grid and planar wake are presented as in Fig. 5, from top to bottom. Figure 7 shows that the average void and cluster lengths are approximately proportional to Re_λ for all turbulent flow in this study. The ratio of proportionality between the Reynolds number Re_λ and the average void length $\langle L_v \rangle/\eta$ is valid both in the standard and in the non-equilibrium regions. While data taken at different U_∞ present some collapse, the transition between both regions is not observed.

If we gather the data from all three datasets, the void and cluster lengths seem to collapse into one single curve as shown in Fig. 8. We can see from Fig. 8 that the proportionality is more obvious with the average void length than with $\langle L_c \rangle/\eta$. The relation between Re_λ and $\langle L_v \rangle$ seems to be consistent with the scaling proposed by Mazellier and Vassilicos (2008), that is to say $\langle L_v \rangle \sim \lambda \mathrm{Re}_\lambda^{1/3}$. In terms of Kolmogorov length scale, this scaling implies that $\langle L_v \rangle/\eta \sim \mathrm{Re}_\lambda^{5/6}$, which is close to $\langle L_v \rangle/\eta \sim \mathrm{Re}_\lambda$. A fit of the data for each scaling is shown on the right panel of Fig. 8. It is difficult to discriminate between both scalings with the present measurements as the two fits give a similar r^2 score. When looking at the results from the planar wake only (see Fig. 7f), the rate at which $\langle L_v \rangle/\eta$ evolves seems to be Re_G-dependent. This behavior is more consistent with a scaling in $\sim \mathrm{Re}_\lambda^{5/6}$, since the slope decreases by half with an increase in Re_G from 1400 to 3300. To see if this behavior is consistent, further studies with a range of Reynolds number covering the gap between the wake and the active grid ($\mathrm{Re}_\lambda \in [400, 600]$) should be carried out. Matching the active grid Reynolds number with the passive grid or planar wake is not possible in the present experimental setup. Lower values of Re_λ for the active grid require very low freestream velocities (where the wind tunnel motors are unstable), while high values of Re_λ in static grids require very large U_∞, resulting in scales too small to be resolved using standard hot-wire anemometry systems.

It is worth emphasising that the void length scale λ_v in Mazellier and Vassilicos (2008) and $\langle L_v \rangle$ in the present study are defined differently: it is defined as the standard deviation of the distance between zero-crossings in Mazellier and Vassilicos (2008) while it is obtained by means of Voronoï tesselations in the present study.

4 Conclusion

This study shows that some aspects of the energy cascade can be estimated using solely statistics of the distance between the longitudinal fluctuating velocity zero-crossings. For instance, using the Rice theorem and McFadden's equation, the separation of scales in turbulent flows is shown to be proportional to $\pi^2/4\ \mathrm{Var}(\Delta Z)\langle \Delta Z \rangle^{-2}$. For an energy cascade that evolves according to Kolmogorov's phenomenology and other scalings consistent with

$C_\varepsilon = cst.$, this implies that the zero-crossings can be used to quantify the turbulent Reynolds number.

As the voids of zero-crossings are known to be the main contributor to the variance of ΔZ, an analysis on the zero-crossings clustering properties is carried out. We define average zero-crossings void and cluster lengths by means of Voronoï tessellations. Both lengths are shown to be approximately proportional to the Reynolds number Re_λ for all turbulent flows studied. Indeed, the length scale of the zero-crossings voids is directly related to some averaged characteristics of the turbulent energy cascade. Future work can explore the ratio between the two different ways to estimate $\mathcal{L}/\lambda$ and the universality of the relationship between $\langle L_v \rangle/\eta$ and the Reynolds number.

Acknowledgements Our work has been partially supported by the LabEx Tec21 (Investissements d'Avenir - Grant Agreement # ANR-11-LABX-0030), and by the ANR project ANR-15-IDEX-02. The experiments in the passive grid were made during the Lille Turbulence Program (LTP). We thank Kostas Steiros, Christophe Cuvier and Pierre Bragança for their help planning and performing the experiments in Lille's wind tunnel.

Author contributions MO and AF collected and curated the data. All authors reviewed and wrote the manuscript.

Funding LabEx Tec21 (Investissements d'Avenir - Grant Agreement # ANR-11-LABX-0030); ANR project ANR-15-IDEX-02.

Availability of data and materials Data will be made available upon reasonable request to the corresponding author.

Code availability Not applicable.

Declarations

Conflict of interest The authors have no conflict nor competing interests.

Ethical approval Not applicable.

Consent to participate Not applicable.

Consent for publication Not applicable.

References

Akinlabi EO, Wacławczyk M, Mellado JP, Malinowski SP (2019) Estimating turbulence kinetic energy dissipation rates in the numerically simulated stratocumulus cloud-top mixing layer: Evaluation of different methods. J Atmos Sci 76(5):1471–1488

Bos WJ, Rubinstein R (2017) Dissipation in unsteady turbulence. Phys Rev Fluids 2(2):022601

Ferenc J-S, Néda Z (2007) On the size distribution of poisson voronoi cells. Phys A Stat Mech Appl 385(2):518–526

Ferran A, Angriman S, Mininni PD, Obligado M (2022) Characterising single and two-phase homogeneous isotropic turbulence with stagnation points. Dynamics 2(2):63–72

Goto S, Vassilicos J (2016) Unsteady turbulence cascades. Phys Rev E 94(5):053108

Huang KY, Katul GG, Hultmark M (2021) Velocity and temperature dissimilarity in the surface layer uncovered by the telegraph approximation. Bound-Layer Meteorol 180(3):385–405

Liepmann H, Robinson M (1953) Counting methods and equipment for mean-value measurements in turbulence research

Mazellier N, Vassilicos J (2008) The turbulence dissipation constant is not universal because of its universal dependence on large-scale flow topology. Phys Fluids 20(1):015101

McFadden J (1958) The axis-crossing intervals of random functions-ii. IRE Trans Inf Theory 4(1):14–24

Meldi M, Vassilicos JC (2021) Analysis of lundgren's matched asymptotic expansion approach to the kármán-howarth equation using the eddy damped quasinormal markovian turbulence closure. Phys Rev Fluids 6(6):064602

Monchaux R, Bourgoin M, Cartellier A (2010) Preferential concentration of heavy particles: a Voronoï analysis. Phys Fluids 10(1063/1):3489987

Mora DO, Obligado M (2020) Estimating the integral length scale on turbulent flows from the zero crossings of the longitudinal velocity fluctuation. Exp Fluids 61(9):1–10. https://doi.org/10.1007/s00348-020-03033-2

Mora DO, Pladellorens E, Riera Turró P, Lagauzere M, Obligado M (2019) Energy cascades in active-grid-generated turbulent flows. Phys Rev Fluids 4:104601. https://doi.org/10.1103/PhysRevFluids.4.104601

Mora DO, Cartellier A, Obligado M (2019) Experimental estimation of turbulence modification by inertial particles at moderate re_λ. Phys Rev Fluids 4:074309. https://doi.org/10.1103/PhysRevFluids.4.074309

Mora D, Bourgoin M, Mininni PD, Obligado M (2021) Clustering of vector nulls in homogeneous isotropic turbulence. Phys Rev Fluids 6(2):024609

Obligado M, Vassilicos J (2019) The non-equilibrium part of the inertial range in decaying homogeneous turbulence. Europhys Lett 127(6):64004

Puga AJ, LaRue JC (2017) Normalized dissipation rate in a moderate taylor reynolds number flow. J Fluid Mech 818:184–204

Rice SO (1945) Mathematical analysis of random noise. Bell Syst Tech J 24(1):46–156

Sinhuber M, Bodenschatz E, Bewley GP (2015) Decay of turbulence at high reynolds numbers. Phys Rev Lett 114:034501. https://doi.org/10.1103/PhysRevLett.114.034501

Smith J, Hopcraft K, Jakeman E (2008) Fluctuations in the zeros of differentiable gaussian processes. Phys Rev E 77(3):031112

Sreenivasan K, Bershadskii A (2006) Clustering properties in turbulent signals. J Stat Phys 125(5–6):1141–1153

Sreenivasan K, Prabhu A, Narasimha R (1983) Zero-crossings in turbulent signals. J Fluid Mech 137:251–272

Steiros K (2022) Balanced nonstationary turbulence. Phys Rev E 105(3):035109

Taylor GI (1935) Statistical theory of turbulence. Proc R Soc Lond Ser A Math Phys Sci 151(873):444–454. https://doi.org/10.1098/rspa.1935.0159

Valente PC, Vassilicos JC (2012) Universal dissipation scaling for non-equilibrium turbulence. Phys Rev Lett 108(21):214503

Vassilicos JC (2015) Dissipation in turbulent flows. Annu Rev Fluid Mech 47:95–114

Zheng Y, Nagata K, Watanabe T (2021) Turbulent characteristics and energy transfer in the far field of active-grid turbulence. Phys Fluids 33(11):115119

An experimental study on the settling velocity of inertial particles in different homogeneous isotropic turbulent flows

4

This chapter presents the following paper on the settling velocity of inertial particles in homogeneous isotropic turbulence:

Ferran, A., Machicoane, N., Aliseda, A., & Obligado, M. (2023). An experimental study on the settling velocity of inertial particles in different homogeneous isotropic turbulent flows. Journal of Fluid Mechanics, 970, A23.

In this study we report an experimental campaign conducted in LEGI's wind tunnel, involving several grid configurations to generate turbulence. Water droplets were injected at the tunnel's inlet, and their settling velocities were measured using a Particle Phase Doppler Analyzer.

The present work extends the results of a previous study by Mora et al. 2021b, operated in the same facility. In the work of Mora et al. 2021b, particle settling was examined under the influence of active-grid generated turbulence solely, resulting in a turbulent Reynolds number within the range of $Re_\lambda \in [200 - 700]$. Unlike many previous studies, particle settling rate has been found to be mostly hindered by turbulence. However, it remained uncertain how this global settling reduction was impacted by the presence of weak circulation currents in the carrier phase. Indeed, several studies have emphasized the numerous challenges of measuring experimentally the particle settling velocity in confined flows (Murray 1970; Good, Gerashchenko, and Warhaft 2012; Sumbekova et al. 2016; Wang, Lam, and Lu 2018; Mora et al. 2021b). Weak recirculation currents in the flow can often develop due to the influence of boundaries or the dispersed phase. Their magnitude can reach the same order of magnitude as the particle settling, significantly impacting the measurements. Since there is still no global consensus on how turbulence and particle properties affect the settling modification (Reynolds number, size of large-scale structure, particle inertia), accurate measurements of particles' vertical velocity are highly valuable.

In this study, we have paid great attention to address experimental biases, including the misalignment of the PDPA and weak recirculation currents in the fluid phase. One new insight included in this paper is the assessment of weak recirculation currents in the carrier flow both in single-phase (with a cobra probe), and in two-phase flow by recording particles' velocities at two different spanwise positions. Confirming the trends observed in Mora et al. 2021b, a reduction in settling velocity was obtained at high Reynolds number generated with the active grid. In the present study, we expanded the range of Reynolds number by incorporating both a passive grid and the active grid in a static configuration, giving a Reynolds number varying between $Re_\lambda \in [30 - 500]$. While the intensity of the maximum of enhancement has been observed to vary non-monotonically with the Reynolds number, the wide range of Re_λ values in the present study demonstrates that the maximum of enhancement globally decreases with an overall increase in Re_λ. In addition, the various grid options enable us to create turbulent carrier flows with similar Reynolds number and turbulent intensities, and yet significantly different integral length scale. This facility feature allows us to isolate the effect of large-scale structures on settling velocity. We observe that, within the range of Rouse and Stokes number studied, large-scale forcing significantly impacts the settling velocity modification. A smaller integral length scale is associated with a more pronounced enhancement, whereas at constant turbulent intensity and larger energy-containing eddies, the settling enhancement is milder.

J. Fluid Mech. (2023), *vol.* 970, A23, doi:10.1017/jfm.2023.579

An experimental study on the settling velocity of inertial particles in different homogeneous isotropic turbulent flows

Amélie Ferran[1,2,†], **Nathanaël Machicoane**[1], **Alberto Aliseda**[2] and **Martín Obligado**[1]

[1]Université Grenoble Alpes, CNRS, Grenoble-INP, LEGI, F-38000 Grenoble, France

[2]Department of Mechanical Engineering, University of Washington, Seattle, WA 98195-2600, USA

(Received 13 July 2022; revised 31 May 2023; accepted 2 July 2023)

We propose an experimental study on the gravitational settling velocity of dense, sub-Kolmogorov inertial particles under different background turbulent flows. We report phase Doppler particle analyser measurements in a low-speed wind tunnel uniformly seeded with micrometre scale water droplets. Turbulence is generated with three different grids (two consisting of different active-grid protocols while the third is a regular static grid), allowing us to cover a very wide range of turbulence conditions in terms of Taylor-scale-based Reynolds numbers ($Re_\lambda \in [30–520]$), Rouse numbers ($Ro \in [0–5]$) and volume fractions ($\phi_v \in [0.5 \times 10^{-5}–2.0 \times 10^{-5}]$). We find, in agreement with previous works, that enhancement of the settling velocity occurs at low Rouse number, while hindering of the settling occurs at higher Rouse number for decreasing turbulence energy levels. The wide range of flow parameters explored allowed us to observe that enhancement decreases significantly with the Taylor–Reynolds number and is significantly affected by the volume fraction ϕ_v. We also studied the effect of large-scale forcing on settling velocity modification. The possibility of changing the inflow conditions by using different grids allowed us to test cases with fixed Re_λ and turbulent intensity but with different integral length scale. Finally, we assess the existence of secondary flows in the wind tunnel and their role on particle settling. This is achieved by characterising the settling velocity at two different positions, the centreline and close to the wall, with the same streamwise coordinate.

Key words: turbulent flows, multiphase and particle-laden flows

---

† Email address for correspondence: amelie.ferran1@univ-grenoble-alpes.fr

1. Introduction

Turbulent flows laden with particles are present in both environmental phenomena and industrial applications. For instance, water droplets, snowflakes and pollutants in atmospheric turbulence, sediments in rivers and industrial sprays all involve turbulent environments carrying inertial particles (Crowe, Troutt & Chung 1996; Shaw 2003; Monchaux, Bourgoin & Cartellier 2012; Li *et al.* 2021). Inertial particles do not follow the fluid velocity field as tracers, having their own dynamics that depend on both their finite size and their density ratio compared with that of the carrier phase.

Two phenomena resulting from the influence of turbulence on the motion of inertial particles have been widely studied: preferential concentration and modification of the settling velocity. Preferential concentration refers to the fact that an initially uniform or random distribution of particles will form areas of clusters and voids (Maxey 1987; Squires & Eaton 1991; Aliseda *et al.* 2002; Obligado *et al.* 2014; Sumbekova *et al.* 2017) due to the accumulation in certain regions of the turbulent flow where the hydrodynamic forces exerted by the flow tend to drive the particles. Furthermore, settling velocity modification occurs when particles immersed in a turbulent flow have their settling speed V_s altered compared with that in a stagnant fluid or laminar flow V_T (Wang & Maxey 1993; Crowe *et al.* 1996; Aliseda & Lasheras 2011). These two features of turbulent-laden flow are known to be linked together as the settling velocity of a particle can be increased due to an increase of the particle local concentration (Aliseda *et al.* 2002; Gustavsson, Vajedi & Mehlig 2014; Huck *et al.* 2018).

Regarding the modification of the settling velocity, multiple experimental and numerical studies have shown that turbulence can both hinder ($V_s < V_T$) or enhance the particle settling velocity ($V_s > V_T$). While several studies have reported enhancement of the settling velocity (Wang & Maxey 1993; Aliseda *et al.* 2002; Bec, Homann & Ray 2014; Rosa *et al.* 2016; Monchaux & Dejoan 2017; Falkinhoff *et al.* 2020), others show evidence of hindering only (Akutina *et al.* 2020; Mora *et al.* 2021) or of both types of modification (Nielsen 1993; Good, Gerashchenko & Warhaft 2012; Sumbekova *et al.* 2016; Petersen, Baker & Coletti 2019). While the nature and number of mechanisms controlling this phenomenon is still a matter of debate, several models have been proposed in the literature, sometimes even giving contradictory predictions.

Enhancement of the settling velocity can be explained by the preferential sweeping mechanism, also known as the fast-tracking effect, where inertial particles tend to spend more time in downwards moving regions of the flow than in upwards flow (Wang & Maxey 1993). Some mechanisms have been proposed as well to explain hindering. The vortex trapping effect describes how light particles can be trapped inside vortices (Nielsen 1993; Aliseda & Lasheras 2006). The loitering mechanism assumes that falling particles spend more time in upward regions of the flow than downward regions (Chen *et al.* 2020), while a nonlinear drag can also explain that particles are slowed down in their fall by turbulence (Good *et al.* 2014). Models have been developed to estimate the influence of clustering and particle local concentration on the settling rate enhancement (Alipchenkov & Zaichik 2009; Huck *et al.* 2018).

However, even in the simplified case of small, heavy particles in homogeneous isotropic turbulence (HIT) no general consensus has been found on the influence of turbulence, through the Taylor-scale-based number Re_λ, on the transition between hindering and enhancement. The Taylor–Reynolds number $Re_\lambda = u'\lambda/\nu$ is based on the Taylor microscale λ where u' and ν are the carrier phase root-mean-square (r.m.s.) of the fluctuating velocity and kinematic viscosity, respectively. The influence of Re_λ on the maximum of enhancement, i.e. when $V_s - V_T$ reaches its maximum, is also still under debate. Depending on the range of Re_λ, some studies found that the maximum enhancement increases with Re_λ (Nielsen 1993; Yang & Lei 1998; Bec *et al.* 2014; Rosa *et al.* 2016; Wang, Lam & Lu 2018), whereas other studies show the opposite trend (Mora *et al.* 2021). Furthermore, a non-monotonic behaviour of $max(V_s - V_T)$ with Re_λ has also been reported (Yang & Shy 2021), where $max(V_s - V_T)$ corresponds to the maximal settling velocity with respect to the terminal velocity, with both V_s and V_T being functions of the particle size.

Several non-dimensional parameters have been found to play a role on the settling velocity. The dispersed phase interactions with turbulent structures are characterised by the Stokes and Rouse numbers (Maxey 1987), whereas the magnitude of turbulence excitation is quantified by the Taylor–Reynolds number. The Stokes number, describing the tuning of particle inertia to turbulent eddies turn over time, is defined as the ratio between the particle relaxation time and a characteristic time scale of the flow $St = \tau_p/\tau_k$, where τ_k has been shown to be represented by the Kolmogorov time scale τ_η. The Rouse number – also known as the settling parameter Sv – is a ratio between the particle terminal speed and the velocity scale of turbulence fluctuations, in this case the turbulent velocity r.m.s., $Ro = V_T/u'$. Hence, it is a competition between turbulence and gravity effects. While all these parameters are relevant for modelling and understanding the interactions of inertial particles and turbulence, there is still no consensus even on the set of non-dimensional numbers required to do so. Furthermore, the determination of length and time flow scales relevant to the settling speed modification has also been the subject of significant discussion in the literature. Yang & Lei (1998) determined that a mixed scaling using both τ_η and u' appears to be an appropriate combination of parameters for the present problem. There is a general agreement that the modification of the settling velocity is a process that encompasses all turbulent scales and, consistent with even single-phase HIT, a single flow scale is not sufficient to completely describe it. It has been shown that the particle settling velocity is affected by larger flow length scales with increasing Stokes number (Tom & Bragg 2019).

Experimentally, the influence of turbulence on the particle settling velocity has been studied in an air turbulence chamber (Good *et al.* 2014; Petersen *et al.* 2019), channel flows (Wang *et al.* 2018), Taylor–Couette flows (Yang & Shy 2021), water tank with vibrating-grids turbulence (Yang & Shy 2003; Poelma, Westerweel & Ooms 2007; Zhou & Cheng 2009; Akutina *et al.* 2020) and wind tunnel turbulence (Aliseda *et al.* 2002; Sumbekova *et al.* 2017; Huck *et al.* 2018; Mora *et al.* 2021). However, measuring the particle settling velocity in confined flows, such as in a wind tunnel, can be challenging due to the recirculation currents that may arise on the carrier phase. Weak carrier phase currents in the direction of gravity can be of the order of the smallest particle velocity and impact significantly the measurements of the settling velocity, (as reported in Good *et al.* (2012), Sumbekova (2016), Wang *et al.* (2018), Akutina *et al.* (2020), De Souza, Zürner & Monchaux (2021), Mora *et al.* (2021) and Pujara *et al.* (2021)). Akutina *et al.* (2020) dealt with this bias by removing the local mean fluid velocity from the particle instantaneous velocity measurements.

Accurate measurements of settling velocity and the local properties of the carrier-phase flow are therefore one aspect of major importance to better understand the role of turbulence on settling velocity modification. This work studies the settling velocity of sub-Kolmogorov water droplets in wind tunnel grid-generated turbulence. Turbulence is generated with three different grids (two consisting of different active grid (AG) protocols while the third is a regular static grid), allowing us to cover a very wide range of turbulence conditions, with the turbulence intensity u'/U_∞ ranging from 2 % to 15 %, $Re_\lambda \in [34, 520]$ and integral length scales $\mathcal{L} \in [1, 15]$ cm.

Particle settling velocity and diameter were quantified using a phase Doppler particle analyser (PDPA), as described in a previous work on the same facility (Mora 2020; Mora *et al.* 2021). Our experimental set-up has three unique features that contribute to the novelty of our results. First, the resolution of the particle vertical velocity is a factor of 10 higher than in Mora *et al.* (2021). This higher resolution enables the study of the settling velocity of particles with very small inertia, as small as 1 μm, corresponding to the range where settling is enhanced. Furthermore, thanks to the increased resolution in the vertical velocity, we can assess the existence of secondary flows in the wind tunnel by analysing the carrier flow vertical velocity with the Cobra probe and the PDPA velocity of tracer particles. We measure the settling velocity at two different positions, the centreline and near the sidewalls, for the same streamwise location. Additionally, we perform measurements of the single-phase velocity with a Cobra probe, a multihole Pitot tube that resolves the average and r.m.s. values of the three-dimensional (3-D) velocity vector (Obligado *et al.* 2022), that allows the quantification of small inhomogeneities in the single-phase flow, for all turbulent conditions studied. We find that the vertical velocity measured in dilute two-phase conditions is consistent with such inhomogeneities. For larger values of volume fraction, the vertical velocities become a non-trivial function of position, streamwise velocity and particle loading. This work, therefore, gives quantitative experimental evidence of the role and relevance of inhomogeneities and recirculation in the quantification of the settling velocity in confined domains.

Finally, the generation of turbulence with three different methods allows us to explore experimental realisations with similar values of Re_λ and u'/U_∞ but significantly different values of $\mathcal{L}$ (a factor of two different). This allows us to disentangle the role of the large turbulent scales on settling velocity modification, opening the door to expand available models to non-homogeneous flows. To the authors' best knowledge, our work presents the first experimental evidence capable of discriminating between the influence of large and small turbulent scales on particle settling. This is relevant not only for real-world physics, but also to learn from different laboratory set-ups and numerical simulations, as the ratio of small to large scales is different in each of these studies. In consequence, the present work is unique as it covers a broad range of turbulent flows, while resolving the settling velocity of particles as small as 1 μm. These measurements were complemented by hot-wire anemometry, that resolves all scales of the flow for the three turbulent conditions studied.

The paper is organised as follows. Section 2 describes the experimental set-up with the generation of turbulence, the injection of inertial particles and the PDPA misalignment correction. Section 3 presents the experimental results, with first the raw data and the presence of secondary currents. The influence of Re_λ, as well as other non-dimensional numbers, on the settling velocity and a scaling of the maximum of enhancement is then displayed. Here Re_λ is shown to have a non-monotonic influence on the settling enhancement. We found that the integral length scale has an influence on the settling velocity even for very low Stokes numbers. Section 4 presents the influence of the turbulent flow large scales on the settling velocity. Finally, § 6 summarises the results and draws conclusions.

2. Experimental set-up

2.1. *Grid turbulence in the wind tunnel*

Experiments were conducted in the Lespinard wind tunnel, a closed-circuit wind tunnel at LEGI (Laboratoire des Ecoulements Géophysiques et Industriels), Grenoble, France.

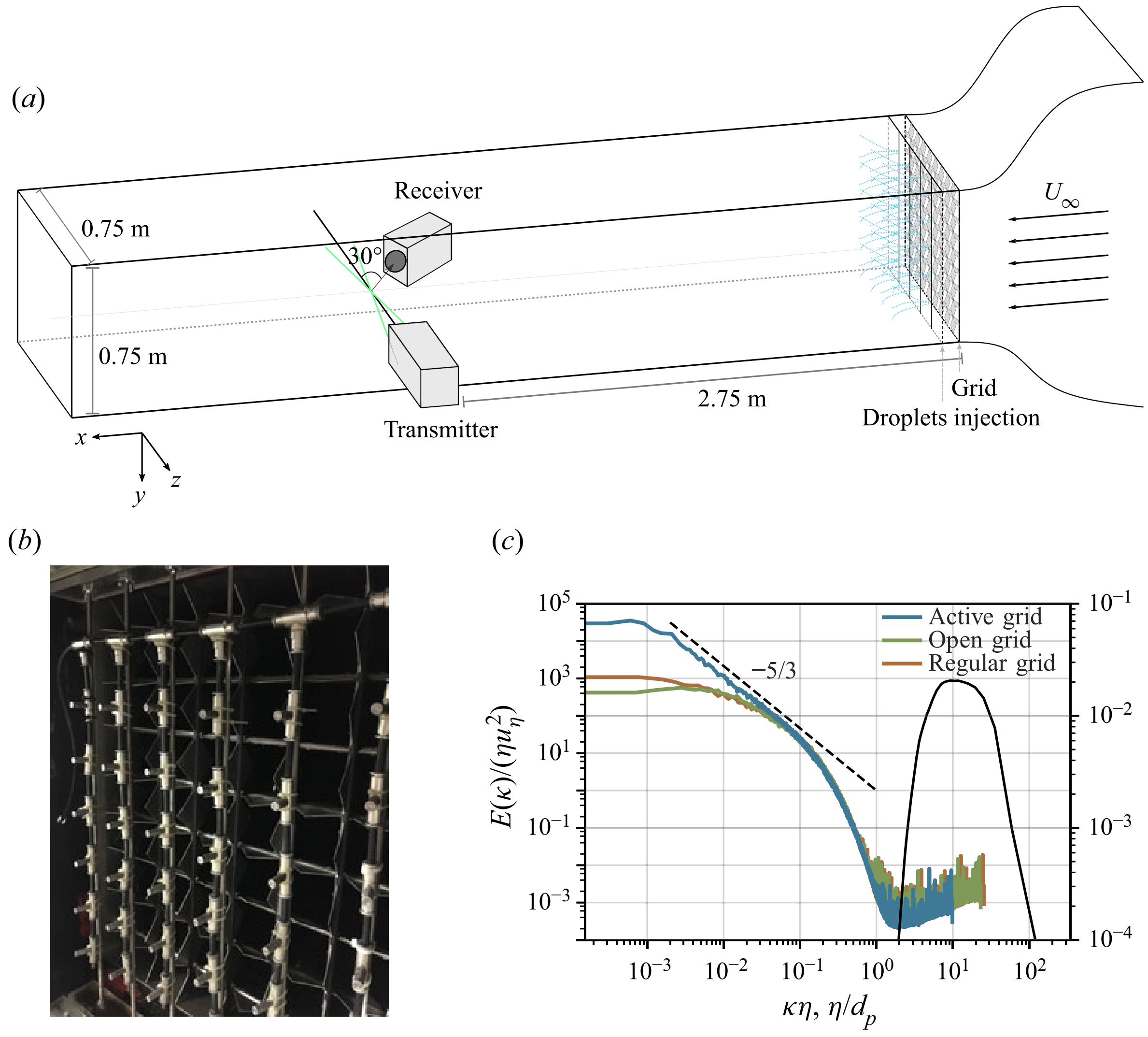

Figure 1. (*a*) Sketch of the wind tunnel with the PDPA measurement system. (*b*) Picture of the droplet injection system and, behind it, of the AG in OG mode. (*c*) Power spectral density of the longitudinal velocity from hot-wire records normalised by the Kolmogorov scale for an inlet velocity around 4 m s^{-1}. The dashed line presents a Kolmogorov $-5/3$ power law scaling, as reference. The inertial particle diameter distribution averaged over all the experiments and normalised by the Kolmogorov scale is shown on the right-hand axis. Note that it is plotted against η/d_p.

The test section is 4 m long with a cross-section of $0.75 \times 0.75\ \mathrm{m}^2$. A sketch of the facility is shown in figure 1(*a*). The turbulence is generated with two different grids: a static (regular) and an AG. The regular grid (RG) is a passive grid composed by seven horizontal and seven vertical round bars forming a square mesh with a mesh size of 10.5 cm. The AG is composed by 16 rotating axes (eight horizontal and eight vertical) mounted with coplanar square blades and a mesh size of 9 cm, (see Obligado *et al.* (2011) and Mora *et al.* (2019*b*) for further details about the AG). Each axis is driven by a motor whose rotation rate and direction can be controlled independently. Two protocols were used with the AG. In the AG protocol – also referred to as 'triple-random' in the literature (Johansson 1991; Mydlarski 2017) – the blades move with random speed and direction, both changing randomly in time, with a certain time scale provided in the protocol. We remark that in the following, AG refers to both the active grid and this protocol. For the open grid (OG) protocol, each axis remains completely static with the grid fully open, minimising blockages. These two protocols have been shown to create a large range of turbulent conditions, from $Re_\lambda \sim 30$ for OG to above 800 for AG (Mora *et al.* 2019*b*; Obligado *et al.* 2020).

The turbulent intensity u'/U_∞ obtained for OG is in the same range as for RG ($\approx 2\,\%$–$3\,\%$). The turbulent intensity created by the AG is much larger, just below 15 %. However, some significant differences exist between RG and OG turbulence: the bar width of the RG is twice that of the OG (2 cm versus 1 cm) and the OG has a 3-D structure due to the square blades (see figure 1*b* for an illustration of the OG). This implies significant differences in the integral length scale $\mathcal{L}$ of the turbulence; ≈ 6 cm for RG versus ≈ 3 cm for RG. These various grid configurations allowed us to explore different Taylor-scale Reynolds numbers Re_λ, from 34 to 513 at a fixed free stream velocity. Additionally, our experimental set-up allowed for the study of particles at similar values of u'/U_∞ and Re_λ, but different $\mathcal{L}$ (with OG versus RG). Matching the AG Reynolds number with the passive grids was not possible as it would require high wind tunnel velocities in the RG/OG cases, which would limit the measurements of the settling velocity due to low resolution.

Hot-wire anemometry measurements were taken to characterise the single-phase turbulence (Mora *et al.* 2019*b*). A constant temperature anemometer (Streamline, Dantec Inc.) was used with a 55P01 hot-wire probe (5 µm in diameter, 1.25 mm in length). The hot-wire was aligned with the centreline of the tunnel (3 m downstream the turbulence generation system). Additional measurements were carried out near the wall of the wind tunnel to check the homogeneity of the turbulence characteristics. Velocity time series were recorded for 180 s with a sampling frequency F_s of 50 kHz. This sampling frequency provides adequate resolution down to the Kolmogorov length scale η.

The background flow was also characterised with a Cobra probe: a multihole pressure probe which is able to capture three velocity components. This multihole Pitot tube probe (Series 100 Cobra Probe, Turbulent Flow Instrument TFI, Melbourne, Australia) was used to characterise possible contributions of the non-streamwise velocity components to the average value. Weak secondary motions in the carrier phase can arise in two-phase flow conditions due to the fall of inertial particles, as we will see in § 3.2, and in single phase condition due to confinement effects. The Cobra probe was used in this study to estimate the mean vertical flow for the latter. The acquisition time of the measurements was set to 180 s with a data rate of 1250 Hz (the maximum attainable). As the turbulence scales may reach beyond this frequency, and may not be resolved due to the finite size of the probe, which has a sensing area of 4 mm^2 (Mora *et al.* 2019*b*; Obligado *et al.* 2022), these measurements are used only to compute the mean and r.m.s. values of the 3-D velocity vector. To estimate the small angle present between the probe head and the direction of the mean flow, measurements were collected in laminar flow conditions (i.e. without any grid in the test section), to estimate the misalignment angle between the Cobra head and the streamwise direction.

Single-point turbulence statistics were calculated for each flow condition. The turbulent Reynolds number based on the Taylor microscale is defined as $Re_\lambda = u'\lambda/\nu$ where u' is the standard deviation of the streamwise velocity component, ν the kinematic viscosity of the flow and λ the Taylor microscale. The Taylor microscale was computed from the turbulent dissipation rate ε with $\lambda = \sqrt{15\nu u'^2/\varepsilon}$, extracted as $\varepsilon = \int 15\nu\kappa^2 E(\kappa)\,\mathrm{d}\kappa$ where $E(\kappa)$ is the energy spectrum along the wavenumber κ. The small scales of the turbulent flow are characterised by the Kolmogorov length, time and velocity scales: $\eta = (\nu^3/\varepsilon)^{1/4}$; $\tau_\eta = (\nu/\varepsilon)^{1/2}$; and $u_\eta = (\nu\varepsilon)^{1/4}$. Different methods were used to estimate the integral length scale. Here $\mathcal{L}$ was first computed by direct integration of the autocorrelation function until the first zero-crossing $\mathcal{L}_a = \int_0^{\rho_\delta} Ruu(\rho)\,\mathrm{d}\rho$ and until the smallest value of ρ for which

Parameters	AG	OG	RG
$U_\infty (\mathrm{m\ s^{-1}})$	2.6–5.0	2.6–5.0	2.6–5.0
Re_λ	268–513	34–55	49–68
$u'/U_\infty (\%)$	13.2–14.9	1.9–2.1	2.5–2.7
$10^3 \times \varepsilon (\mathrm{m^2\ s^{-3}})$	140.1–1251.4	6.9–26.8	9.9–59.5
$\eta (\mu\mathrm{m})$	230–406	634–868	511–792
$\tau_\eta (\mathrm{ms})$	3.5–11.0	26.7–50.2	17.4–41.9
$\lambda (\mathrm{cm})$	1.02–1.29	0.92–1.16	0.83–1.09
$\mathcal{L}_{a0} (\mathrm{cm})$	16.3–22.4	3.0–3.1	5.5–8.7
$\mathcal{L}_{a\delta} (\mathrm{cm})$	8.5–9.6	1.8–1.9	2.2–2.4
$\mathcal{L}_{voro} (\mathrm{cm})$	14.0–24.0	2.3–2.8	3.7–4.5

Table 1. Turbulence parameters for the carrier phase, sorted by grid category computed from hot-wire anemometry measurements 3 m downstream of the grid. Here U_∞ is the free stream velocity, u' the r.m.s. of the streamwise velocity fluctuations, $Re_\lambda = u'\lambda/\nu$ the Taylor–Reynolds number and $\varepsilon = 15\nu u'^2/\lambda^2$ the turbulent energy dissipation rate. Here $\eta = (\nu^3/\varepsilon)^{1/4}$ and $\tau_\eta = (\nu/\varepsilon)^{1/2}$ are the Kolmogorov length and time scales. Here $\lambda = \sqrt{15\nu u'^2/\varepsilon}$ and $\mathcal{L}$ are the Taylor microscale and the integral length scale, respectively, where three different methods are used to compute $\mathcal{L}$.

$Ruu(\rho_\delta) = 1/e$ (Puga & Larue 2017; Mora *et al.* 2019*b*). The integral length scale was also estimated from a Voronoï analysis of the longitudinal fluctuating velocity zero-crossings $\mathcal{L}_{voro}$, following the method recently proposed in Mora & Obligado (2020), where an extrapolation of the 1/4 scaling law was performed when needed. The latter is particularly relevant for the AG mode, where the value of R_{uu} has been found, in some cases, to not cross zero (Puga & Larue 2017). The estimation of $\mathcal{L}$ using $\mathcal{L} = C_\varepsilon u'^3/\varepsilon$ was not used in this study as the prefactor C_ε is not fixed for different turbulent conditions (i.e. different grids).

Table 1 summarises the flow parameters for all experimental conditions studied. Figure 1(*c*) shows the power spectral density of the streamwise velocity computed from hot-wire time signals at the measurement location ($x \approx 3$ m for all cases). The three spectra depicted in the figure were obtained from the three different grid configurations, all of them with an inlet velocity of approximately 4 m s^{-1}. The power spectral density was normalised by the Kolmogorov length and velocity scales η and u_η. As expected, the turbulent flow generated by the AG exhibits a considerably wider inertial range. On the right-hand side of the figure, for large values of $\kappa\eta$, the diameter distribution averaged over all the experiments is displayed. The diameter distribution, discussed in the next section, was normalised by the smallest Kolmogorov scale among all conditions (i.e. the Kolmogorov scale of the AG turbulent flow). It can be observed that the distribution is polydisperse and particles are always much smaller than the Kolmogorov scale of the turbulence. Figure 2 shows the Taylor Reynolds number Re_λ and the Taylor microscale λ for different wind tunnel velocities 3 m downstream (at approximately $x/M \approx 30$).

2.2. *Particle injection*

Water droplets were injected in the wind tunnel by means of a rack of 18 or 36 injectors distributed uniformly across the cross-section. The outlet diameter of the injectors is of 0.4 mm, and atomisation is produced by high-pressure at 100 bars. The water flow rate introduced in the test-section by the droplet injection system was measured with a flow meter for each experiment and varied between 0.5 and 3.4 l min^{-1}. The air

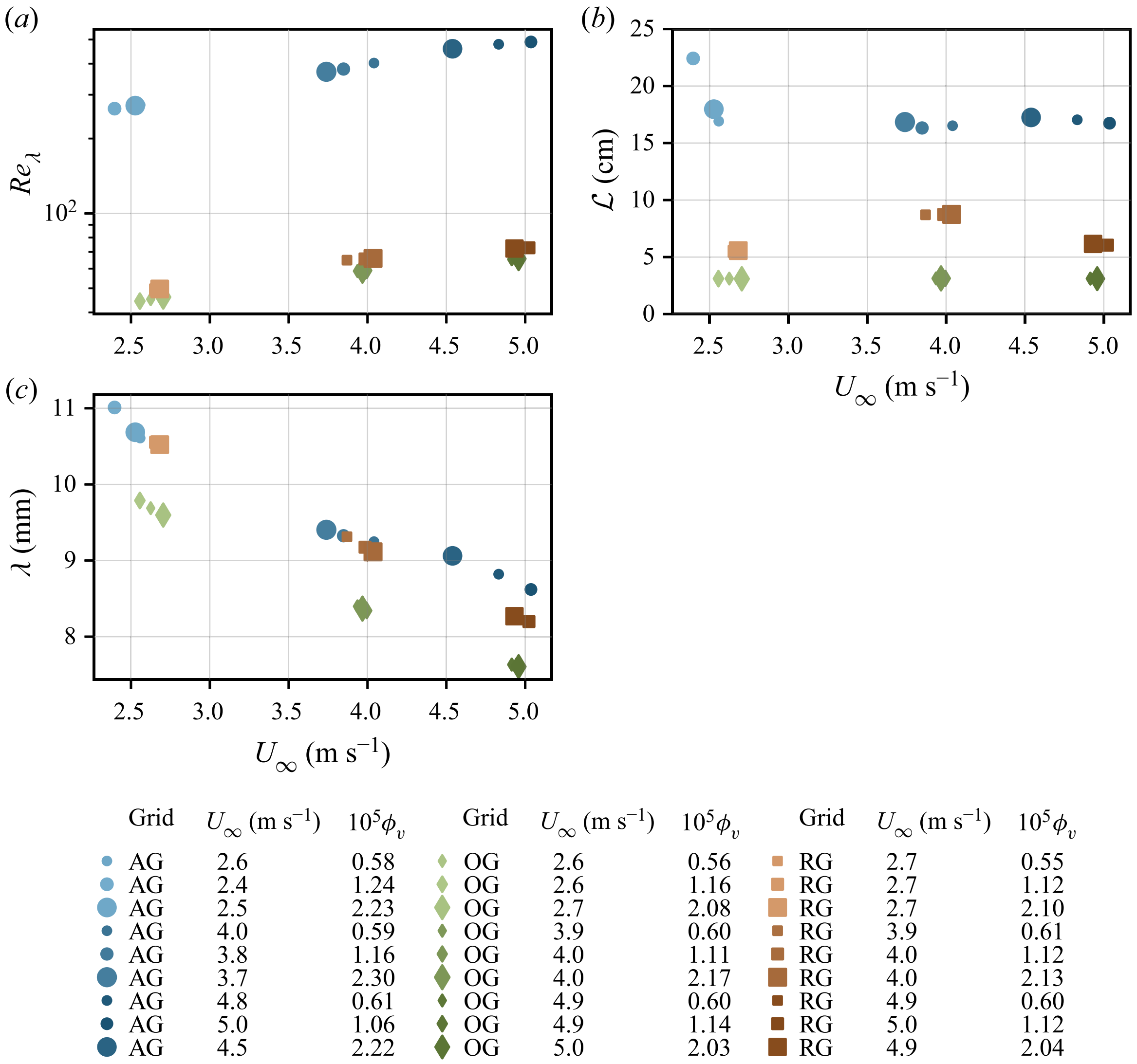

	Grid	U_∞ (m s^{-1})	$10^5\phi_v$		Grid	U_∞ (m s^{-1})	$10^5\phi_v$		Grid	U_∞ (m s^{-1})	$10^5\phi_v$
●	AG	2.6	0.58	♦	OG	2.6	0.56	■	RG	2.7	0.55
●	AG	2.4	1.24	♦	OG	2.6	1.16	■	RG	2.7	1.12
●	AG	2.5	2.23	♦	OG	2.7	2.08	■	RG	2.7	2.10
●	AG	4.0	0.59	♦	OG	3.9	0.60	■	RG	3.9	0.61
●	AG	3.8	1.16	♦	OG	4.0	1.11	■	RG	4.0	1.12
●	AG	3.7	2.30	♦	OG	4.0	2.17	■	RG	4.0	2.13
●	AG	4.8	0.61	♦	OG	4.9	0.60	■	RG	4.9	0.60
●	AG	5.0	1.06	♦	OG	4.9	1.14	■	RG	5.0	1.12
●	AG	4.5	2.22	♦	OG	5.0	2.03	■	RG	4.9	2.04

Figure 2. (*a*) Taylor–Reynolds number Re_λ; (*b*) integral length scale from the integration of the autocorrelation to the first zero-crossing; (*c*) Taylor microscale λ. All plotted versus the mean streamwise velocity obtained from hot-wire measurements. The different symbols (■), (•) and (♦) represent the RG, AG and OG, respectively. The size of the symbol is proportional to the volume fraction and darker colours correspond to higher mean velocities.

flow rate in the tunnel was computed using the measured mean streamwise velocity and the cross-sectional area. The particle volume fraction $\phi_v = F_{water}/F_{air}$ describes the ratio between the liquid and air volumetric flow rates. With the range of liquid flow rates and air velocities used in the experiments, the volume fraction ϕ_v varied between $\phi_v \in [0.5 \times 10^{-5}, 2.0 \times 10^{-5}]$. Here, 18 or 36 injectors were used depending on the experimental conditions, as low volume fractions could not be reached with 36 injectors. The resulting inertial water droplets have a polydisperse size distribution with a D_{max} and D_{32} of $\approx 30\ \mu$m and $\approx 65\ \mu$m, respectively (Sumbekova *et al.* 2017), as shown in figure 1(*c*), with D_{32} the Sauter mean diameter. The droplet Reynolds numbers Re_p are smaller than unity. For each grid mode, three different volume fractions were tested, with three different free stream velocities ($U_\infty = 2.6, 4.0, 5.0$ m s^{-1}). This results in 27 different experimental conditions.

Measurements were collected with a PDPA (Bachalo & Houser 1984). The PDPA (PDI-200MD, Artium Technologies) is composed of a transmitter and a receiver positioned at opposite sides of the wind tunnel. The transmitter emits two solid-state lasers, green at 532 nm wavelength and blue at 473 nm wavelength. Both lasers are split into two beams of equal intensity and one of these is shifted in frequency by 40 MHz, so that when they overlap in space they form an interference pattern. The 532 nm beam enables us to take the particle's vertical velocity and diameter simultaneously. The second beam is oriented to measure the horizontal velocity. The PDPA measurements were non-coincident, i.e. horizontal and vertical velocities were taken independently, since recording only coincident data points can significantly reduce the validation rate. The particle's horizontal velocity $\langle U \rangle$ is assumed to be very close to the unladen incoming velocity $\langle U \rangle \approx U_\infty$. Contrary to the study of Mora *et al.* (2021) in the same facility, the transmitter and the receiver had a smaller focal length of 500 mm. This enabled us to measure the particle vertical velocity with better resolution. The vertical and streamwise velocity components were recorded with a resolution of 1 mm s^{-1}. The PDPA configuration allows us to detect particles with diameters ranging from 1.5 μm to 150 μm. We verified that all velocity distribution were Gaussian, as expected under HIT conditions (see Appendix B). The measurement volume was positioned 3 m downstream of the droplet injection (at approximately the same streamwise distance as the hot-wire and Cobra measurements). In order to quantify the effect of recirculation currents, data were collected on the centreline of the wind tunnel and at an off-centre location, 10 cm from the wind tunnel wall. For each set of experimental conditions, at least 5×10^5 samples were collected. Depending on the water flow rate and the wind tunnel inlet velocity, the measurement sampling rate varied from 20 Hz to 4800 Hz with an average of 1030 and 580 Hz for the streamwise and vertical velocities, respectively.

2.3. *Angle correction*

As the settling velocity is only a small fraction of the particle velocity, any slight misalignment of the PDPA with the vertical axis (y) would result in a large error on the measurements of this important variable. To correct the optical alignment bias, the misalignment angle β was computed from very small ($d_p < 4$ μm) olive oil droplet measurements, as described in Mora *et al.* (2021). Olive oil generators produce monodisperse droplet distributions ($\langle d_p \rangle \approx 3$ μm), that behave as tracers. Using the empirical formula from Schiller & Nauman (Clift, Grace & Weber 1978) for the settling velocity of particles, and assuming that the mean centreline velocity is purely streamwise, the misalignment between the PDPA and gravity was estimated. Data from the alignment bias correction is given in Appendix C. The angle β was determined to be $\beta = 1.5^\circ \pm 0.3^\circ$. The vertical velocity measurements were then corrected subtracting the V_β misalignment bias (proportional to the streamwise velocity and the sine of the misalignment angle).

3. Results

3.1. *Settling velocity of inertial particles as a function of size*

Figure 3 presents the corrected averaged settling velocity $\langle V \rangle_D - V_\beta$ against the diameter D and the Stokes number St. Vertical velocity is defined as positive when downwards. In all figures, we averaged the settling velocity in 10 μm bins, from 0 to 150 μm.

For each experimental condition, as expected, the velocity measurements show that, on average, larger particles have higher settling velocity.

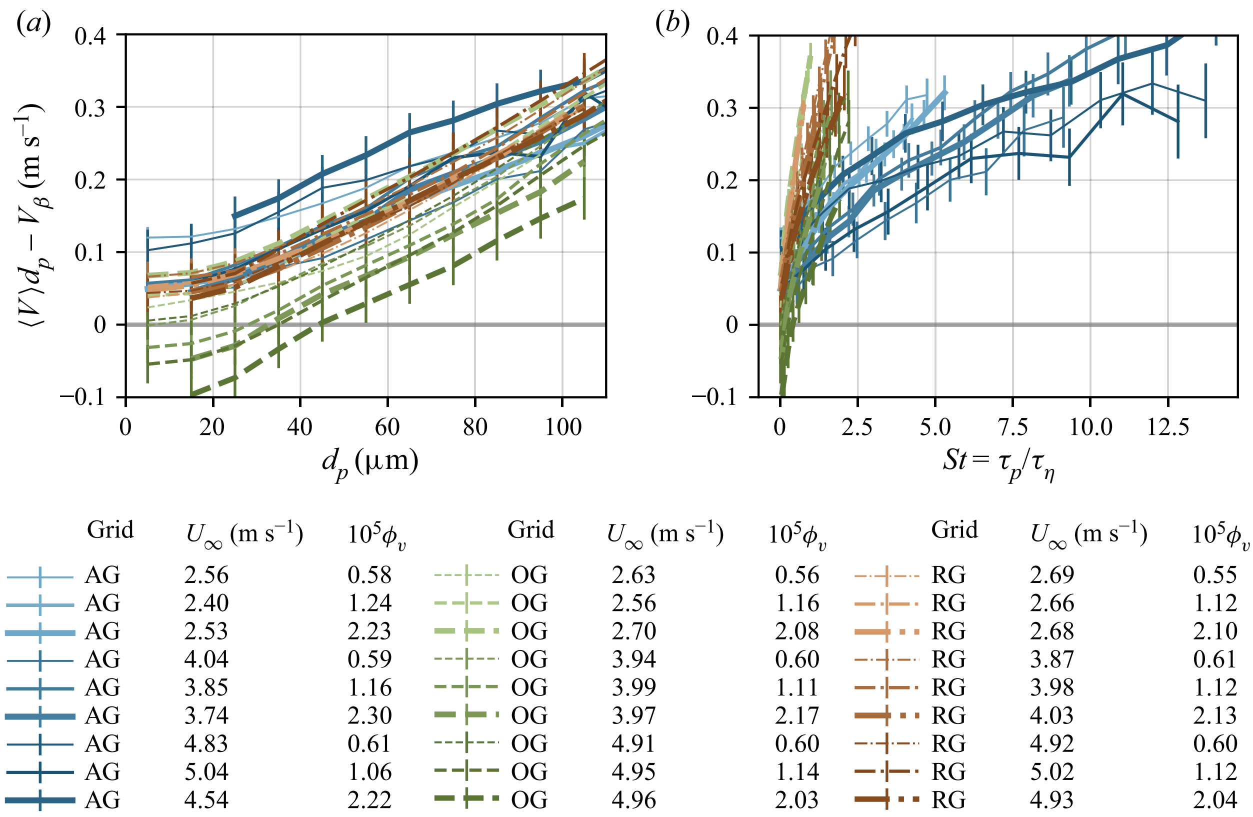

	Grid	U_∞ (m s^{-1})	$10^5\phi_v$		Grid	U_∞ (m s^{-1})	$10^5\phi_v$		Grid	U_∞ (m s^{-1})	$10^5\phi_v$
—┼—	AG	2.56	0.58	--┼--	OG	2.63	0.56	-·┼-·	RG	2.69	0.55
—┼—	AG	2.40	1.24	--┼--	OG	2.56	1.16	-·┼-·	RG	2.66	1.12
—┼—	AG	2.53	2.23	--┼--	OG	2.70	2.08	-·┼-·	RG	2.68	2.10
—┼—	AG	4.04	0.59	--┼--	OG	3.94	0.60	-·┼-·	RG	3.87	0.61
—┼—	AG	3.85	1.16	--┼--	OG	3.99	1.11	-·┼-·	RG	3.98	1.12
—┼—	AG	3.74	2.30	--┼--	OG	3.97	2.17	-·┼-·	RG	4.03	2.13
—┼—	AG	4.83	0.61	--┼--	OG	4.91	0.60	-·┼-·	RG	4.92	0.60
—┼—	AG	5.04	1.06	--┼--	OG	4.95	1.14	-·┼-·	RG	5.02	1.12
—┼—	AG	4.54	2.22	--┼--	OG	4.96	2.03	-·┼-·	RG	4.93	2.04

Figure 3. Corrected particle vertical velocity $\langle V \rangle_D - V_\beta$ averaged over bins of 10 μm against the diameter (*a*) and the Stokes number (*b*). The data from the AG are in solid lines, the OG in dashed line and the RG in dash–dotted line. The error bars show the estimation of the error in the velocity measurements. Darker colours correspond to higher mean velocities U_∞ and the line width is proportional to the volume fraction.

3.2. *Non-zero mean vertical flow in the limit of very small diameter*

The ensemble average of the particle equation of motion projected in the direction of gravity gives

$$\langle v_y^p(t) \rangle = \langle u_y(\boldsymbol{x}^p(t), t) \rangle + V_T, \tag{3.1}$$

where y is the vertical coordinate directed towards gravity, $\boldsymbol{x}^p(t)$ and $v_y^p(t)$ are the particle position and particle vertical velocity. Here $u_y(\boldsymbol{x}^p(t), t)$ is defined as the fluid vertical velocity at the position of the particle, and V_T is the terminal velocity in a still fluid.

If particles have inertia, they preferentially sample the underlying flow field following the preferential sweeping mechanism as described by Maxey (1987); as a consequence $\langle u_y(x^p(t), t) \rangle$ differs from the Eulerian mean fluid velocity $\langle U_y(t) \rangle$. In the absence of particle inertia, they sample uniformly the flow field and $\langle u_y(x^p(t), t) \rangle = \langle U_y(t) \rangle$.

Similarly as in Maxey (1987), the one-point Eulerian statistics and the one-point Lagrangian statistics are equal for homogeneous and stationary turbulence. If we rewrite (3.1) for the case of inertialess particles, we get

$$\langle V_y(t) \rangle|_{St=0} = \langle U_y(t) \rangle + V_T|_{St=0}, \tag{3.2}$$

where $\langle V_y(t) \rangle$ is the mean Eulerian particle vertical velocity and $\langle U_y(t) \rangle$ is the Eulerian mean fluid vertical velocity.

In the limit of zero particle inertia, the particle relaxation time τ_p tends to zero, and therefore V_T (which can be computed as $V_T = g\tau_p$) also tends to zero. Consequently, in the zero-inertia limit and for very dilute conditions, particles should behave as tracers and follow the fluid streamlines. Assuming that the air flow has no mean motion in the vertical direction in the centreline, the mean corrected vertical particle velocity $\langle V\rangle_D - V_\beta$ should tend to zero for small diameters.

However, experimental data shown in figure 3 present an offset velocity when the diameter tends to zero. This offset velocity for very small particles was already encountered in this facility (Sumbekova 2016; Mora *et al.* 2021) and suggests a vertical component due to secondary motion in the air in the wind tunnel, $\langle U_y(t)\rangle \neq 0$. A mean gas velocity in the vertical direction could be due to two different physical phenomena. First, as discussed previously, confinement effects (that would be different for each type of the grid) can be responsible for secondary recirculation motion inside the tunnel. Second, the injection of droplets could modify the background flow, since falling droplets may entrain gas in their fall. Even if the volume fraction is low enough for the particles to not affect the global turbulence statistics, the dispersed phase can exert a significant back reaction on the fluid in their vicinity (two way coupling effect) (Monchaux & Dejoan 2017; Tom, Carbone & Bragg 2022). Entrainment in the wake of falling particles might induce a downward mean gas flow, with a velocity that should be proportional to the dispersed-phase volume fraction (Alipchenkov & Zaichik 2009; Sumbekova 2016). To compensate the downward gas secondary motion near the centreline of the wind tunnel, an upwards flow in the gas near the walls should be present (and *vice versa* for upwards gas velocity at the centreline).

Other studies have encountered similar difficulties due to recirculating secondary motions when measuring particle settling velocity (Wang *et al.* 2018; Akutina *et al.* 2020). Akutina *et al.* (2020) corrected for this bias by subtracting the local mean fluid velocity measurements from the instantaneous vertical velocity of the particle (available in the point-particle simulations).

We estimated the existence and strength of recirculating secondary motion in the wind tunnel by taking PDPA measurements in the centre and close to the wall of the wind tunnel. We quantified the carrier-phase vertical velocity using the mean settling velocity of the smallest particles with enough statistical convergence. This parameter is referred to as $V_{physical}$. Figure 4 shows $V_{physical}$, measured in the centre (figure 4*a*) and near the wind tunnel wall (figure 4*b*).

Figure 4 shows downward motion ($V_{physical} > 0$) at the centre and upward motion ($V_{physical} < 0$) near the wind tunnel sidewall, in most cases. A different behaviour is observed for the OG (star symbols), with opposite direction of secondary motion, for some volume fractions.

Two possible causes of a mean vertical flow were explained above: confinement effects and the fluid dragging effect of the particles. With Cobra probe measurements, we observed that, even in the absence of particles recirculating currents arise in the carrier phase. Regarding the fluid dragging effect, there are evidences of the particle back-reaction on the fluid in our measurements since larger values of $V_{physical}$ are observed in the presence of particles than in the measurements without particles. One would expect that the fluid-dragging contribution to $V_{physical}$ would increase with volume fraction (Alipchenkov & Zaichik 2009; Sumbekova 2016); however, there is no clear trend observed for $V_{physical}$ with volume fraction. This lack of volume fraction influence on $V_{physical}$ can be explained by the limited range investigated. In short, the first-order contribution to $V_{physical}$ seems to be caused by confinement effects whereas a second minor contribution is due to the fluid dragging effect of the particles.

It is worth noticing that the Stokes number could have an influence on $V_{physical}$ as the entrainment of the carrier flow by the dispersed phase is connected to the particle inertia. We would then expect $V_{physical}$ to increase with the average Stokes number of the particles

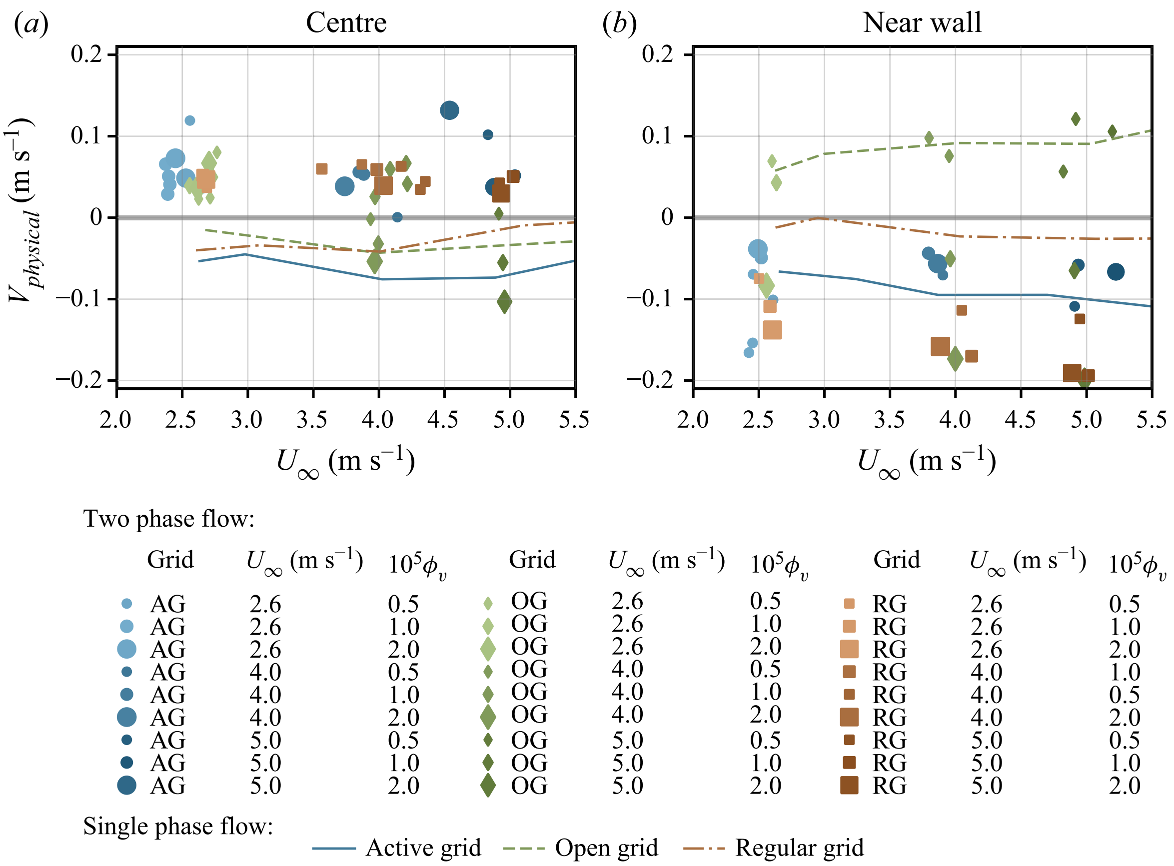

Figure 4. Average settling velocity of the particles for the smallest diameter class (*a*) at the centre, and (*b*) near the wall of the wind tunnel. The different symbols represent the RG (■), AG (•) and OG (♦). The size of the symbols is proportional to the volume fraction and a darker colour corresponds to a higher mean velocity. Carrier-phase vertical velocity measurements with the Cobra probe are presented at the two locations with coloured lines. Similar to figure 3, AG, OG and RG are in solid line, dashed line and dash–dotted line, respectively.

in the flow. In the present experiments, however, the particle size distribution is fixed due to the atomisation system. The value of $V_{physical}$, which is the best estimation of the vertical velocity of the carrier flow, results from the interaction of the entire range of diameters (i.e. $St \in [0, 14]$) with the turbulent gas flow. Thus, $V_{physical}$ cannot be computed independently for different particle Stokes numbers. It would then be expected that, in an experiment with different polydispersity, the value of $V_{physical}$ would change because of the different Stokes numbers. While our current experimental set-up does not allow for polydispersity variations, further studies may help to understand the role of St in $V_{physical}$.

We also observed recirculating secondary motions in the single-phase flow measured with the Cobra probe. Lines in figure 4 show the mean single-phase vertical velocity for the three turbulence conditions, against the mean streamwise velocity. Measurements with the Cobra probe provide evidence that there are weak secondary flows in the wind tunnel, even in the absence of particles. Moreover, these secondary flows are dependent on the turbulence generation mechanism, as the OG (dashed line) causes an opposite sense of motion than the AGs or RGs. Surprisingly, single-phase measurements confirm the same trends as the particle velocity measurements. At the most dilute case (i.e. for the lowest volume fraction, the vertical velocity of the secondary motion is the same order of magnitude in the single- and two-phase flows: 0.1 m s^{-1}).

In figure 4, each point corresponds to a single realisation of the experiment, where some realisations are repetitions of the same experimental conditions. We observe low but not insignificant dispersion between the different realisations of the single condition. However, the trend that we discuss is still robust: the sign of $V_{physical}$ does not change for the different realisations of the same conditions, although the magnitude does change.

To conclude, measurements in both laden and unladen flows show the existence of downward motion in the centre and upward motion near the sidewalls (with the AG and RG, with the opposite sense of motion for the OG). To the best of the authors' knowledge, this constitutes the first experimental evidence of the existence of $V_{physical}$ as a quantification of the carrier-phase vertical velocity in wind tunnel experiments. From now on, $V_{physical}$ and V_β are subtracted from the measurements of vertical velocity, $\langle V\rangle_{d_p} - V_\beta - V_{physical}$, to quantify settling velocity enhancement and/or hindering (corrected from these two experimental biases).

3.3. *Influence of the carrier flow turbulent Reynolds number on the particle settling velocity*

To quantify modifications of the settling velocity, we subtract the particle terminal speed in a stagnant fluid V_T from the vertical velocity. We define this difference as ΔV, where positive values imply settling velocity enhancement and negative correspond to hindering. The value of V_T is estimated using the Schiller–Naumann empirical formula for the particle relaxation time τ_p (Clift *et al.* 1978):

$$V_T = \tau_p g \quad \text{with}\ \tau_p = \frac{\rho_p d_p^2}{18\mu_f(1+0.15Re_p^{0.687})}, \tag{3.3}$$

where μ_f is the carrier flow dynamic viscosity, g the gravitational acceleration, d_p the particle diameter, $\rho_p = 900\ \mathrm{kg\ m^{-3}}$ the oil droplet density and $Re_p = V_T d_p/\nu$ the particle Reynolds number.

Here ΔV is usually normalised by the r.m.s. of the carrier-phase fluctuations, u', or by the particle terminal velocity, V_T. Normalising ΔV by u' was first proposed by Wang & Maxey (1993), and Yang & Lei (1998) confirmed u' is a better velocity scale than u_η to express the settling velocity enhancement. It has been widely used in other studies (Rosa *et al.* 2016; Huck *et al.* 2018). Consequently, ΔV is normalised by u', although this non-dimensionalisation of ΔV is still under scrutiny.

Figure 5 shows the normalised velocity difference $\Delta V/u'$ against particle diameter. All the measurements were taken at the same location, at the centreline of the wind tunnel. All the curves show the same trend: the settling velocity is enhanced for small particles, and this enhancement reaches a maximum, $max(\Delta V/u')$. After the maximum, the settling velocity enhancement decreases until it reaches a point where it is negative, that is, particle settling is hindered by turbulence. For very large particles (not attainable with our injection system), $\Delta V/u'$ would eventually become zero as they follow ballistic trajectories, unimpeded by turbulence. A discussion on the mechanisms that control enhancement and hindering of the settling velocity is available in § 5.

Particle settling velocity tends to depend on the turbulence characteristics, that is, in this study, it depends on the type of grid used in the experiments. Series taken with the OG configuration show a higher enhancement for all volumes fractions (green dashed line). On the contrary, AG turbulence (in blue solid lines) causes mostly hindered settling, with enhancement present only for a small range of diameters. Finally, measurements taken with the RG (red dash–dotted lines) show an intermediate behaviour between the two other grid configurations.

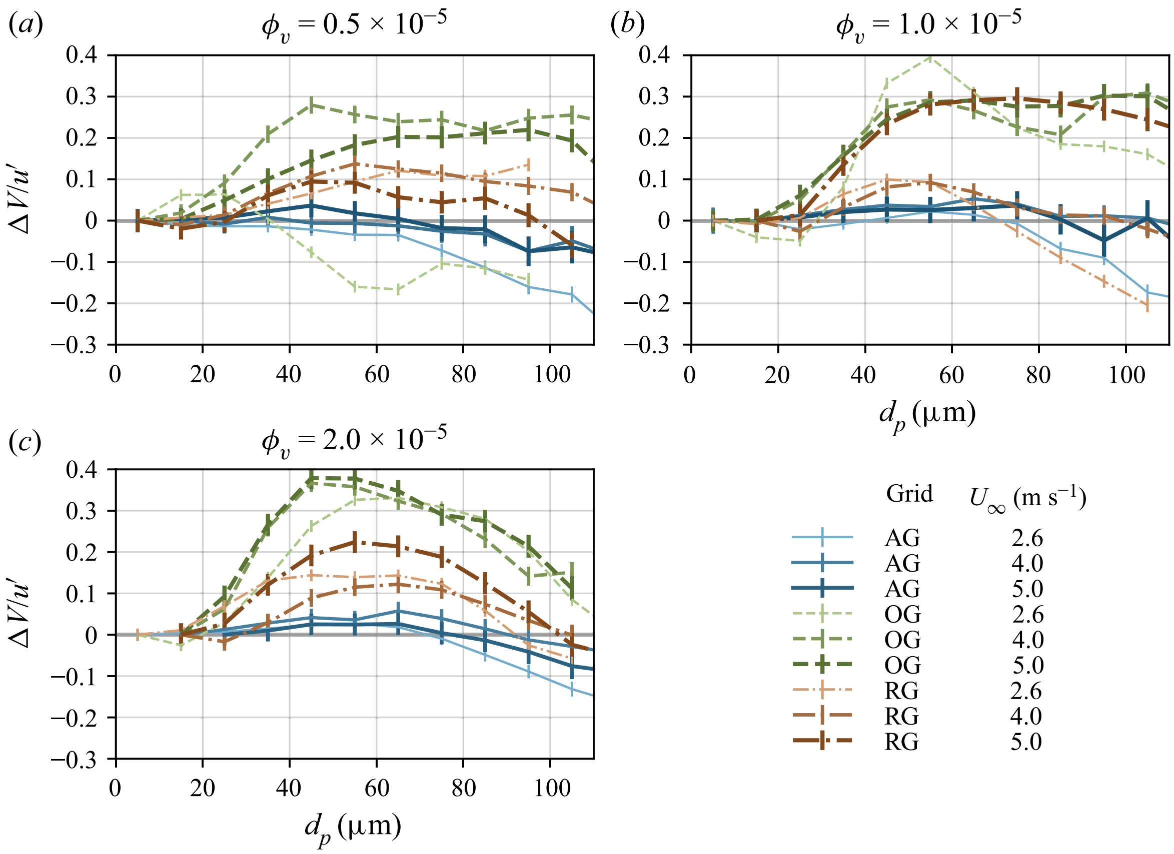

Figure 5. Particle velocity over the carrier phase fluctuations $\Delta V/u' = (\langle V\rangle_{d_p} - V_\beta - V_{physical} - V_T)/u'$ against the particle's diameter d_p for a volume fraction of 0.5×10^{-5} (*a*), 1.0×10^{-5} (*b*) and 2.0×10^{-5} (*c*). The data from the AG are in solid lines, the OG in dashed line and the RG in dash–dotted lines. The error bars show the estimation of the error in the velocity measurements induced by the determination of the misalignment angle. A darker colour corresponds to a higher mean velocity U_∞.

A combination between the Rouse and Stokes numbers, *Ro St*, has already been proven to be an interesting scaling (Ghosh *et al.* 2005), as it was shown in several studies to collapse the data better (Good *et al.* 2014; Petersen *et al.* 2019; Mora *et al.* 2021; Yang & Shy 2021). The Rouse–Stokes number can be expressed as a ratio between a characteristic length of the particle L_p and a characteristic length of the flow. Here L_p can be seen as the distance that a particle will travel to adjust its velocity to the surrounding fluid starting with a velocity V_T. Using the Kolmogorov time scale in the Stokes number and u' in the Rouse number, the Taylor microscale appears to be the characteristic length scale of the flow:

$$Ro\,St = \frac{\tau_p}{\tau_\eta}\frac{V_T}{u'} = \sqrt{15}\frac{V_T\tau_p}{\lambda} = \sqrt{15}\frac{L_p}{\lambda} \quad \text{with } L_p = V_T\tau_p \text{ as } \lambda = \sqrt{15}\tau_\eta u'. \tag{3.4}$$

In figure 6, we present $\Delta V/u'$ against the Rouse–Stokes number *Ro St*. Similar to figure 5, each panel presents data from a different value of volume fraction.

The *Ro St* number gives a better collapse of the position of maximum of enhancement than the Rouse number or Stokes number alone. Figure 6 indicates that enhancement of the settling velocity reaches a maximum for a Rouse–Stokes number around 0.6, which is consistent with previous findings. Yang & Shy (2021) reported a maximum for a *Ro St* around 0.72–1 in a Taylor–Couette flow, whereas Petersen *et al.* (2019) presented a maximum of enhancement for *Ro St* of order 0.1. Alternative scalings have been tested on our data, with the results provided for completion in Appendix A. These measurements

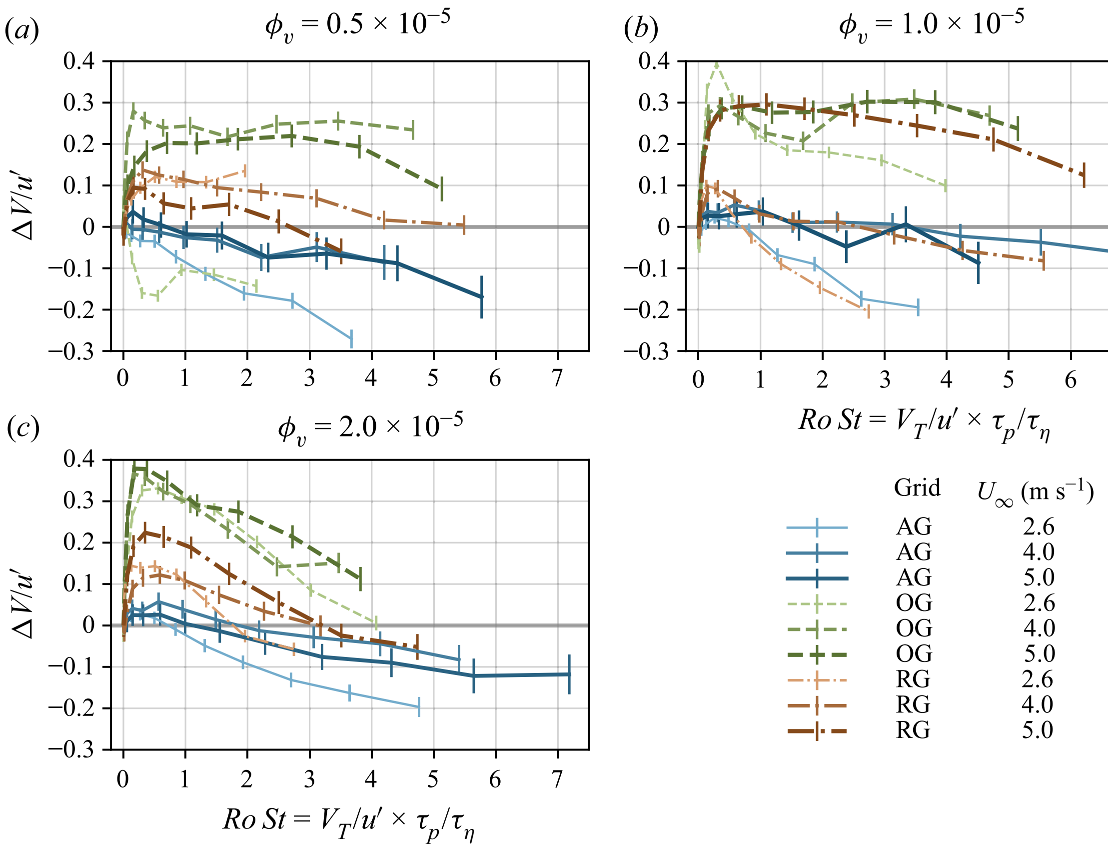

Figure 6. Enhancement of the particle velocity, normalised by the turbulent r.m.s. velocity, $\Delta V/u'$, against the Rouse–Stokes number: (*a*) $\phi = 0.5 \times 10^{-5}$; (*b*) $\phi = 1.0 \times 10^{-5}$; and (*c*) $\phi = 2.0 \times 10^{-5}$. Lines follow the legend of figure 5.

reveal that, for a fixed Re_λ, the enhancement increases with volume fraction, consistent with Aliseda *et al.* (2002) and Monchaux & Dejoan (2017).

We observe that the enhancement is much stronger for the low values of Re_λ ($\in$ [30–70], OG and RG) than for the higher Re_λ ($\in$ [260–520], AG) for all volume fractions. As shown in figure 2(*a*), the settling enhancement decreases significantly with an increase in the flow Taylor–Reynolds number, with Taylor–Reynolds number significantly higher for the AG turbulence than for the two other grids $Re_{\lambda AG} \gg Re_{\lambda RG} > Re_{\lambda OG}$. However, we observe when the Taylor–Reynolds number is varied by increasing the inlet velocity U_∞ alone, while keeping the same grid turbulence generation system, the trend is reversed: the settling enhancement increases with an increase in Re_λ within the small range achieved with each grid, and keeping a quasiconstant large-to-small scales ratio. Thus, settling enhancement depends strongly on the characteristics of the turbulence, as reported in Mora *et al.* (2021). While the study of Mora *et al.* (2021) obtained the same trend by comparing with data from the literature, in this study the entire range of Reynolds number and turbulent length scales were explored in the same facility.

This would suggest that the maximum of enhancement has a non-monotonic behaviour with the turbulent Reynolds number, as reported in Mora *et al.* (2021). A non-monotonic dependency of the degree of enhancement with Reynolds number has also been observed recently in Yang & Shy (2021). This effect of Re_λ on the maximum of enhancement confirms that the settling velocity modification is a multiscale phenomenon and one turbulent scale is not sufficient to characterise it (Tom & Bragg 2019).

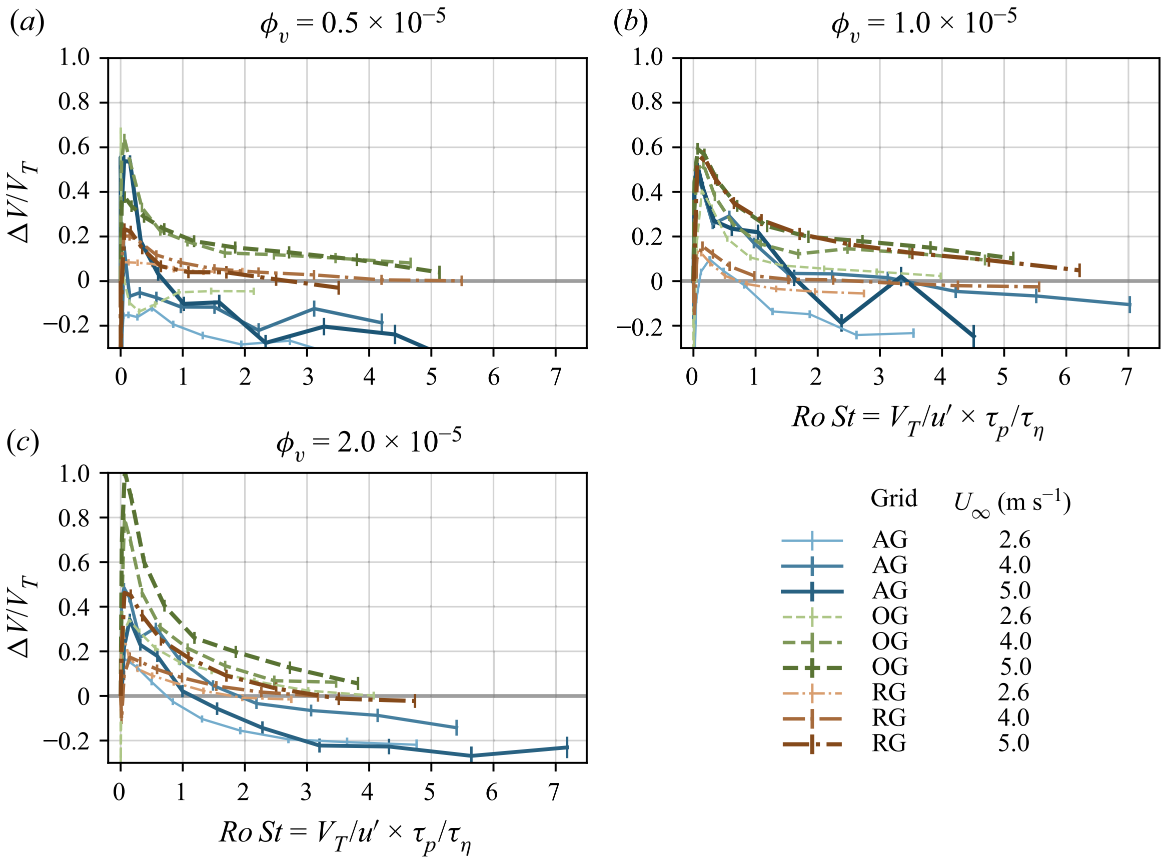

Figure 7. Enhancement of the particle velocity, normalised by the particle terminal velocity, $\Delta V/V_T$, against the Rouse–Stokes number: (*a*) $\phi = 0.5 \times 10^{-5}$; (*b*) $\phi = 1.0 \times 10^{-5}$; and (*c*) $\phi = 2.0 \times 10^{-5}$. Lines follow the legend of figure 5.

Although u' has been widely used in the literature to normalise ΔV, it has already been pointed out that there is no consensus on the scale for settling modification (Tom & Bragg 2019). The influence of the Reynolds number on the settling modification is also affected by normalising ΔV with u'. Since the range of flow scales that interact with the particles depends on the Stokes number, an interesting choice would be to non-dimensionalise ΔV with a vertical velocity that depends on *St*. Similarly to previous studies (Good *et al.* 2014; Rosa *et al.* 2016), a normalisation of the results with the terminal velocity $V_T = Stg\tau_\eta$ is proposed in figure 7. Figure 7 uses the same legend as figures 5 and 6. Normalising with V_T, the three different sets of curves for the three turbulence generation schemes are observed to collapse in figure 6. However, looking closely at figure 7, the Reynolds number dependency of the settling velocity modification is still non-monotonic, even after normalising with a velocity scale different than u'.

3.4. *Variance of the vertical particle velocity*

The variance of the vertical particle velocity $\langle (v_y')^2 \rangle$ normalised by the Kolmogorov velocity square is shown in figure 8. In figure 8(*a*), we observe that the variance increases with the Reynolds number Re_λ. This is expected since the fluid velocity variance increases with the Reynolds number and so does the particle velocity variance. The normalised particle velocity variance was also computed for each bin of diameters to have the influence of the Stokes number and the Rouse number on this metric. Figure 8(*b*) shows that the variance decreases slowly with the Rouse–Stokes number. This is consistent with the fact

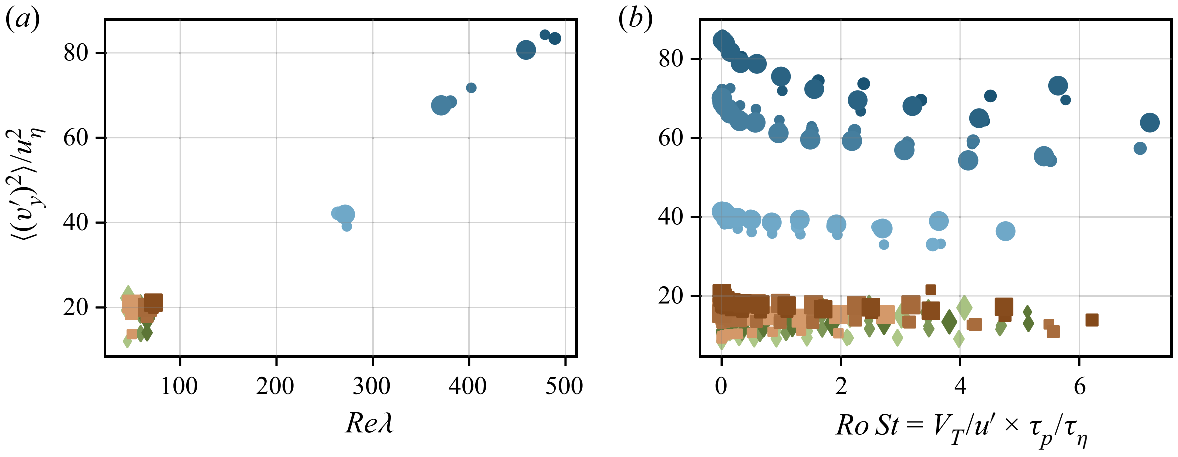

	Grid	U_∞ (m s^{-1})	$10^5\phi_v$		Grid	U_∞ (m s^{-1})	$10^5\phi_v$		Grid	U_∞ (m s^{-1})	$10^5\phi_v$
●	AG	2.56	0.58	◆	OG	2.63	0.56	■	RG	2.69	0.55
●	AG	2.40	1.24	◆	OG	2.56	1.16	■	RG	2.66	1.12
●	AG	2.53	2.23	◆	OG	2.70	2.08	■	RG	2.68	2.10
●	AG	4.04	0.59	◆	OG	3.94	0.60	■	RG	3.87	0.61
●	AG	3.85	1.16	◆	OG	3.99	1.11	■	RG	3.98	1.12
●	AG	3.74	2.30	◆	OG	3.97	2.17	■	RG	4.03	2.13
●	AG	4.83	0.61	◆	OG	4.91	0.60	■	RG	4.92	0.60
●	AG	5.04	1.06	◆	OG	4.95	1.14	■	RG	5.02	1.12
●	AG	4.54	2.22	◆	OG	4.96	2.03	■	RG	4.93	2.04

Figure 8. Variance of the vertical particle velocity $\langle (v'_y)^2\rangle$ normalised by the Kolmogorov velocity square u_η^2. The variance is plotted towards the Reynolds number Re_λ in (*a*) and towards the Stokes number in (*b*). The symbols follow the legend of figure 4.

that the filtering by inertial particles becomes more important as inertia increases. Inertial particles with higher Stokes number are less sensitive to the carrier flow's high velocity fluctuations.

3.5. *Scaling of the maximum of enhancement*

As no theoretical consensus have been found on the settling velocity modification, empirical scalings are proposed. This study focuses on the value and location of maximum of enhancement $max(\Delta V/u')$, and not on the critical *Ro St*, where enhancement turns into hindering, as most cases with the passive grid did not reach the transition enhancement/hindering for high Rouse number, contrary to Mora *et al.* (2021). As said in the previous section, the enhancement seems to increase when varying only the wind tunnel velocity U_∞. In order to take this trend into account, a global Reynolds number is introduced, $Re_G = MU_\infty/\nu$, based on U_∞ and M the mesh spacing in the turbulence-generating grid. Several dimensionless parameters were tested to scale $max(\Delta V/u')$: the global Reynolds number Re_G, the volume fraction ϕ_v, the Taylor-scale Reynolds number Re_λ, a Reynolds number based on the integral length scale, and the *Ro* or *St* numbers corresponding to the maximum of enhancement. The best scaling from the parameters above was found to be a combination of Re_λ, Re_G and ϕ_v.

Figure 9(*a*) represents $max(\Delta V/u')$ against $Re_\lambda^\alpha \phi_v^\beta Re_G^\gamma$, where α, β and γ are best-fit exponents:

$$max(\Delta V/u') \sim Re_\lambda^\alpha \phi_v^\beta Re_G^\gamma, \tag{3.5}$$

with $\alpha = -1.1$, $\beta = 0.6$ and $\gamma = 0.9$. The values of α, β and γ are consistent with previous observations: the maximum of enhancement increases with inlet velocity and

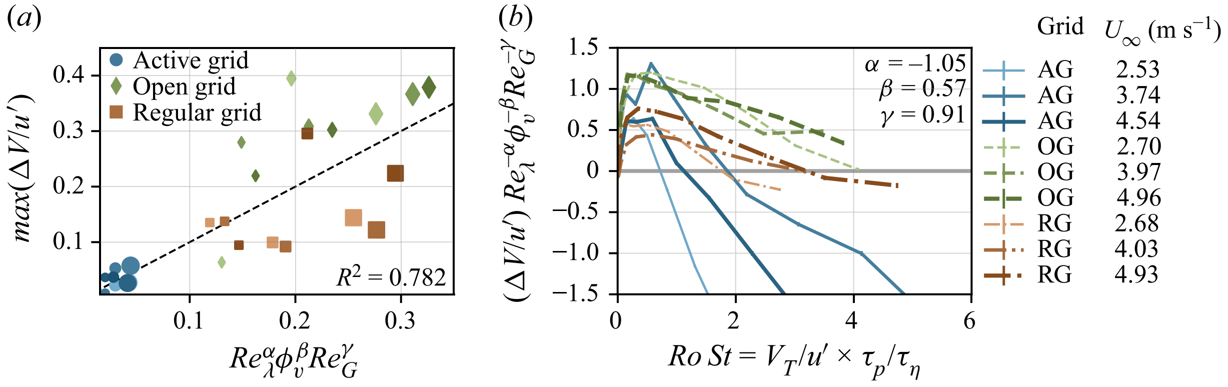

Figure 9. Scaling of the settling velocity with Re_λ, Re_G and ϕ_v: (*a*) $max(\Delta V/u')$ versus $Re_\lambda^\alpha \phi_v^\beta Re_G^\gamma$ with the fitted value of α, β and γ; (*b*) $max(\Delta V/u')$ divided by the scaling versus the Rouse–Stokes number.

volume fraction but decreases with an overall increase of Re_λ (when varying the Reynolds number on the entire range [30, 520]).

Figure 9 shows figure 6(*c*) with $\Delta V/u'$ divided by the power law scaling. A gap in data exists due to the jump in Reynolds number between the AG and the two passive grids (see figure 2). No measurements were taken for Re_λ between 70 and 260, since the present experimental set-up cannot reach those intermediate values.

Figure 9 shows that no simple scaling of the peak of settling enhancement can be inferred from this data. The dispersion of the results is partly due to the effect of the different large-scale turbulence, as discussed in the next section.

4. Influence of large-scale structures

Although the OG and RG create very similar values of turbulent intensity, the settling speed of inertial particles in these two flows are very different. Indeed, RG data (dash–dotted lines) is as different from OG data as it is from AG data (see figures 5 and 6). This discrepancy between RG and OG behaviours can be explained by the difference in integral length scales between these two turbulent flows (see table 1 and figure 2).

Figure 10 illustrates the settling velocity modification from two series with similar Reynolds numbers, turbulent intensities and volume fractions, but different integral length scales $\mathcal{L}_{a0}$. The figure is plotted against *Ro St* but presents a similar trend when made with *Ro* or *St*. It can be seen that the degree of settling enhancement is stronger for a smaller integral length scale and this behaviour is consistent for different volume fractions and wind tunnel Reynolds numbers. This suggests that the integral length scale and large-scale structures play a role in the settling velocity modification. According to the study of Tom & Bragg (2019), there is a length scale $l_c(St)$ above which the effects of particle inertia are negligible and only the flow scales smaller than l_c contribute to the settling velocity enhancement. Here l_c has been proposed to be an increasing function of the Stokes number, thus, as *St* increases, the range of flow scales impacting the settling velocity becomes larger. Consequently, we would expect the integral length scale to play a role on $\Delta V/u'$ only when the Stokes number is above $St(l_c)$. With our experiments, we provide the first evidence of settling velocity modification by turbulence where the integral length scale is the only difference between two turbulent datasets, in figure 10. According to the l_c hypothesis, one would expect the curves from the RG and the OG to collapse for the $St < St(l_c)$ data. Figure 10 reveals that the integral length scale has a measurable influence on the settling velocity modification for almost the entire range of *Ro St* number studied,

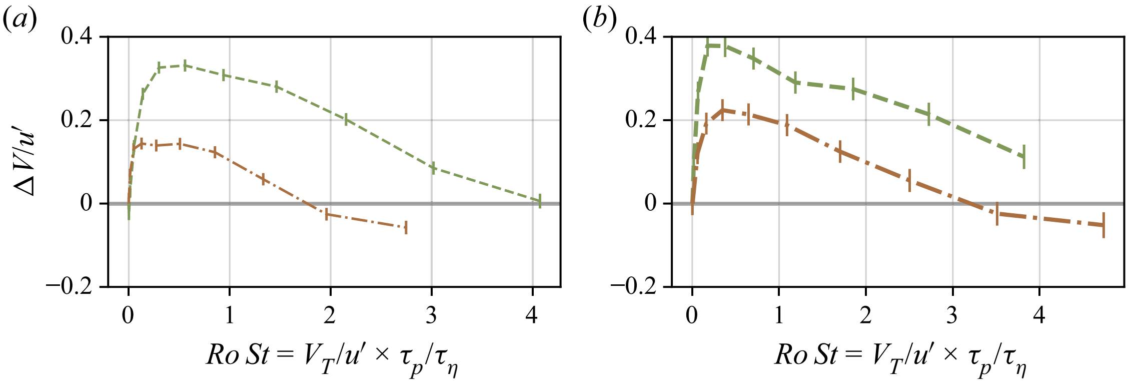

Grid	U_∞ (m s^{-1})	$10^5\phi_v$	I_{uu} (%)	Re_λ	$\mathcal{L}_{a0}$ (cm)
OG	2.70	2.08	2.70	46	3.1
RG	2.68	2.10	2.68	50	5.6

Grid	U_∞ (m s^{-1})	$10^5\phi_v$	I_{uu} (%)	Re_λ	$\mathcal{L}_{a0}$ (cm)
OG	4.96	2.03	2.65	66	3.1
RG	4.93	2.04	2.69	72	6.2

Figure 10. The OG and RG data. Settling velocity difference over the carrier-phase fluctuations $(\Delta V)/u'$ against the Rouse–Stokes number, for a volume fraction of 2.0×10^{-5}. Panel (*a*) displays data taken with an inlet velocity of 2.7 m s^{-1}, whereas the bulk velocity in (*b*) is 5.0 m s^{-1}.

and not only for the large $Ro\,St$. The data presented in figure 10 shows a collapse for $Ro\,St < 0.1$, suggesting that the integral length scale does not play a role in settling velocity modification for very small $Ro\,St$. This contradicts the hypothesis in Tom & Bragg (2019), unless $l_c < \mathcal{L}$ for the smallest particles in the flow. However, Tom & Bragg (2019) showed that $l_c(St)$ is larger than expected and can be larger than the flow integral scale even for $St = O(0.1)$.

As a consequence of the evidence provided in this paper, the preferential sweeping mechanism is more accurate at explaining the observations in flows where the large-scale structures are reduced in size.

5. Mechanisms of the settling velocity modification

5.1. *Competition between preferential sweeping and loitering*

The different models of the settling velocity modification require the measurement of fluid variables (flow structure, slip velocity, etc.) that is not possible, at least in an instantaneous manner, in large Reynolds number two-phase flows. Nevertheless, qualitative comparison of our experimental data with theoretical models for the proposed mechanisms shows good agreement. The enhancement of the settling velocity for small Stokes number, i.e. small diameter, particles found in our experiments is consistent with the preferential sweeping mechanism (Maxey 1987). The hindering for large Stokes number found at high Reynolds numbers, on the other hand, is consistent with the loitering mechanism proposed by Nielsen (1993). The mechanisms and the parameters that control the transition between enhancement and hindering, for which this manuscript provides novel data at turbulent Reynolds numbers and length scales not studied before, remain poorly understood and needs theoretical analysis.

Indeed, the Ro, St or $Ro\,St$ critic that set the transition between enhancement and hindering have a non-monotonic dependence with the Reynolds number. No simple scaling of the Stokes or Rouse critic could be found from other non-dimensional parameters (i.e. volume fraction, global Reynolds number or Taylor-based Reynolds). However, the fact that the maximum of enhancement collapses for $Ro\,St \approx 0.6$–1.0 gives a threshold for which the loitering effect starts to balance out the preferential sweeping mechanism (although enhancement remains the main outcome).

As mentioned before, the $Ro\,St$ number can be expressed as the ratio between L_p and λ, where L_p is the distance that a particle will travel to adjust its velocity to the surrounding fluid starting with a velocity V_T. Furthermore, the Taylor microscale can be seen as the separation between two large-scale eddies (Mazellier & Vassilicos 2008). When L_p starts to be larger than λ the preferential sweeping mechanism becomes less and less important since particles take a longer time and distance to respond to the fluid. As particles are less often swept in the downward side of eddies with an increase in L_p they cross both upward and downward regions of the flow which result in a more frequent loitering. Consistently, figure 10 shows that the preferential sweeping mechanism is more effective when the flow's large-scale structures are smaller.

5.2. *Collective effects*

Numerous studies have shown an increase in the particle settling velocity with the particle local concentration (Aliseda *et al.* 2002; Monchaux & Dejoan 2017; Huck *et al.* 2018). An estimate of the particle local concentration can be obtained with the use of Voronoï tessellations (Monchaux, Bourgoin & Cartellier 2010). In this study, only one-dimensional statistics of a 3-D flow are collected with the PDPA. For such signals, special attention is required as the analysis of preferential concentration via Voronoï tessellations has shown to present some bias (Mora *et al.* 2019*a*). A Voronoï cell is defined as the portion of the temporal signal closer to one particle than to any other ones. The inverse of the Voronoï cell length L gives an indication of the particle local concentration $C = 1/L$. Preferential concentration is observed when small and large Voronoï cells are over represented compared with a random Poisson process (RPP). In other words, the probability distribution function (PDF) of the normalised Voronoï cell length $\mathcal{V} = L/\langle L\rangle$ crosses the PDF of a RPP twice. Before the first crossing, small Voronoï cells are over represented showing the presence of over populated regions, or clusters. Similarly, after the second crossing large Voronoï cells are more probable than for a RPP showing the presence of depleted regions (i.e. voids). Clusters and voids are defined as a group of connected cells with cell length smaller than the first, respectively larger than the second, crossing with the PDF of a RPP. According to Mora *et al.* (2019*a*), clustering can be present and not be detected by the use of one-dimensional Voronoï tessellations. However, if the standard deviation of the normalised cell length σ_ν is larger than for a RPP distribution $\sigma_\nu > \sigma_{RPP}$, it is a reliable evidence of the presence of preferential concentration. For the next, we will only consider cases for which $\sigma_\nu/\sigma_{RPP} > 1.2$ to avoid time series that present a lack of information.

Figure 11(*c*) shows the conditional particle velocity on the local concentration compared with the average settling velocity over all particles $\langle v_y(t)\rangle$ versus the normalised concentration $C/C_0 = 1/\mathcal{V}$. In agreement with previous studies (Huck *et al.* 2018), the settling velocity is constant or increased with the particle local concentration.

The mean settling velocity for particles in clusters and particles in voids are shown in figures 11(*a*) and 11(*b*). For low Reynolds number, the settling velocity for particles in clusters is, for most cases, larger than the global settling while particles in voids settle slower than the unconditional average. Figure 11 shows that the particle local concentration and collective effects have an influence on the settling rate in our dataset as previously observed in Aliseda *et al.* (2002), Huck *et al.* (2018) and Petersen *et al.* (2019).

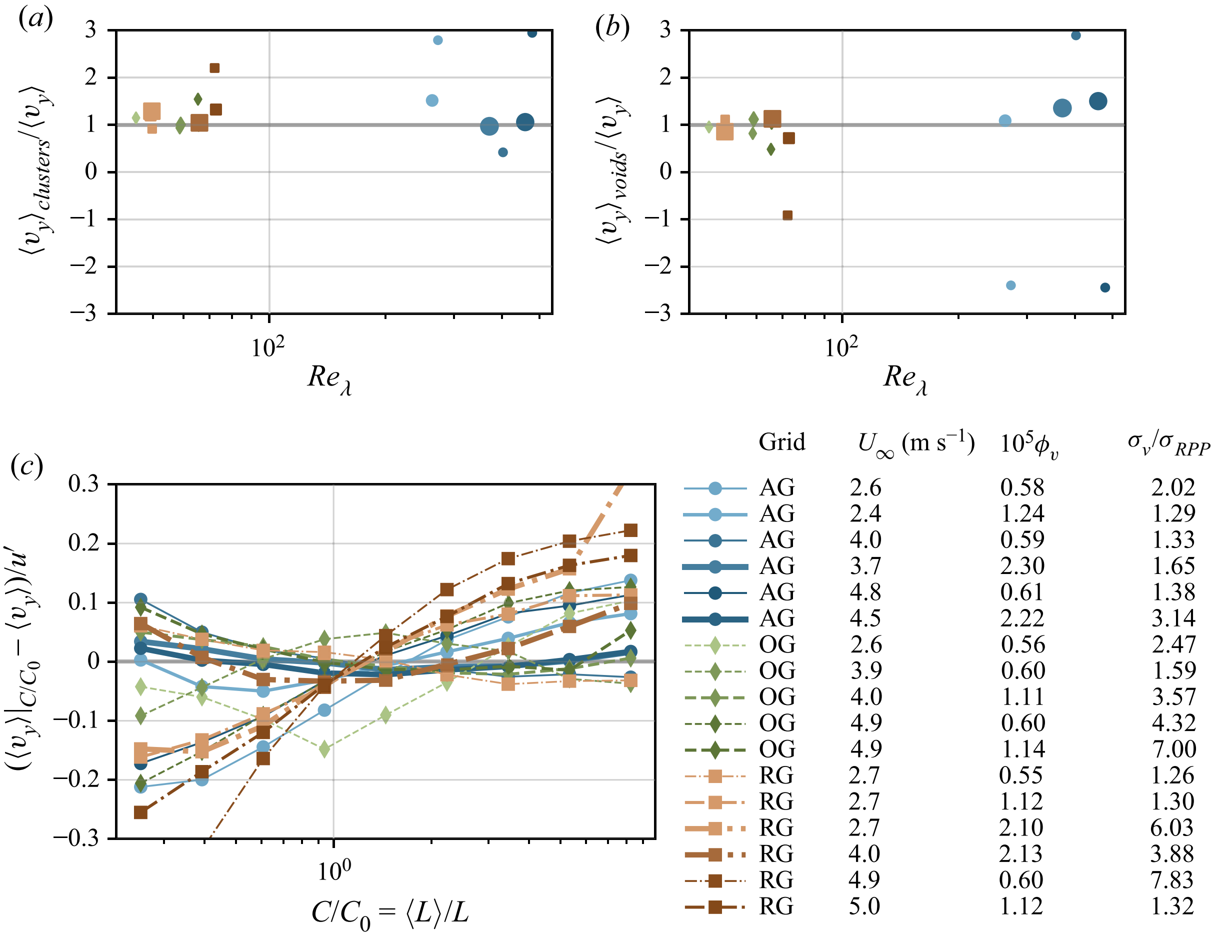

Figure 11. Mean settling velocity of particles in clusters $\langle v_y \rangle_{clusters}$ (*a*) and particles in voids $\langle v_y \rangle_{voids}$ (*b*) normalised by the unconditional average $\langle v_y \rangle$. Panel (*c*) shows the settling velocity conditioned on the particle local concentration $\langle v_y \rangle|_{C/C_0}$ normalised by the r.m.s. of the carrier phase fluid fluctuations. Symbols and lines follow the legend of figure 4.

5.3. *Sweep-stick mechanism*

The sweep-stick mechanism proposed by Chen, Goto & Vassilicos (2006), Goto & Vassilicos (2008) and Coleman & Vassilicos (2009) states that there is a strong correlation between the carrier flow zero-acceleration points and inertial particle positions. This mechanism was first proposed to explain the preferential concentration of inertial particles for direct numerical simulation data with zero gravity. The modified sweep-stick mechanism (Falkinhoff *et al.* 2020) suggests that, in the presence of gravity, particles stick to low, but non-zero, acceleration points. Zero-acceleration points were shown to have an average lifetime of $\tau_{\mathcal{L}}$ with $\tau_{\mathcal{L}} = \mathcal{L}/u'$ the flow integral time scale (Coleman & Vassilicos 2009). This mechanism is restricted to cases where the particle relaxation time is much smaller than the zero acceleration points life-time, that is to say when $\tau_p \ll \tau_{\mathcal{L}}$ or $St_{\mathcal{L}} = \tau_p/\tau_{\mathcal{L}} \ll 1$ and for $St > 1$.

The average acceleration of the fluid at the particle's position can be estimated from the ensemble average of the Maxey–Riley equation,

$$\frac{\langle v_y^p(t) \rangle}{V_T} = \frac{\langle u_y(\boldsymbol{x}^p(t), t) \rangle}{V_T} + 1. \tag{5.1}$$

Similarly as in Falkinhoff *et al.* (2020), we use the approximation that $\langle a_y(\boldsymbol{x}^p(t), t) \rangle \sim \langle u_y(\boldsymbol{x}^p(t), t) \rangle / \tau_{\mathcal{L}}$ with $a_y(\boldsymbol{x}^p(t), t)$ the fluid acceleration at the particle position. The term

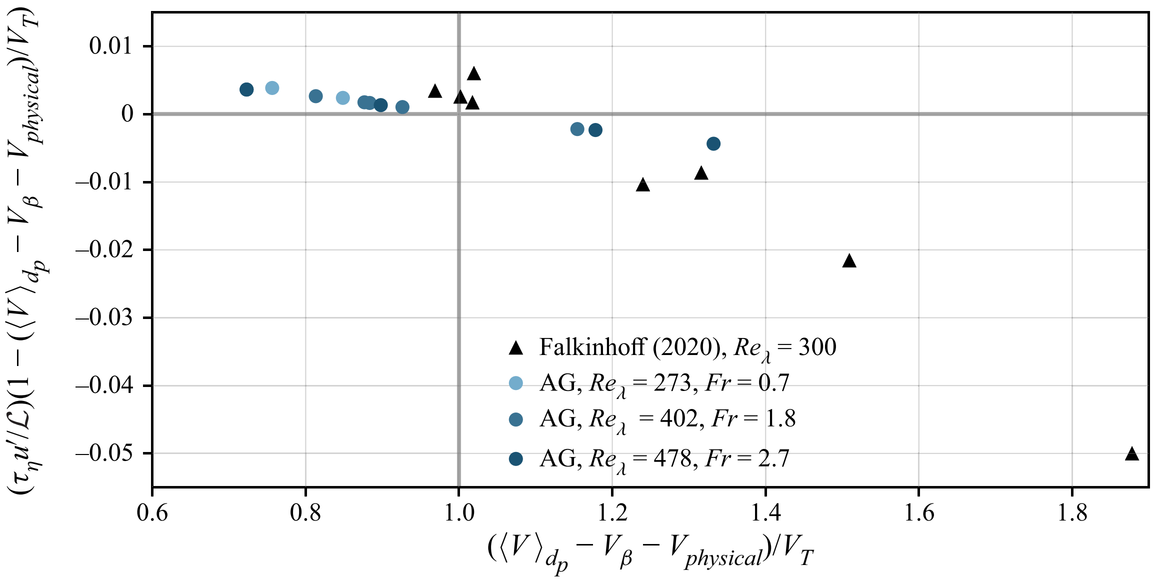

Figure 12. Average normalised acceleration of the fluid elements $\langle a_y(\boldsymbol{x}^p(t),t)\rangle/(gSt)$ following (5.3) as a function of the corrected settling velocity normalised by the terminal velocity $(\langle V\rangle_{d_p}-V_\beta-V_{physical})/V_T$. The black triangles present the data from the study of Falkinhoff *et al.* (2020). The data from the present study, taken with the AG and a volume fraction of 0.5×10^{-5}, are shown in blue.

$\langle u_y(\boldsymbol{x}^p(t),t)\rangle/V_T$ can be rewritten as $\langle a_y(\boldsymbol{x}^p(t),t)\rangle/(gSt_{\mathcal{L}})$ with $St_{\mathcal{L}}=\tau_p/\tau_{\mathcal{L}}$, as follows:

$$\frac{\langle a_y(\boldsymbol{x}^p(t),t)\rangle}{gSt_{\mathcal{L}}}=\frac{\langle v_y^p(t)\rangle}{V_T}-1. \tag{5.2}$$

Then with the fact that $\tau_{\mathcal{L}}=\mathcal{L}/u'$ and $St_{\mathcal{L}}/St=\tau_\eta u'/\mathcal{L}$ we get

$$\frac{\langle a_y(\boldsymbol{x}^p(t),t)\rangle}{gSt}=(\tau_\eta u'/\mathcal{L})\left(\frac{\langle v_y^p(t)\rangle}{V_T}-1\right). \tag{5.3}$$

To be able to compare with the data from Falkinhoff *et al.* (2020) for which the vertical axes is directed in the opposite direction, we plot the quantity $(\tau_\eta u'/\mathcal{L})(1-\langle v_y^p(t)\rangle/V_T)$ in figure 12. This quantity is positive when there is hindering ($\langle v_y^p(t)\rangle < V_T$) and negative in the case of enhancement ($\langle v_y^p(t)\rangle > V_T$).

Figure 12 presents the estimation of the normalised fluid acceleration at the particles' position for the AG data. The data from the direct numerical simulation of Falkinhoff *et al.* (2020), also shown in figure 12, correspond to a turbulent flow Reynolds number of $Re_\lambda\approx 300$, various Stokes numbers and Froude number ($St=1,3,6,8,9$), and Froude numbers ($Fr=(\varepsilon^3/\nu)^{1/4}1/g=0.15, 0.23, 0.45, 1.36$). As for the experimental data where the fluid velocity at the particle position is not accessible, we can only compare the value of the acceleration of the fluid elements between the experiments and the simulation. To better compare with the numerical simulation, only samples taken with the AG and with a *St* number close to 1, 3, 6, 8, 9 are presented in figure 12. There is a reasonable agreement in the value of $\langle a_y(\boldsymbol{x}^p(t),t)\rangle/(gSt_{\mathcal{L}})$ between both studies. The slope of the data is controlled by the value of $\tau_\eta u'/\mathcal{L}$, and thus depends only upon the flow characteristics. Discrepancies can be found between the values from the numerical simulation and the experiment since the Froude number and the flow integral length scale are different.

6. Conclusion

The settling velocity of sub-Kolmogorov inertial particles in wind tunnel decaying turbulence is presented and analysed. Accurate settling velocity measurements were carefully collected and calibrated, by correcting different experimental sources of potential bias. First, a correction for the PDPA misalignment angle is computed and applied. Second, secondary flows in the wind tunnel test section were characterised, $V_{physical}$, for both single-phase and two-phase flows. High resolution in the vertical velocity, compared with Mora *et al.* (2021), was obtained thanks to a new PDPA set-up. This, together with the detailed measurements of alignment and secondary motions, created a more accurate dataset of settling velocity for small Stokes number particles.

The results in this study confirm and extend the trends observed previously (among others by Wang & Maxey (1993), Aliseda *et al.* (2002), Good *et al.* (2014) and Mora *et al.* (2021)). Specifically, the settling velocity enhancement, that has been observed under a wide range of conditions, disappears with an increase of global (wind tunnel) Reynolds number, and turns to hindering at high Reynolds numbers $Re_\lambda > 260$. This dependence with Reynolds number is in contradiction with most numerical studies (Bec *et al.* 2014; Rosa *et al.* 2016; Tom & Bragg 2019). However, for a smaller range of Reynolds numbers, the maximum of enhancement is proportional to the inlet velocity U_∞, and therefore to the global Reynolds number. A new phenomenological scaling considering the influence of the bulk velocity has been proposed.

The range of volume fractions investigated is limited, and precludes the influence of this variable on settling enhancement from appearing. Different turbulence generation schemes allow for flows with different integral and Taylor length scales, at the same turbulent intensities and Reynolds numbers. We show that even if the Reynolds number and the turbulent intensity are similar, significant differences in the settling modification remain, due to widely different integral length scales. This suggests an important role of the large flow structures on the settling velocity modification.

The settling rate modification observed in this study is due to the intervention of several mechanisms, including at least preferential sweeping, loitering and sweep-stick mechanisms, operating on different ranges of Stokes and Rouse numbers. In addition to the aforementioned mechanisms, our results show that collective effects might take a part in the settling velocity modification.

Acknowledgements. We also would like to thank L. Vignal for her help with the PDPA measurements and V. Govart for producing experimental rigs.

Funding. This work has been supported by a LabEx Tec21 grant (Investissements d'Avenir – grant agreement no. ANR-11-LABX-0030).

Declaration of interest. The authors report no conflict of interest.

Author ORCIDs.
Amélie Ferran https://orcid.org/0000-0001-9851-8809;
Nathanaël Machicoane https://orcid.org/0000-0001-6492-8412;
Martín Obligado https://orcid.org/0000-0003-3834-3941.

Appendix A. Additional scalings

Particle settling velocity is often presented against the Stokes number (Wang & Maxey 1993; Yang & Lei 1998; Aliseda *et al.* 2002; Good *et al.* 2014; Rosa *et al.* 2016; Petersen *et al.* 2019; Yang & Shy 2021), the Rouse number (Good *et al.* 2012, 2014; Mora *et al.*

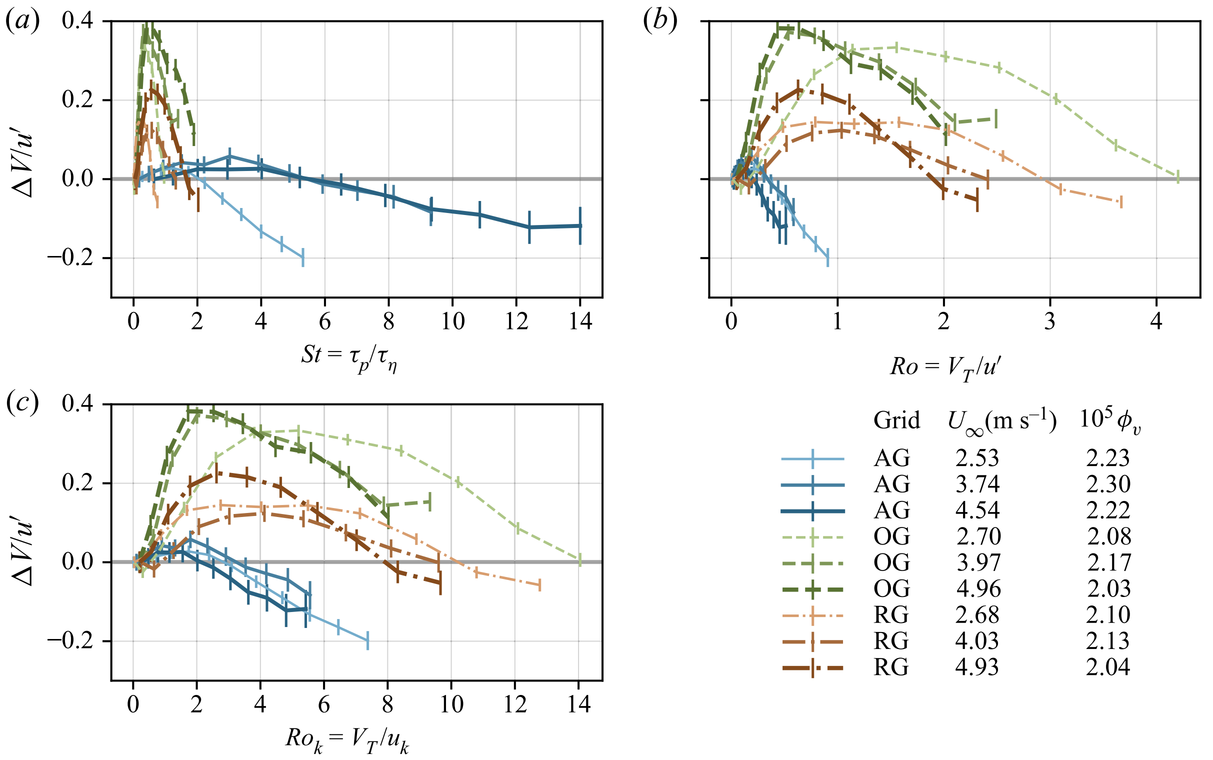

Figure 13. Particle velocity over the carrier phase fluctuations $\Delta V/u'$ against the Stokes number (*a*), Rouse number (*b*) and the Rouse number based on the Kolmogorov scale (*c*) for a volume fraction of 2.0×10^{-5}. Line styles follow the caption of figure 5.

2021) and a Rouse number based on the Kolmogorov scale V_T/u_η (Good *et al.* 2014). Figure 13 shows the present data against these three different parameters.

Appendix B. Stationarity of the temporal signal and PDF of particles' velocities

In this section we show the raw velocity obtained with the PDPA. The temporal signals are stationary (see figure 14). In this figure, one portion of the time signals is presented for each of the three grids using a volume fraction of $\phi_v = 1.0 \times 10^{-5}$ and an inlet velocity of $U_\infty \approx 4.0\ \mathrm{m\,s^{-1}}$. Figure 14(*a*) corresponds to the streamwise velocity whereas figure 14(*b*) represents the vertical velocity.

It can also be observed that all inertial particles horizontal and vertical velocities have a Gaussian distribution (see figure 15). The skewness ($\mu_3/\mu_2^{3/2}$) and the kurtosis (μ_4/μ_2^2) have been computed for each velocity distribution (with μ_n the nth central moment). The average values over all these experiments for both of these moments are

$$\frac{\mu_3}{\mu_2^{3/2}}(V_x) = -0.12, \quad \frac{\mu_4}{\mu_2^2}(V_x) = 3.00, \quad \frac{\mu_3}{\mu_2^{3/2}}(V_y) = 0.08 \quad \text{and} \quad \frac{\mu_4}{\mu_2^2}(V_y) = 3.17. \tag{B1a–d}$$

In figure 16 the skewness and the kurtosis for each velocity PDF is shown against the mean streamwise velocity U_∞. Since the skewness always falls between −0.5 and 0.5, the velocity distributions are considered symmetrical. The values of the flatness are also relatively close to 3, the value of the Gaussian distribution.

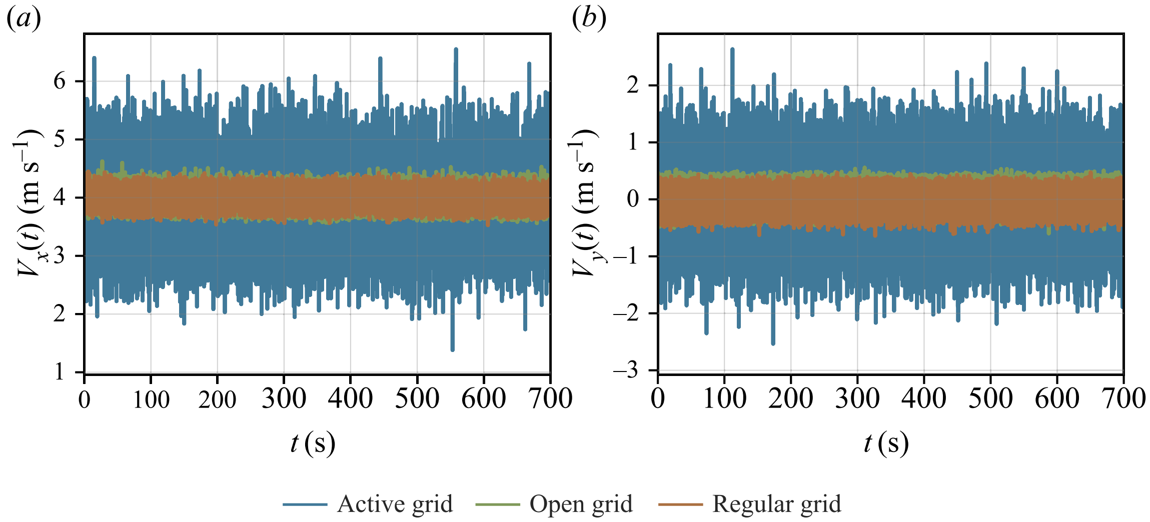

Figure 14. Temporal signals of the streamwise (*a*) and the vertical velocity (*b*). One example of temporal PDPA signal is shown for each of the three grids: AG in blue; OG in green; and RG in brown. The measurements were taken for a volume fraction of $\phi_v = 1.0 \times 10^{-5}$ and an inlet velocity $U_\infty \approx 4.0$ m s^{-1}.

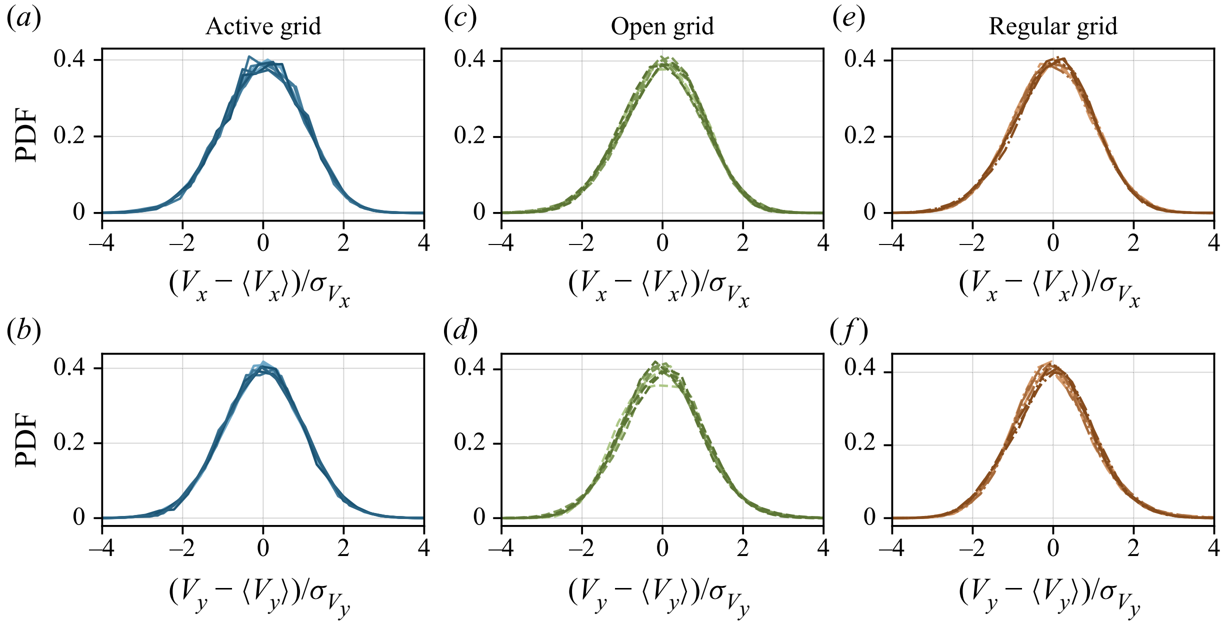

Figure 15. The PDF of the streamwise (*a*,*c*,*e*) and vertical (*b*,*d*,*f*) velocity for each type of grid: AG (*a*,*b*); OG (*c*,*d*); and RG (*e*,*f*).

Appendix C. Determination of the PDPA misalignment angle

A small deviation angle between the PDPA axes and the wind tunnel axes is always present even if the best precautions were taken during the set up of the device. The deviation angle has a negligible impact on the horizontal velocity but can induce a significant bias on the measurements of the settling velocity, since the particle's horizontal velocity component is much larger than the vertical one.

We call β the angle between the axes of the PDPA and the axes of the wind tunnel. Here V_{XPDPA} and V_{YPDPA} are, respectively, the streamwise and vertical components of the velocity measured by the instrument while V_{XWT} and V_{YWT} are the exact particle velocity components in the wind tunnel coordinate system (see Mora *et al.* 2021).

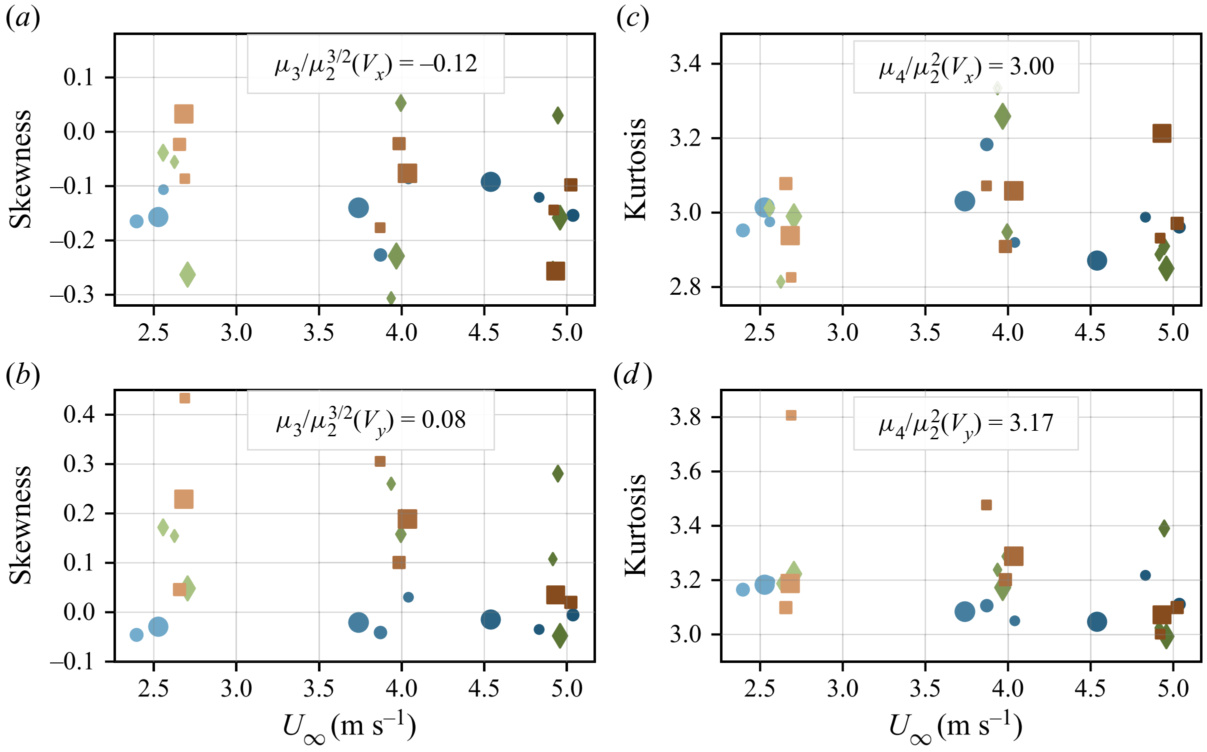

	Grid	U_∞ (m s^{-1})	$10^5\phi_v$		Grid	U_∞ (m s^{-1})	$10^5\phi_v$		Grid	U_∞ (m s^{-1})	$10^5\phi_v$
●	AG	2.56	0.58	◆	OG	2.63	0.56	■	RG	2.69	0.55
●	AG	2.40	1.24	◆	OG	2.56	1.16	■	RG	2.66	1.12
●	AG	2.53	2.23	◆	OG	2.70	2.08	■	RG	2.68	2.10
●	AG	4.04	0.59	◆	OG	3.94	0.60	■	RG	3.87	0.61
●	AG	3.87	1.15	◆	OG	3.99	1.11	■	RG	3.98	1.12
●	AG	3.74	2.30	◆	OG	3.97	2.17	■	RG	4.03	2.13
●	AG	4.83	0.61	◆	OG	4.91	0.60	■	RG	4.92	0.60
●	AG	5.04	1.06	◆	OG	4.95	1.14	■	RG	5.02	1.12
●	AG	4.54	2.22	◆	OG	4.96	2.03	■	RG	4.93	2.04

Figure 16. Skewness (*a*,*b*) and kurtosis (*c*,*d*) of the velocity PDF against the mean streamwise velocity U_∞. Panels (*a*,*c*) show the moments for the horizontal velocity whereas (*b*,*d*) correspond to the vertical velocity. The different symbols (■), (●) and (◆) represent the RG, AG and OG, respectively. The size of the symbol is proportional to the volume fraction and darker colours correspond to higher mean velocities. The quantity given in each panel is the mean value over all the conditions.

By projecting the accurate droplet velocity in the frame of reference of the PDPA we get

$$\overrightarrow{V_{YWT}} = \left(\underbrace{V_{YPDPA}\cos(\beta)}_{\approx V_{YPDPA}} - V_{XPDPA}\sin(\beta)\right)\overrightarrow{y}. \tag{C1}$$

Since the PDPA was set in non-coincident mode, we do not have access to the horizontal component V_{XPDPA} corresponding to the biased settling velocity. We then approximate by using the mean of the time series horizontal velocity $V_{XPDPA} \approx \langle U\rangle$ and define the angle-corrected velocity as follows:

$$V_{YWT} = V_{YPDPA} - \underbrace{\langle U\rangle \sin(\beta)}_{V_\beta}. \tag{C2}$$

In order to compute the vertical velocity due to the horizontal component projection V_β, we estimated the misalignment angle β through measurements of olive oil droplets settling velocities. We used olive oil to be closer to the limit of very small diameter and

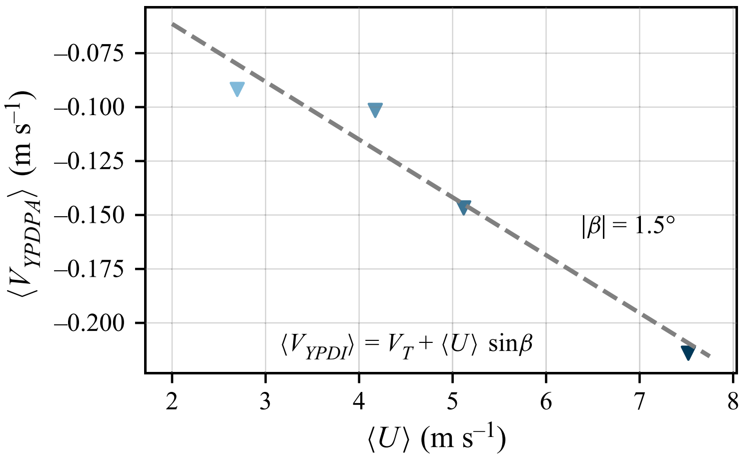

Figure 17. Here $\langle V_{YPDI}\rangle$ against $\langle U\rangle$ for the different incoming velocities with olive oil droplets measurements. A linear fit of the data is shown in dashed line.

very small volume fraction ϕ_v. Indeed, olive oil droplets have a much smaller average diameter, $\langle d_p\rangle \approx 3\ \mu\text{m}$, and a less polydispersed size distribution than water droplets.

The settling velocity of olive oil droplets were collected for different free stream velocities in the absence of a grid in order to have a flow as laminar as possible. Measurements were taken when the probe volume was situated on the centre, close to the wall of the wind tunnel and each time the PDPA had to be realigned. The particle speed in a still fluid is computed from the particle relaxation time τ_p including the nonlinear drag from the Schiller–Naumann semiempirical equation (Clift *et al.* 1978):

$$V_T = \tau_p g \quad \text{with } \tau_p = \frac{\rho_p d_p^2}{18\mu_f(1 + 0.15 Re_p^{0.687})}, \tag{C3}$$

where μ_f is the air dynamic viscosity, g the gravitational acceleration, d_p the particles' diameter, the oil droplet density $\rho_p = 900\ \text{kg m}^{-3}$ and $Re_p = V_T d_p/\nu$ the particle Reynolds number. As the diameter of olive oil droplets is extremely small the actual velocity is supposed to be equal to the Stokes velocity $V_{YWT} = V_T$. We then get from (C2) that

$$\langle V_{YPDPA}\rangle = V_T + \langle U\rangle \sin(\beta). \tag{C4}$$

With several free stream velocities and (C4) a least-squares polynomial fit on the values of $\langle V_{YPDPA}\rangle$ and $\langle U\rangle$ can be performed to estimate $\sin(\beta)$. Figure 17 shows $\langle V_{YPDPA}\rangle$ against $\langle U\rangle$ for the probe volume on the centre where a linear fit was done and the slope gives the value of $\sin(\beta)$. In our case, β is found equal to $\beta = 1.5° \pm 0.3°$.

REFERENCES

AKUTINA, Y., REVIL-BAUDARD, T., CHAUCHAT, J. & EIFF, O. 2020 Experimental evidence of settling retardation in a turbulence column. *Phys. Rev. Fluids* **5** (1), 14303.

ALIPCHENKOV, V.M. & ZAICHIK, L.I. 2009 Effect of particle clustering on the gravitational settling velocity in homogeneous turbulence. *Fluid Dyn.* **44** (3), 397–404.

ALISEDA, A., CARTELLIER, A., HAINAUX, F. & LASHERAS, J.C. 2002 Effect of preferential concentration on the settling velocity of heavy particles in homogeneous isotropic turbulence. *J. Fluid Mech.* **468**, 77–105.

ALISEDA, A. & LASHERAS, J.C. 2006 Effect of buoyancy on the dynamics of a turbulent boundary layer laden with microbubbles. *J. Fluid Mech.* **559**, 307–334.

ALISEDA, A. & LASHERAS, J.C. 2011 Preferential concentration and rise velocity reduction of bubbles immersed in a homogeneous and isotropic turbulent flow. *Phys. Fluids* **23** (9), 093301.

Bachalo, W.D. & Houser, M.J. 1984 Phase/doppler spray analyzer for simultaneous measurements of drop size and velocity distributions. *Opt. Engng* **23** (5), 583–590.

Bec, J., Homann, H. & Ray, S.S. 2014 Gravity-driven enhancement of heavy particle clustering in turbulent flow. *Phys. Rev. Lett.* **112** (18), 1–5.

Chen, L., Goto, S. & Vassilicos, J.C. 2006 Turbulent clustering of stagnation points and inertial particles. *J. Fluid Mech.* **553**, 143–154.

Chen, X., Liu, Z., Chen, Y. & Wang, H. 2020 Analytical expression for predicting the reduced settling velocity of small particles in turbulence. *Environ. Fluid Mech.* **20** (4), 905–922.

Clift, R., Grace, J.R. & Weber, M.E. 1978 *Bubbles, Drops, and Particles*, vol. 11. Academic.

Coleman, S.W. & Vassilicos, J.C. 2009 A unified sweep-stick mechanism to explain particle clustering in two- and three-dimensional homogeneous, isotropic turbulence. *Phys. Fluids* **21** (11), 1–10.

Crowe, C.T., Troutt, T.R. & Chung, J.N. 1996 Numerical models for two-phase turbulent flows. *Annu. Rev. Fluid Mech.* **28** (1), 11–43.

De Souza, D., Zürner, T. & Monchaux, R. 2021 Simple distinction of similar-looking inertial particles and fluid tracers on camera images. *Exp. Fluids* **62** (5), 1–14.

Falkinhoff, F., Obligado, M., Bourgoin, M. & Mininni, P.D. 2020 Preferential concentration of free-falling heavy particles in turbulence. *Phys. Rev. Lett.* **125** (6), 1–8.

Ghosh, S., Davila, J., Hunt, J.C.R., Srdic, A., Fernando, H.J.S. & Jonas, P.R. 2005 How turbulence enhances coalescence of settling particles with applications to rain in clouds. *Proc. R. Soc.* A*: Math. Phys. Engng Sci.* **461** (2062), 3059–3088.

Good, G.H., Gerashchenko, S. & Warhaft, Z. 2012 Intermittency and inertial particle entrainment at a turbulent interface: the effect of the large-scale eddies. *J. Fluid Mech.* **694**, 371–398.

Good, G.H., Ireland, P.J., Bewley, G.P., Bodenschatz, E., Collins, L.R. & Warhaft, Z. 2014 Settling regimes of inertial particles in isotropic turbulence. *J. Fluid Mech.* **759**, R3.

Goto, S. & Vassilicos, J.C. 2008 Sweep-stick mechanism of heavy particle clustering in fluid turbulence. *Phys. Rev. Lett.* **100** (5), 1–4.

Gustavsson, K., Vajedi, S. & Mehlig, B. 2014 Clustering of particles falling in a turbulent flow. *Phys. Rev. Lett.* **112** (21), 1–5.

Huck, P.D., Bateson, C., Volk, R., Cartellier, A., Bourgoin, M. & Aliseda, A. 2018 The role of collective effects on settling velocity enhancement for inertial particles in turbulence. *J. Fluid Mech.* **846**, 1059–1075.

Johansson, A.V. 1991 *Proceedings of the Third European Turbulence Conference*. Springer Science & Business Media.

Li, C., Lim, K., Berk, T., Abraham, A., Heisel, M., Guala, M., Coletti, F. & Hong, J. 2021 Settling and clustering of snow particles in atmospheric turbulence. *J. Fluid Mech.* **912**, 1–24.

Maxey, M.R. 1987 The gravitational settling of aerosol particles in homogeneous turbulence and random flow fields. *J. Fluid Mech.* **174**, 441–465.

Mazellier, N. & Vassilicos, J.C. 2008 The turbulence dissipation constant is not universal because of its universal dependence on large-scale flow topology. *Phys. Fluids* **20** (1), 015101.

Monchaux, R., Bourgoin, M. & Cartellier, A. 2010 Preferential concentration of heavy particles: a Voronoï analysis. *Phys. Fluids* **22** (10), 103304.

Monchaux, R., Bourgoin, M. & Cartellier, A. 2012 Analyzing preferential concentration and clustering of inertial particles in turbulence. *Intl J. Multiphase Flow* **40** (June 2020), 1–18.

Monchaux, R. & Dejoan, A. 2017 Settling velocity and preferential concentration of heavy particles under two-way coupling effects in homogeneous turbulence. *Phys. Rev. Fluids* **2** (10), 1–16.

Mora, D.O. 2020 Clustering and settling dynamics of inertial particles under turbulence. PhD thesis, Université Grenoble Alpes.

Mora, D.O., Aliseda, A., Cartellier, A. & Obligado, M. 2019*a* Pitfalls measuring 1D inertial particle clustering. In *Progress in Turbulence VIII: Proceedings of the iTi Conference in Turbulence 2018*, pp. 221–226. Springer.

Mora, D.O., Muñiz Pladellorens, E., Riera Turró, P., Lagauzere, M. & Obligado, M. 2019*b* Energy cascades in active-grid-generated turbulent flows. *Phys. Rev. Fluids* **4** (10), 104601.

Mora, D.O. & Obligado, M. 2020 Estimating the integral length scale on turbulent flows from the zero crossings of the longitudinal velocity fluctuation. *Exp. Fluids* **61** (9), 1–10.

Mora, D.O., Obligado, M., Aliseda, A. & Cartellier, A. 2021 Effect of $Re\lambda$ and Rouse numbers on the settling of inertial droplets in homogeneous isotropic turbulence. *Phys. Rev. Fluids* **6** (4), 1–19.

Mydlarski, L. 2017 A turbulent quarter century of active grids: from Makita (1991) to the present. *Fluid Dyn. Res.* **49** (6), 061401.

Nielsen, P. 1993 Turbulence effects on the settling of suspended particles. *J. Sedim. Res.* **63** (5), 835–838.

Obligado, M., Brun, C., Silvestrini, J.H. & Schettini, E.B.C. 2022 Dissipation scalings in the turbulent boundary layer at moderate $Re\theta$. *Flow Turbul. Combust.* **108** (1), 105–122.

Obligado, M., Cartellier, A., Aliseda, A., Calmant, T. & De Palma, N. 2020 Study on preferential concentration of inertial particles in homogeneous isotropic turbulence via big-data techniques. *Phys. Rev. Fluids* **5** (2), 024303.

Obligado, M., Missaoui, M., Monchaux, R., Cartellier, A. & Bourgoin, M. 2011 Reynolds number influence on preferential concentration of heavy particles in turbulent flows. *J. Phys.: Conf. Ser.* **318**, 052015.

Obligado, M., Teitelbaum, T., Cartellier, A., Mininni, P. & Bourgoin, M. 2014 Preferential concentration of heavy particles in turbulence. *J. Turbul.* **15** (5), 293–310.

Petersen, A.J., Baker, L. & Coletti, F. 2019 Experimental study of inertial particles clustering and settling in homogeneous turbulence. *J. Fluid Mech.* **864**, 925–970.

Poelma, C., Westerweel, J. & Ooms, G. 2007 Particle-fluid interactions in grid-generated turbulence. *J. Fluid Mech.* **589**, 315–351.

Puga, A.J. & Larue, J.C. 2017 Normalized dissipation rate in a moderate Taylor Reynolds number flow. *J. Fluid Mech.* **818**, 184–204.

Pujara, N., Du Clos, K.T., Ayres, S., Variano, E.A. & Karp-Boss, L. 2021 Measurements of trajectories and spatial distributions of diatoms (Coscinodiscus spp.) at dissipation scales of turbulence. *Exp. Fluids* **62** (7), 1–15.

Rosa, B., Parishani, H., Ayala, O. & Wang, L.P. 2016 Settling velocity of small inertial particles in homogeneous isotropic turbulence from high-resolution DNS. *Intl J. Multiphase Flow* **83**, 217–231.

Shaw, R.A. 2003 Particle-turbulence interactions in atmospheric clouds. *Annu. Rev. Fluid Mech.* **35**, 183–227.

Squires, K.D. & Eaton, J.K. 1991 Preferential concentration of particles by turbulence. *Phys. Fluids* A*: Fluid Dyn.* **3**, 1169–1178.

Sumbekova, S. 2016 Clustering of inertial sub-Kolmogorov particles: structure of clusters and their dynamics. PhD thesis, Université Grenoble Alpes.

Sumbekova, S., Aliseda, A., Cartellier, A. & Bourgoin, M. 2016 Clustering and settling of inertial particles in turbulence. *Springer Proc. Phys.* **185**, 475–482.

Sumbekova, S., Cartellier, A., Aliseda, A. & Bourgoin, M. 2017 Preferential concentration of inertial sub-Kolmogorov particles: the roles of mass loading of particles, Stokes numbers, and Reynolds numbers. *Phys. Rev. Fluids* **2** (2), 1–19.

Tom, J. & Bragg, A.D. 2019 Multiscale preferential sweeping of particles settling in turbulence. *J. Fluid Mech.* **871**, 244–270.

Tom, J., Carbone, M. & Bragg, A.D. 2022 How does two-way coupling modify particle settling and the role of multiscale preferential sweeping? *J. Fluid Mech.* **947**, 1–33.

Wang, Y., Lam, K.M. & Lu, Y. 2018 Settling velocity of fine heavy particles in turbulent open channel flow. *Phys. Fluids* **30** (9), 095106.

Wang, L.-P. & Maxey, M.R. 1993 Settling velocity and concentration distribution of heavy particles in homogeneous isotropic turbulence. *J. Fluid Mech.* **256**, 27–68.

Yang, C.Y. & Lei, U. 1998 The role of the turbulent scales in the settling velocity of heavy particles in homogeneous isotropic turbulence. *J. Fluid Mech.* **371**, 179–205.

Yang, T.S. & Shy, S.S. 2003 The settling velocity of heavy particles in an aqueous near-isotropic turbulence. *Phys. Fluids* **15** (4), 868–880.

Yang, T.-S. & Shy, S. 2021 The preferential accumulation and the settling velocity of small heavy particles in Taylor–Couette flows. *J. Mech.* **37**, 651–658.

Zhou, Q. & Cheng, N.S. 2009 Experimental investigation of single particle settling in turbulence generated by oscillating grid. *Chem. Engng J.* **149** (1–3), 289–300.

5

Inertial particles in a turbulent/non-turbulent interface

In Seattle, we transitioned from the ideal case of homogeneous isotropic turbulence to a more complex flow including a turbulent interface. This chapter presents a part of the experimental work conducted with the wind tunnel at the University of Washington included in the following article under preparation:

Ferran, A., Obligado, M. & Aliseda, A. Inertial particles in a turbulent/turbulent interface. To be submitted to the International Journal of Multiphase Flows.

As mentioned in chapter 1, while numerous studies have focused on the homogeneous case, fewer experiments have investigated particle motion when the background flow is intentionally anisotropic. This work aims at feeding this gap, by proposing an experimental study on the entrainment of particles initially situated in a turbulent flow and subsequently mixed within an unladen less turbulent co-flow. Understanding the motion of inertial particles in such configurations could be relevant for cloud modeling. Indeed, the temporal and spatial distribution of cloud droplets play a role in many processes, including collision-coalescence mechanisms, condensation growth of droplets, or cloud radiative properties (Vaillancourt and Yau 2000).

The present work builds upon the study by Good, Gerashchenko, and Warhaft 2012, which has previously investigated the motion of inertial particles in a shearless turbulent/non-turbulent interface using wind tunnel experiments. Here, we developed a method to create a turbulent interface separating two flow regions with distinct properties, including different turbulent intensities, mean velocities and large-scale structures. The highly turbulent region was seeded with inertial particles, and we observed how they were transported transversely into the initially unladen less turbulent fluid. Particle velocities were measured by means of Phase Doppler Interferometry at different locations across the interface.

The results from this chapter validate the previously observed trend that, within the mixing layer, regions of high local flow fluctuations are oversampled with inertial particles. This suggests the advection of inertial particles into the unladen region by large-scale intermittent turbulent bursts. As a result, particle velocities progressively deviate from a Gaussian distribution as we transition from the homogeneous fully developed turbulent region toward the low-turbulence zone. Furthermore, enhancement of particle clustering and settling velocity were also observed in the mixing region. However, it remains uncertain whether this particle settling enhancement originates from the local flow properties or the enhanced particle clustering.

Inertial particles in a turbulent/turbulent interface

Amélie Ferran[a,b], Martín Obligado[a], Alberto Aliseda[b]

[a] *LEGI, Université Grenoble Alpes, Grenoble, F-38000, France*
[b] *Department of Mechanical Engineering, University of Washington, Seattle, 98195-2600, WA, USA*

Abstract

Turbulent interfaces are ubiquitous in the nature and in many important canonical flows (wakes, jets, mixing layers, boundary layers). In nature, the sharp edges of atmospheric clouds are defined by a turbulent interface, where the droplet-laden turbulent cloud interior mixes with the unladen outer air. This study presents statistics of sub-Kolmogorov-scale inertial particles, such as cloud droplets, in a sheared turbulent-turbulent interface. We focus mainly on the effect of the inhomogeneous turbulent field on the particles' clustering properties and settling velocity modification. Wind tunnel experiments were carried out using a passive grid containing 81 independent gas/liquid sprays to generate turbulence and introduce water droplets. These atomizers, at the entrance of the test section, contribute significantly to the carrier phase turbulence and sheared velocity profile. Selecting the atomizer injection profile enables us to control the gradient of turbulent intensity through the tunnel cross-sectional area. The carrier flow results in a hybrid mixing layer, presenting a gradient of mean velocity and separating two regions with different turbulent scales. Particles' velocities and diameter were recorded at several positions across the turbulent interface with a Phase Doppler Particle Analyser (PDPA). Confirming previous studies on the topic (Good et al., 2012), particles are shown to be transported from the turbulent side to the low turbulent side by large scale energetic eddies. Our results show an enhancement of particle preferential concentration and settling velocity in the mixing region.

Keywords: inertial particles, turbulence, turbulent interface, experiments

---

1. Introduction

Particle-laden turbulence is a topic that has received great attention from the scientific community over the last decades due to its ubiquity in various environmental and industrial systems, including sediments in rivers, microplastics in the oceans, aerosols and pollutants in the atmosphere, industrial sprays, and more. Interestingly, most of the pioneering work on the influence of turbulent structures over a particle concentration field has been conducted with free shear flows (Crowe et al., 1988; Eaton and Fessler, 1994), such as shear mixing layers (Kamalu et al., 1988; Lázaro and Lasheras, 1989, 1992), wakes, jets (Chung and Troutt, 1988; Longmire and Eaton, 1992) and boundary layers. However, over the last three decades, the main advancements in the study of particle-turbulence interactions have been conducted in the ideal case of three-dimensional homogeneous isotropic turbulence due to its analytical simplicity. A significant amount of studies has been carried out within this simplified framework, giving valuable insights into various aspects of inertial particles behavior in turbulence, such as their clustering properties (Squires and Eaton, 1991; Wang and Maxey, 1993; Aliseda et al., 2002; Monchaux et al., 2012; Obligado et al., 2014; Sumbekova et al., 2017; Baker et al., 2017; Petersen et al., 2019; Mora et al., 2023), the modification of their settling velocity by turbulence (Maxey, 1987; Nielsen, 1993; Aliseda et al., 2002; Good et al., 2014; Bec et al., 2014; Rosa et al., 2016; Huck et al., 2018; Tom and Bragg, 2019; Mora et al., 2021b; Ferran et al., 2023), their impact on the turbulence (Gore and Crowe, 1991; Elghobashi, 1994; Hassaini and Coletti, 2022), or their acceleration statistics (Bec et al., 2006).

Although most of the available data and theoretical advances have been obtained in the ideal case of homogeneous and isotropic turbulence, turbulent motions encountered in nature are usually more complicated. From the aerodynamics of rigid structures, such as aircrafts and vehicles, the impact zone of a plunging jet, the thermocline in the ocean to the sharp edges of atmospheric clouds, most turbulent flows are bounded by a fluid at a different turbulent state. All these flows present an interface layer (turbulent/non-turbulent or turbulent/turbulent interface), separating flow regions of different turbulent intensities or a turbulent flow with an irrotational flow (da Silva et al., 2014). Many canonical flows that are frequently studied exhibit such interfacial layers, it is the case for jets, wakes, mixing layers and boundary layers.

In the natural environment, these interfacial layers are frequently loaded with inertial particles, such as in the case of cloud boundaries. While the adiabatic core of cumulus clouds can be assimilated to three-dimensional homogeneous turbulence (Vaillancourt and Yau, 2000), the fluid motions at cloud edges are known to present anisotropic characteristics (Bhat and Narasimha, 1996). The role of small-scale turbulence in cumulus clouds plays an important part in determining their macroscopic properties such as their lifetime, expansion, precipitation efficiency, and optical properties (Shaw, 2003). Moreover, the entrainment of dry air at their edges has been shown to be of significant importance for their overall development (Blyth, 1993).

The mechanisms impacting the distribution of particles are similar in many flows, but the definition of an appropriate timescale controlling the phenomena may vary from one flow to another (Eaton and Fessler, 1994). In homogeneous and isotropic turbulence, the most relevant timescale governing the particles dynamics is associated with the smallest turbulent eddies, known as the Kolmogorov timescale τ_η. Indeed, particles interact most with turbulence when their relaxation time τ_p is of the same order of magnitude as the Kolmogorov timescale. The phenomena of particle preferential concentration and settling velocity modification have been observed to be more pronounced when the Stokes number, defined as the ratio between the particle and fluid timescales, $St = \tau_p/\tau_\eta$, is approximately one. However, it may vary in the case of anisotropic turbulent flows, as many of them are dominated by large-scale quasi two-dimensional coherent structures, such as mixing layers, wakes, and jets. In such flows, a relevant timescale for studying particle motion is based on the characteristics of these large coherent vortices (Crowe et al., 1988; Eaton and Fessler, 1994). The complexity of the particle-turbulence interaction problem increases when the background flow involves a mixing region between two turbulent flows featuring different large-scale sizes.

Although there is a multitude of studies on the dispersion of inertial particles in free shear flows and in homogeneous isotropic turbulence, fewer experimental works have focused on the entrainment of particles by a turbulent/turbulent front (Gerashchenko et al., 2011; Good et al., 2012; Gerashchenko and Warhaft, 2013). We aim to build upon the previous studies of Good et al. (2012) by examining the entrainment of water droplets across a sheared turbulent/turbulent interface. In the present study, the background stream consists of two co-flows featuring different properties: a region of high turbulence moving alongside a less turbulent, slower fluid. The droplets are only injected into the high-turbulence side, mimicking processes relevant to cloud dynamics, where the particle-laden cloud interior exhibits greater turbulent fluctuations than the adjacent dry air flow. Several fundamental questions remained to be investigated regarding the dynamics of inertial particles in such flows. In particular, we aim to examine the mechanisms responsible for the entrainment of inertial particles on the low-turbulence side. The determination of the most relevant turbulent scale governing the entrainment process is also of great interest. Finally, we are interested in how the turbulent front may impact the particles' clustering properties and settling velocities.

The outline of the present paper is as follows. In section 2, we describe the experimental apparatus and the different experimental techniques used. Section 3 is dedicated to the characterisation of the carrier phase and the turbulent/turbulent interface. The main findings on particle statistics, which encompass particle probability densities, conditional statistics based on the underlying flow properties, particle clustering properties, and settling velocities, are presented in Section 4. Finally, the main conclusions are summarized in section 5.

2. Experimental setup

2.1. The experimental facility

Experiments were conducted in the wind tunnel of the Department of Mechanical Engineering at the University of Washington, Seattle. This wind tunnel has previously been characterised and used in former experimental studies of turbulent multiphase flow (Bateson and Aliseda, 2012; Huck et al., 2018). It is an open-loop wind tunnel with a 4.0m long test section and a 1.0m × 1.0m constant cross-sectional area. The test section walls are made of acrylic panels, allowing for full optical access. The free-stream velocity is generated using a rack of 25 PC fans. A sketch of the experimental facility can be found in figure 1(a).

Before entering the test section, the airflow passes over a passive grid formed by 9×9 aluminium tubes, forming a square mesh with a mesh size M of 10 cm. This passive grid serves two purposes: it generates homogeneous and isotropic turbulence in the test section and it supports the water droplet injection system. For the injection of droplets, 81 atomizers are positioned at each intersection between a horizontal and a vertical grid bar. Each injector consists of an air jet impacting with a water jet at a significant angle, resulting in the liquid atomization and the formation of a dense spray of micrometer-sized droplets. The injectors water and air supply lines are placed inside the tubing of the passive grid axes. Droplet size distribution and volume fraction -which is the ratio between the liquid and air volumetric flow rate- can be controlled by varying the water and air flow rate independently.

2.2. Generation of the turbulent interface

The air jets from the atomizers generate a significant momentum to the main airflow, contributing significantly to the mean velocity and background turbulence intensity. There is the option to independently activate the water and air supply for each droplet injector. Given the substantial contribution of the atomizers to the degree of turbulence, it is possible to create a gradient of turbulent intensity by deactivating a portion of them. In this study, we aimed to create a vertical turbulent/turbulent interface, aligned with gravity and the streamwise direction by deactivating two columns of atomizers. The schematic in Figure 1(b) illustrates the interface generation from a top view of the tunnel. Water droplets were injected only on the side of the activated atomizers, and our interest is on understanding how they are entrained to the other side of the interface. Downstream of the activated jets, the flow is particle-laden and more turbulent than the slower unladen adjacent co-flow. Due to the momentum generated by the atomizers, the

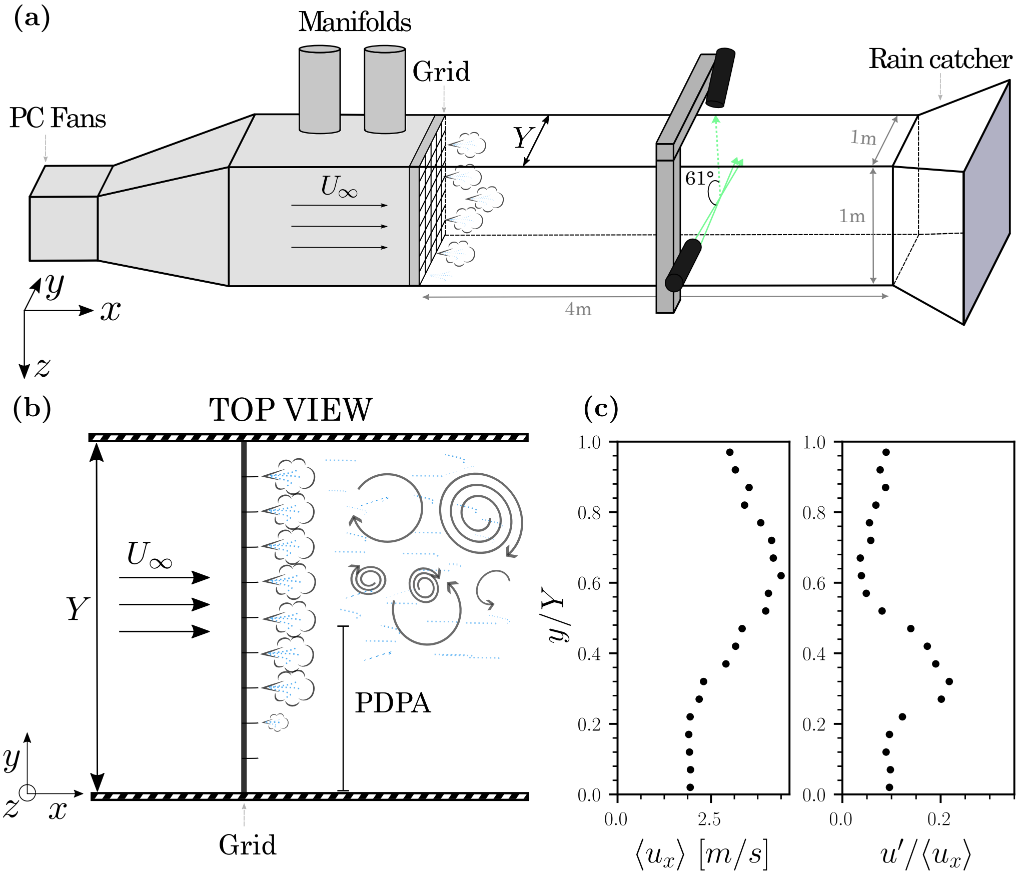

Figure 1: (a) Sketch of the wind tunnel experimental facility. (b) Top view of the wind tunnel with a representation of the 9 atomizers columns and the interface generation. Two columns of atomizers were disabled, for $y/Y < 0.25$, to create the interface. (c) Characterisation of the interface with Pitot tube measurements, with the mean velocity profile $\langle U \rangle$ and the turbulent intensity profile $u_{rms}/\langle U \rangle$ along the spanwise direction y.

mixing layer between the two flows is sheared, exhibiting a gradient in both mean velocity and turbulent fluctuations.

Characterisation of the interface was carried out with Pitot tube measurements to determine the mean flow velocity and standard deviation. Profiles of the mean velocity and turbulent intensity are displayed in figure 1(c). A distinct shear of mean velocity, and a peak of turbulent intensity are observed in the range of spanwise locations $y/Y \in [0.2, 0.6]$ from the wind tunnel wall, with $Y = 1.0$ m the wind tunnel width. It is within this range, transversely across the interface, that we recorded particle velocities, as explained in the following section.

For homogeneous and isotropic turbulence (HIT) working conditions, all 81 atomizers are turned on. With this HIT configuration, the operating water flow rate and air flow rate were set to 1.5 lpm and 900 lpm respectively. When the grid was configured to generate the interface, the operating water and air flow rate were lowered and set at 1.25 lpm and 800 lpm respectively, to compensate for the reduced number of injectors.

2.3. Experimental instruments

Single-phase turbulence statistics were measured via hot-wire anemometry (HWA), while a Phase Doppler Particle Analyzer (PDPA) was used to record droplet velocities in two-phase flow conditions. The measurement location was situated 200 cm downstream the grid, i.e. at $x = 20M$. For single-phase measurements, we sampled height different spanwise positions across the interface at this fixed streamwise coordinate. PDPA measurements were taken at roughly the same x coordinate, but only at four spanwise positions across the mixing layer due to the time-consuming sample collection and laser realignement. Due to experimental constraints, it was only possible to access half of the wind tunnel width with the PDPA. With both instruments, the statistics for the homogeneous and isotropic turbulence case were also recorded at the wind tunnel centerline for comparison.

The PDPA system, manufactured by TSI Incorporated, emits two pairs of laser beams: one green with a 515 nm wavelength and one blue with a wavelength of 488 nm. The PDPA transmitter was positioned facing the wind tunnel wall, while the receiver was positioned above the tunnel at a 61°angle from the beam direction (see the experimental setup schema in figure 1(a)). As the receiver looks into the wind tunnel with an angle, the light ray might refract as it passes through the top of the wind tunnel. To avoid this issue, two triangular acrylic prisms were attached to both sides of the test section's upper wall. A thin layer of glycerol, with a similar refractive index as acrylic, was also added between the acrylic prisms and the wall. The emitter had a focal length of 500 mm, allowing to measure approximately at the centerline of the test section, whereas the receiver's focal length was set to 750 mm. Both receiver and transmitter were attached to the same traverse system, facilitating their simultaneous movement in the spanwise direction without losing their alignment. The PDPA was oriented such that the particle's diameter and streamwise velocity were recorded simultaneously with the green beam, while the vertical velocity was recorded with the blue beam independently, in non-coincident mode.

For the single-phase measurements, a hot-wire was used with a AN-1005 anemometer system. Hot-wire calibration was conducted at the tunnel's centerline for each series of measurements, with the use of a Pitot tube.

3. Characterisation of the single-phase turbulent/turbulent interface

Single-phase velocity measurements were obtained by means of hot-wire anemometry for height different spanwise positions across the mixing layer, and for the homogeneous and isotropic turbulence configuration. Single-point turbulence statistics were computed from the resulting times series data. The one-dimensional energy spectra for the longitudinal velocity fluctuations $E_{11}(\kappa_1)$, displayed in Figure 2, were computed from the temporal series by applying Taylor's hypothesis of frozen turbulence. Here, the energy spectrum functions are normalised by the Kolmogorov length η and velocity scale u_η. We can notice from the figure that the dissipative range is not well-resolved, making it challenging to accurately estimate the mean energy dissipation rate through the integration of the dissipation spectra. Furthermore, the hot-wire statistics exhibit higher mean velocities when compared to the values obtained with the PDPA. This velocity difference between single-phase and two-phase conditions, although taken at similar air flow rates and wind tunnel settings, can be attributed to the momentum loss resulting from the particle injection and the hot-wire probe's incapacity to measure very low and negative velocities.

We then opted to employ the power spectral energy density computed from the particle velocity measurements acquired with the PDPA. Although power spectral analysis of LDV and PDPA data

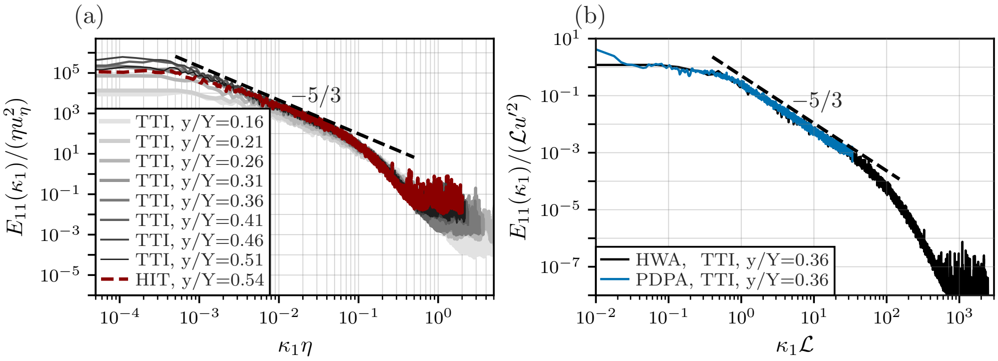

Figure 2: (a) Power spectral density function of the longitudinal velocity from hot-wire records normalized by the by the large scales, u' an $\mathcal{L}$. Different locations across the interface are presented with darker colours corresponding to the high-turbulence region, while lighter colours indicate the low-turbulence region. The homogeneous and isotropic turbulence case is also shown with a red dashed line. (b) Comparison between spectra obtained with particle velocities (blue) and fluid velocities (black), at $y/Y = 0.36$. In both panels, a Kolmogorov $-5/3$ power-law scaling is shown as a reference.

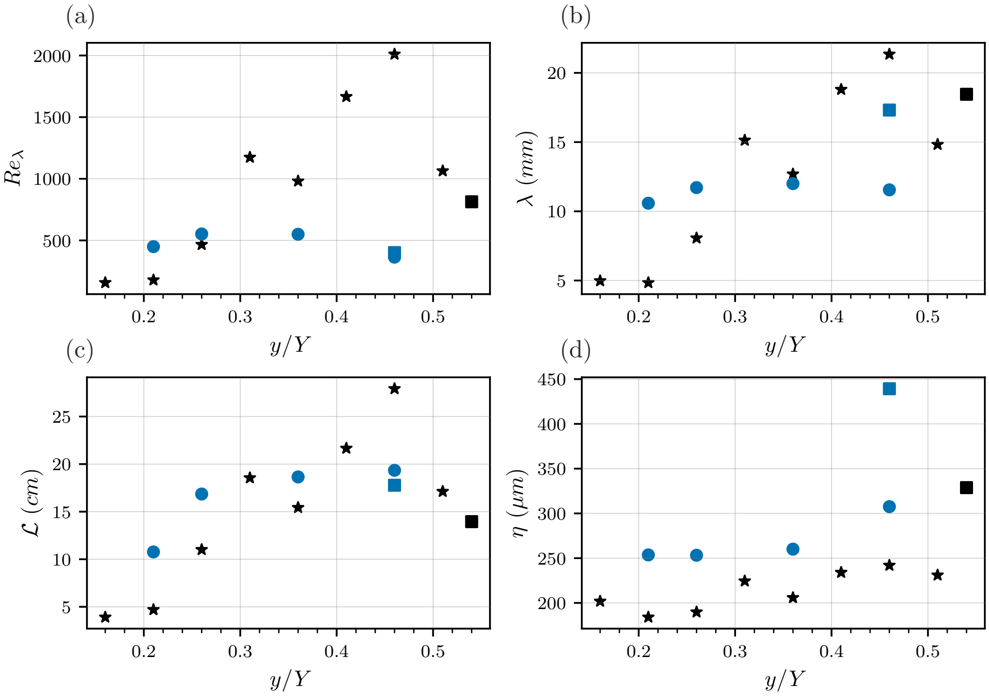

Figure 3: Turbulent statistics estimated with measurements of the carrier phase (black stars) and with particle velocities (blue circles) for different spanwise positions across the interface y: (a) Taylor scale-based Reynolds number Re_λ, (b) Kolmogorov length scale η, (c) Taylor microscale λ, and (d) the integral length scale from integration of the autocorrelation function. The homogeneous isotropic turbulence case is presented for both measurement techniques with square symbols.

has been performed previously (Adrian and Yao, 1987; Mora et al., 2019), it may present certain challenges. One difficulty is related to the random arrival times of particles in the measurement volume (Adrian and Yao, 1987). To conduct a relevant spectral analysis, a high number particle density is necessary, meaning measuring a maximum number of particles within one Taylor microscale. An opposite limitation implies that the simultaneous number of particles in the measurement volume is less than one, as only one valid Doppler burst can be detected at a given moment. Most studies overcome this issue of unevenly spaced samples by interpolating the particles' velocity. In this study, we performed an interpolation of the particles' velocity at a frequency matching the average data rate and employing a nearest-neighbor interpolation method.

An example of energy spectrum obtained with the particle velocity is displayed in figure 2, superimposed on the hot-wire spectrum recorded at the same location y/Y. Consistently with the spectra obtained from HW measurements, shown in figure 2(a), all the spectra computed from PDPA data exhibit Kolmogorov's theory power-law behavior, with an exponent equal to $-5/3$ in what is known as the inertial range. The presence of this power laws validates the possibility to determine the mean turbulent energy dissipation rate, ε, by using the inertial range of the PDPA spectrum and Kolmogorov's law of turbulence (Kolmogorov, 1941). In the inertial range, the one-dimensional longitudinal energy spectrum function is known to follow the form:

$$E_{11}(\kappa_1) = C_K \varepsilon^{2/3} \kappa_1^{-5/3} \tag{1}$$

with $C_K = 0.52$ being a universal constant, according to Sreenivasan (1995). This procedure leads to a rough estimation of ε, as this universal constant is truly constant only for turbulent flows following a canonical turbulent energy cascade. Indeed, the value of C_K has been shown to deviate from a constant in various flows that do not follow a Kolmogorov energy cascade (Vassilicos, 2015).

From the turbulent dissipation rate, we get an estimation of the Taylor microscale λ and the Kolmogorov length scale η, with $\lambda = \sqrt{15\nu u'^2/\varepsilon}$ and $\eta = (\nu^3/\varepsilon)^{1/4}$. The Taylor scale Reynolds number, shown in Figure 3(a) for different positions across the mixing layer, was calculated as $Re_\lambda = u'\lambda/\nu$. To determine the integral length scale $\mathcal{L}$, several methods were considered (Puga and Larue, 2017; Mora and Obligado, 2020). Ultimately, we opted for integrating the autocorrelation function $R_{uu}(\rho)$ up to the first value above which $R_{uu}(\rho)$ falls below e^{-1}, as suggested by Puga and Larue (2017). This method results in an underestimated value of $\mathcal{L}$, but it prevents the influence of large scale mixing effects to contaminate the value of this scale. The profiles of the Taylor microscale, the integral length scale and the Kolmogorov length scale are shown in panels (b), (c) and (d) of figure 3 respectively.

From the energy spectra, as seen in figure 2, we observe that the separation of turbulent scales is larger on the high-turbulence side compared to the low-turbulent region, leading to a more defined inertial range for increasing values of y/Y. We also observe that the energy contained in the large scales is more important on the turbulent side, as the plateau at low wavenumbers reaches higher values. However, as displayed in figure 2, it appears that the plateau at low wavenumbers exhibits a maximum value for locations at $y/Y = [0.41, 0.46]$. This is confirmed by the profiles of turbulent scales and Reynolds number in figure 3. The Taylor microscale, integral length scale and Reynolds number initially increase when moving into the mixing region from the fully turbulent side, until reaching a maximum value at some point within the layer. Then, as we move to smaller values of y/Y, the length scales and the Reynolds number are progressively decreasing.

4. Inertial particles in the turbulent interface

4.1. Distribution of particle velocities and diameter

In this section, we describe the droplets' velocity and size distribution. The left panel of figure 4 presents the particle streamwise velocity probability distribution functions for several recorded signals. Different measurement locations across the interface, $y/Y = [0.21, 0.26, 0.36, 0.46]$, are shown in solid blue lines. For this figure and the rest of the study, darker colours correspond to the high-turbulence side, while lighter colours represent the originally unladen airflow. The case of homogeneous isotropic turbulence, with every air/liquid atomizer enabled, is displayed in red dashed line.

Comparing the HIT case and the TTI case at the same recording location, approximately at the wind tunnel centreline at $y/Y = 0.46$, we can already observe the influence of the interface. The PDF of the homogeneous isotropic turbulent case resembles more closely to a Gaussian distribution. While in the presence of the interface, the distribution becomes skewed with an overabundance of low velocities. As we transition from the high-turbulence side to the low-turbulence region, the longitudinal velocity PDFs depart even more from a Gaussian distribution. Some PDFs even appear to exhibit bimodal characteristics, with two peaks. This can be attributed to the mixing of the two co-flows, each having different mean velocities.

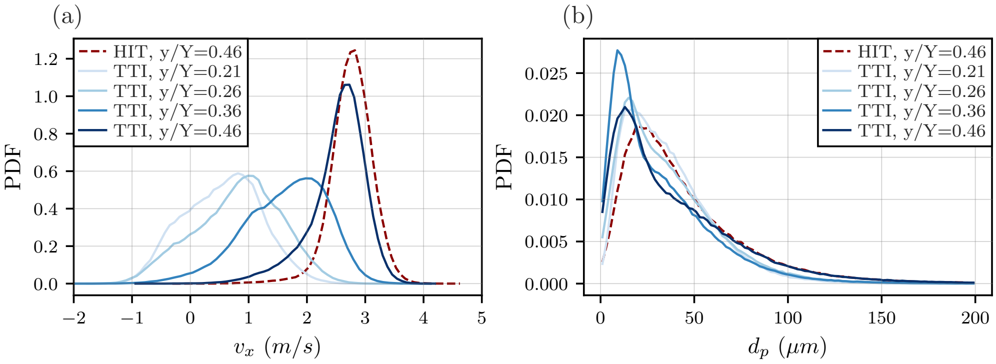

Figure 4: Probability distribution functions (PDF) of particle velocity and diameter recorded at various spanwise positions across the mixing layer. (a) The left panel shows the PDF of the particles' longitudinal velocity, and (b) presents the PDF of particle diameter, both measured using the PDPA. Solid blue lines are used to present the turbulent/turbulent interface case while the fully homogeneous and isotropic turbulent case is in a red dashed line. Different colours indicate the different positions across the interface with darker colours corresponding to the fully homogeneous turbulence region.

The probability distribution function of particle diameters, d_p, are displayed in figure 4(b) for the same five cases. The diameter distributions appear relatively consistent across the different background turbulence conditions. Nevertheless, there is an exception for the turbulent/turbulent interface case at $y/Y = 0.36$, where a smaller mean diameter is observed.

4.2. Conditional statistics of droplet velocities and number density

Studies on single-phase turbulent/non-turbulent interfaces or turbulence mixing layers have described the boundary between both regions to be a sharp and thin layer of fluid moving intermittently (Corrsin and Kistler, 1955; Veeravalli and Warhaft, 1989; Westerweel et al., 2009; da Silva et al., 2014). This implies that a probe situated stationary in the mixing region, will be swept over by successive sections of turbulent bursts and non-turbulent fluid. Furthermore, most experimental studies focusing on particle-laden anisotropic turbulence have reported that the transport of particles is governed by large-scale energetic eddies (Crowe et al., 1988; Eaton and Fessler, 1994; Gerashchenko et al., 2011; Good et al., 2012; Gerashchenko and Warhaft, 2013). Good et al. (2012) found that the entrainment of particles from the fully developed turbulent part to the mixing layer is intermittent, with inertial particles being carried by large-scale bursts.

Similar to the approach in the study by Gerashchenko and Warhaft (2013), we aim at presenting particle statistics conditioned on whether a particle belongs to a burst or not. To condition the particles on their underlying flow properties, we employ a detection criteria, based on the streamwise velocity signal. This typically involves the definition of an intermittency factor, denoted as γ, which is defined as the relative time spent by the probe in turbulent bursts compared to the background fluid, at a fixed transversal position. An intermittency factor γ was first introduced by Townsend (1947) to determine the fractional duration of a signal in fully developed turbulence, and has since been extensively used to detect turbulent intermittency in various flows, including turbulent front in jets, turbulent/non-turbulent interfaces, wakes and turbulent boundary layers (Corrsin and Kistler, 1955; Bisset et al., 2002; Gerashchenko and Warhaft, 2013).

To discriminate between the ”bursty” regions of the flow and the calmer background fluid, we employed a detection criteria based on a variable interval time-averaging (VITA) technique, following the approach described in Blackwelder and Kaplan (1976). Averaging the streamwise velocity, v_x, over extended time periods leads to a loss of information regarding the intermittent nature of these structures, while averaging over shorter time intervals can give insights into the local mean velocity and turbulent fluctuations. A time window T needs to be defined for averaging the longitudinal velocity, and it should be a time scale relevant to the phenomena under study. In our case, we selected a time interval equal to the integral time scale in homogeneous and isotropic conditions. It is calculated as $T = \tau_{\mathcal{L}} = \mathcal{L}/u' \approx 0.5\ m/s$, with u' the root mean of the longitudinal velocity fluctuations, and $\mathcal{L}$ estimated as described in section 3. The local mean velocity, $\widehat{v_x}(t)$, is then defined as,

$$\widehat{v_x}(t) = \frac{1}{\tau_{\mathcal{L}}} \int_{t-\frac{1}{2}\tau_{\mathcal{L}}}^{t+\frac{1}{2}\tau_{\mathcal{L}}} v_x(t')\mathrm{d}t' \tag{2}$$

This averaging method can also be viewed as a low-pass filter with a cutoff frequency equal to $1/\tau_{\mathcal{L}}$. It’s worth noting that, due to the random arrival of particles in the measurement volume, the window averaging is performed on a variable number of samples. Within the same time window, we also defined a local variance, denoted as $\widehat{var}$. It should also be noted that the primary goal of the present analysis is not to determine the precise location of the interface but rather to establish a correlation between regions of high-velocity fluctuations and particle behavior.

Figure 5 presents the local mean velocity (left panel) and variance (right panel) calculated using equation 2. In panel (a), we can see that the local average velocity present spikes, particularly in the temporal signals recorded around the midpoint of the mixing layer, i.e. at $y/Y = 0.36$. These extreme events, frequently associated to low velocities, are present in the local variance temporal signals, shown in panel (b). Indeed, frequent peaks of the local variance are revealed for the various locations across the mixing layer, $y/Y \in [0.26 - 0.46]$. In contrast, the homogeneous isotropic turbulence case and the velocities recorded in the low-speed, low-turbulence region exhibit significantly less extreme values of the local variance.

Following the work of Blackwelder and Kaplan (1976), the threshold for the detection criteria

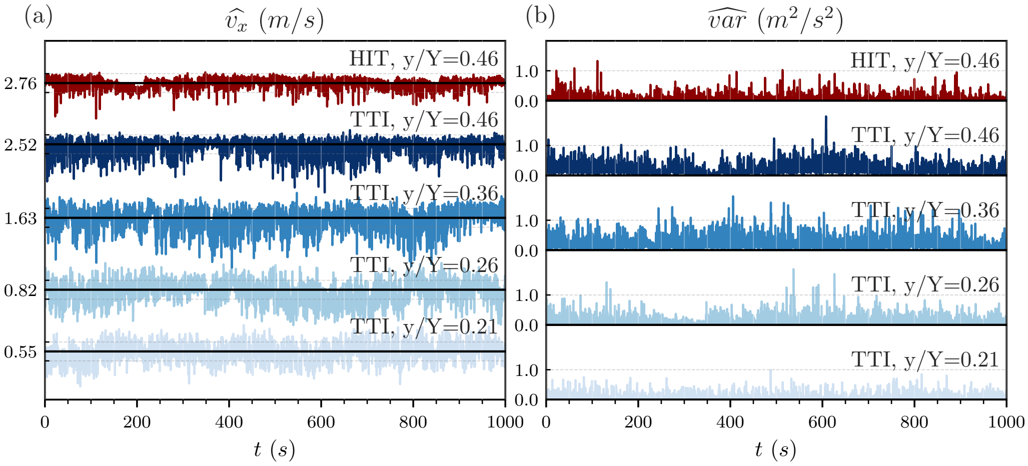

Figure 5: The local longitudinal mean velocity (panel (a)) and the local velocity variance (panel (b)) are calculated by applying equation 2 on the PDPA signals. The four different positions across the mixing layer and the homogeneous isotropic turbulence case are represented with different colors.

is based on the local variance signal. A particle is said to be belonging to a 'burst' if it is associated with a local variance above the following threshold:

$$\widehat{var} > k.v'^2 \tag{3}$$

With k a threshold level and v' the root mean square fluctuating velocity of the complete recorded signal at each different location. Different values of k were tested in this analysis, and a value equal to one was selected. The trends described in the following remained consistent across all the range of tested k values.

The following figure displays some particle statistics conditioned on the local underlying flow properties by employing this burst detection criterion. The conditional averages of the particles' mean longitudinal velocity, average diameter and number density are respectively shown in panels (a), (b) and (c) of figure 6. The conditioned profiles are represented with filled symbols, while the regular statistics are indicated with open symbols. Regarding the streamwise velocity (panel (a)), particles within bursts appear to be related to a slower longitudinal velocity, consistent with the observations from figure 5. Figure 10(b) reveals that particles inside bursts are smaller on average for all cases across the interface, probably due to the increased filtering effect of larger particles. Last but not least, panel (c) of this figure displays the mean particle number density profile. In the high-turbulence region, at large values of y/Y, there are, on average, fewer particles in regions of high local variance. While the opposite is observed in the low-turbulence region, where particles seem to oversample the flow regions with high fluctuations. This confirms the findings of Good et al. (2012), stating that particles are carried into the originally particle-free co-flow by large-scale energetic events.

Given that particles appear to oversample regions of high energetic fluctuations, it raises questions about how the turbulent interface affects the preferential concentration of particles. The next section investigates the clustering properties of inertial particles at various positions across the interface.

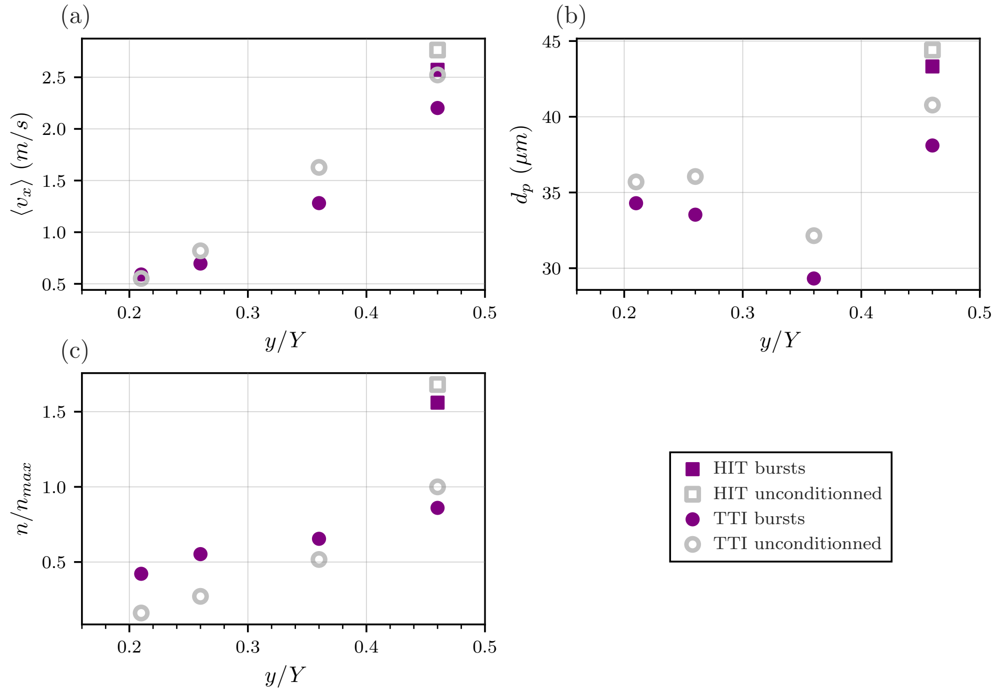

Figure 6: Profiles of mean streamwise velocity (a), particle diameter (b) and the mean droplet number density (c) are shown for the TTI with round symbols. Conditional statistics are represented using filled symbols, while raw statistics are shown with open symbols. The statistics for the homogeneous and isotropic turbulence case are also show in square symbols.

4.3. Preferential concentration of particles across the interface

We may wonder whether, similar to the findings in Good et al. (2012), the entrainment of droplets in the unladen region results in the formation of large-scale clusters. To answer this question, we employed Voronoï tesselations on the particles' arrival times at the measurement location. These arrival times were then converted into particle spatial positions using Taylor's hypothesis of frozen turbulence. The Voronoï tesselations procedure involves segmenting the particle spatial position signal into different portions, named Voronoï cells, with each cell being associated with a specific particle. Each Voronoï cell is defined as the portion of the signal closer to the respective particle than to any other. As a result, particles associated with small Voronoï cells are situated in regions of high local concentration.

Figure 7(a) presents the probability distribution function of Voronoi cell sizes for various signals recorded at different spanwise positions across the interface. The probability distribution of a random Poisson process (RPP), referring to the case with the absence of correlations between particle positions at all scales, is also shown with a dashed line. Small and large Voronoï cell sizes ($\mathcal{V} < 0.3$ and $\mathcal{V} > 2$) are over-represented compared to an RPP distribution, as the curves are situated above the PDF of the RPP case. The presence of over-depleted regions and over-concentrated regions of particles indicates the existence of particle clustering. To quantify the clustering intensity, the PDFs of Voronoï cell lengths can be characterized by their standard deviation $\sigma_{\mathcal{V}}$. Clustering is detected when this metric exceeds the standard deviation of an RPP,

$\sigma_{\mathcal{V}} > \sigma_{RPP}$, following the criteria from Monchaux et al. (2010). It is important to note that unidimensional Voronoï tessellations may present some biases in assessing the existence of particle clustering, as discussed in Mora et al. (2018, 2023). However, it has been demonstrated that if evidence of particle clustering is recovered using the criteria $\sigma_{\mathcal{V}}/\sigma_{RPP} > 1$, then particle clusters are undeniably present in the flow, while the opposite is not always true (Mora et al., 2018).

The bottom panels of figure 7 show the PDFs normalised standard deviation, characterising the clustering intensity, versus the spanwise position (panel (c)) and the Reynolds number Re_λ (panel (d)). From figure 7(c), we can see that clustering becomes more and more pronounced as we move to the region with a lower turbulence level, since σ_v/σ_{RPP} increases for smaller values of y/Y.

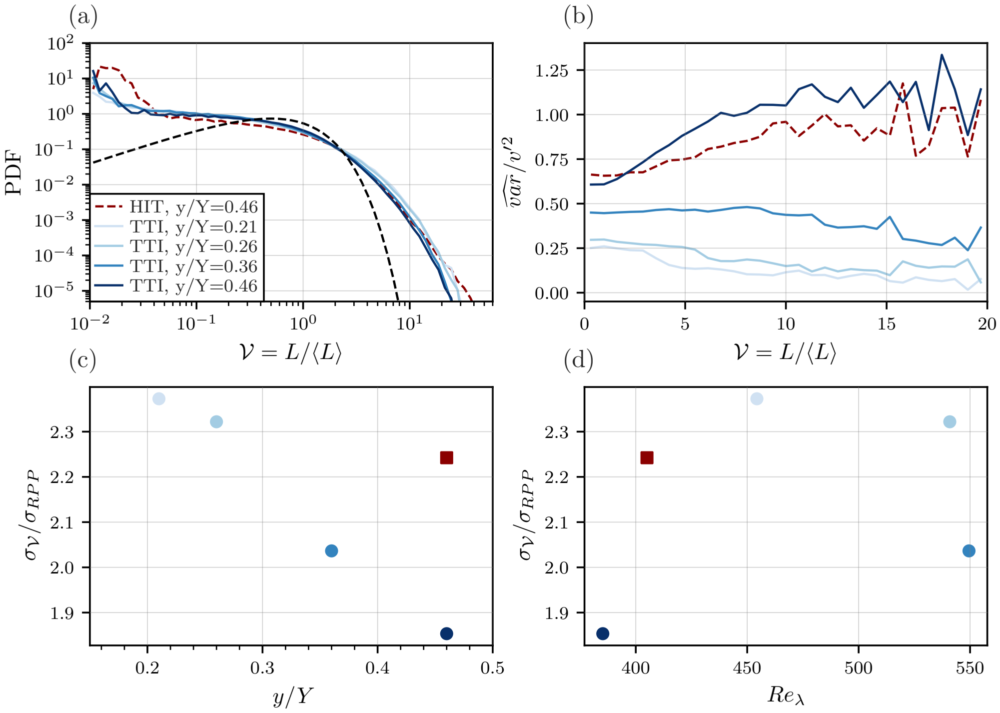

Figure 7: (a) Probability distribution function of the normalised Voronoï lenght $\mathcal{V} = L/\langle L\rangle$. (b) Local variance of the longitudinal velocity, $\widehat{var}$, conditionned on the normalised Voronoï length $\mathcal{V}$. (c) Ratio of the standard deviation of Voronoï cells lengths with respect to the standard deviation of a random Poisson distribution (RPP), $\sigma_{\mathcal{V}}/\sigma_{RPP}$, as a function of the position across the interface. (d) The same ratio $\sigma_{\mathcal{V}}/\sigma_{RPP}$ as a function of the Reynolds number Re_λ. Lines and symbols follow legend of figure 4 and 6.

Each particle is associated with a Voronoï cell length and a value of the longitudinal velocity local variance, calculated from equation 2. We can then plot the particles' local variance as a function of their Voronoï cell length, as shown in figure 7(b). This plot describes how the local variability of the streamwise velocity signal varies with the local concentration of particles. We observe that the relationship between local variance and local concentration reverses across the interface. In the turbulent region and in the homogeneous isotropic turbulence case (in dashed line), particle voids (associated with a large $\mathcal{V}$) are related to a larger local variability of the signal. On the opposite, in the unladen, less turbulent co-flow, events with a high local turbulent intensity are associated with particle clusters rather than particle voids. Indeed, for $y/Y < 0.36$, $\widehat{var}$ decreases with an increase in $\mathcal{V}$. These observations confirm the hypothesis that, within the mixing region and further into the low-turbulence side, particles are transported by large-scale energetic bursts. These events, oversampled by inertial particles, lead to the formation of large-scale particle clusters, resulting in an enhanced particle clustering (and a larger $\sigma_{\mathcal{V}}$ as shown in Figure 7(c)).

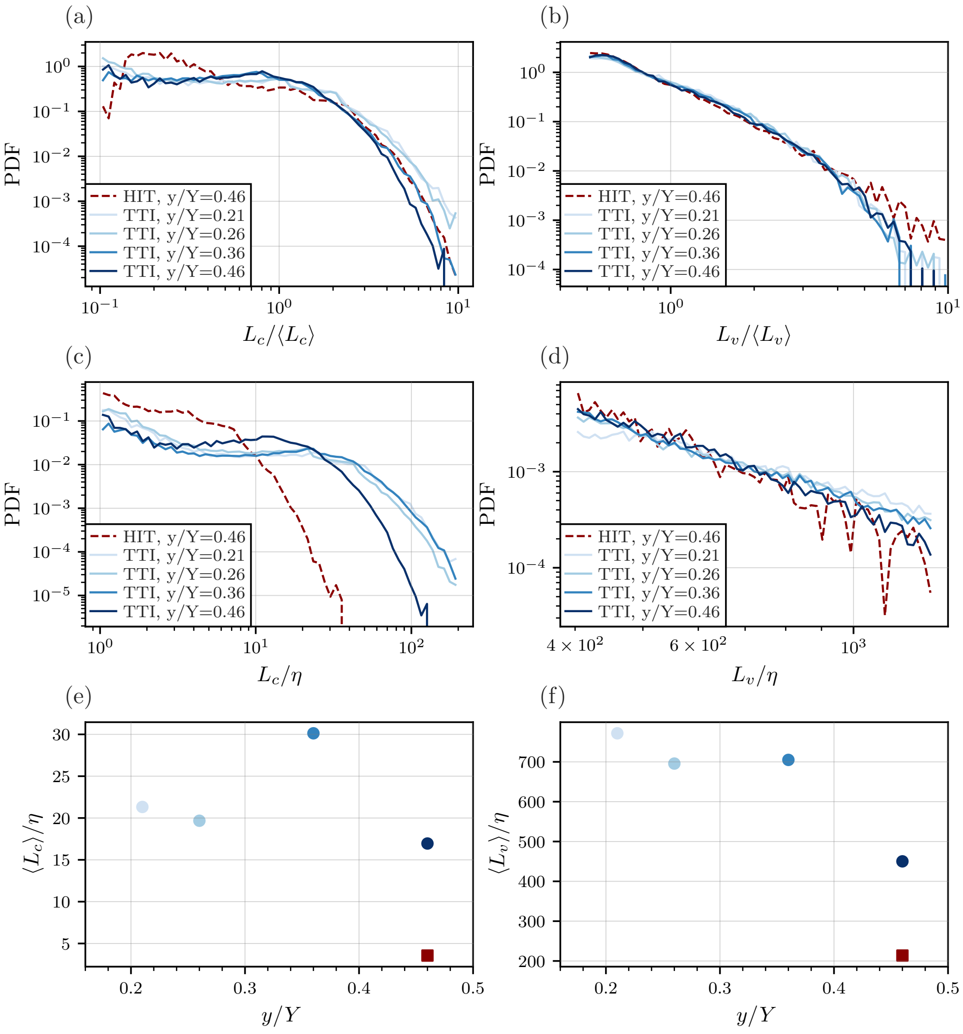

Figure 8: The PDFs of the clusters and voids lengths L_c and L_v are shown normalised by the average clusters and voids sizes in panels (a) and (b), and by the Kolmogorov length scale η in panels (c) and (d). Profiles of the mean clusters and voids length $\langle L_c\rangle$ and $\langle L_v\rangle$ normalised by η are shown in panels (e) and (f). Lines and symbols follow legend of figure 4 and 6.

To gain better insights on the particle clustering within the mixing region, we employ the

Voronoï cells to define and analyse clusters and voids properties. Similarly to previous studies (Monchaux et al., 2010; Obligado et al., 2014; Sumbekova et al., 2017), clusters and voids are defined as groups of connected Voronoï cells which are smaller or larger than a certain threshold. The two thresholds are selected at the intersections of the experimental Voronoï cell sizes distribution and the RPP distribution. Thus, clusters are defined by at least two particles with connected Voronoï cells satisfying $\mathcal{V} < \mathcal{V}_C$, with $\mathcal{V}_C$ the first intersection between the PDF of $\mathcal{V}$ and the RPP. In the same way, particles with connected cells fulfilling the condition $\mathcal{V} > \mathcal{V}_V$ are counted as belonging to voids, with $\mathcal{V}_V$ the second crossing.

The cluster and void sizes, sums of cell sizes belonging to the same cluster or void, are presented in figure 8. The probability distribution functions of cluster sizes L_c and void sizes L_v are shown with two different normalisations: normalised by the average cluster and void sizes in panels (a) and (b), and by the turbulent Kolmogorov length scale η in panels (c) and (d), with η estimated as discussed previously for each position. We observe from figure 8(a) that there is a larger proportion of smaller clusters in the HIT case (red dashed line). Indeed, the probability density is higher for clusters for which $L_c < \langle L_c \rangle$ compared to the other PDFs. Whereas in the mixing region, there is a greater percentage of large clusters, as for high values of L_c the light blue curve is situated above the turbulent region case at $y/Y = 0.46$ and the HIT case. Regarding void sizes, there is an increased probability of having large voids in the low-turbulence region (see figure 8(d)). On the opposite, the trend is inverted in the fully turbulent region, with a greater probability of having small voids and a smaller probability of having large voids compared to the mixing region.

Profiles of the mean cluster and void sizes, nondimensionalised by η, are presented in panels (e) and (f) of figure 8. We can observe that the average void size consistently increases when moving toward the low-turbulence side. This is consistent with the fact that the initially particle-free side is composed of larger particle voids since the inertial particles present on that side are mainly transported by intermittent transversal large-scale events. However, with regard to the average cluster size, the maximum in the profile is located somewhere in the middle of the interface, at $y/Y = 0.36$. This indicates that coherent large-scale clusters are more prevalent at the interface position, while they seem to vanish for measurements further into the low-turbulent region.

4.4. *Particle settling velocity*

Particle settling velocity modification is known to occur within the range of Stokes number and Rouse number covered by the present study. The turbulent scales impacting the settling velocity of inertial particles have been the subject of significant debate (Yang and Lei, 1998; Tom and Bragg, 2019; Ferran et al., 2023). In the range of dimensionless parameters investigated in this study, it has been shown that large-scale structures and the turbulent integral length scale significantly influence the settling velocity even at constant turbulent intensity (Ferran et al., 2023). Considering that this flow results from the combination of two co-flows, each with distinct turbulent scales on either side of the interface, we may wonder how the particles' average settling velocity is affected when they are carried from the turbulent large-scale side to the low-turbulence region.

We collected a sufficient amount of data, with at least 200,000 samples at each position, to condition the particles' settling velocity based on diameter bins. Bins of diameter had a size of $10\,\mu\text{m}$ and spanned the range $d_p \in [0, 150]\mu\text{m}$. However, the particle diameters were recorded simultaneously with the streamwise velocity (using channel 1 of the PDPA), while the vertical was measured independently (using channel 2). To associate each particle's settling velocity with a Stokes and Rouse number, we had to coincide the particles' vertical velocity with their diameter beforehand, using the particle arrival time information from both channels.

The mean particle settling velocity increases monotonically with the diameter (not shown), consistently with the fact that larger particles settle faster. It has been shown that inertial particles settling velocity measurements can be impacted by significant biases due to the presence of weak recirculation currents in the carrier phase (Good et al., 2012; Akutina et al., 2020; Mora et al., 2021a; Ferran et al., 2023). Weak mean secondary motions in the background phase can arise due to confinements effects or the local influence of the dispersed phase on the fluid. To mitigate this bias, we subtracted the average vertical velocity of the smallest particles in the flow to each series of measurement, simarly as in Ferran et al. (2023). We assume that the velocity of the small particles, for which $d_p < 10\ \mu m$, is representative of the background flow vertical velocity since they are associated with very small Stokes number. To investigate the modification of settling velocity compared to the stagnant fluid case, we compute the quantity ΔV as the difference between the measured settling velocity $\langle v_z \rangle$ and the particle terminal velocity V_T, while subtracted the mean background fluid vertical velocity $\langle v_z \rangle|_{d_p<10\mu m}$:

$$\Delta V = \langle v_z \rangle - \langle v_z \rangle|_{d_p<10\mu m} - V_T \tag{4}$$

This quantity ΔV is presented normalised by $V_T(d_{10})$, the terminal velocity of the particle distribution mean diameter, against the Stokes number and the Rouse number in figure 9. In the present case, the Stokes number is based on the Kolmogorov time scale, $St = \tau_p/\tau_\eta$, while the Rouse number is based on the root mean square of the longitudinal fluctuations $Ro = V_T/v'$.

Consistently with previous studies (Maxey, 1987; Wang and Maxey, 1993; Aliseda et al., 2002; Mora et al., 2021b), the settling velocity difference initiates from zero when both the Stokes and Rouse numbers are null, as it is the case for inertialess particles. Then, we observe a large increase of enhancement in settling velocity at small Stokes and Rouse numbers, until reaching the maximum value of $\Delta V/V_T(d_{10})$. After the maximum, the enhancement progressively decreases as particle inertia increases, creating a bell-shaped curve. In some cases, ΔV reaches negative values at large Rouse and Stokes number, where hindering of the settling velocity becomes the predominant outcome. In figure 9, we mainly observe enhancement of the settling velocity, since ΔV is above zero for most of the dataset. The only significant hindering of the settling velocity is observed for measurements taken on the low-turbulence side, $y/Y \in [0.21, 0.26]$, at large Stokes and Rouse number. Comparing the different locations across the layer, we observe that the settling velocity enhancement is more pronounced for the position in the middle of the mixing layer at $y/Y = 0.36$.

Figure 10 presents settling velocity statistics conditioned on whether particles are part of a burst or not (in panel (a)), in a similar way as in figure 6, and based on the local particle concentration determined using the Voronoï cell information (panel (b)). The profile of the mean particle vertical velocity $\langle v_z \rangle$ is shown in figure 10(a), with the statistics associated with particles in bursts (in filled symbols) and the regular statistics (in open symbols). We can observe that, in the high level of turbulence region $y/Y > 0.4$, particles involved in high-energetic events settle on average slightly slower than the overall particle population. However, the trend clearly reverses within the mixing layer for smaller values of y/Y, where particles in bursts settle faster than the average. It is worth noting a prominent peak at $y/Y = 0.26$, where the settling velocity of particles in bursts is significantly higher than the average.

The right panel, figure 10(b), displays the conditional particle settling velocity against the local concentration (inverse of the Voronoï cell size) compared to the settling velocity of all

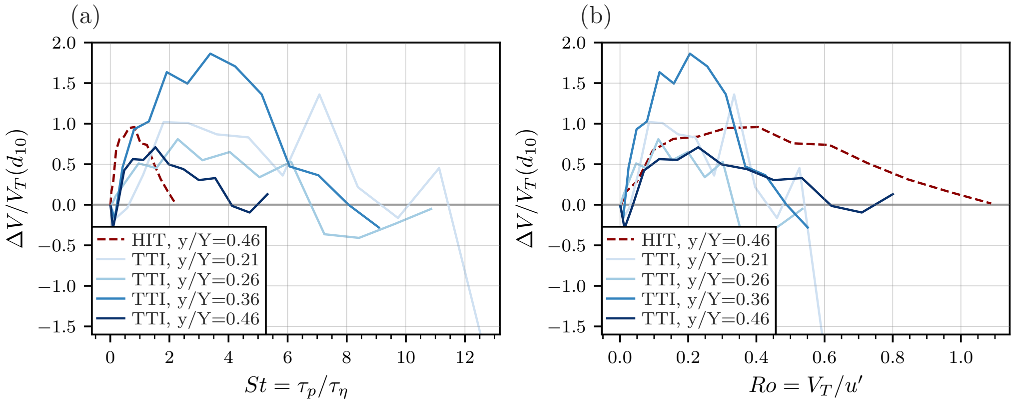

Figure 9: Particle velocity difference over the terminal velocity of the mean diameter distribution $\Delta V/V_T(d_1 0)$ versus the Stokes number (a) and the Rouse number (b). Line styles follow the legend of figure 4

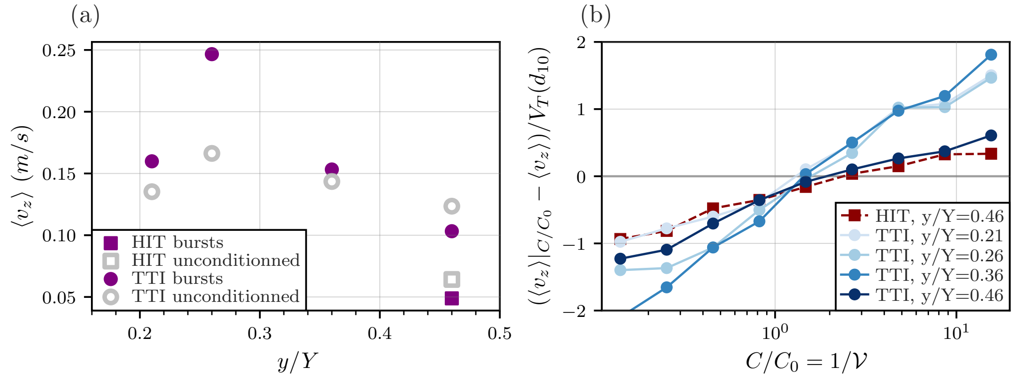

Figure 10: (a) Profile of the mean vertical velocity for the conditionnal statistics (filled symbols) and for the regular statistics (open symbols). (b) Settling velocity conditioned on the local concentration $\langle v_z \rangle|_{C/C_0}$ normalised by the terminal velocity of the mean diameter distribution. Symbols and lines follow legend of figure 4.

particles $\langle v_z \rangle$ and normalized by $V_T(d_{10})$. Indeed, the normalized local particle concentration can be related to the Voronoï cell size through $C/C_0 = \langle L \rangle / L = 1/\mathcal{V}$, where C_0 represents the average particle concentration, i.e., the number of particles divided by the signal length. As indicated by several previous studies (Aliseda et al., 2002; Huck et al., 2018), the settling velocity of inertial particles increases with the local concentration. However, in our case, the rate of increase is significantly larger for measurements within the mixing region than for those in the fully turbulent flow. It is well-known that the mechanisms of settling velocity modification are strongly coupled with the phenomenon of preferential concentration. Indeed, particles in clusters have consistently been observed to settle faster than the average (Aliseda et al., 2002; Huck et al., 2018; Petersen et al., 2019). The steeper slopes observed for $y/Y < 0.36$ may indicate a stronger influence of the local particle concentration on the settling velocity at the interface position. This could be attributed to several possible interpretations. On one hand, particles transported into the dry fluid by large-scale clusters may exert a collective drag on the surrounding flow, resulting in an increased settling rate. On the other hand, particles carried away from the high-turbulence side may be over-represented in downward regions of the flow.

Corroborating the observations from previous figures, bursts in the mixing layer, that is to say, high-energy events featuring a larger local variance, are associated with a higher particle concentration and a stronger particle settling. However, it remains unclear whether this increased settling velocity at the interface location is primarily driven by the intensified particle clustering and collective effects or by underlying flow properties. Indeed, flows with smaller large scale have been found to provoke a larger settling enhancement at constant turbulent intensity (Ferran et al., 2023).

5. Conclusion

The motion of inertial particles have been investigated in wind tunnel experiments within a turbulent/turbulent interface. This interface was generated using a passive grid supporting 81 air sprays. The flow resulted in a sheared turbulent/turbulent interface featuring variations of integral length scale, turbulent intensity, turbulent Reynolds number, and mean velocity. The underlying anisotropic turbulent flow was characterized by hot-wire anemometry and pitot tubes measurements. A burst detection method was proposed to relate particle properties with local flow fluctuations. The particle settling velocities and clustering properties were also presented and analyzed.

Among the results presented in this study, particle velocity probability distributions have been shown to deviate from Gaussianity within the turbulent/turbulent interface, while they consistently exhibit a Gaussian distribution in the homogeneous isotropic turbulence case. Regarding particle sizes, no significant differences were found in droplet diameter distributions. Counterintuitively, we notice that turbulent bursts, associated with larger local fluctuations, present, on average, slower mean velocities. This trend aligns with the negative skewness of the particle velocity probability density function, indicating a higher probability of smaller velocities. Additionally, the particle population in turbulent bursts is characterized by smaller droplet sizes and a larger number density in the small-scale turbulent region. Particle clusters and voids were analyzed using Voronoï tesselations. The bursting phenomena results in an enhanced particle clustering in the mixing layer. Larger particle clusters and voids are observed in the originally unladen side compared to the fully developed turbulence region. The main results from section 4.2 and 4.3 confirm the findings from (Gerashchenko et al., 2011; Good et al., 2012; Gerashchenko and Warhaft, 2013), i.e. particles are transported into the low-turbulence region by energetic bursts that are associated with high particle concentration. Moreover, we provide insights into particle settling velocities for various Stokes and Rouse numbers at different locations across the interface. When examining the measured particle vertical velocity, we observe that enhancement is more pronounced at the interface midpoint, while some hindering of the settling rate is present in the low turbulence region at high Ro and St. Turbulent bursts, associated with a larger particle concentration, appear to be also correlated with more important settling. However, it is uncertain whether the enhanced settling in the bursts is caused by the interface's influence on the particles or by collective effects created with the increase in local concentration.

Given that interfacial layers are known to expand laterally with time or distance (Westerweel et al., 2009; da Silva et al., 2014), it is worth analyzing the particle statistics at a further downstream location. Additionnaly, a velocity component that has yet to be studied but should be of primordial importance for the bursting phenomena is the transversal velocity. Thus, modifying the experimental setup to measure this velocity component could provide valuable insights into particle entrainment. Moreover, important insights on particle motions can be obtained with Particle Tracking Velocimetry (PTV) measurements. PTV measurements can offer valuable information on the particle acceleration statistics, and simultaneous sampling of their settling velocity and local concentration. The range of experimental parameters covered by this study, $Ro \in [0, 1]$ $St \in [0, 12]$, except for the turbulent Reynolds number Re_λ, is known to be relevant for the study of cloud boundaries (Vaillancourt and Yau, 2000; Siebert et al., 2010).

References

Adrian, R.J., Yao, C.S., 1987. Power spectra of fluid velocities measured by laser Doppler velocimetry. Experiments in Fluids 5, 17–28. doi:10.1007/BF00272419.

Akutina, Y., Revil-Baudard, T., Chauchat, J., Eiff, O., 2020. Experimental evidence of settling retardation in a turbulence column. Physical Review Fluids 5, 14303. doi:10.1103/PhysRevFluids.5.014303.

Aliseda, A., Cartellier, A., Hainaux, F., Lasheras, J.C., 2002. Effect of preferential concentration on the settling velocity of heavy particles in homogeneous isotropic turbulence. Journal of Fluid Mechanics 468, 77–105. doi:10.1017/S0022112002001593.

Baker, L., Frankel, A., Mani, A., Coletti, F., 2017. Coherent clusters of inertial particles in homogeneous turbulence. Journal of Fluid Mechanics 833, 364–398. doi:10.1017/jfm.2017.700.

Bateson, C.P., Aliseda, A., 2012. Wind tunnel measurements of the preferential concentration of inertial droplets in homogeneous isotropic turbulence. Experiments in Fluids 52, 1373–1387. doi:10.1007/s00348-011-1252-6.

Bec, J., Biferale, L., Boffetta, G., Celani, A., Cencini, M., Lanotte, A., Musacchio, S., Toschi, F., 2006. Acceleration statistics of heavy particles in turbulence. Journal of Fluid Mechanics 550, 349–358. doi:10.1017/S002211200500844X, `arXiv:0508012`.

Bec, J., Homann, H., Ray, S.S., 2014. Gravity-driven enhancement of heavy particle clustering in turbulent flow. Physical Review Letters 112, 1–5. doi:10.1103/PhysRevLett.112.184501, `arXiv:1401.1306`.

Bhat, G.S., Narasimha, R., 1996. A volumetrically heated jet: Large-eddy structure and entrainment characteristics. Journal of Fluid Mechanics 325, 303–330. doi:10.1017/S0022112096008130.

Bisset, D., Hunt, J., Rogers, M., 2002. The turbulent/non-turbulent interface bounding a far wake. Journal of Fluid Mechanics 451, 383–410. doi:10.1017/s0022112001006759.

Blackwelder, R., Kaplan, R., 1976. On the wall structure of the turbulent boundary layer. Journal of Fluid Mechanics 76, 89–112.

Blyth, A., 1993. Entrainment in cumulus clouds. Journal of Applied Meteorology and Climatology 32, 626–641. doi:10.1175/1520-0450(1993)032¡0626:EICC¿2.0.CO;2.

Chung, J.N., Troutt, T.R., 1988. Simulation of particle dispersion in an axisymmetric jet. Journal of Fluid Mechanics 186, 199–222. doi:10.1017/S0022112088000102.

Corrsin, S., Kistler, A., 1955. Free-stream boundaries of turbulent flows. Technical Report. Johns Hopkins University.

Crowe, C., Chung, J., Troutt, T., 1988. Particle mixing in free shear flows. Progress in Energy and Combustion Science 14, 171–194. doi:10.1016/0360-1285(88)90008-1.

da Silva, C., Hunt, J., Eames, I., Westerweel, J., 2014. Interfacial Layers Between Regions of Different Turbulence Intensity. Annual Review of Fluid Mechanics 46, 567—-590. doi:10.1146/annurev-fluid-010313-141357.

Eaton, J., Fessler, J., 1994. Preferential concentration of particles by turbulence. International Journal of Multiphase Flow 20, 169–209. doi:https://doi.org/10.1016/0301-9322(94)90072-8.

Elghobashi, S., 1994. On predicting particle-laden turbulent flows. Applied Scientific Research 52, 309–329. doi:10.1007/BF00936835.

Ferran, A., Aliseda, A., Obligado, M., 2023. Characterising the energy cascade using the zero - crossings of the longitudinal velocity fluctuations. Experiments in Fluids , 1–13doi:10.1007/s00348-023-03722-8.

Gerashchenko, S., Good, G., Warhaft, Z., 2011. Entrainment and mixing of water droplets across a shearless turbulent interface with and without gravitational effects. Journal of Fluid Mechanics 668, 293–303. doi:10.1017/S002211201000577X.

Gerashchenko, S., Warhaft, Z., 2013. Conditional entrainment statistics of inertial particles across shearless turbulent interfaces. Experiments in Fluids 54. doi:10.1007/s00348-013-1631-2.

Good, G., Gerashchenko, S., Warhaft, Z., 2012. Intermittency and inertial particle entrainment at a turbulent interface: The effect of the large-scale eddies. Journal of Fluid Mechanics 694, 371–398. doi:10.1017/jfm.2011.552.

Good, G., Ireland, P., Bewley, G., Bodenschatz, E., Collins, L., Warhaft, Z., 2014. Settling regimes of inertial particles in isotropic turbulence. Journal of Fluid Mechanics 759, R3. doi:10.1017/jfm.2014.602.

Gore, R., Crowe, C., 1991. Modulation of Turbulence by a Dispersed Phase. Journal of Fluids Engineering 113, 304–307. doi:10.1115/1.2909497.

Hassaini, R., Coletti, F., 2022. Scale-to-scale turbulence modification by small settling particles. Journal of Fluid Mechanics , 1–22doi:10.1017/jfm.2022.762.

Huck, P.D., Bateson, C., Volk, R., Cartellier, A., Bourgoin, M., Aliseda, A., 2018. The role of collective effects on settling velocity enhancement for inertial particles in turbulence. Journal of Fluid Mechanics 846, 1059–1075. doi:10.1017/jfm.2018.272.

Kamalu, N., Wen, F., Troutt, T., Crowe, C., Chung, J., 1988. Particle dispersion by ordered motion in turbulent mixing layers, in: ASME Cavitation and Multiphase Flow Forum, pp. 150–154.

Kolmogorov, A., 1941. The local structure of turbulence in incompressible viscous fluid for very large reynolds. Numbers. In Dokl. Akad. Nauk SSSR 30, 301.

Lázaro, B., Lasheras, J., 1989. Particle dispersion in a turbulent, plane, free shear layer. Physics of Fluids A 1, 1035–1044. doi:10.1063/1.857394.

Lázaro, B., Lasheras, J., 1992. Particle dispersion in the developing free shear layer. Part 2. Forced flow. Journal of Fluid Mechanics 235, 143–178. doi:10.1017/S0022112092001071.

Longmire, E., Eaton, J., 1992. Journal of Fluid Mechanics 236, 217–257. doi:10.1017/S002211209200140X.

Maxey, M., 1987. The gravitational settling of aerosol particles in homogeneous turbulence and random flow fields. Journal of Fluid Mechanics 174, 441–465. doi:10.1017/S0022112087000193.

Monchaux, R., Bourgoin, M., Cartellier, A., 2010. Preferential concentration of heavy particles: A Voronoï analysis. Physics of Fluids 22. doi:10.1063/1.3489987.

Monchaux, R., Bourgoin, M., Cartellier, A., 2012. Analyzing preferential concentration and clustering of inertial particles in turbulence. International Journal of Multiphase Flow 40, 1–18. doi:10.1016/j.ijmultiphaseflow.2011.12.001.

Mora, D., Aliseda, A., Cartellier, A., Obligado, M., 2018. Pitfalls measuring 1d inertial particle clustering, in: iTi Conference on Turbulence, Springer. pp. 221–226.

Mora, D., Aliseda, A., Cartellier, A., Obligado, M., 2023. Characterizing inertial particle clustering with 1d signals. Measurement Science and Technology .

Mora, D., Bourgoin, M., Mininni, P., Obligado, M., 2021a. Clustering of vector nulls in homogeneous isotropic turbulence. Physical Review Fluids 6, 24609. doi:10.1103/PhysRevFluids.6.024609.

Mora, D., Cartellier, A., Obligado, M., 2019. Experimental estimation of turbulence modification by inertial particles at moderate Reλ. Physical Review Fluids 4, 1–10. doi:10.1103/PhysRevFluids.4.074309.

Mora, D., Obligado, M., 2020. Estimating the integral length scale on turbulent flows from the zero crossings of the longitudinal velocity fluctuation. Experiments in Fluids 61, 1–10. doi:10.1007/s00348-020-03033-2, `arXiv:2005.06055`.

Mora, D., Obligado, M., Aliseda, A., Cartellier, A., 2021b. Effect of Reλ and Rouse numbers on the settling of inertial droplets in homogeneous isotropic turbulence. Physical Review Fluids 6, 1–19. doi:10.1103/PhysRevFluids.6.044305.

Nielsen, P., 1993. Turbulence effects on the settling of suspended particles. Journal of Sedimentary Petrology 63, 835–838. doi:10.1306/d4267c1c-2b26-11d7-8648000102c1865d.

Obligado, M., Teitelbaum, T., Cartellier, A., Mininni, P., Bourgoin, M., 2014. Preferential concentration of heavy particles in turbulence. Journal of Turbulence 15, 293–310. doi:10.1080/14685248.2014.897710.

Petersen, A., Baker, L., Coletti, F., 2019. Experimental study of inertial particles clustering and settling in homogeneous turbulence. Journal of Fluid Mechanics 864, 925–970. doi:10.1017/jfm.2019.31, `arXiv:1812.04055`.

Puga, A., Larue, J., 2017. Normalized dissipation rate in a moderate Taylor Reynolds number flow. Journal of Fluid Mechanics 818, 184–204. doi:10.1017/jfm.2017.47.

Rosa, B., Parishani, H., Ayala, O., Wang, L., 2016. Settling velocity of small inertial particles in homogeneous isotropic turbulence from high-resolution DNS. International Journal of Multiphase Flow 83, 217–231. doi:10.1016/j.ijmultiphaseflow.2016.04.005.

Shaw, R., 2003. Particle-turbulence interactions in atmospheric clouds. Annual Review of Fluid Mechanics 35, 183–227. doi:10.1146/annurev.fluid.35.101101.161125.

Siebert, H., Gerashchenko, S., Gylfason, A., Lehmann, K., Collins, L.R., Shaw, R.A., Warhaft, Z., 2010. Towards understanding the role of turbulence on droplets in clouds: In situ and laboratory measurements. Atmospheric Research 97, 426–437. doi:10.1016/j.atmosres.2010.05.007.

Squires, K., Eaton, J., 1991. Measurements of particle dispersion obtained from direct numerical simulations of isotropic turbulence. Journal of Fluid Mechanics 226, 1–35. doi:10.1017/S0022112091002276.

Sreenivasan, K., 1995. On the universality of the Kolmogorov constant. Physics of Fluids 7, 2778–2784. doi:10.1063/1.868656.

Sumbekova, S., Cartellier, A., Aliseda, A., Bourgoin, M., 2017. Preferential concentration of inertial sub-Kolmogorov particles: The roles of mass loading of particles, Stokes numbers, and Reynolds numbers. Physical Review Fluids 2, 1–19. doi:10.1103/PhysRevFluids.2.024302, `arXiv:1607.01256`.

Tom, J., Bragg, A., 2019. Multiscale preferential sweeping of particles settling in turbulence. Journal of Fluid Mechanics 871, 244–270. doi:10.1017/jfm.2019.337, `arXiv:1812.08830`.

Townsend, A.A., 1947. Measurements in the turbulent wake of a cylinder. Proceedings of the Royal Society of London. Series A. Mathematical and Physical Sciences 190, 551–561.

Vaillancourt, P., Yau, M., 2000. Review of particle-turbulence interactions and consequences for cloud physics. Bulletin of the American Meteorological Society 81, 285–298. doi:10.1175/1520-0477(2000)081¡0285:ROPIAC¿2.3.CO;2.

Vassilicos, J., 2015. Dissipation in turbulent flows. Annual Review of Fluid Mechanics 47, 95–114. doi:10.1146/annurev-fluid-010814-014637.

Veeravalli, S., Warhaft, Z., 1989. The shearless turbulence mixing layer. Journal of Fluid Mechanics 207, 191–229. doi:10.1017/S0022112089002557.

Wang, L., Maxey, M., 1993. Settling velocity and concentration distribution of heavy particles in homogeneous isotropic turbulence. Journal of Fluid Mechanics 256, 27–68. doi:10.1017/S0022112093002708.

Westerweel, J., Fukushima, C., Pedersen, J.M., Hunt, J.C., 2009. Momentum and scalar transport at the turbulent/non-turbulent interface of a jet. Journal of Fluid Mechanics 631, 199–230. doi:10.1017/S0022112009006600.

Yang, C.Y., Lei, U., 1998. The role of the turbulent scales in the settling velocity of heavy particles in homogeneous isotropic turbulence. Journal of Fluid Mechanics 371, 179–205. doi:10.1017/S0022112098002328.

6 Particle Tracking Velocimetry campaign

As mentioned in the previous chapter (chapter 5), obtaining two-dimensional or three-dimensional measurements of particle velocities would be very valuable for the comprehension of their dynamics across the interface. For instance, utilizing a Particle Tracking Velocimetry (PTV) technique would provide access to particle 3D positions and trajectories, enabling us to extract information on their accelerations or two-dimensional particle concentration fields. Following the work of Huck et al. 2018 and Mora-Paiba 2020, both conducted in the same facility, we have planned a stereo-PTV experimental campaign.

This chapter describes the stereo-PTV experimental campaign carried out in the wind tunnel in Seattle in August 2023. Due to the time constraints for completing the current thesis, we only report a brief description of the experimental setup and the recorded datasets that will be presented in future publications.

6.1 Description of the experimental setup

Three high-speed cameras were employed for these experiments. In comparison to the prior work done by Mora-Paiba 2020, an additional camera was incorporated to provide unambiguous stereomatching of inertial particles across the different frames. While two cameras are theoretically sufficient to estimate the three-dimensional particle positions, experimental fluid dynamicists often employ more than two cameras to improve depth perception (Bourgoin and Huisman 2020). Indeed, difficulties were encountered with the present experimental setup when attempting to stereomatch inertial particles from the recordings of two cameras. To avoid ambiguities and enhance accuracy and robustness in the determination of the 3D particle positions, a third camera was added to the experimental setup.

The three cameras were positioned in the same longitunal vertical plane, observing the measurement volume from the side of the tunnel. Two cameras were set at the same height, vertically aligned with the region of interest, while the third one was positioned on top of the two others in an attempt to form a pyramidal scheme. An illustration of the experimental setup is shown in Figure 6.1a. This arrangement resulted in a steeper angle for the third camera in the vertical direction. The field of view captured by the cameras was then aligned with the streamwise and vertical direction of the wind tunnel. Cameras were situated approximately half a meter away from the field of view, using an effective focal length of 135 mm. The resulting area captured by the cameras had approximate dimensions of 12 cm (in the streamwise direction) by 8 cm (in the vertical direction).

The inertial particles were illuminated with a solid-state dual-head laser (TerraPIV, Continuum, San Jose, CA, USA), emitting short pulses of visible light with a wavelength of 527 nm, and a duration on the order of $O(10^{-8})$ s. The setup of the laser optical path can be seen in Figure 6.1b. The light ray emanating from the laser cavity, situated in the bottom right corner of picture 6.1a, was directed to illuminate the field of view from the top of the wind tunnel. Spherical and a cylindrical lenses were assembled to create a laser sheet with a thickness of approximately 5 mm. Coinciding with the cameras' field of view, the laser plane was aligned with the vertical and streamwise directions.

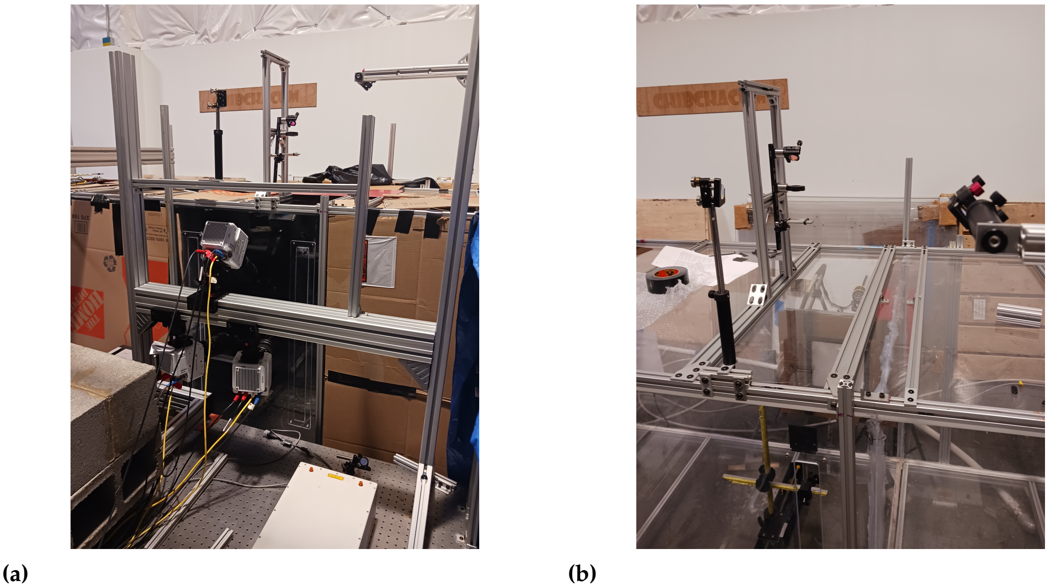
(a)

(b)

Figure 6.1: (a) An overview of the PTV experimental setup featuring the three cameras and the laser head (positioned on the optical table at the bottom of the image). (b) An illustration of the optical path setup for the laser sheet.

The cameras' frame rate was set to 1 kHz and synchronized with the laser pulses, resulting in a constant interval time dt of 1 ms between two successive snapshots. Given that the particles are advected with a velocity of around 1 m/s, the droplets' mean displacement between two successive frames is expected to be approximately 1 mm, corresponding to roughly 20 pixels on the image frame. The cameras had a resolution of 2560 x 1600 pixels and a 12-bit color depth, resulting in an image size of 3.90 MB. At least two sets of 3000 snapshots each were recorded for each camera and experimental conditions.

The measurement volume sampled by the cameras was located 35 meshes downstream the passive grid, where the turbulence is fully developed and isotropic under homogeneous spray conditions. Two different spanwise positions in the tunnel were sampled, and the necessary calibration was recorded at each position. In the first place, measurements were taken at the wind tunnel centerline, corresponding to $y = 54$ cm from wind tunnel wall on the camera side. To investigate the influence of the interface on particle statistics, we shifted the field of view to $y = 26$ cm, approximately at the quarter width of the wind tunnel. In this experimental campaign, we generated a turbulent/turbulent interface using the same procedure as described in chapter 5. This transversal position should be situated in the region where the turbulent interface fluctuates intermittently.

For both sets of experimental data, at the two different spanwise positions, we recorded both inertial particle velocities and fluid flow statistics. The inertial particles, being the water droplets, were injected at the wind tunnel inlet with the spray grid in the same manner as in chapter 5. To sample the fluid flow, olive oil droplets were used as seeding particles, acting as tracers due to their monodispersed small sizes and very low inertia. The olive oil droplets were atomized into the flow using a TSI's oil droplet generator (model 9307-6), supplied with pressurized air at 20 psi by an autonomous PowerLite high-pressure compressor.

6.2 Calibration

The quality of the measurements depends critically on the stereoscopic calibration procedure. To perform the conversion from pixels coordinates in the recorded images to real world three-dimensional positions, we used a drilled calibration target. The calibration target was positioned inside the tunnel at the location of the laser sheet and was illuminated using backscatter lighting. In total 11 calibration images were captured at 11 different y spanwise positions, each separated by 1 mm. Calibration images were captured for the two distinct laser sheet positions, and when a significant time has passed between two sets of measurements.

Figure 6.2a shows the experimental setup used for the calibration, with the mire and the LED panel. A picture of the calibration target taken by the left camera is shown as an illustration in Figure 6.2b.

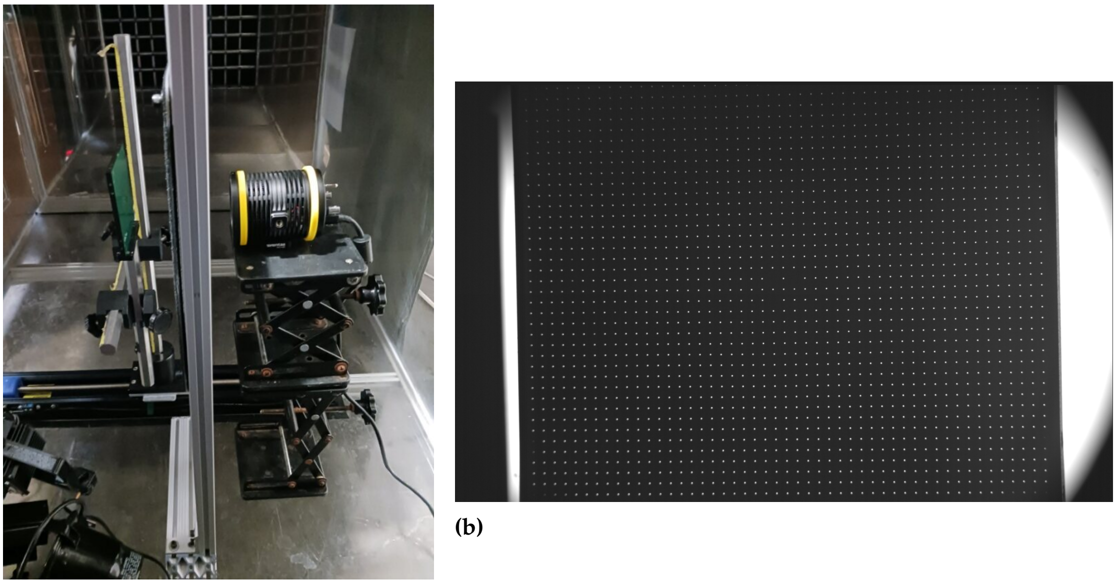

(a)

(b)

Figure 6.2: (a) Illustration of the experimental setup for the calibration. (b) Example of an image of the calibration target.

The pixel-to-real-world conversion, the particle stereomatching procedure between the three cameras, and the particle tracking were performed using a code developed by the team of ENS Lyon (Bourgoin and Huisman 2020). The stereomatching algorithm is based on the introduction of rays of light emerging from the detected particles in the image frame and a three-dimensional grid of voxels. The stereomatched position of the particle is then determined as the three-dimensionnal coordinates of the intersection of the rays of light emerging from the three cameras.

To ensure the reliability of stereomatching with the present camera alignment, we reconstructed the three-dimensional positions of the target points. We considered the points detected on the calibration images to be particles and determined their coordinates as so with the algorithm. Figure 6.3 presents the result from the target planes reconstruction. Each calibration image taken at a different plane is shown using a distinct color, with black dots corresponding to $y = 5$ mm and white dots corresponding to $y = -5$ mm. The right panel of Figure 6.3 presents the matching error for the central plane of the laser sheet. The matching error is defined as the root mean square value of the distance between the stereomatched position and the light rays.

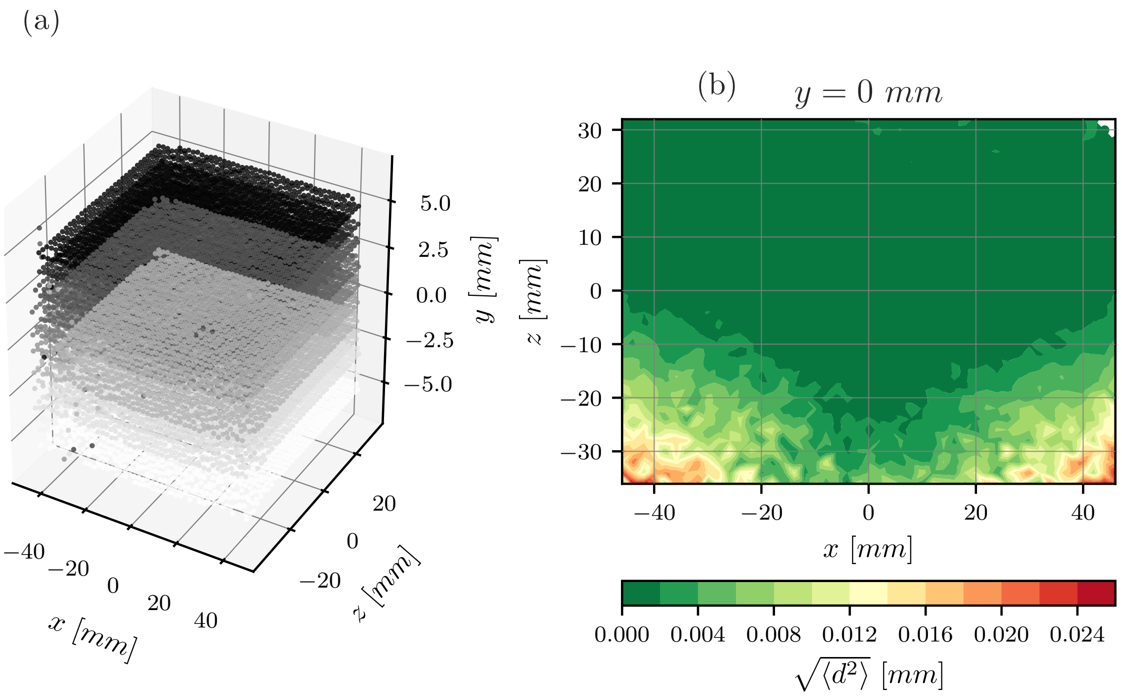

Figure 6.3: (a) Reconstruction of the 11 calibration planes with the stereomatching algorithm. Different colors represent different calibration images with black dots corresponding to the image taken at $y = 5$ mm and white dots corresponding to $y = -5$ mm. (b) The matching error for the calibration plane at the center of the laser sheet, $y = 0$ mm. x, y and z correspond to the streamwise, spanwise and vertical coordinate respectively.

6.3 Preliminary particle trajectories

We intend to track inertial particles in the measurement volume with the objective to determine their positions, their three velocity components, and acceleration statistics conditioned on their local concentration. We are currently in the process of optimizing parameters relevant for particle detection, stereomatching, and particle tracking.

This section provides preliminary information on trajectory statistics. We focus on the homogeneous and isotropic turbulent flow sampled at the centerline of the wind tunnel, 30 meshes downstream the grid. In the analysis, very short trajectories, defined by less than three successive frames, are excluded. The left panel of Figure 6.4 displays examples of particle trajectories obtained with the code from Bourgoin and Huisman 2020. The histogram of trajectory lengths (in terms of the number of frames, N) is presented in Figure 6.4(b). In the future, we will focus on optimizing parameters to obtain long trajectories, which are scarce in the data shown in Figure 6.4.

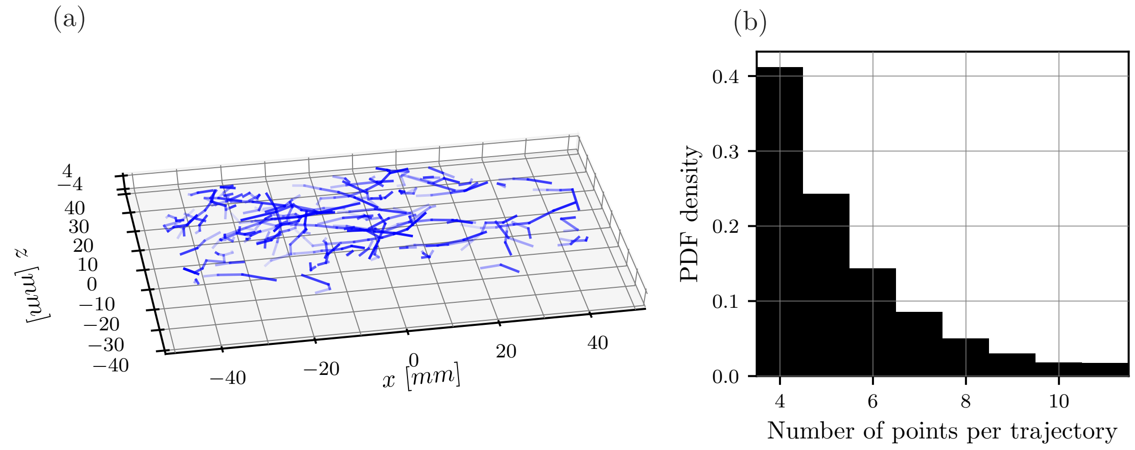

Figure 6.4: (a) Examples of tracks obtained for homogeneous isotropic turbulence condition. (b) Histogram showing the probability density of the number of frames per track.

7

Conclusions and Perspectives

The main findings reported by this thesis can be summarized in three key parts. The first chapter was dedicated to the study of single-phase turbulent flows, offering new insights into the energy cascade through a novel approach to estimate their characteristics. We then introduced inertial particles into the fluid, and examined the modification of their settling velocity by a homogeneous isotropic turbulent flow. The particle-turbulence problem was further complicated by studying the motion of inertial particles advected in anisotropic turbulence with a turbulent interface.

7.1 Conclusions

In the first part of this thesis, we investigated methods to characterize the carrier turbulent phase. Plenty of information on the turbulence energy cascade can be inferred from points in the flow where the velocity is null. With the statistical properties of these points, such as their mean spatial separation, previous studies have determined the Taylor microscale and the integral length scale of turbulence. Here, we combined McFadden equation and the Rice theorem to establish a relationship between the flow Reynolds number and the variance of the distance between two consecutive zeros ($\mathscr{L}/\lambda \approx \pi^2/4 \; Var(\Delta Z)\langle \Delta Z\rangle^{-2}$). The relationship obtained informs us that the level of turbulence is controlled by the variability of the distance between two consecutive zeros. It also indicates that large separations between zeros, i.e., voids of zero crossings, are the main contributors to the value of the turbulent Reynolds number Re_λ. This approach has been shown to be valid in both the canonical Kolmogorov energy cascade and in flows featuring an out-of-equilibrium turbulent cascade. By using Voronoï tesselations, we also determine a proportionality relationship between zero-crossing voids and the turbulent Reynolds number.

In a second step, the settling velocity of sub-Kolmogorov inertial particles in wind tunnel decaying isotropic turbulence was analyzed, considering corrections for the misalignment angle and secondary motions in the fluid phase. The study confirms and extends previous trends, revealing that the settling velocity enhancement disappears at high Reynolds numbers and hindering of the settling rate becomes the main outcome. Probably the most important result of this study suggests that different turbulence large-scale forcing, even with similar Reynolds numbers and turbulent intensities, lead to significant differences in settling modification. Finally, we analyzed the possible mechanisms responsible for the settling velocity modification in the range of dimensionless parameters covered by the study, including preferential sweeping, loitering, sweep-stick and collective effects.

Finally, we designed an experiment to generate a sheared turbulent interface within grid-generated wind tunnel turbulence. Great attention was given to the interface generation by varying the number of disabled atomizers and systematically characterizing the resulting flow with Pitot tubes. Profiles of fluid and particle velocities were then recorded using a PDPA instrument and a hot-wire anemometer. We proposed a burst detection method to link the particle properties with local flow fluctuations. Additionally, we applied Voronoï tesselations to the particle spatial positions to quantify clustering and analyzed their settling velocity. Among the multiple findings provided from this study, we noticed non-Gaussian probability density functions for the longitudinal particle velocities within the interface. Turbulent bursts, associated with larger local fluctuations, exhibited slower mean velocities, smaller droplet sizes, a higher number density and a more pronounced settling in the low-scale turbulent region. Voronoï tessellations revealed enhanced particle clustering in the mixing layer, characterized by larger clusters and voids compared to the fully developed turbulence region. Finally, the measured particle vertical velocities mostly revealed enhancement of the settling velocity, especially at the interface midpoint.

Chapter 6 concludes by presenting a particle tracking velocimetry campaign and demonstrating its feasibility in the tunnel. We provide initial results for homogeneous isotropic turbulence. A more in-depth analysis, including the turbulent/non-turbulent interface, will be conducted in the future.

7.2 Perspectives

The study of zero-crossings statistics has increasingly provided valuable insights into numerous aspects of turbulent flows (Sreenivasan, Prabhu, and Narasimha 1983; Mazellier and Vassilicos 2008; Mora and Obligado 2020). However, potential limits of zero-crossing-based approaches may need further exploration. Future works should consider extending these findings to more complex flows, and other types of measurement techniques. While we strongly believe that zero-crossing-based characterization of turbulence is applicable to field measurements or two-phase flow studies (Mora, Cartellier, and Obligado 2019), it has yet to be generalized. The study in appendix A aims to test some of these limits by extending the Rice theorem to two-phase three-dimensional flow. We attempted to determine the carrier phase Taylor microscale using dispersed phase velocity stagnation points (three-dimensional counterparts to zero-crossings) in direct numerical simulations. However, the strategy was unsuccessful since it necessitates to recover the totality of the fluid phase stagnation points, which are known to exhibit pronounced clustering.

Nevertheless, there is hope that the integral length scale in two-phase 3D flows can be deduced from the particle velocity field. Indeed, the integral length scale is less susceptible to be impacted by the filtering effect of inertial particles. Additionally, techniques from Mora and Obligado 2020 could be extended to two-dimensional particle image velocimetry experiments. Within this framework, new concerns might be addressed, such as understanding the sensitivity of the technique to particle inertial clustering or determining the upper limit of Stokes number beyond which the method becomes inapplicable. These approaches could provide a more robust procedure to determine $\mathscr{L}$ in challenging situation, such as field experiments where measuring the carrier phase is not always feasible (Li et al. 2021).

The study of the turbulent interface is preliminary and most of the trends presented need confirmation through additional measurements at different locations, or with multiple inlet

Reynolds number. Measurements of the particles and flow statistics at another downstream position, further away from the grid, would be very valuable to the present analysis. Indeed, turbulent interfacial layers, such as in jets or wakes, are known for expanding laterally with streamwise distance. It is worth investigating how the mixing process evolves, on average, with the distance and whether particle statistics, including mean number density and velocity distributions, tend to become more uniform at greater distances.

In our experiment, no splitter plate or other apparatus was employed to separate the two adjacent flows. Consequently, the precise location of the turbulent front can be somewhat ambiguous, particularly if it is expected to vary with downstream distance. An idea could be to focus on establishing an accurate experimental determination of the turbulent interface average position. This could involve setting up some sort of threshold on certain turbulent flow characteristics, similarly as methods employed in simulations, to determine the average location of the interface.

One variable of significant interest that has not yet been studied is the transverse velocity, perpendicular to the interface direction. Indeed, this velocity component is expected to play a crucial role in the transport of particles in the low-turbulence region and the bursting phenomena (Veeravalli and Warhaft 1989). An approach could involve employing cross wires in single-phase turbulence to study simultaneously streamwise and transverse velocity components. For two-phase flows, one option is to use 3D measurements techniques such as Particle tracking Velocimetry (PTV) to access this component.

Finally, Particle tracking Velocimetry would provide valuable insights by enabling access to other particle statistics: three velocity components, two-dimensional map of local concentration and particle accelerations.

APPENDIX

Characterising Single and Two-Phase Homogeneous Isotropic Turbulence with Stagnation Points

A

Presentation of the article:

Ferran, A., Angriman, S., Mininni, P. D., & Obligado, M. (2022). Characterising single and two-phase homogeneous isotropic turbulence with stagnation points. Dynamics, 2(2), 63-72.

In chapter 3 of this thesis, we explored novel approaches to evaluate some important turbulent flow characteristics through the zero crossings of the longitudinal velocity. As discussed in the conclusion, we wonder if zero-crossing-based methods could be applicable to multiphase flows. In other words, which information can we obtain about the carrier phase turbulent scales using solely the dispersed phase velocity statistics? This idea builds upon the inertial filtering effect of the particles, suggesting that particle velocities consist of a low-pass filtered version of the fluid phase. As a result, certain properties of one phase can be inferred from measurements of the other.

The Rice theorem has already been applied to particle-laden flow in a study by Mora, Cartellier, and Obligado 2019 to estimate the turbulence modulation by the particles. This Rice theorem was also previously generalized to three-dimensional flows stagnation points in the work of Goto and Vassilicos 2009. In this study, we wish to combined the two aforementioned ideas: utilizing the three-dimensional velocity field of the dispersed phase to obtain the carrier phase Taylor microscale.

This work uses data of direct numerical simulations in homogeneous isotropic turbulence of single-phase and two-phase flows, that were previously presented in the study of Mora et al. 2021a. The advantage of numerical simulations relies in the access to all three-dimensional variables of the fluid and particle phases in the entire domain, providing the true value of the Taylor microscale. If the method works with simulated flow field, we can consider extending it to experimental multi-dimensional measurements of particle velocities. However, we found that while the Rice theorem was valid for the single-phase part of our dataset, it was unsuccessful for two-phase flow measurements. Indeed, the interpolated particle velocity fields cannot resolve all the carrier phase stagnation points, resulting in an incorrect estimation of the Taylor microscale.

dynamics

Article

Characterising Single and Two-Phase Homogeneous Isotropic Turbulence with Stagnation Points

Amélie Ferran [1,2], Sofía Angriman [3], Pablo D. Mininni [3] and Martín Obligado [1,*]

[1] Université Grenoble Alpes, CNRS, Grenoble-INP, LEGI, F-38000 Grenoble, France; amelie.ferran1@univ-grenoble-alpes.fr
[2] Department of Mechanical Engineering, University of Washington, Seattle, DC 98195-2600, USA
[3] Departamento de Física & IFIBA, CONICET, Facultad de Ciencias Exactas y Naturales, Universidad de Buenos Aires, Ciudad Universitaria, Buenos Aires 1428, Argentina; sangriman@df.uba.ar (S.A.); mininni@df.uba.ar (P.D.M.)
* Correspondence: martin.obligado@univ-grenoble-alpes.fr

Abstract: It has been shown that, for dense, sub-Kolmogorov particles advected in a turbulent flow, carrier phase properties can be reconstructed from the particles' velocity field. For that, the instantaneous particles' velocity field can be used to detect the stagnation points of the carrier phase. The Rice theorem can therefore be used, implying that the Taylor length is proportional to the mean distance between such stagnation points. As this model has been only tested for one-dimensional time signals, this work discusses if it can be applied to two-phase, three-dimensional flows. We use direct numerical simulations with turbulent Reynolds numbers Re_λ between 40 and 520 and study particle-laden flows with a Stokes number of $St = 0.5$. We confirm that for the carrier phase, the Taylor length is proportional to the mean distance between stagnation points with a proportionality coefficient that depends weakly on Re_λ. Then, we propose an interpolation scheme to reconstruct the stagnation points of the particles' velocity field. The results indicate that the Rice theorem cannot be applied in practice to two-phase three-dimensional turbulent flows, as the clustering of stagnation points forms very dense structures that require a very large number of particles to accurately sample the flow stagnation points.

Keywords: turbulent flow; direct numerical simulations; particle-laden turbulent flows

check for updates

Citation: Ferran, A.; Angriman, S.; Mininniand, P.D.; Obligado, M. Characterising Single and Two-Phase Homogeneous Isotropic Turbulence with Stagnation Points. *Dynamics* **2022**, 2, 63–72. https://doi.org/10.3390/dynamics2020004

Academic Editor: Christos Volos

Received: 9 March 2022
Accepted: 11 April 2022
Published: 15 April 2022

1. Introduction

Turbulent flows laden with inertial particles are widely encountered in nature, playing a preeminent role in particles dispersion in the atmosphere, rain formation and marine snow sedimentation, among others [1,2]. They are also relevant for several industrial flows, such as fuel or coal combustion, fluidized beds reactors and separation techniques. One of the main challenges to characterizing these flows is the need to simultaneously resolve the particle positions and velocities and the flow velocity field at their scale [3,4]. All these configurations involve highly turbulent three-dimensional flows, which can be highly inhomogeneous and unsteady, where possible finite-size effects from particles may also be present. In this work we focus on a simplified case: homogeneous isotropic turbulent flows (HIT) laden with point-like inertial particles.

The stagnation points of velocity fields in turbulent flows present several relevant characteristics that can be used to gain further understanding of these systems. For instance, the zero-crossings of fluctuating one-dimensional velocity signals have been extensively studied, as they can be used to quantify the Taylor microscale λ of homogeneous isotropic turbulence via the Rice theorem [5–7]. As a consequence, these structures have been intensively studied over the last years, in works that cover the energy cascade of turbulence [8,9] and atmospheric flows [10,11], among others. They present several advantages, such as the zero-crossings of a velocity signal being robust when the flow is unsteady and/or the calibration of probes is not guaranteed. Furthermore, it has recently been shown that they can also be used to quantify the integral length scale L [12,13].

While most works focus on zero crossings, others have considered the case of stagnation points (STPS), defined as the set of velocity nulls satisfying $\mathbf{v}(\mathbf{x_n}) = 0$, where $\mathbf{v}$ is the fluid velocity field [14,15]. In particular, Goto and Vassilicos [16] generalized the Rice theorem, finding a relation between the number density of STPS and λ,

$$\lambda = B n_s^{-1/3}, \tag{1}$$

with B a constant that may vary with Re_λ due to the dependency of the non-Gaussianity of velocity derivatives with this parameter. While the study from Goto and Vassilicos [16] confirmed the validity of this theorem, it did not explore a sufficiently large range of Reynolds numbers based on the Taylor scale Re_λ to report on the dependency $B(Re_\lambda)$.

Although these studies concern single-phase turbulent flows, it has recently been proposed that the Rice theorem can be applied to particle-laden turbulent flows. The work by Mora et al. [17] developed an experimental method to estimate the carrier-flow turbulent kinetic energy dissipation rate ε in the presence of inertial sub-Kolmogorov particles at moderate Re_λ. Its foundations rely on the unladen flow dissipation calculation using the Rice theorem, and the density of zero crossings n_s. Moreover, the results from such a model apply, in principle, also to three-dimensional particle velocities depending on the simplified equation of motion,

$$\frac{d\mathbf{v}_p}{dt} = -\frac{1}{\tau_p}[\mathbf{v}_p - \mathbf{u}(\mathbf{x}_p, t)], \tag{2}$$

with $\mathbf{v}_p$ the particle velocity and $\mathbf{u}(\mathbf{x}_p, t)$ the carrier's flow velocity evaluated at the particle's location $\mathbf{x}_p$, and τ_p the particle viscous response (defined in the next section). This simplified model relies on two conditions: the diameter of the particles must be smaller than the Kolmogorov lengthscale of turbulence η, and their density must be much larger than the carrier's flow density. The Fourier transform of Equation (2) yields,

$$\hat{\mathbf{v}}_p = \frac{\hat{\mathbf{u}}}{i\omega\tau_p + 1}. \tag{3}$$

As a consequence, the particle field velocity is a low-pass filtered version of the carrier phase one, with a cut-off frequency of $f_c = \tau_p^{-1}/2\pi$, or $f_c\tau_\eta = (2\pi St)^{-1}$. The cut-off frequency therefore depends on the Stokes number of inclusions, defined as $St = \tau_p/\tau_\eta$, with $\tau_\eta = (\nu/\varepsilon)^{1/2}$ the flow Kolmogorov time scale (ν is the fluid kinematic viscosity). We can then deduce from Equation (3) that if the cut-off frequency f_c is large enough to resolve the dissipation scales, n_s should be recovered. Thus, it is possible to deduce the value of λ from the particles' velocities. As stated above, while this model has been developed for 1D signals and zero crossings, Equation (3) is already defined for three-dimensional velocities, and the zero-crossings number density can also be redefined as the stagnation points number density [16].

We can therefore conclude, in principle, that the generalized Rice theorem and the model from Mora et al. [17] can be combined to deduce the carrier phase value of λ using inertial particles. This rationale can also give access to other small-scale quantities, such as ε and η, among others. Beyond its fundamental interest, this could also be used to quantify the carrier phase properties in experiments of two-phase turbulent flows. Indeed, to resolve the carrier phase simultaneously with the inclusions velocities in such conditions is beyond the possibilities of current experimental techniques. Finally, to quantify these properties of the carrier phase would also help to detect the presence of two-way coupling between the inertial particles and the carrier flow.

The first two conditions for the applicability of this model are: (i) that Equation (3) holds, and (ii) that the cut-off frequency verifies the relation $f_c\tau_\eta = (2\pi St)^{-1} > 10^{-2}$. This condition is proposed based on the fact that Vassilicos and collaborators [8,9] found that, when low-pass filtering zero crossings n_s with cut-off frequencies at least one order of magnitude larger than the Kolmogorov length-scale, such low-pass filtered velocity records were still able to resolve the value of λ. The last condition, (iii) is to have enough particles to sample all the stagnation points present in the flow. This latter condition has the added constraint that stagnation points are known to form dense clusters [14], thus making the sampling of these points more difficult.

This work aims at studying the applicability of the aforementioned model for stagnation points. We use direct numerical simulations (DNSs) with random forcing, that avoid experimental errors that may contaminate the counting of stagnation points [7]. The results could be extended to experimental fields of particles advected by turbulent flows. We will first focus on verifying the applicability of the generalized Rice theorem (Equation (1)) to our DNSs, which span a wide range of Re_λ that goes between 40 and 520. We will particularly focus on the dependency of B with Re_λ, not discussed in previous works, and in verifying the applicability of Equation (1) to instantaneous velocity fields. Then, on a second part, we will use the method of Mora et al. [17] to study DNSs of two-phase flows with $Re_\lambda = 240$, using up to 10^7 tracers (i.e., $St = 0$) that follow the streamlines of the flow, and inertial particles ($St = 0.5$) that evolve according to Equation (2). Our results indicate that the model may not apply unless an extremely large number of particles is injected, as the clusters of stagnation points require a very large spatial resolution (or particle densities) to be resolved.

2. Numerical Simulations

Our study was conducted using DNSs at five different values of Re_λ using the GHOST code [18,19]. These simulations follow standard practices regarding their temporal integration, dealiasing procedures, and have an adequate spatial resolution of the smallest scales, i.e., $\kappa\eta \gtrsim 1$ (where $\kappa = N/3$ is the maximum resolved wavenumber in Fourier space and N the linear spatial resolution [20]). The Kolmogorov lengthscale η is defined as $\eta = (\nu^3/\varepsilon)^{1/4}$. Fully dealiased pseudospectral methods with second-order Runge–Kutta methods for the time stepping are used. The 3D simulation domain for all datasets has dimensions of $2\pi \times 2\pi \times 2\pi$. All relevant parameters can be found in Table 1.

Table 1. Relevant parameters from the DNS used in this study. N is the number of points in the DNS in one axis, such that N^3 is the total number of grid points in the simulation domain. $\mathcal{L}/(2\pi)$ is the integral lengthscale in units of the domain linear size 2π. η is the Kolmogorov dissipation scale. Re_λ is the Reynolds number based on the Taylor microscale λ. "# snapshots" is the number of snapshots of the vector fields used for the analysis, and $\langle\text{\# STPS}\rangle_{snps}$ the averaged number of STPS (i.e., stagnation points) over the total number of snapshots.

Dataset	N	$\mathcal{L}/(2\pi)$	η	Re_λ	# Snapshots	$\langle\text{\# STPS}\rangle_{snps}$
DNS-64	64	0.304	50×10^{-3}	40	80	68
DNS-128	128	0.291	24×10^{-3}	70	50	267
DNS-256	256	0.291	12×10^{-3}	120	50	700
DNS-512	512	0.238	6×10^{-3}	240	15	5707
DNS-1024	1024	0.309	3×10^{-3}	520	9	7078

Numerical simulations solve the incompressible Navier–Stokes equations for the velocity $\mathbf{u}$ with a random solenoidal forcing $\mathbf{f}$,

$$\frac{D\mathbf{u}}{Dt} = \frac{\partial \mathbf{u}}{\partial t} + \mathbf{u} \cdot \nabla \mathbf{u} = -\nabla p' + \nu \nabla^2 \mathbf{u} + \mathbf{f}, \tag{4}$$

where $p' = p/\rho$ (with p the pressure and ρ a uniform mass density), which is obtained from the incompressibility condition $\nabla \cdot \mathbf{u} = 0$. In Equation (4), $D\mathbf{u}/Dt = \mathbf{a}$ is the Lagrangian acceleration of the fluid elements. We define the r.m.s. velocity as $u' = \left\langle |u_i|^2 \right\rangle^{1/2}$ (where u_i is a Cartesian component of the velocity and Einstein notation is used), the Taylor microscale is $\lambda = (15\nu u'^2/\varepsilon)^{1/2}$, and the integral scale is $\mathcal{L} = \pi/(2u'^2) \int E(k)/k\, dk$ (where $E(k)$ is the isotropic energy spectrum).

The solenoidal forcing $\mathbf{f}$ is given by a superposition of Fourier modes with random phases in the shell with wavenumber $k = 1$. A new random forcing was generated every 0.5 large-scale turnover time, and the forcing was linearly evolved from its previous state to the next state along this period of time. This results in a continuous and slowly evolving random forcing with a correlation time of 0.5 turnover times, which at the largest resolution considered has an integral scale $\mathcal{L}/(2\pi) \approx 0.309$, and which will be useful for simulations with inertial particles, as discussed below. The simulations also use the largest Reynolds number attainable at their spatial resolution, with $\kappa\eta \approx 1$ (see Table 1).

We use five numerical datasets, labeled in the following as "DNS-N", where N is the linear resolution of each dataset. The Taylor-based Reynolds number, $Re_\lambda = u'\lambda/\nu$, spans more than one decade. We have $Re_\lambda \in [40, 520]$ for spatial resolutions of 64^3, 128^3, 256^3, 512^3, and 1024^3 grid points (see Figure 1). We stored enough snapshots of the vector fields to have adequate global statistics. For all datasets, we applied the method proposed by Haynes and collaborators [21–23] to compute the stagnation points. This method goes through each cell of the DNS domain and uses the velocity values of the eight cell's corners. If there is a change of sign in all the three velocity components, a local trilinear interpolation function is created with the corner's velocity values. Then the Newton method is used to find any velocity nulls within the cell. If there is no change of sign in any of the three velocity components then no velocity nulls should be contained in the cell for a well resolved DNS. Both elliptic and hyperbolic stagnation points were considered. More details about this method can be found in references [14,21].

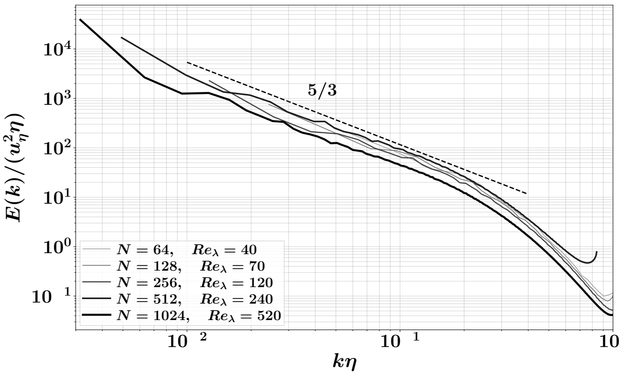

Figure 1. Power spectral density as a function of the wavenumber normalized by the Kolmogorov scale η and velocity u_η (defined as $u_\eta = (\nu\varepsilon)^{1/4}$), for the five DNSs at different resolutions. The dashed line represents a Kolmogorov $-5/3$ power law scaling shown as a reference.

For DNS-512 we also have data of tracers and inertial point particles without gravity. Particles are integrated following Equation (2), which can be written as:

$$\frac{d\mathbf{x}_p}{dt} = \mathbf{v}_p, \quad \frac{d\mathbf{v}_p}{dt} = \frac{1}{\tau_p}\left[\mathbf{u}(\mathbf{x}_p) - \mathbf{v}_p\right]. \tag{5}$$

These equations are integrated with a high-order Runge–Kutta method to evolve in time and a high-order three-dimensional spatial spline interpolation to estimate the fluid velocity $\mathbf{u}(\mathbf{x}_p)$ at the particle position (see [24,25] for details). Simulations with particles are conducted as follows: first, a DNS of the Eulerian flow is conducted without particles, until a turbulent steady state is reached. Then, particles are injected with a uniform random distribution in space, and with the same initial velocity as the velocity of the fluid element at the particle position. Particles are integrated for several turnover times (in the case of tracers) or for several particle relaxation times (in the case of inertial particles) before data starts to be collected for the analysis.

In order to apply the method described in the introduction, the particles' velocities $\mathbf{v}_p$ were interpolated using the 'griddata' function in the interpolate module of the SciPy library. Particles' velocities were thus interpolated on the DNS Eulerian grid points with a linear interpolation. For points outside the particles' position range, on the boundaries of the DNS domain, the nearest method was employed, obtaining a synthetic velocity field from the particles for each snapshot. We therefore proceeded to apply the method from Haynes [21] and collaborators here too, to detect the stagnation points.

As discussed above, we used two types of particles: inertial particles with $St = 0.5$ and tracers with $St = 0$. While tracers are expected to sample the flow uniformly, the former have been reported to cluster [14]. For each type of particle, two DNSs were run, one with 10^6 particles and another with 10^7. This will allow us in the next sections to analyse the influence of the number of particles in the convergence of the Rice theorem, and to verify if it actually applies for our datasets (we remind the reader that particles are injected only for the $N^3 = 512^3$ run, i.e., with $\approx 1.3 \times 10^8$ Eulerian grid points). In the following, our datasets with particles will be labelled as:

- DNS-512-1: $N = 512$, 10^6 tracers, $St = 0$.
- DNS-512-2: $N = 512$, 10^6 inertial particles with $St = 0.5$.
- DNS-512-3: $N = 512$, 10^7 tracers, $St = 0$.
- DNS-512-4: $N = 512$, 10^7 inertial particles with $St = 0.5$.

As each run was performed independently, and given that we used random forcing, the temporal evolution of the single-phase flow is not expected to be identical for all datasets.

3. Results

3.1. Validation of the Generalized Rice Theorem in Single-Phase Turbulent Flows

We first verify the validity of the generalized Rice theorem for our DNSs. To this end, in Figure 2 we plot the prefactor B in the Rice theorem (defined in Equation (1)) as a function of Re_λ. Figure 2a is deduced for each instantaneous Eulerian velocity field from the DNSs at $N = 512$, with Re_λ also computed instantaneously for each snapshot (n_{sf} denotes the density of stagnation points in the Eulerian fluid velocity). On the other hand, Figure 2b shows the value of B for all resolutions N in the DNSs, and averaged over all snapshots corresponding to that run as detailed in Table 1 (Re_λ is also computed from the averaged characteristic quantities). Our results are in good agreement with the generalized Rice theorem, as we find B is of order unity and has a small dependency with Re_λ. Furthermore, our results are consistent with the study from Goto and Vassilicos [16] on a similar flow. Note that while this study focused on the range $Re_\lambda \in [60, 150]$, in Figure 2b we extend the validity of the theorem to $Re_\lambda \in [40, 520]$.

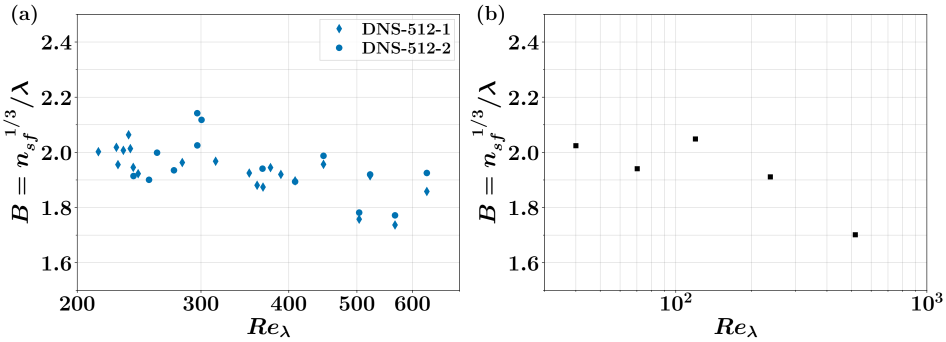

Figure 2. Prefactor B in the Rice theorem, as a function of Re_λ, and computed from the density of stagnation points of the Eulerian fluid velocity n_{sf}. In panel (**a**) we show the instantaneous value of B versus an instantaneous Re_λ for the 512-DNS simulation. Panel (**b**) presents an averaged B plotted against Re_λ computed from averaged quantities, for the five different DNS resolutions.

Our DNSs also show that B is a slowly decreasing function with Re_λ, and therefore presents the opposite trend as the one found for zero-crossings of the fluctuating velocity [8] (but consistent with the constant value found in [9], where the same flow was studied for a large range of Re_λ). This result is surprising, as it suggests that the contribution of small-scale intermittency effects decreases when Re_λ is increased.

The good collapse of all fields shown in Figure 2a,b suggests that the generalized Rice theorem is valid not only when averaging in time Eulerian fields, but also for instantaneous realisations. To confirm this feature, Figure 3a shows the temporal evolution of $n_{sf}^{-1/3}$ and λ for DNS-512-1 and DNS-512-2 for the Eulerian fluid velocity field. It can be observed that both curves present almost identical trends, with values of B that remain almost constant (see Figure 3b). We therefore conclude that the generalized Rice theorem applies to our datasets, for a wide range of Re_λ as well as for instantaneous velocity fields.

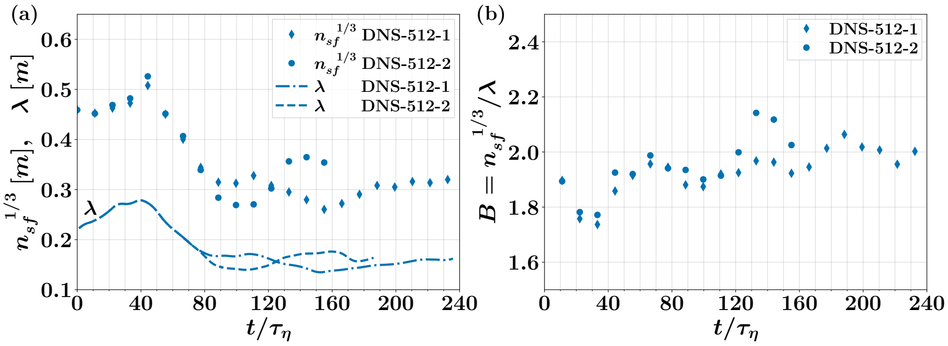

Figure 3. (**a**) Density of the velocity stagnation points $n_{sf}^{-1/3}$ for the fluid phase (symbols), and Taylor microscale λ (lines) along time. (**b**) Time evolution of B, i.e., the ratio of $n_{sf}^{-1/3}$ to λ. This figure only shows the fluid phase data of the DNS-512-1 and DNS-512-2 simulations.

3.2. Validation of the Rice Theorem in Two-Phase Turbulent Flows

We now proceed to study the applicability of the generalized Rice theorem to particle-laden flows. It can be easily seen that for both $St = 0$ and $St = 0.5$ the condition $f_c \tau_\eta = (2\pi St)^{-1} > 10^{-2}$ holds. Additionally, the applicability of Equation (2) is trivially valid in our case, as particles evolve according to it in the simulations. Figure 4 shows the reconstructed (i.e., interpolated) x velocity field component using 10^7 particles with $St = 0$ or $St = 0.5$, compared to the actual Eulerian flow velocity component. Fields are very similar, although not identical. The squared point-wise differences between the three velocity fields are presented in Figure 5. Discrepancies between the flow field and inertial particles are expected (Figures 4c and 5b), as Equation (3) implies that the STPS may be preserved but not the velocity values elsewhere. Furthermore, this is also expected when comparing the flow velocity and the tracers (Figure 4a,b respectively, or see Figure 5a), as the latter are also expected to preserve the null points but, depending on the number of particles present in the flow, could result in a coarse-grained reconstruction of the former. Moreover, as expected, the tracers' reconstructed field shows fewer differences with the flow field than the inertial particles (see Figure 5a,b).

We can therefore study the validity of Equation (1) in our DNSs. A first test is to compare the number of STPS detected for the carrier phase and for the interpolated (tracer or inertial) particle velocity fields (Figure 6a). Surprisingly, we see that for any of the particle sets, a smaller number of STPS are detected, and even when injecting 10^7 tracers we have 30% fewer STPS in the interpolated field (Figure 6a). This surprising result points towards the inapplicability of the model from Mora et al. [17] to our datasets. This is confirmed when comparing $n_{sp}^{-1/3}$ for the tracers' interpolated field and λ in Figure 6b, as we find values of B to always be larger than those found for the Eulerian flow velocity in Figure 3b. Nevertheless, Figure 6b suggests that, while the generalized Rice theorem does not apply exactly, some trends are still recovered. In other words, a calibrated value of $B(St, N_{\text{part}}, \dots)$ (where N_{part} is the total number of particles) could be used if data are available from, e.g., numerical simulations.

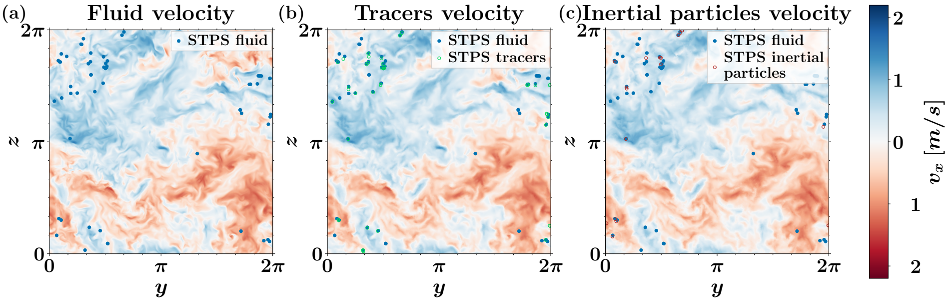

Figure 4. (**a**) Two dimensional (2D) slice of the fluid velocity at $x = \pi/2$ and $t = 22\tau_\eta$. (**b**) Same slice showing the tracers' interpolated velocity. (**c**) Same slice showing the inertial particles' interpolated velocity. In (**b**,**c**), 10^7 tracers or particles were used. In all panels, blue dots correspond to the positions of STPS in the single phase flow. Black and red circles correspond to STPS detected from the tracers and inertial particles fields, respectively. As the amount of STPS in a 2D slice can be small, in all panels we show all STPS in a slice with 6 grid points in x (i.e., the STPS detected in $x \in \pi/2 \pm 6\pi/512$).

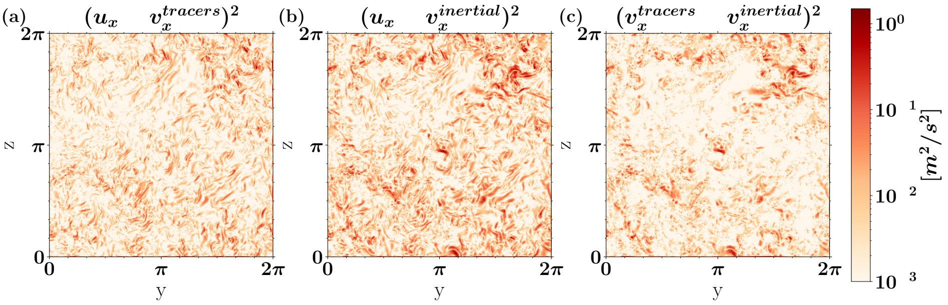

Figure 5. Point-wise squared difference between the different slices presented in Figure 4. The three panels correspond to the differences between the fluid velocity and tracers' interpolated velocity (**a**), fluid velocity and inertial particles' velocity (**b**) and tracers and inertial particles velocity (**c**).

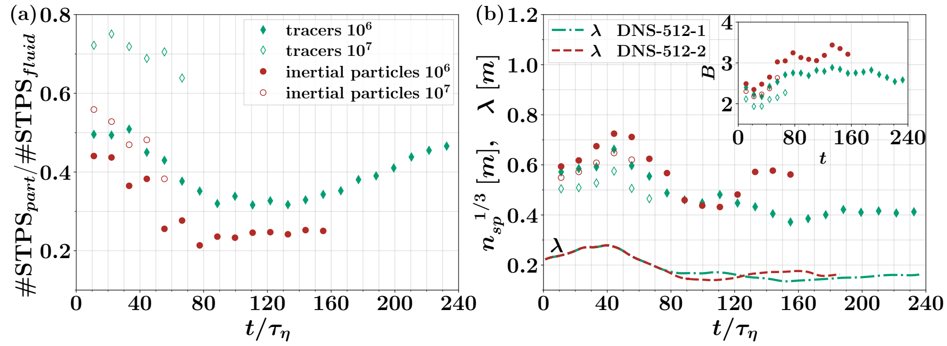

Figure 6. (**a**) Number of stagnation points in the interpolated velocity field for tracers (green diamonds) and inertial particles (red circles), normalized by the number of stagnation points in their respective fluid phase versus the time normalized by τ_η. (**b**) Temporal evolution of the stagnation points density $n_{sp}^{-1/3}$ for the interpolated tracers and inertial particles velocity (symbols), and Taylor microscale (lines). The inset shows the time evolution of the prefactor $B = n_{sp}^{-1/3}/\lambda$ of the Rice theorem for the four two-phase flows DNS. Note the simulations with 10^7 particles are shorter in time.

As the only condition that may be violated is to have enough particles to sample all stagnation points in the flow, we will now analyse this hypothesis. For all $N = 512$ DNSs, we find that the carrier phase has values of $n_{sf}^{-1/3}$ of around 0.3. This implies that we have around 30 stagnation points per unit of volume (with a total volume of $(2\pi)^3$ in our DNSs). Conversely, we have 4×10^3 and 4×10^4 (inertial or tracer) particles per unit of volume when injecting, respectively, 10^6 and 10^7 inclusions.

These densities imply that, in principle, all stagnation points should be resolved by the interpolated fields. However, as we discussed in the introduction, this consideration does not take into account the clustering of stagnation points. Indeed, Figure 7a,b shows the presence of strong clusters of STPS in the flow. Using similar DNSs, a previous work [14] showed that stagnation points form very dense clusters, and that clustering increases significantly with Re_λ (as shown in Figure 7c). Such clustering (against, e.g., an homogeneous spatial distribution of points) implies that to resolve all stagnation points would require injecting many more particles, as dense regions of stagnation points also require larger densities of particles to be resolved with our interpolation scheme. This can also be seen in Figure 4, where the interpolated fields for both tracers and inertial particles do not recover all stagnation points in dense regions. We remark that tracers are instead distributed homogeneously in space, while inertial particles are also known to form clusters in turbulent flows, but the positions of such clusters are not directly related to the positions of those formed by the stagnation points [14].

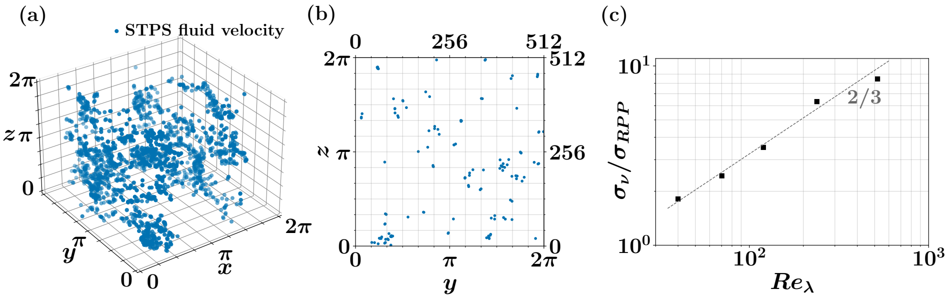

Figure 7. Illustration of the fluid velocity clustering of stagnation points in DNS-512-2. (**a**) Three dimensional (3D) view of the fluid velocity stagnation points positions for $t = 22\tau_\eta$. (**b**) 2D view of an y, z plane at the same instant for a 6 grid points slice with $x \in \pi/3 \pm 6\pi/512$. (**c**) Ratio of the standard deviation of the Voronoï cells volumes of stagnation points with respect to the standard deviation of a Poisson distribution (RPP) for the DNSs with the five resolutions. This parameter is expected to quantify clustering intensity [14] (i.e., when $\sigma_\mathcal{V}/\sigma_{RPP}$ increases, clustering becomes more important).

Besides this effect, another important effect that can explain why the particles see fewer zeros than the number of STPS in the Eulerian field is associated with the stability of stagnation points in 3D flows [26]. Even in the simpler 2D case, most instantaneous stagnation points can be classified into elliptic or hyperbolic types, depending on their local stability. Tracers and inertial particles can be expected to spend longer times around elliptic points, whereas hyperbolic points should quickly push nearby tracers and inertial particles along their unstable manifolds. In 3D, the possible topologies of velocity field nulls are more complex, but any 3D stagnation point with an unstable manifold should have the same effect. As a result, STPS are sampled differently depending on their topology, and some STPS will be less sampled than others. This can be another important reason behind the lower number of detected zeros from the 3D particles' fields.

4. Conclusions

Throughout this work we used DNS data to study the applicability of the generalized Rice theorem to single and two-phase flows. Our results can be summarised as follows:

- We verified the validity of the generalized Rice theorem for our dataset, which covers the range $Re_\lambda \in [40, 520]$. Furthermore, we showed that the prefactor B in Equation (1), that quantifies the non-Gaussianity of velocity derivatives, has a weak dependence with Re_λ, and that it tends to decrease when this parameter is increased.

- Furthermore, we showed that the generalized Rice theorem applies for time-averaged three-dimensional velocity fields, but also for instantaneous realizations.
- We proposed an interpolation scheme to reconstruct the stagnation points using the particles' velocity field. Our results indicate that the Rice theorem cannot be applied in practice to two-phase three-dimensional turbulent flows, as the clustering of stagnation points forms very dense structures that require a very large number of particles to accurately sample the flow stagnation points. Even with 10^7 tracers or inertial particles, we did not manage to apply the Rice theorem satisfactorily.
- We find that this lack of resolution of stagnation points is consistent with the strong clustering of STPS, as it implies the presence of very dense regions of these points, which require the injection of a very high number density of particles to be resolved. Another possible explanation for the lower number of STPS detected with the particles' velocity field is the local stability of 3D STPS with unstable manifolds.
- While the number of the carrier phase STPS is always larger than the one obtained when using the interpolation scheme proposed here, we do find that they evolve over time following similar trends. This feature requires further study to be validated.

In conclusion, our study suggests that the generalized Rice theorem and the rationale from Mora et al. [17] cannot be used in a practical way to reconstruct the carrier phase from particles' measurements in turbulent two-phase flows. Its application would require a number of particles that would make such study extremely hard using modern experimental techniques.

Author Contributions: A.F.: Investigation, Methodology, Data curation, Visualization; S.A.: Investigation, Methodology, Data curation, Visualization; P.D.M.: Conceptualisation, Investigation, Methodology; M.O.: Conceptualisation, Investigation, Methodology. All authors have read and agreed to the published version of the manuscript.

Funding: This work was partially supported by the ECOS project A18ST04. A.F. and M.O. acknowledge the LabEx Tec21 (Investissements d'Avenir-Grant Agreement # ANR-11-LABX-0030), and the ANR project ANR-15-IDEX-02 for funding this work. S.A. and P.D.M. acknowledge support from UBACYT Grant No. 20020170100508BA and PICT Grant No. 2018-4298.

Institutional Review Board Statement: Not applicable.

Informed Consent Statement: Not applicable.

Data Availability Statement: Data will be made available by corresponding authors upon reasonable request.

Acknowledgments: The authors thank Daniel Mora for fruitful discussions.

Conflicts of Interest: The authors declare no conflict of interest. The funders had no role in the design of the study; in the collection, analyses, or interpretation of data; in the writing of the manuscript, or in the decision to publish the results.

References

1. Toschi, F.; Bodenschatz, E. Lagrangian Properties of Particles in Turbulence. *Annu. Rev. Fluid Mech.* **2009**, *41*, 375–404. [CrossRef]
2. Balachandar, S.; Eaton, J.K. Turbulent dispersed multiphase flow. *Annu. Rev. Fluid Mech.* **2010**, *42*, 111–133. [CrossRef]
3. Monchaux, R.; Bourgoin, M.; Cartellier, A. Analyzing preferential concentration and clustering of inertial particles in turbulence. *Int. J. Multiph. Flow* **2012**, *40*, 1–18. [CrossRef]
4. Crowe, C.; Troutt, T.; Chung, J. Numerical models for two-phase turbulent flows. *Annu. Rev. Fluid Mech.* **1996**, *28*, 11–43. [CrossRef]
5. Rice, S.O. Mathematical analysis of random noise. *Bell Syst. Tech. J.* **1945**, *24*, 46–156. [CrossRef]
6. Liepmann, H.; Robinson, M. *Counting Methods and Equipment for Mean-Value Measurements in Turbulence Research*; NACA: Washington, DC, USA, 1953.
7. Sreenivasan, K.; Prabhu, A.; Narasimha, R. Zero-crossings in turbulent signals. *J. Fluid Mech.* **1983**, *137*, 251–272. [CrossRef]
8. Mazellier, N.; Vassilicos, J. The turbulence dissipation constant is not universal because of its universal dependence on large-scale flow topology. *Phys. Fluids* **2008**, *20*, 015101. [CrossRef]

9. Mora, D.O.; Muñiz Pladellorens, E.; Riera Turró, P.; Lagauzere, M.; Obligado, M. Energy cascades in active-grid-generated turbulent flows. *Phys. Rev. Fluids* **2019**, *4*, 104601. [CrossRef]
10. Akinlabi, E.O.; Wacławczyk, M.; Mellado, J.P.; Malinowski, S.P. Estimating turbulence kinetic energy dissipation rates in the numerically simulated stratocumulus cloud-top mixing layer: Evaluation of different methods. *J. Atmos. Sci.* **2019**, *76*, 1471–1488. [CrossRef]
11. Wacławczyk, M.; Ma, Y.F.; Kopeć, J.M.; Malinowski, S.P. Novel approaches to estimating the turbulent kinetic energy dissipation rate from low-and moderate-resolution velocity fluctuation time series. *Atmos. Meas. Tech.* **2017**, *10*, 4573–4585. [CrossRef]
12. Mora, D.O.; Obligado, M. Estimating the integral length scale on turbulent flows from the zero crossings of the longitudinal velocity fluctuation. *Exp. Fluids* **2020**, *61*, 199. [CrossRef]
13. Zheng, Y.; Nagata, K.; Watanabe, T. Turbulent characteristics and energy transfer in the far field of active-grid turbulence. *Phys. Fluids* **2021**, *33*, 115119. [CrossRef]
14. Mora, D.; Bourgoin, M.; Mininni, P.; Obligado, M. Clustering of vector nulls in homogeneous isotropic turbulence. *Phys. Rev. Fluids* **2021**, *6*, 024609. [CrossRef]
15. Davila, J.; Vassilicos, J. Richardson's pair diffusion and the stagnation point structure of turbulence. *Phys. Rev. Lett.* **2003**, *91*, 144501. [CrossRef] [PubMed]
16. Goto, S.; Vassilicos, J. The dissipation rate coefficient of turbulence is not universal and depends on the internal stagnation point structure. *Phys. Fluids* **2009**, *21*, 035104. [CrossRef]
17. Mora, D.O.; Cartellier, A.; Obligado, M. Experimental estimation of turbulence modification by inertial particles at moderate Re_λ. *Phys. Rev. Fluids* **2019**, *4*, 074309. [CrossRef]
18. Mininni, P.; Rosenberg, D.; Reddy, R.; Pouquet, A. A hybrid MPI–OpenMP scheme for scalable parallel pseudospectral computations for fluid turbulence. *Parallel Comput.* **2011**, *37*, 316–326. [CrossRef]
19. Rosenberg, D.; Mininni, P.D.; Reddy, R.; Pouquet, A. GPU Parallelization of a Hybrid Pseudospectral Geophysical Turbulence Framework Using CUDA. *Atmosphere* **2020**, *11*, 178. [CrossRef]
20. Pope, S.B. *Turbulent Flows*; Cambridge University Press: Cambridge, UK, 2000.
21. Haynes, A.L.; Parnell, C.E. A trilinear method for finding null points in a three-dimensional vector space. *Phys. Plasmas* **2007**, *14*, 082107. [CrossRef]
22. Haynes, A.; Parnell, C. A method for finding three-dimensional magnetic skeletons. *Phys. Plasmas* **2010**, *17*, 092903. [CrossRef]
23. Murphy, N.A.; Parnell, C.E.; Haynes, A.L. The appearance, motion, and disappearance of three-dimensional magnetic null points. *Phys. Plasmas* **2015**, *22*, 102117. [CrossRef]
24. Yeung, P.; Pope, S. An algorithm for tracking fluid particles in numerical simulations of homogeneous turbulence. *J. Comput. Phys.* **1988**, *79*, 373–416. [CrossRef]
25. Angriman, S.; Mininni, P.D.; Cobelli, P.J. Velocity and acceleration statistics in particle-laden turbulent swirling flows. *Phys. Rev. Fluids* **2020**, *5*, 064605. [CrossRef]
26. Mancho, A.M.; Small, D.; Wiggins, S. A tutorial on dynamical systems concepts applied to Lagrangian transport in oceanic flows defined as finite time data sets: Theoretical and computational issues. *Phys. Rep.* **2006**, *437*, 55–124. [CrossRef]

B

Clustering in laboratory and numerical turbulent swirling

This appendix present the work conducted with funding from the ECOS project and published in the following paper:

Angriman, S., Ferran, A., Zapata, F., Cobelli, P. J., Obligado, M., & Mininni, P. D. (2022). Clustering in laboratory and numerical turbulent swirling flows. Journal of Fluid Mechanics, 948, A30.

Previous work, performed by the research group in Buenos Aires, focused on comparing experimental von Kármán flow with direct numerical simulations using a Taylor-Green forcing (Angriman, Mininni, and Cobelli 2020; Angriman et al. 2021). Both setups have been shown to present an interesting benchmark for studying inhomogeneous turbulent swirling flows. Using the same DNS code from Mininni et al. 2011, Mora et al. 2021a investigated the clustering properties of inertial particles as well as nulls in the velocity, acceleration, and vorticity fields within homogeneous isotropic turbulence. One remaining unanswered question concerns the influence of the DNS forcing on the particle clustering and on velocity field nulls.

The present study builds upon the aforementionned papers. We are interested in the clustering of nulls of the carrier phase flow fields and of inertial particles in turbulent swirling flows using both experimental and numerical datasets. Results from the Taylor Green forcing were also compared with those in homogeneous and isotropic turbulence.

The author of the present thesis was in charge of conducting the Taylor-Green simulation and analyzing its results. The results analysis involved computing the null positions for the three-dimensional velocity, acceleration, and vorticity fields of the carrier phase using the method of (Haynes and Parnell 2007; Mora et al. 2021a). Subsequently, a Voronoï tesselations procedure was applied to the positions of particles and nulls. The Voronoï analysis included the study of the Voronoï cell distributions, the cluster volumes distributions, and statistics on the number of points per cluster.

J. Fluid Mech. (2022), *vol.* 948, A30, doi:10.1017/jfm.2022.713

Clustering in laboratory and numerical turbulent swirling flows

Sofía Angriman[1,2,†], Amélie Ferran[3,4], Florencia Zapata[1,2], Pablo J. Cobelli[1,2], Martin Obligado[3] and Pablo D. Mininni[1,2]

[1]Departamento de Física, Facultad de Ciencias Exactas y Naturales, Universidad de Buenos Aires, Buenos Aires 1428, Argentina

[2]Instituto de Física de Buenos Aires (IFIBA), CONICET – Universidad de Buenos Aires, Buenos Aires 1428, Argentina

[3]Université Grenoble Alpes, CNRS, Grenoble-INP, LEGI, F-38000 Grenoble, France

[4]Department of Mechanical Engineering, University of Washington, Seattle, WA 98195-2600, USA

(Received 17 March 2022; revised 14 August 2022; accepted 14 August 2022)

We study the three-dimensional clustering of velocity stagnation points, of nulls of the vorticity and of the Lagrangian acceleration, and of inertial particles in turbulent flows at fixed Reynolds numbers, but under different large-scale flow geometries. To this end, we combine direct numerical simulations of homogeneous and isotropic turbulence and of the Taylor–Green flow, with particle tracking velocimetry in a von Kármán experiment. While flows have different topologies (as nulls cluster differently), particles behave similarly in all cases, indicating that Taylor-scale neutrally buoyant particles cluster as inertial particles.

Key words: multiphase flow

1. Introduction

As is often the case in the study of complex systems, turbulence theory has flourished together with the development of laboratory and numerical methods. For homogeneous and isotropic turbulence (HIT), wind tunnel experiments (Taylor 1938; Shen & Warhaft 2002) and numerical simulations in periodic boxes (Kaneda *et al.* 2003; Buaria *et al.* 2019) have played central roles, allowing comparisons with the theory and pushing new ideas. Nonetheless, in non-homogeneous, or multiphase flows, we lack such benchmarks that would allow a much-needed comparison between theory, experiments and simulations.

---

† Email address for correspondence: sangriman@df.uba.ar

In recent years, the von Kármán swirling flow in the laboratory (Mordant *et al.* 2002; Mordant, Lévêque & Pinton 2004; Poncet, Schiestel & Monchaux 2008; Volk *et al.* 2008; Huck, Machicoane & Volk 2017; Angriman, Mininni & Cobelli 2020), and the akin Taylor–Green (TG) flow in numerical simulations (Green & Taylor 1937; Mininni *et al.* 2011; Kreuzahler *et al.* 2014), have provided ways to reach large Reynolds numbers in non-isotropic, non-homogeneous and, in many cases, multiphase flow regimes. Comparisons of experiments and simulations showed that these flows, albeit differing in the forcing mechanism and boundary conditions, share geometrical (Mininni *et al.* 2011; Huck *et al.* 2017; Angriman *et al.* 2020), topological (Huck *et al.* 2017; Angriman *et al.* 2021) and statistical properties (Angriman *et al.* 2020) in both Eulerian and Lagrangian frameworks.

A step forward in these comparisons, that would allow a better understating of flow geometries and that has applications in multiphase flows, is to study the geometrical properties of zeros and accumulation points (Goto & Vassilicos 2006, 2008; Monchaux, Bourgoin & Cartellier 2010; Fiabane *et al.* 2013; Obligado *et al.* 2014; Mora *et al.* 2021). Moreover, the recent study by Mora *et al.* (2021) has performed a combined analysis of nulls spatial properties and inertial particles clustering via Voronoï tessellations. The stagnation points, sampled by inertial particles, have also been used to characterize three-dimensional (3-D) geometrical properties of HIT flows using the Rice theorem (Ferran *et al.* 2022). It is known that even in HIT, nulls of the velocity, vorticity and of the Lagrangian acceleration do not distribute homogeneously in space, forming clusters (Goto & Vassilicos 2006; Mora *et al.* 2021). In multiphase flows, certain particles tend to accumulate preferentially in the vicinity of some of these zeros, affecting their mean free path, and ultimately altering relevant physical processes such as droplet formation in clouds, mixing of chemicals and phase transitions. The effect of mean flows and of flow anisotropy and inhomogeneity in the clustering of nulls of the flow vector fields and of particles is unclear and requires further investigation.

Furthermore, not all particles cluster, and it is still uncertain what parameters govern this phenomenon. Very small (i.e. of the size of the Kolmogorov scale) heavy particles display clustering (Obligado *et al.* 2019). No clustering has been observed for small (below the Taylor microscale, but larger than the Kolmogorov scale) neutrally buoyant particles in experiments of HIT (Fiabane *et al.* 2012), but clustering has been reported for large particles with sizes comparable to the flow integral scale in von Kármán experiments (Machicoane *et al.* 2014, 2016), and attributed to global preferential sampling of the particles of flow inhomogeneities. The intermediate regime, with neutrally buoyant particles of the size of the Taylor microscale has not been studied, and it is unclear whether clustering in such a regime would take place, and in that case whether it would be caused by large-scale flow sampling effects or by inertial clustering mechanisms associated with the existence of certain topological points in the turbulent flow.

In this work we perform a numerical and experimental study of the clustering properties of different single- and two-phase turbulent swirling flows. To this aim, we study and compare the topology of different flows at similar Reynolds numbers (HIT, a Taylor Green flow and a von Kármán experiment) using 3-D Voronoï tessellations of velocity stagnation points (STPS), zeros of the vorticity (WZEROs) and zeros of the Lagrangian acceleration (ZAPS), as well as the clustering of Taylor-scale neutrally buoyant particles (PART) in the von Kármán experiment. Finally, we compare the particles' experimental results with numerical simulations using a minimal model of heavy point particles, to study whether the statistical properties of the clusters of Taylor-scale particles resemble known results of clustering mechanisms in inertial particles.

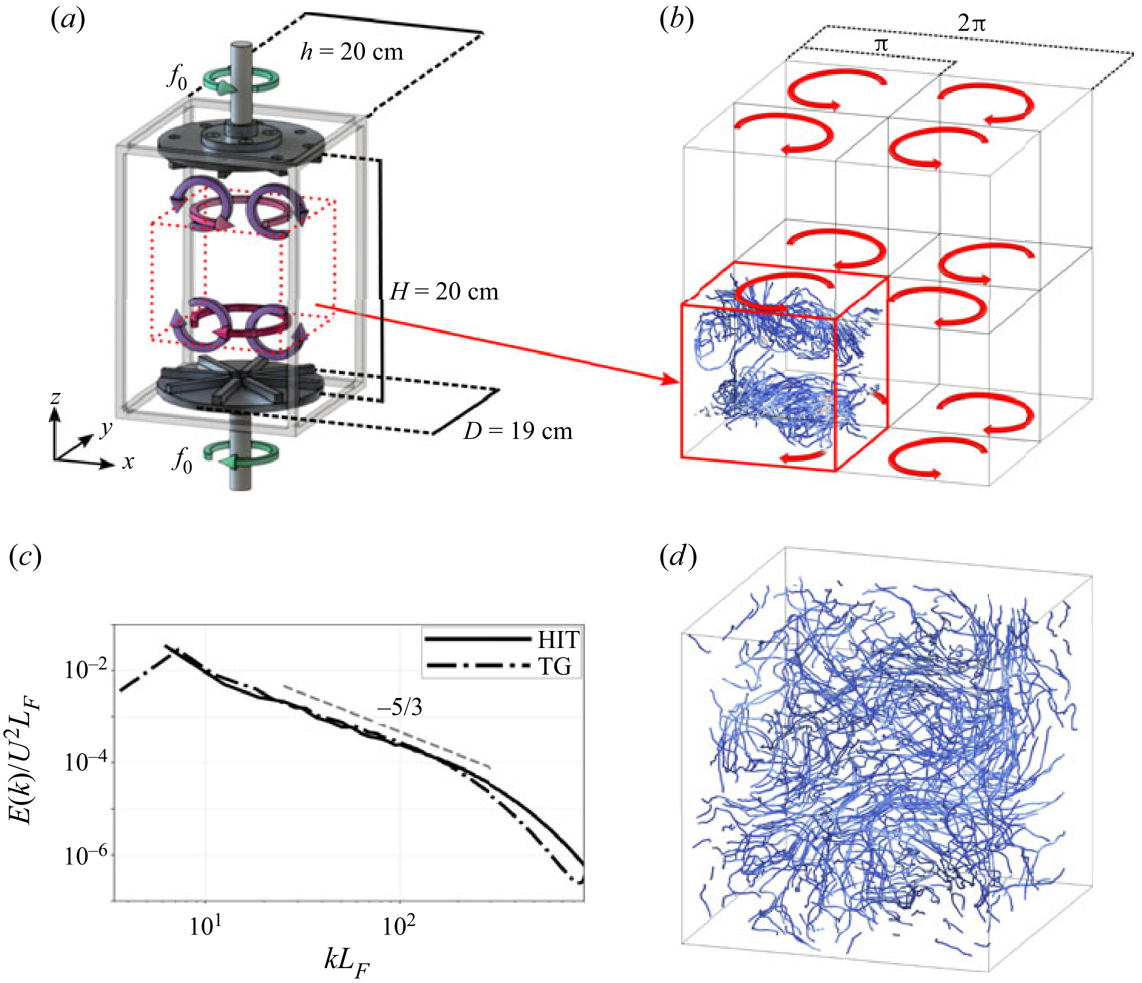

Figure 1. (*a*) Experimental set-up, (*b*) TG and (*d*) HIT simulations. In the 3-D renderings (done with VAPOR; Clyne *et al.* (2007)), the blue lines are streamlines. For the TG simulation in (*b*), streamlines are shown in one 'VK cell', streamlines in the other cells are similar. The curved red arrows indicate the TG forcing direction. (*c*) Eulerian energy spectrum for TG and HIT direct numerical simulations (DNSs), Kolmogorov scaling is shown as a reference.

2. Description of the datasets and particle model

The von Kármán experiment (denoted herein as EXP) consists of two facing disks of diameter $D = 19$ cm (equal to the forcing-based integral scale, L_F^{EXP}), with eight straight blades each, separated by a vertical distance of $H = 20$ cm. The impellers are in a cell of square cross-sectional size $(20 \times 20 \times 50)\ \text{cm}^3$ (room is left at the back of the impellers for shafts to connect them to motors, and for refrigeration coils to remove heat), filled with distilled water from a double-pass reverse osmosis system. The accessible experimental volume, in-between the two disks, is thus of $(20 \times 20 \times 20)\ \text{cm}^3$. Each impeller is driven by a brushless rotary Yaskawa SMGV-20D3A61 servomotor, with Yaskawa SGDV-8R4D01A servo controllers (see Angriman *et al.* (2020) for further details). The two impellers rotate in opposite directions with angular velocity $\pm 2\pi f_0$ ($f_0 =$ 50 revs per minute). This generates two large counter-rotating circulation cells producing, on average, a strong shear layer at the midplane between the disks. A secondary circulation in the axial direction is also generated by the impellers, resulting in a 3-D turbulent flow with an anisotropic large-scale mean flow (depicted schematically in figure 1). We seeded this flow with inertial particles of radius $R = 3$ mm, which are plastic spheres with density 1.02 times the fluid density, 3-D-printed using acrylonitrile butadiene styrene

Dataset	λ/L_F	η/L_F	Re_λ	Re	St	Re_p	$\sigma_{\mathcal{V}}/\sigma_{RPP}$				$\langle V_C\rangle^{1/3}/\eta$			
	$\times 10^{-2}$	$\times 10^{-4}$		$\times 10^{3}$			S	Z	W	P	S	Z	W	P
EXP	2.0	5.0	430	21	9.95	398	—	—	—	2.33	—	—	—	930
TG	3.6	12	227	6.4	9.41	371	4.09	2.69	2.81	2.84	152	39	22	47
HIT	3.3	8.7	377	14	9.88	317	5.41	3.24	3.17	4.15	215	49	25	46

Table 1. Parameters for the experiment (EXP), and for TG and HIT DNSs. Here $\lambda = (15\nu U^2/\varepsilon)^{1/2}$ is the Taylor microscale, with ν the kinematic viscosity, ε the energy injection rate, U the root mean square velocity and $\eta = (\nu^3/\varepsilon)^{1/4}$ is the Kolmogorov length scale, both normalized by the forcing scale L_F; $Re_\lambda = U\lambda/\nu$ and $Re = UL_F/\nu$ are the Taylor and integral scale Reynolds numbers, respectively; St and $Re_p = 2R|\boldsymbol{u} - \boldsymbol{v}|/\nu$ are the particles Stokes and Reynolds numbers; $\sigma_{\mathcal{V}}/\sigma_{RPP}$ is the ratio of standard deviations of the normalized Voronoï volumes to those from a random Poisson process (RPP), while $\langle V_c\rangle^{1/3}$ is the mean linear cluster size, for STPS (S), ZAPS (Z), WZERO (W) and PART (P).

(known as ABS). The particles radius is such that $R/\lambda = 0.77$ and $R/\eta = 31$, with λ the Taylor microscale and η the Kolmogorov length scale (see table 1 for definitions). Measurements of particles' dynamics were carried out in a large observation volume V_{obs}^{EXP} of size $(16 \times 16 \times 16)\ \mathrm{cm}^3$, centred about the geometrical midpoint of the cell, using particle tracking velocimetry with two high-speed Photron FASTCAM SA3 cameras at a sampling rate of 125 frames per second. In total we have $O(10^5)$ frames. In each frame the mean number of particles simultaneously recorded is 11, while their maximum recorded number is 29 (note particles can exit and re-enter the observation volume, exploring also the regions behind the impellers).

We also performed DNSs of the Navier–Stokes equations

$$\partial_t \boldsymbol{u} + \boldsymbol{u} \cdot \nabla \boldsymbol{u} = -\nabla p + \nu \nabla^2 \boldsymbol{u} + \boldsymbol{F}, \tag{2.1}$$

where $\boldsymbol{u}$ is the solenoidal fluid velocity field ($\nabla \cdot \boldsymbol{u} = 0$), p is the pressure per unit mass density, ν is the kinematic viscosity and $\boldsymbol{F}$ is an external volumetric mechanical forcing. Equations are written in dimensionless units based on a unit length L_0 and a unit velocity U_0, and solved in a 3-D 2π-periodic cubic box using a parallel pseudospectral method with the GHOST code (Mininni *et al.* 2011; Rosenberg *et al.* 2020). A fixed spatial resolution of $N^3 = 768^3$ grid points is used. To mimic the geometry of the large-scale flow in the von Kármán experiment, the external forcing $\boldsymbol{F}$ is given by the TG flow,

$$\boldsymbol{F}_{TG} = F_0 \left[\sin(x)\cos(y)\cos(z)\,\hat{x} - \cos(x)\sin(y)\cos(z)\,\hat{y}\right]. \tag{2.2}$$

This forcing corresponds to a periodic array of counter-rotating large-scale vortices, which in the domain $[0, \pi) \times [0, \pi) \times [0, \pi)$ reduces to just two counter-rotating vortices separated vertically by a shear layer (see figure 1, where we call this domain a 'VK cell' by analogy with the von Kármán flow). We also performed a simulation of HIT with random forcing, to compare with the TG DNS and EXP. The HIT simulation was performed following the same procedures used for the TG DNS, using a spatial resolution of 768^3 grid points. Turbulence was sustained by injecting energy in all modes in the vicinity of the Fourier shell with wavenumber $k = 1$, with constant solenoidal amplitude and random phases, i.e. the forcing $\boldsymbol{F}$ is given by

$$\boldsymbol{F}_{HIT} = F_0 \sum_{|\boldsymbol{k}| \in (0,2)} \mathrm{Re}\left\{ \frac{\mathrm{i}\,\boldsymbol{k} \times \hat{\boldsymbol{e}}_{\boldsymbol{k}}}{|\boldsymbol{k}|} \exp\left(\mathrm{i}(\boldsymbol{k} \cdot \boldsymbol{r} + \phi_{\boldsymbol{k}})\right) \right\}, \tag{2.3}$$

where Re denotes real part, $\hat{\boldsymbol{e}}_{\boldsymbol{k}}$ is a unit vector and $\phi_{\boldsymbol{k}}$ is a random phase. The random phases for each mode are slowly evolved in time, with a correlation time of 0.5 large-scale eddy turnover times. For the TG DNS the magnitude of the forcing wavenumber satisfies $|\boldsymbol{k}_F^{TG}| = \sqrt{3}$, so the forcing length scale is defined as $L_F^{TG} = 2\pi/|\boldsymbol{k}_F^{TG}| = 2\pi/\sqrt{3}$, while for HIT $|\boldsymbol{k}_F^{HIT}| = 1$, and then $L_F^{HIT} = 2\pi$ (see table 1 for relevant parameters).

In both simulations we integrate a minimal model of heavy inertial point particles, satisfying the effective equations of motion

$$\dot{\boldsymbol{x}}_p = \boldsymbol{v}(t), \quad \dot{\boldsymbol{v}} = [\boldsymbol{u}(\boldsymbol{x}_p, t) - \boldsymbol{v}(t)]/\tau_p, \tag{2.4a,b}$$

where $\boldsymbol{v}(t)$ and τ_p are the particles velocity and Stokes time, respectively. As the particles radius in EXP is such that the Maxey–Riley approximation is not valid (see, e.g. Qureshi *et al.* (2007), Calzavarini *et al.* (2008), Volk *et al.* (2008) and Homann & Bec (2010) for detailed studies of limitations of this approximation, and of (2.4*a,b*) in particular), and as the equations of motion of our particles are not known, (2.4*a,b*) should be considered as a model with effective parameters, or as a reference model to compare with, to determine whether the clustering of the particles in the experiment resembles the one expected from clustering mechanisms in the case of inertial particles. Note also that, while higher-order terms in the particles radius of the full Maxey–Riley equations could be considered (for instance, considering added mass forces, as done by Calzavarini *et al.* (2008), or keeping Faxén corrections (Calzavarini *et al.* 2009) and Basset–Boussinesq forces (Brennen 2005)), the particles in the experiment have $R \gg \eta$, and therefore the perturbative expansion in R in the Maxey–Riley approximation is not valid (indeed, neutrally buoyant particles slightly larger than η in such approximation do not cluster, see, e.g. the studies in Calzavarini *et al.* (2008) and Reartes & Mininni (2021)). We thus regard (2.4*a,b*) simply as an effective equation with only one tunable parameter. For a brief analysis of how other forces affect the clustering of particles, see appendix A.

The tunable parameter in (2.4*a,b*) depends on the Stokes number of the particles in EXP. For finite-size particles, it is known that their dynamics can depend on many parameters (Fiabane *et al.* 2012), and that the conventional definition of the Stokes number does not properly characterize the particles' dynamics (Xu & Bodenschatz 2008; Fiabane *et al.* 2012). Let us consider the Stokes number $St = \tau_p/\tau_f$, where τ_p is the particle's response time, and τ_f is some characteristic time of the flow. Using the standard definition of the viscous relaxation time of the particle (Cartwright *et al.* 2010),

$$\tau_p^v = \frac{2}{9}\left(\frac{\rho_p}{\rho_f} + \frac{1}{2}\right)\frac{R^2}{\nu}, \tag{2.5}$$

where ρ_p/ρ_f is the particle-to-fluid mass density ratio, and setting τ_f as the Kolmogorov time scale τ_η, for the particles in EXP we obtain $St_v^{EXP} = \tau_p^v/\tau_\eta = 312$. This choice would result in particles almost decoupled from the fluid (i.e. with too much inertia) if used in (2.4*a,b*).

To calculate an effective τ_p for EXP we then set the Stokes number as $St = \tau_p/\tau_\eta$ and we estimate an effective particle time $\tau_p^{EXP} = (R^2/\varepsilon)^{1/3}$ as the turbulent turnover time at the particle radius (Angriman *et al.* 2020). This choice can be understood as follows. For a spherical particle of radius R and mass m_p moving with velocity $\boldsymbol{v}$ in a uniform velocity field $\boldsymbol{u}$, the drag force $\boldsymbol{F}_D$ acting on the particle per unit mass can be estimated as (Batchelor 2000)

$$\frac{\boldsymbol{F}_D}{m_p} = \frac{1}{2}\frac{\rho_p}{m_p} S\, C_D(Re_p)|\boldsymbol{u} - \boldsymbol{v}|(\boldsymbol{u} - \boldsymbol{v}), \tag{2.6}$$

where $\rho_p = 3m_p/(4\pi R^3)$ is the particle's density and $S = 4\pi R^2$ represents its surface. Here $C_D(Re_p)$ is the drag coefficient, which is a function of the particle Reynolds number, defined as $Re_p = 2R|\boldsymbol{u} - \boldsymbol{v}|/\nu$. Then, (2.6) reads

$$\frac{\boldsymbol{F}_D}{m_p} = \frac{3}{2} C_D(Re_p) \frac{|\boldsymbol{u} - \boldsymbol{v}|}{R} (\boldsymbol{u} - \boldsymbol{v}), \tag{2.7}$$

which can be approximated as $\boldsymbol{F}_D/m_p \approx (\boldsymbol{u} - \boldsymbol{v})/\tau_p$, with

$$\tau_p \sim \frac{2}{3} \frac{1}{C_D(Re_p)} \frac{R}{\langle|\boldsymbol{u} - \boldsymbol{v}|\rangle}, \tag{2.8}$$

where angle brackets denote time averages. For finite-size neutrally buoyant particles, Cisse, Homann & Bec (2013) estimated $\langle|\boldsymbol{u} - \boldsymbol{v}|\rangle \sim (\varepsilon R)^{1/3}$, assuming Kolmogorov scaling and proposing a self-similar solution in the surroundings of the particle, and verified the validity of this estimation using DNSs. Substituting their result in (2.8) leads to

$$\tau_p \sim \frac{2}{3} \frac{1}{C_D(Re_p)} \left(\frac{R^2}{\varepsilon}\right)^{1/3}. \tag{2.9}$$

In EXP we can also estimate the particle–fluid slip velocity $|\boldsymbol{u} - \boldsymbol{v}| \approx (|\langle u\rangle^2 - \langle v\rangle^2|)^{1/2}$ from the 3-D root mean square flow and particles' velocities (Bellani & Variano 2012), which gives $Re_p \approx 400$. For this value of Re_p, $C_D \approx 0.6$ (Batchelor 2000; Morrison 2013), and then the dimensionless prefactor $2/[3C_D(Re_p)] \approx 1.1$; thus, the particle response time $\tau_p^{EXP} = (R^2/\varepsilon)^{1/3}$ can be interpreted as an effective time that takes into account the mean effect of nonlinear drag corrections. This in turn yields $St^{EXP} = 9.95$. Other alternative definitions of the Stokes number have been introduced in the literature. For instance, Xu & Bodenschatz (2008) and Schmitt & Seuront (2008) propose to use $\tau_p = \tau_p^{\nu*} = (1/18)(\rho_p/\rho_f)(4R^2/\nu)$, and to set τ_f as the turbulent dynamic time at the scale of the particle, i.e. $\tau_f = (4R^2/\varepsilon)^{1/3}$. For the EXP data this yields $St_{\nu*}^{EXP} = \tau_p^{\nu*}/\tau_R = 14$, which is of the same order of magnitude as our estimation.

In the DNSs, τ_p is set equal to τ_p^{EXP} in units of τ_η (i.e. we set the same Stokes number St within statistical fluctuations). In other words, given the values of τ_η^{DNS} in the simulations, and of the Stokes number St^{EXP} in the experiment, we set τ_p in (2.4*a*,*b*) as $\tau_p^{DNS} = St^{EXP}\tau_\eta^{DNS}$. An effective radius of the particles in the DNSs can then be estimated consistently with (2.9) as $R = [\varepsilon(\tau_p^{DNS})^3]^{1/2}$, and to compute the value of Re_p reported in table 1 for the simulations we use $\boldsymbol{u}$ and $\boldsymbol{v}$ for each particle at every instant. Note both the experimental and numerical estimations of the Reynolds particle number yield $Re_p \gg 1$, reinforcing the fact that models for particles of moderate size do not apply in our case, and that the equations for inertial particles in the DNSs should be understood only as a crude effective model. All the values of St and Re_p for EXP, TG and HIT data are listed in table 1.

3. Results

3.1. *Voronoï volumes probability distribution*

Nulls of all vector fields were computed in the DNSs using the methods described in Haynes & Parnell (2007) and Mora *et al.* (2021). Using the positions of the zeros, and the particles' positions in the experiment and DNSs, 3-D Voronoï tessellations were computed

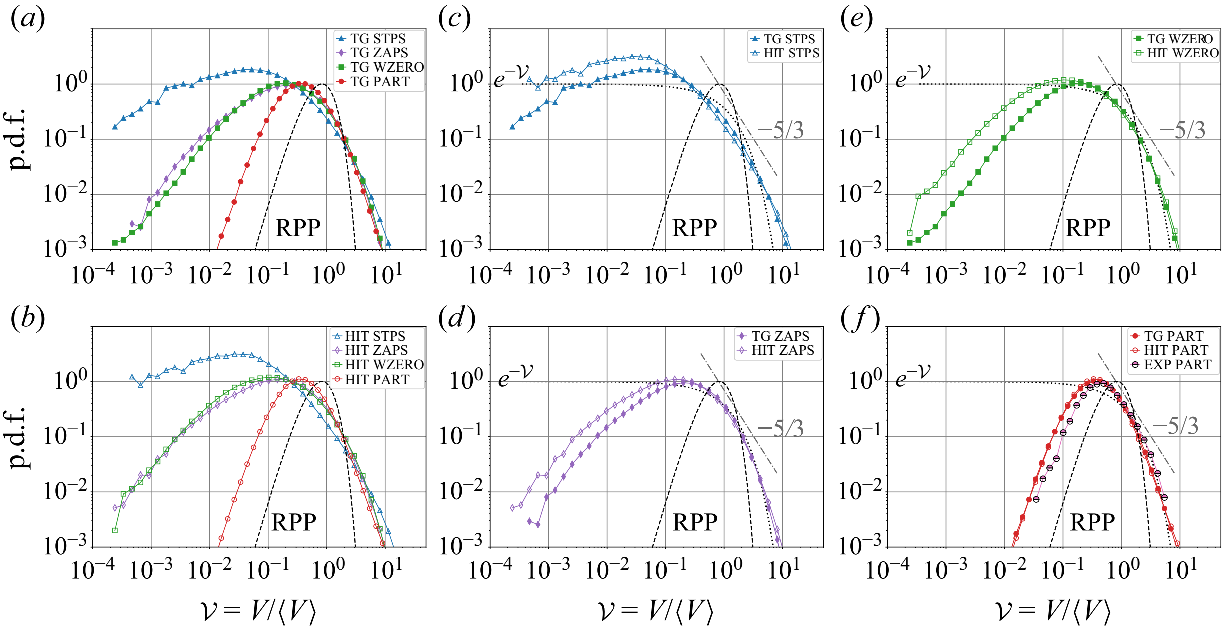

Figure 2. The p.d.f.s of normalized Voronoï volumes, $\mathcal{V} = V/\langle V\rangle$, for STPS, ZAPS, WZERO and inertial particles positions (PART). Panels (*a*,*b*) show a comparison of all quantities in TG and HIT. The p.d.f.s of (*c*) STPS, (*d*) ZAPS and (*e*) WZERO for TG and HIT. (*f*) The p.d.f.s of PART for TG, HIT and EXP. A RPP, an exponential and a $-5/3$ power law are shown as references.

for all datasets. While the DNSs use 10^6 particles, in the experiment we have a maximum of $\approx$29 particles in each frame, resulting in a significantly smaller number of closed 3-D Voronoï cells; there are an average of three closed cells per snapshot. When considering all snapshots this results in a total number of closed cells of 1.9×10^5. Also, in DNSs, the tessellations were performed with periodic boundary conditions. These two observations will be relevant in interpreting some of the results.

Figure 2 shows the probability density functions (p.d.f.s) of the normalized volumes of the Voronoï cells, $\mathcal{V} = V/\langle V\rangle$, for STPS, ZAPS and ZWEROs in TG and HIT, and the p.d.f.s of the Voronoï cells for the particles in the DNSs and the experiment. For the experimental data, since the total number of particles fluctuates in time (as particles can enter or exit the observation volume V_{obs}^{EXP}, and as already mentioned, can explore regions behind the disks), $\langle V\rangle_{EXP}$ is defined as the volume occupied by the fluid between the propellers divided by the mean number of particles per image, calculated from all of the available images. This choice is robust to variations in the number of particles (Fiabane *et al.* 2013), and to the presence of spurious volumes near the boundaries of the images as will be discussed later.

It has been hypothesized that the forcing mechanism or the large-scale flow can introduce changes in the clustering of nulls of the fluid vector fields (Goto & Vassilicos 2009). This figure confirms this is indeed the case: HIT displays stronger clustering of all fields than TG (i.e. larger probabilities for small volumes). In the figures, the p.d.f. resulting from a RPP (corresponding to homogeneous distribution of nulls or particles) is shown as a reference. The larger standard deviation of the p.d.f.s (compared with the RPP, whose standard deviation is $\sigma_{RPP} \approx 0.42$) and the stronger tails (of clusters to the left, and of voids to the right) indicate enhanced clustering. However, the Voronoï cell volumes of the particles is similar for the three flows, and notably, the level of clustering as quantified by $\sigma_{\mathcal{V}}$ is similar for TG and EXP (see table 1). As will be discussed next, differences between EXP and TG can be associated with finite sampling and with boundary effects.

In figure 2 we also show an exponential and a $-5/3$ power law to serve only as references for the comparison. Note STPS in HIT are more similar to the $\mathcal{V}^{-5/3}$ power law in the vicinity of $\mathcal{V} \approx 1$ (i.e. for intermediate volumes, their distribution is closer to a power law than to an exponential decay), which is a consequence of the power-law behaviour of the velocity autocorrelation function (Davila & Vassilicos 2003; Smith, Hopcraft & Jakeman 2008). The TG STPS display a less clear scaling, which is compatible with contamination of the scaling of the velocity by the mean flow (Angriman *et al.* 2020). The ZAPS and WZERO do not exhibit a power law behaviour, and are closer to an almost exponential decay $\sim \mathrm{e}^{-\mathcal{V}}$ in all DNSs for large volumes (i.e. for $\mathcal{V} > 1$), with the aforementioned differences between HIT and TG for very small values of $\mathcal{V}$. Remarkably, the p.d.f.s of Voronoï cells of all particles are very similar in spite of the differences in the distribution of zeros, and for intermediate and large volumes ($\mathcal{V} \gtrsim 1$) are closer to an exponential decay, indicating the clustering of particles for those volumes is more akin to the distribution of either ZAPS or WZERO than to the distribution of STPS. It is worth recalling that some studies of finite-size, neutrally buoyant particles in HIT laboratory flows indicate that small particles do not cluster and behave as tracers (Fiabane *et al.* 2012), at least from a Voronoï tessellation point of view. Fiabane *et al.* (2012) considered neutrally buoyant particles whose radii ranged from 2.25η to 8.5η (0.0875λ to 0.23λ). The particles employed here are well outside this range, with a size comparable to the Taylor microscale, a scale at which viscous effects from the turbulent flow become less relevant. Our results suggest that Taylor-scale neutrally buoyant particles cluster similarly to inertial particles. The numerical particle data thus serve the purpose of gauging the level of clustering the experimental particles experience when compared with the minimal model in the simulations. As particles in the DNS cluster akin to different flow nulls, the comparison allows us to further relate the clustering in the experiment with specific properties of the background flow.

3.2. *Biases in the evaluation of Voronoï tessellation using particles' positions*

Measurement of 3-D clustering in experiments poses multiple challenges. Particle seeding must be sufficiently small to remain in the regime of a dilute suspension (Elghobashi 1994), which results in a few particles per measurement. When computing 3-D Voronoï tessellations, this results in a small number of closed cells, roughly proportional to the cube root of the total number of detected particles. Thus, the number of closed Voronoï cells scales slowly with the number of particles (see Tagawa *et al.* (2012) for another study of 3-D clustering in experiments). Lastly, boundaries have a drastic effect on the statistics. In this section we compare DNSs, synthetically post-processed DNSs and laboratory data, to quantify the effect of these ever-present limitations. We therefore evaluate possible sources of biases in the 3-D Voronoï tessellation calculated from the inertial particles' instantaneous positions by processing DNS data so as to mimic experimental conditions.

We first focus on the effect of boundaries. Particles near the boundaries of the observation region in the experiment occupy either open cells (which are always discarded in the analyses) or artificially large cells, as particles closing their cells (or the domain walls) are not visible in the cameras field of view. The result is depicted in figure 3(*a*) (inset), which shows the Voronoï tessellation on the raw EXP data without imposing any restriction on the cells near boundaries (labelled 'no BC' in the figure); note the power-law tail for very large $\mathcal{V}$. We reproduced this situation in the TG DNS by computing the

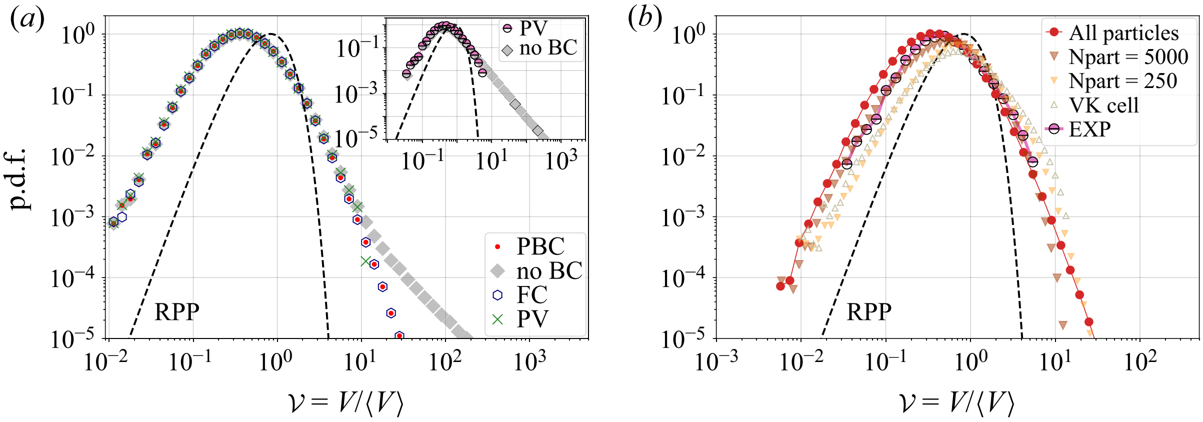

Figure 3. (*a*) The TG data tessellated without any boundary conditions (no BC), with periodic boundary conditions (PBC), removing frontier cells (FC) or keeping only physical volumes (PV). Inset shows EXP data. Note the spurious tails for large $\mathcal{V}$. (*b*) The TG data subsampled to 250 or 5000 particles, and subsampled in only a VK cell with an average of 13 particles, is compared with the tessellation keeping all particles and to EXP data. Note the lower probability of small volumes when subsampling.

tessellation imposing periodic boundary conditions (‘PBC’, considered as ground truth), by imposing no condition on the boundaries (‘no BC’, which results in a power-law dependence), by removing all cells close to boundaries (labelled ‘FC’ in the figure), and by dropping the largest cells that resulted in a total volume larger than the observation volume (that is, keeping only ‘physical’ volumes, ‘PV’), see figure 3(*a*). The latter method, when applied to EXP data, results in the p.d.f. shown in the inset of figure 3(*a*) (the strategy also used in figure 2*f*). In each case, $\langle V\rangle$ is the total volume occupied by the fluid divided by the mean number of particles, to remove biases (especially when large spurious volumes are kept). Boundaries mainly affect the statistics of large cells, but the left tails of the p.d.f.s remain the same regardless of the strategy used for treating the boundaries. This suggests boundaries do not affect significantly the determination of clusters (as clusters are formed by small volumes $\mathcal{V}$ below some threshold, as will be discussed in the following section). Furthermore, we verified that when analysing DNS data in the same way as EXP data (i.e. by considering the non-periodic VK cells in the TG DNS and keeping only ‘physical’ Voronoï cells), the distribution of cluster volumes reported in the following section remains unchanged.

The relatively low number of particles in experiments also has an effect on the p.d.f.s. Figure 3(*b*) shows EXP data together with the original TG data (tessellated using periodic boundary conditions), and the TG data subsampled to a maximum of 250 and 5000 particles. These subsampled sets were built so as to follow the same distribution of number of particles per frame as in the experiments. This was done in the following way. The maximum number of particles N_{max} considered (either 250 or 5000) represents the DNS-equivalent of the total number of particles inside the experimental vessel (but not necessarily within the observation volume at once); e.g. $N_{max} = 250$ corresponds to roughly 31 particles available in each of the eight individual VK cells that the DNS comprises. The experimental variability in the actual number of particles that simultaneously occupy the observation volume at any time instant was mimicked in these numerical datasets based on the occupation probability distribution (i.e. the probability of observing a certain number of particles at each time instant), which was calculated empirically from the EXP data. As a result, for $N_{max} = 250$, the mean number of particles per frame in the complete numerical domain of volume $(2\pi)^3$ is ≈ 111, leading to approximately 13 particles per VK cell of the TG flow, comparable to what is attained in the experiments. These subsampled datasets were then processed in a manner identical to what was done with the experimental data; namely, employing a tessellation scheme without considering periodic boundary conditions and keeping only physical volumes in the entire $(2\pi)^3$ domain. To further mimic the experimental conditions, the subsampling of the TG data was also performed in one VK cell, i.e. in just the octant comprised by the subdomain $[0, \pi) \times [0, \pi) \times [0, \pi)$, thus keeping an average of only 13 particles per snapshot. The tessellation was then carried out as in the case of $N_{max} = 250$ and $N_{max} = 5000$ but in the smaller subdomain; the resulting p.d.f. is shown in figure 3(*b*) as well.

Decreasing the number of particles in the DNS in these ways – in both the $(2\pi)^3$ domain and in the VK cell – as shown in figure 3(*b*), results in p.d.f.s whose left tails slowly move towards the RPP, partially explaining the slight defect of small volumes $\mathcal{V}$ seen in the EXP data. The reduction in the number of particles, and the treatment of boundaries discussed above, also has a small effect in the concavity of the right tail of the observed p.d.f. For a detailed study of other experimental biases in two-dimensional (2-D) Voronoï tessellation, including subsampling effects, see Monchaux (2012), and for an investigation of finite-size effects on Voronoï analysis of randomly placed spheres, see Uhlmann (2020).

3.3. *Effect of preferential sampling of large-scale inhomogeneities in the experiment*

While small (larger than the Kolmogorov scale) particles do not cluster (Fiabane *et al.* 2012), neutrally buoyant particles with sizes of the order of the flow integral scale have been reported to cluster in von Kármán experiments (Machicoane *et al.* 2014). The clusters in that case were found to be associated with large-scale flow inhomogeneities (i.e. preferential sampling by the particles) and with confinement effects (Machicoane *et al.* 2016), rather than with inertial effects. It is then worth analysing whether the clustering behaviour observed in our finite-size particles is the result of, or at least affected by, a global preferential sampling such as the one reported by Machicoane *et al.* (2014). To this end we computed the 3-D spatial concentration map $C(\boldsymbol{x})$ of the particles in the experiment, using all available snapshots and normalized so that the average in the entire observation volume is $\langle C(\boldsymbol{x})\rangle_{V_{obs}^{EXP}} = 1$. Figure 4(*a*,*b*) show 2-D probability density maps of the particles' positions (proportional to the 2-D concentration maps) in the x–z and y–z planes, respectively, where $\hat{z}$ is chosen parallel to the rotation axis of the propellers and to the direction of gravity. Our particles present a more uniform distribution than the larger particles considered in Machicoane *et al.* (2014) and Machicoane *et al.* (2016). This is consistent with previous observations: in Machicoane *et al.* (2014) the larger particles are the ones that display the stronger inhomogeneous preferential sampling, while their smaller particles (with $R/\lambda \approx 2.6$) sample the flow more uniformly than their larger particles. In spite of this, in figure 4 a very small tendency for our particles to be in the lower half of the cell ($z < 0$) can still be observed, especially near the corners. This may be partially due to asymmetries in the position of the shear layer in the von Kármán flow (Ravelet *et al.* 2004; Huck *et al.* 2017), to a small effect of gravity, and to the particles entering and exiting the region behind the propellers; the latter effect is particularly visible in the lower corners of the concentration maps.

To quantify the effect that the particles' preferential sampling has on the observed clustering, we computed the Voronoï cells compensating each cell volume $\mathcal{V}$ by its local particle concentration. The purpose of doing this is to correct any underestimation (overestimation) of the cell volumes resulting from the cells being located in regions of

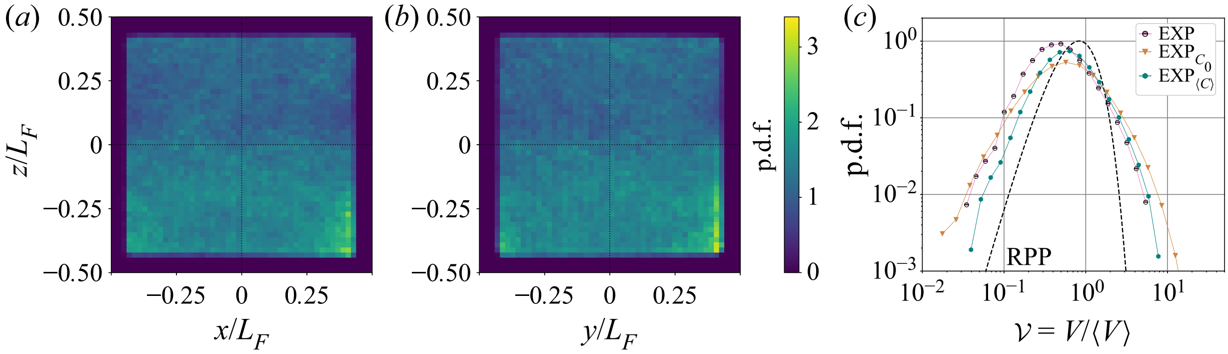

Figure 4. The 2-D p.d.f.s of inertial particles positions in EXP, (*a*) x–z plane and (*b*) y–z plane, where $\hat{z}$ is parallel to the axis of rotation of the propellers. (*c*) The p.d.f. of the original normalized Voronoï volumes for EXP, same p.d.f. compensating each volume by the concentration at the corresponding particle position $C_0 = C(\boldsymbol{x}_0)$ (i.e. p.d.f. of $\mathcal{V}C_0$), and compensating by the average concentration in each volume $\langle C\rangle = \langle C(\boldsymbol{x})\rangle_{\mathcal{V}}$.

space with higher (lower) particle concentration. This can be done in two ways. For a given particle located at $\boldsymbol{x}_0$, the volume of its Voronoï cell $\mathcal{V}$ can be multiplied by the concentration at the particle position $C(\boldsymbol{x}_0)$, i.e. $\mathcal{V}C(\boldsymbol{x}_0)$, or by the average concentration in the entire cell that contains that particle $\langle C(\boldsymbol{x})\rangle_{\mathcal{V}}$, i.e. $\mathcal{V}\langle C\rangle_{\mathcal{V}}$. We thus computed p.d.f.s using these two compensated cell volumes, which are shown in figure 4(*c*) along with the p.d.f. of $\mathcal{V}$ without any compensation. The overall shape of the p.d.f.s remain similar, with the heavy tails that deviate from the RPP being preserved. The second compensation, using the mean concentration in each cell, does not change significantly the distribution of large volumes, but does decrease slightly the probability of finding small volumes. Even so, the compensated p.d.f.s indicate that large-scale sampling effects as reported in Machicoane *et al.* (2014) play a smaller role in our case, and confirm that the clustering observed in the experiment is at least partially associated with inertial effects. As a reference, the standard deviation of the Voronoï volumes compensated by $\langle C\rangle_{\mathcal{V}}$ is $\sigma_{\mathcal{V}_{\langle C\rangle}}/\sigma_{RPP} \approx 2.73$, which is slightly larger than $\sigma_{\mathcal{V}}/\sigma_{RPP} \approx 2.33$ for the uncompensated Voronoï volumes in the experiment (see table 1), and closer to the reference value for the minimal model of inertial particles in the TG DNSs.

3.4. *Cluster volumes probability distribution*

Figure 5 shows the p.d.f.s of the volumes of the clusters V_c (formed by at least two adjacent cells with $\mathcal{V} < \mathcal{V}_c$, where $\mathcal{V}_c$ is the first crossing between the p.d.f. of $\mathcal{V}$ with the RPP, see Monchaux *et al.* (2010)), for all vector fields nulls and for the particles, in the DNSs and EXP. From Mora *et al.* (2021) we expect a $V_c^{-5/3}$ scaling for STPS, and V_c^{-2} for ZAPS and WZEROs, resulting from the fractal nature of the spatial distribution of these zeros. Hence, the presence or not of these power laws provides information about the clusters geometry and their fractality (see Obligado *et al.* (2014) and Mora *et al.* (2021) for simple models and a review of the origin of these power laws). For all nulls, HIT shows a slight excess of smaller volume clusters when compared with TG, but overall the p.d.f.s and scalings are similar.

Figure 5(*f*) also shows the p.d.f.s of V_c for particles in the DNSs and EXP (in the latter case, with and without corrections by the mean average concentration per volume), which are expected to follow a −2 power-law scaling, with a shorter range as a result of the large *St* considered. Clusters of particles in the experiment have different p.d.f.s than in TG or HIT. The right tails of the p.d.f.s in the experiment, associated with volumes $V_c > \langle V\rangle$,

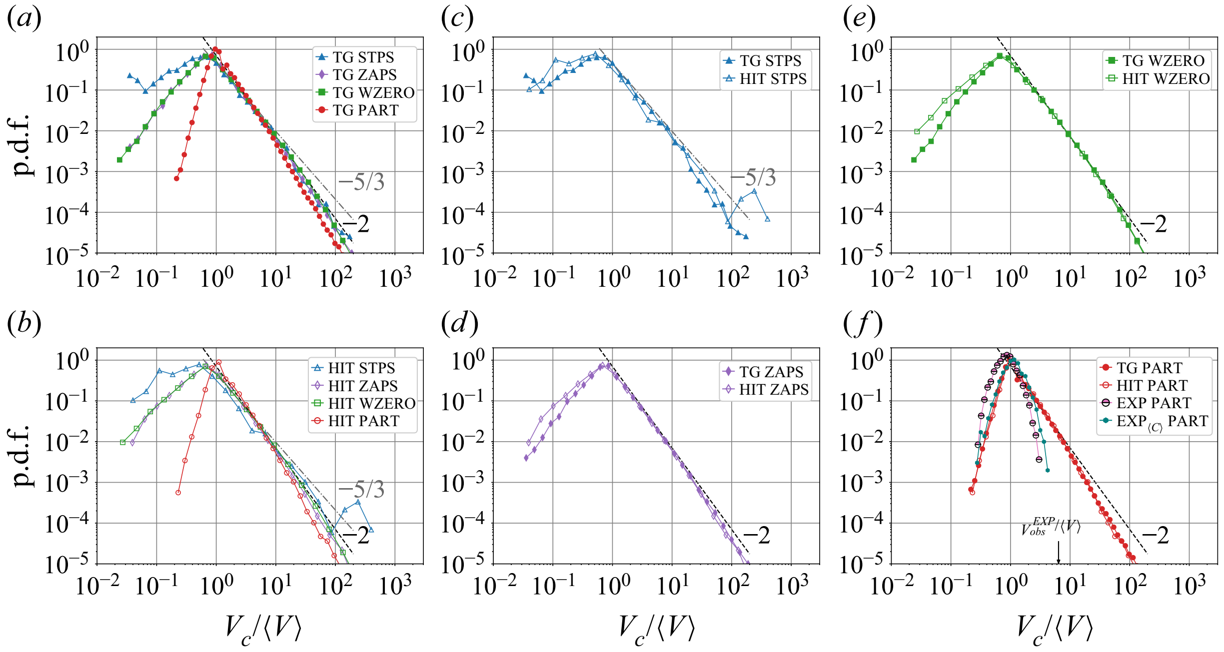

Figure 5. The p.d.f.s of the cluster volumes normalized by the average Voronoï volume, $V_c/\langle V\rangle$, for STPS, ZAPS, WZERO and PART, in DNSs and EXP. Labels for the panels are as in figure 2. Panel (*f*) also shows the EXP data when corrected by the mean concentration per volume $\langle C\rangle$. The normalized observation volume in EXP is indicated by an arrow in the same panel. Power laws with exponents $-5/3$ and -2 are shown as references.

present a sharp drop, as the cluster size cannot be larger than the observation volume ($V_{obs}^{EXP}/\langle V\rangle$ is indicated by the arrow in the figure). On the other hand, in the p.d.f. of uncompensated EXP volumes, the probability of having small clusters (with $V_c < \langle V\rangle$) is larger than in the DNSs. We verified that this is not an effect of subsampling or boundaries, so this difference underlines limitations in the scope of the toy model considered in (2.4*a*,*b*) and, ultimately, in the effect of the mean large-scale flow as captured by the model, either from missing physical effects or from preferential sampling. Neglected interactions between particles is not the probable cause, as the volumetric loading ratio is $\lesssim 2\times 10^{-4}$. However, particles in the DNSs, while subjected to Stokes drag, are point particles that can only sense pressure gradients indirectly through the carrier velocity field. On the other hand, finite-size particles are expected to sense the pressure gradient directly as a force acting on their surface, as well as velocity gradients (and thus, shear stresses) that the point particles in the DNSs cannot sense. Pressure gradients have already been pointed out as important in the understanding of the formation of clusters of finite-size particles (Fiabane *et al.* 2012). Finally, when compensating each EXP particle volume by the mean concentration, the probability of finding smaller clusters decreases and becomes closer to that of the model, suggesting that the small preferential concentration induced by the large-scale flow geometry plays a role here. This is confirmed by the fact that small and large clusters in TG and EXP flows occur at slightly different places, which could also explain why their p.d.f.s look different.

In table 1 a comparison of the mean linear cluster size $\langle V_c\rangle^{1/3}$ for all quantities is given, normalized by η. The mean linear cluster sizes of WZERO and ZAPS are similar for TG and HIT, but STPS clusters are slightly larger for HIT, a difference that may be related to the fact that the HIT forcing scale is larger than in TG, and thus larger clusters may appear. The mean linear cluster size of particles in EXP is much larger than in TG or HIT. Even when conditioning the data as discussed in § 3.2 (that is, subsampling the number of particles in the DNS, and considering boundary effects), or as in § 3.3

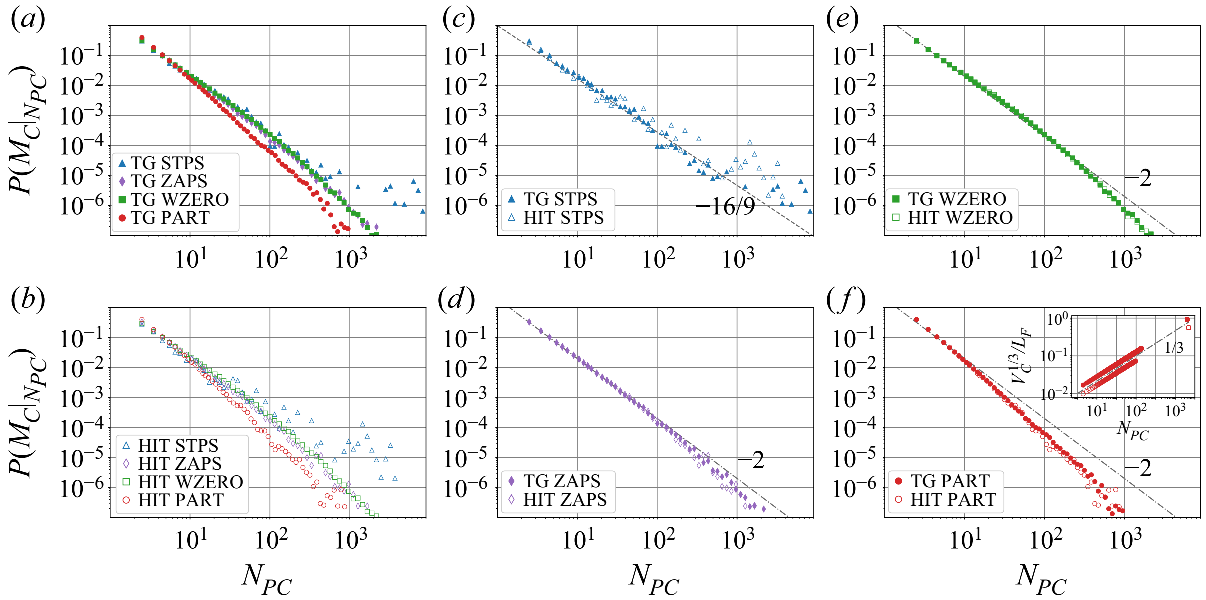

Figure 6. Probability conditioned to having clusters with N_{PC} points for STPS, ZAPS, WZERO and PART in DNSs. Labels for all panels are as in figure 2. The linear cluster size, normalized by L_F and as a function of N_{PC} is shown in the inset of panel (*f*). Several power laws are shown as references.

(i.e. correcting by the particles concentration), we observe that clusters in the experiment are still three times larger, on average, than in TG. This difference is associated with the finite volume of the particles in EXP. Note that finite-size particles can only form clusters with a minimum linear size of order $4R$, which for EXP data is greater than 120η. In other words, some clusters in TG cannot be realized in the experiment without the actual particles overlapping.

The p.d.f.s of the number of clusters M_c with N_{PC} points inside each cluster are shown for the DNSs in figure 6. These p.d.f.s follow a power-law behaviour with an exponent close to $-16/9$ for STPS, and -2 for ZAPS and WZERO, as expected from Mora *et al.* (2021). Figure 6(*c*) indicates that the probability of having clusters of STPS with a larger number of nulls is larger for HIT than for TG, consistent with the larger mean linear size of clusters of STPS in HIT. Inertial particles also follow a power law with an exponent close to -2 for clusters with $N_{PC} \lesssim 10$, a behaviour consistent with the one reported by Yoshimoto & Goto (2007). Overall, the observed scaling is similar for ZAPS, WZERO and inertial particles, which is compatible with the sweep-stick mechanism (Goto & Vassilicos 2008; Coleman & Vassilicos 2009; Oka & Goto 2021). The deviation from the power law observed for particles in figure 6(*f*) might relate to the fact that particles with large Stokes number filter out small flow scales. Indeed, these kinds of particles are expected to be less responsive to small scale motions in the fluid, so clusters with a larger number of particles around very dense nulls in the carrier flow are less likely to form. Finally, the inset in figure 6(*f*) shows the linear cluster size normalized by L_F, as a function of the number of particles per cluster for the inertial particles. Note the cluster size grows with the number of particles with a 1/3 scaling.

4. Discussion

Comparison of clustering in numerical simulations of homogeneous isotropic turbulence and TG turbulence with von Kármán experiments provides a powerful tool to characterize geometrical and topological properties of turbulence, and of multiphase flows.

Moreover, the similarities between the TG flow and the laboratory von Kármán flow allow for detailed studies of possible biases when considering limitations in experiments such as low number of particles, boundary effects or the effect of preferential sampling of the large-scale flow by the particles.

Our results also show that 3-D Voronoï tessellation constitutes a powerful tool to study the topology of nulls and clusters, shedding light on dominant effects in the dynamics of the flow. For the case of the TG and von Kármán flows, these are: (1) a lower probability of finding very densely packaged zeros of the velocity field, the vorticity, and of the Lagrangian acceleration in the TG flow when compared with HIT; (2) a deviation in the scaling of the number of Voronoï volumes of STPS with $\mathcal{V}$ in the TG flow, probably associated with the effect of the mean flow on the velocity autocorrelation function; (3) similar clustering properties of a minimal model of inertial particles in TG and of neutrally buoyant Taylor-scale particles in von Kármán flows as in inertial particles in HIT, probably resulting from the negligible differences (for intermediate cell volumes $\mathcal{V}$) in the statistics of ZAPS and WZERO observed in TG and HIT.

In the experiment, we find that particles with a size comparable to the Taylor microscale form clusters that are very similar in intensity and size distribution as the point particles in the simulations. This contrasts with previous results, for particles whose sizes were a fraction of λ, and which did not exhibit clustering (Qureshi *et al.* 2007; Fiabane *et al.* 2012, 2013), while close to point particles in experiments were found to form clusters (Obligado *et al.* 2019), as well as much larger particles (Machicoane *et al.* 2014, 2016) were also found to cluster for different reasons. This points towards the possibility that intermediate, Taylor-scale neutrally buoyant particles cluster as a result of inertial effects.

These results are promising as they further confirm TG and von Kármán flows share many geometrical and statistical properties, even when considering preferential concentration of particles in multiphase turbulence. Moreover, they indicate that many clustering properties of HIT can be extended to multiscale flows with a large-scale circulation, at least in cases in which turbulent fluctuations are large (as in the TG and VK flows). Further studies will consider other forcing mechanisms and different large-scale geometries.

Acknowledgements. The authors thank D. Mora for help with data analysis of nulls calculation. The authors gratefully acknowledge suggestions by an anonymous referee of studying the spatial concentration map of the particles in the experiment.

Funding. This work has been partially supported by ECOS-Sud project no. A18ST04. S.A., F.Z., P.J.C. and P.D.M. acknowledge support from UBACYT grant no. 20020170100508BA and PICT grant no. 2018-4298. A.F. and M.O. acknowledge the LabEx Tec21 (Investissements d'Avenir – Grant Agreement no. ANR-11-LABX-0030).

Declaration of interests. The authors report no conflict of interest.

Author ORCIDs.
Sofía Angriman https://orcid.org/0000-0003-2390-2800;
Amélie Ferran https://orcid.org/0000-0001-9851-8809;
Florencia Zapata https://orcid.org/0000-0001-8633-480X;
Pablo J. Cobelli https://orcid.org/0000-0003-2968-1877;
Martin Obligado https://orcid.org/0000-0003-3834-3941;
Pablo D. Mininni https://orcid.org/0000-0001-6858-6755.

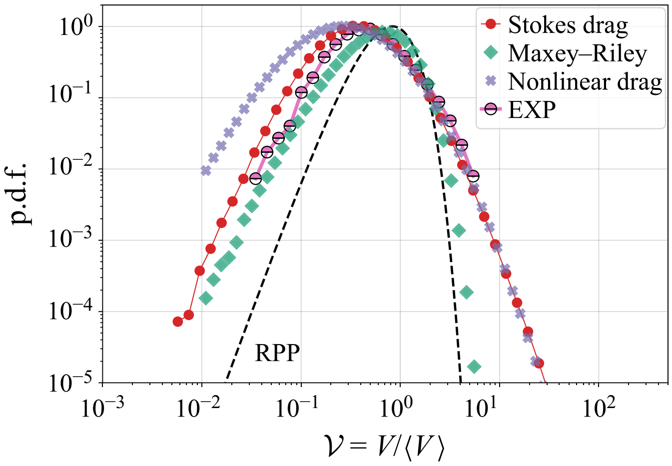

Figure 7. The p.d.f.s of normalized Voronoï volumes for inertial particles in a TG flow considering only Stokes drag as in (2.4*a*,*b*), the Maxey–Riley equation (with Stokes drag, gravity, particle acceleration and added mass effects) and nonlinear drag. The EXP data is shown as well for comparison.

Appendix A. Models with other forces and their effect on clustering

In this appendix we briefly consider other possible models for the equations of motion of particles in the simulations. On the one hand we consider particles subjected to a nonlinear drag force as in Wang & Maxey (1993), whose equations of motion read

$$\dot{\boldsymbol{x}}_p = \boldsymbol{v}(t), \qquad \dot{\boldsymbol{v}} = \frac{1 + 0.15 Re_p^{0.687}}{\tau_p}(\boldsymbol{u} - \boldsymbol{v}), \qquad \text{(A1}a,b\text{)}$$

where $Re_p = \sqrt{18\tau_p/\nu}|\boldsymbol{u} - \boldsymbol{v}|$. On the other hand we consider the Maxey–Riley equation (Maxey & Riley 1983) up to terms linear in the particle's radius, that is, we consider the Stokes drag, gravity and particle acceleration and added mass effects (and therefore neglecting Faxén corrections and the Basset–Boussinesq history term). Thus, particles evolve according to

$$\dot{\boldsymbol{x}}_p = \boldsymbol{v}(t), \qquad \dot{\boldsymbol{v}} = \frac{1}{\tau_p}(\boldsymbol{u} - \boldsymbol{v}) - g\frac{1-\gamma}{1+\gamma/2}\hat{z} + \frac{3}{2}\frac{\gamma}{1+\gamma/2}\frac{\mathrm{D}\boldsymbol{u}}{\mathrm{D}t}, \qquad \text{(A2}a,b\text{)}$$

where g is the gravitational acceleration, $\mathrm{D}/\mathrm{D}t = \partial/\partial t + \boldsymbol{u}\cdot\nabla$ and $\gamma = \rho_f/\rho_p$. Particles whose dynamics are governed by either (A1*a*,*b*) or (A2*a*,*b*) were evolved in the turbulent flow with TG mechanical forcing with a spatial resolution of 768^3 grid points, following the same procedures as previously described for the TG DNSs. A total of 10^6 particles were integrated. For the sake of comparison, and as both equations are missing other forces (see, e.g. Calzavarini *et al.* 2008, 2009), we use in all cases the effective particle response time τ_p instead of the viscous relaxation time τ_p^ν, and in (A2*a*,*b*) we use $\gamma = 1/1.02 \approx 0.98$ and the value of g to match the experiment. We performed a Voronoï tessellation of the particles' positions, and the resulting cell volume's p.d.f.s are shown in figure 7, along with the p.d.f.s corresponding to particles evolving solely under Stokes drag as in (2.4*a*,*b*), and the experimental data. As expected, considering particle acceleration and added mass effects in the Maxey–Riley equation results in less clustering: (A2*a*,*b*) is well suited for smaller particles with small particle Reynolds number, which tend to cluster less (Fiabane *et al.* 2012, 2013). Note in particular how the statistics of voids (i.e. of large Voronoï cells) approaches the statistics of the RPP; the standard deviation of this p.d.f. is $\sigma_{\mathcal{V}} = 1.31\sigma_{RPP}$. Considering nonlinear drag as in (A1*a*,*b*) may be more relevant for particles of our size and with larger particle Reynolds number. This model results instead in more clustering, with a p.d.f. with $\sigma_{\mathcal{V}} = 2.92\sigma_{RPP}$. The stronger clustering may be related to our choice of using an effective τ_p. In the future, it may be of interest to compare nonlinear drag using the viscous response time of the particles (or other choices for the effective response time) against the simplified point particle model with the effective parameter in (2.4*a*,*b*). Note in particular that the results in figure 7 do not necessarily imply that (2.4*a*,*b*) is a better model for Taylor-scale neutrally buoyant particles, as to that end a more detailed comparison would be needed.

REFERENCES

ANGRIMAN, S., COBELLI, P.J., BOURGOIN, M., HUISMAN, S.G., VOLK, R. & MININNI, P.D. 2021 Broken mirror symmetry of tracer's trajectories in turbulence. *Phys. Rev. Lett.* **127** (25), 254502.

ANGRIMAN, S., MININNI, P.D. & COBELLI, P.J. 2020 Velocity and acceleration statistics in particle-laden turbulent swirling flows. *Phys. Rev. Fluids* **5**, 064605.

BATCHELOR, G.K. 2000 *An Introduction to Fluid Dynamics*. Cambridge Mathematical Library. Cambridge University Press.

BELLANI, G. & VARIANO, E.A. 2012 Slip velocity of large neutrally buoyant particles in turbulent flows. *New J. Phys.* **14** (12), 125009.

BRENNEN, C.E. 2005 *Fundamentals of Multiphase Flow*, 1st edn. Cambridge University Press.

BUARIA, D., PUMIR, A., BODENSCHATZ, E. & YEUNG, P.-K. 2019 Extreme velocity gradients in turbulent flows. *New J. Phys.* **21** (4), 043004.

CALZAVARINI, E., KERSCHER, M., LOHSE, D. & TOSCHI, F. 2008 Dimensionality and morphology of particle and bubble clusters in turbulent flow. *J Fluid Mech.* **607**, 13–24.

CALZAVARINI, E., VOLK, R., BOURGOIN, M., LÉVÊQUE, E., PINTON, J.-F. & TOSCHI, F. 2009 Acceleration statistics of finite-sized particles in turbulent flow: the role of Faxén forces. *J. Fluid Mech.* **630**, 179–189.

CARTWRIGHT, J.H.E., FEUDEL, U., KÁROLYI, G., DE MOURA, A., PIRO, O. & TÉL, T. 2010 Dynamics of finite-size particles in chaotic fluid flows. In *Nonlinear Dynamics and Chaos: Advances And Perspectives* (ed. M. Thiel, J. Kurths, M.C. Romano, G. Károlyi & A. Moura), pp. 51–87. Springer.

CISSE, M., HOMANN, H. & BEC, J. 2013 Slipping motion of large neutrally buoyant particles in turbulence. *J. Fluid Mech.* **735**, R1.

CLYNE, J., MININNI, P., NORTON, A. & RAST, M. 2007 Interactive desktop analysis of high resolution simulations: application to turbulent plume dynamics and current sheet formation. *New J. Phys.* **9**, 301.

COLEMAN, S.W. & VASSILICOS, J.C. 2009 A unified sweep-stick mechanism to explain particle clustering in two- and three-dimensional homogeneous, isotropic turbulence. *Phys. Fluids* **21**, 113301.

DAVILA, J. & VASSILICOS, J.C. 2003 Richardson's pair diffusion and the stagnation point structure of turbulence. *Phys. Rev. Lett.* **91**, 144501.

ELGHOBASHI, S. 1994 On predicting particle-laden turbulent flows. *Appl. Sci. Res.* **52** (4), 309–329.

FERRAN, A., ANGRIMAN, S., MININNI, P.D. & OBLIGADO, M. 2022 Characterising single and two-phase homogeneous isotropic turbulence with stagnation points. *Dynamics* **2** (2), 63–72.

FIABANE, L., VOLK, R., PINTON, J.-F., MONCHAUX, R., CARTELLIER, A. & BOURGOIN, M. 2013 Do finite-size neutrally buoyant particles cluster? *Phys. Scr.* **2013** (T155), 014056.

FIABANE, L., ZIMMERMANN, R., VOLK, R., PINTON, J.-F. & BOURGOIN, M. 2012 Clustering of finite-size particles in turbulence. *Phys. Rev.* E **86**, 035301.

GOTO, S. & VASSILICOS, J.C. 2006 Self-similar clustering of inertial particles and zero-acceleration points in fully developed two-dimensional turbulence. *Phys. Fluids* **18** (11), 115103.

GOTO, S. & VASSILICOS, J.C. 2008 Sweep-stick mechanism of heavy particle clustering in fluid turbulence. *Phys. Rev. Lett.* **100** (5), 054503.

GOTO, S. & VASSILICOS, J.C. 2009 The dissipation rate coefficient of turbulence is not universal and depends on the internal stagnation point structure. *Phys. Fluids* **21**, 035104.

GREEN, A.E. & TAYLOR, G.I. 1937 Mechanism of the production of small eddies from larger ones. *Proc. R. Soc.* A **158** (895), 499–521.

HAYNES, A.L. & PARNELL, C.E. 2007 A trilinear method for finding null points in a three-dimensional vector space. *Phys. Plasmas* **14**, 082107.

HOMANN, H. & BEC, J. 2010 Finite-size effects in the dynamics of neutrally buoyant particles in turbulent flow. *J. Fluid Mech.* **651**, 81–91.

HUCK, P.D., MACHICOANE, N. & VOLK, R. 2017 Production and dissipation of turbulent fluctuations close to a stagnation point. *Phys. Rev. Fluids* **2** (8), 084601.

KANEDA, Y., ISHIHARA, T., YOKOKAWA, M., ITAKURA, K. & UNO, A. 2003 Energy dissipation rate and energy spectrum in high resolution direct numerical simulations of turbulence in a periodic box. *Phys. Fluids* **15** (2), L21–L24.

KREUZAHLER, S., SCHULZ, D., HOMANN, H., PONTY, Y. & GRAUER, R. 2014 Numerical study of impeller-driven von Kármán flows via a volume penalization method. *New J. Phys.* **16** (10), 103001.

MACHICOANE, N., LÓPEZ-CABALLERO, M., FIABANE, L., PINTON, J.-F., BOURGOIN, M., BURGUETE, J. & VOLK, R. 2016 Stochastic dynamics of particles trapped in turbulent flows. *Phys. Rev.* E **93** (2), 023118.

MACHICOANE, N., ZIMMERMANN, R., FIABANE, L., BOURGOIN, M., PINTON, J.-F. & VOLK, R. 2014 Large sphere motion in a nonhomogeneous turbulent flow. *New J. Phys.* **16** (1), 013053.

MAXEY, M.R. & RILEY, J.J. 1983 Equation of motion for a small rigid sphere in a nonuniform flow. *Phys. Fluids* **26** (4), 883–889.

MININNI, P.D., ROSENBERG, D., REDDY, R. & POUQUET, A. 2011 A hybrid MPI–OpenMP scheme for scalable parallel pseudospectral computations for fluid turbulence. *Parallel Comput.* **37** (6–7), 316–326.

MONCHAUX, R. 2012 Measuring concentration with Voronoï diagrams: the study of possible biases. *New J. Phys.* **14** (9), 095013.

MONCHAUX, R., BOURGOIN, M. & CARTELLIER, A. 2010 Preferential concentration of heavy particles: a Voronoï analysis. *Phys. Fluids* **22** (10), 103304.

MORA, D.O., BOURGOIN, M., MININNI, P.D. & OBLIGADO, M. 2021 Clustering of vector nulls in homogeneous isotropic turbulence. *Phys. Rev. Fluids* **6** (2), 024609.

MORDANT, N., DELOUR, J., LÉVEQUE, E., ARNÉODO, A. & PINTON, J.-F. 2002 Long time correlations in Lagrangian dynamics: a key to intermittency in turbulence. *Phys. Rev. Lett.* **89** (25), 254502.

MORDANT, N., LÉVÊQUE, E. & PINTON, J.-F. 2004 Experimental and numerical study of the Lagrangian dynamics of high Reynolds turbulence. *New J. Phys.* **6**, 116.

MORRISON, F.A. 2013 *Data Correlation for Drag Coefficient for Sphere*, vol. 49931. Department of Chemical Engineering, Michigan Technological University.

OBLIGADO, M., TEITELBAUM, T., CARTELLIER, A., MININNI, P.D. & BOURGOIN, M. 2014 Preferential concentration of heavy particles in turbulence. *J. Turbul.* **15** (5), 293–310.

OBLIGADO, M., VOLK, R., MORDANT, N. & BOURGOIN, M. 2019 Preferential concentration of finite solid particles in a swirling von Kármán flow of water. In *Turbulent Cascades II* (ed. M. Gorokhovski & F.S. Godeferd), pp. 207–216. Springer.

OKA, S. & GOTO, S. 2021 Generalized sweep-stick mechanism of inertial-particle clustering in turbulence. *Phys. Rev. Fluids* **6**, 044605.

PONCET, S., SCHIESTEL, R. & MONCHAUX, R. 2008 Turbulence modeling of the von Kármán flow: viscous and inertial stirrings. *Intl J. Heat Fluid Flow* **29** (1), 62–74.

QURESHI, N.M, BOURGOIN, M., BAUDET, C., CARTELLIER, A. & GAGNE, Y. 2007 Turbulent transport of material particles: an experimental study of finite size effects. *Phys. Rev. Lett.* **99**, 184502.

RAVELET, F., MARIÉ, L., CHIFFAUDEL, A. & DAVIAUD, F. 2004 Multistability and memory effect in a highly turbulent flow: experimental evidence for a global bifurcation. *Phys. Rev. Lett.* **93** (16), 164501.

REARTES, C. & MININNI, P.D. 2021 Settling and clustering of particles of moderate mass density in turbulence. *Phys. Rev. Fluids* **6**, 114304.

ROSENBERG, D., MININNI, P.D., REDDY, R. & POUQUET, A. 2020 GPU parallelization of a hybrid pseudospectral geophysical turbulence framework using CUDA. *Atmosphere* **11** (2), 178.

SCHMITT, F.G. & SEURONT, L. 2008 Intermittent turbulence and copepod dynamics: increase in encounter rates through preferential concentration. *J. Mar. Syst.* **70** (3–4), 263–272.

SHEN, X. & WARHAFT, Z. 2002 Longitudinal and transverse structure functions in sheared and unsheared wind-tunnel turbulence. *Phys. Fluids* **14**, 370–381.

SMITH, J.M., HOPCRAFT, K.I. & JAKEMAN, E. 2008 Fluctuations in the zeros of differentiable Gaussian processes. *Phys. Rev.* E **77** (3), 031112.

TAGAWA, Y., MERCADO, J., PRAKASH, V.N., CALZAVARINI, E., SUN, C. & LOHSE, D. 2012 Three-dimensional Lagrangian Voronoïanalysis for clustering of particles and bubbles in turbulence. *J. Fluid Mech.* **693**, 201–215.

TAYLOR, G.I. 1938 The spectrum of turbulence. *Proc. R. Soc.* A **164** (919), 476–490.

Uhlmann, M. 2020 Voronoï tessellation analysis of sets of randomly placed finite-size spheres. *Physica* A **555**, 124618.

Volk, R., Calzavarini, E., Verhille, G., Lohse, D., Mordant, N., Pinton, J.-F. & Toschi, F. 2008 Acceleration of heavy and light particles in turbulence: comparison between experiments and direct numerical simulations. *Physica* D **237** (14–17), 2084–2089.

Wang, L.-P. & Maxey, M.R. 1993 Settling velocity and concentration distribution of heavy particles in homogeneous isotropic turbulence. *J. Fluid Mech.* **256**, 27–68.

Xu, H. & Bodenschatz, E. 2008 Motion of inertial particles with size larger than Kolmogorov scale in turbulent flows. *Physica* D **237** (14–17), 2095–2100.

Yoshimoto, H. & Goto, S. 2007 Self-similar clustering of inertial particles in homogeneous turbulence. *J. Fluid Mech.* **577**, 275–286.

Bibliography

Akutina, Y., T. Revil-Baudard, J. Chauchat, and O. Eiff (2020). 'Experimental evidence of settling retardation in a turbulence column'. *Physical Review Fluids* 5.1, p. 14303. DOI: `10.1103/PhysRevFluids.5.014303`.

Aliseda, A., A. Cartellier, F. Hainaux, and J. C. Lasheras (2002). 'Effect of preferential concentration on the settling velocity of heavy particles in homogeneous isotropic turbulence'. *Journal of Fluid Mechanics* 468, pp. 77–105. DOI: `10.1017/S0022112002001593`.

Angriman, S., P.J. Cobelli, M. Bourgoin, S.G. Huisman, R. Volk, and P.D. Mininni (2021). 'Broken mirror symmetry of tracer's trajectories in turbulence'. *Physical Review Letters* 127.25, p. 254502. DOI: `10.1103/PhysRevLett.127.254502`.

Angriman, S., P. D. Mininni, and P. J. Cobelli (2020). 'Velocity and acceleration statistics in particle-laden turbulent swirling flows'. *Physical Review Fluids* 5.6, pp. 1–27. DOI: `10.1103/PhysRevFluids.5.064605`.

Bachalo, W. D. and M. J. Houser (1984). 'Phase/Doppler Spray Analyzer For Simultaneous Measurements Of Drop Size And Velocity Distributions'. *Optical Engineering* 23.5, pp. 583–590. DOI: `10.1117/12.7973341`.

Bachalo, W.D. (1980). 'Method for measuring the size and velocity of spheres by dual-beam light-scatter interferometry'. *Appl. Opt.* 19.3, pp. 363–370. DOI: `10.1364/AO.19.000363`.

Baker, L., A. Frankel, A. Mani, and F. Coletti (2017). 'Coherent clusters of inertial particles in homogeneous turbulence'. *Journal of Fluid Mechanics* 833, pp. 364–398. DOI: `10.1017/jfm.2017.700`.

Balachandar, S. and J.K. Eaton (2010). 'Turbulent dispersed multiphase flow'. *Annual Review of Fluid Mechanics* 42, pp. 111–133. DOI: `10.1146/annurev.fluid.010908.165243`.

Basset, A.B. (1888). *A treatise on hydrodynamics: with numerous examples*. Vol. 2. Deighton, Bell and Company.

Batchelor, G.K. (1953). *The theory of homogeneous turbulence*. Cambridge university press.

Bateson, C. P. and A. Aliseda (2012). 'Wind tunnel measurements of the preferential concentration of inertial droplets in homogeneous isotropic turbulence'. *Experiments in Fluids* 52.6, pp. 1373–1387. DOI: `10.1007/s00348-011-1252-6`.

Bec, J., L. Biferale, G. Boffetta, A. Celani, M. Cencini, A. Lanotte, S. Musacchio, and F. Toschi (2006). 'Acceleration statistics of heavy particles in turbulence'. *Journal of Fluid Mechanics* 550, pp. 349–358. DOI: `10.1017/S002211200500844X`.

Bec, J., H. Homann, and S. S. Ray (2014). 'Gravity-driven enhancement of heavy particle clustering in turbulent flow'. *Physical Review Letters* 112.18, pp. 1–5. DOI: `10.1103/PhysRevLett.112.184501`.

Befeno, I. and R. Schiestel (2007). 'Non-equilibrium mixing of turbulence scales using a continuous hybrid RANS/LES approach: Application to the shearless mixing layer'. *Flow, Turbulence and Combustion* 78.2, pp. 129–151. DOI: `10.1007/s10494-006-9055-1`.

Berk, T. and Filippo C. (2021). 'Dynamics of small heavy particles in homogeneous turbulence: A Lagrangian experimental study'. *Journal of Fluid Mechanics* 917, pp. 1–27. DOI: `10.1017/jfm.2021.280`.

Bisset, D.K., J.C.R. Hunt, and M.M. Rogers (2002). 'The turbulent/non-turbulent interface bounding a far wake'. *Journal of Fluid Mechanics* 451, pp. 383–410. DOI: `10.1017/s0022112001006759`.

Blyth, A.M. (1993). 'Entrainment in cumulus clouds'. *Journal of Applied Meteorology and Climatology* 32.4, pp. 626–641. DOI: `10.1175/1520-0450(1993)032<0626:EICC>2.0.CO;2`.

Bourgoin, M. and S.G. Huisman (2020). 'Using ray-traversal for 3D particle matching in the context of particle tracking velocimetry in fluid mechanics'. *Review of Scientific Instruments* 91.8. DOI: `10.1063/5.0009357`.

Boussinesq, J. (1903). *Théorie analytique de la chaleur: mise-en harmonie avec la thermodynamique et avec la théorie mécanique de la lumière: Tome 2: Refroidissement et échauffement par rayonnement conductibilité des tiges, lames et masses cristallines courants de conveçtion. Théorie mécanique de la lumière*. Gauthier-Villars Paris.

Brandt, L. and F. Coletti (2022). 'Particle-Laden Turbulence: Progress and Perspectives'. en. *Annual Review of Fluid Mechanics* 54.1, pp. 159–189. DOI: `10.1146/annurev-fluid-030121-021103`.

Brown, G.L. and A. Roshko (1974). 'On density effects and large structure in turbulent mixing layers'. *Journal of Fluid Mechanics* 64.4, pp. 775–816. DOI: `10.1017/S002211207400190X`.

Buevich, Y.A. (1966). 'Motion resistance of a particle suspended in a turbulent medium'. *Fluid Dynamics* 1.6, pp. 119–119. DOI: `https://doi.org/10.1007/BF01022298`.

Calzavarini, E., R. Volk, M. Bourgoin, E. Lévêque, J. F. Pinton, and F. Toschi (2009). 'Acceleration statistics of finite-sized particles in turbulent flow: The role of Faxén forces'. *Journal of Fluid Mechanics* 630, pp. 179–189. DOI: `10.1017/S0022112009006880`.

Chein, R. and J.N. Chung (1988). 'Simulation of particle dispersion in a two-dimensional mixing layer'. *AIChE Journal* 34.6, pp. 946–954. DOI: `https://doi.org/10.1002/aic.690340607`.

Chen, L., S. Goto, and J. C. Vassilicos (2006). 'Turbulent clustering of stagnation points and inertial particles'. *Journal of Fluid Mechanics* 553, pp. 143–154. DOI: `10.1017/S0022112006009177`.

Cheng, N.-S. and A.W.-K. Law (2001). 'Measurements of turbulence generated by oscillating grid'. *Journal of Hydraulic Engineering* 127.3, pp. 201–208. DOI: `10.1061/(ASCE)0733-9429(2001)127:3(201)`.

Chung, J. N. and T. R. Troutt (1988). 'Simulation of particle dispersion in an axisymmetric jet'. *Journal of Fluid Mechanics* 186, pp. 199–222. DOI: `10.1017/S0022112088000102`.

Clift, R., J.R. Grace, and M.E. Weber (1978). *Bubbles, drops, and particles*. Vol. 11. Academic Press, pp. 263–264.

Coleman, S. W. and J. C. Vassilicos (2009). 'A unified sweep-stick mechanism to explain particle clustering in two- and three-dimensional homogeneous, isotropic turbulence'. *Physics of Fluids* 21.11, pp. 1–10. DOI: `10.1063/1.3257638`.

Comte-Bellot, G. (1976). 'Hot-wire anemometry'. *Annual review of fluid mechanics* 8.1, pp. 209–231.

Comte-Bellot, G. and S. Corrsin (1971). 'Simple Eulerian time correlation of full-and narrow-band velocity signals in grid-generated, 'isotropic' turbulence'. *Journal of Fluid Mechanics* 48.2, pp. 273–337. DOI: `10.1017/S0022112071001599`.

Corrsin, S. and A.L. Kistler (1955). *Free-stream boundaries of turbulent flows*. Tech. rep. Johns Hopkins University.

Corrsin, S. and J. Lumley (1956). 'On the equation of motion for a particle in turbulent fluid'. *Applied Scientific Research, Section A* 6.2, pp. 114–116. DOI: `10.1007/BF03185030`.

Crowe, C.T., J.N. Chung, and T.R. Troutt (1988). 'Particle mixing in free shear flows'. *Progress in Energy and Combustion Science* 14.3, pp. 171–194. DOI: `10.1016/0360-1285(88)90008-1`.

Crowe, C.T., R.A. Gore, and T.R. Troutt (1985). 'Particle dispersion by coherent structures in free shear flows'. *Particulate Science and Technology* 3.3-4, pp. 149–158. DOI: `10.1080/02726358508906434`.

da Silva, C.B., J.C.R. Hunt, I. Eames, and J. Westerweel (2014). 'Interfacial Layers Between Regions of Different Turbulence Intensity'. *Annual Review of Fluid Mechanics* 46, pp. 567–590. DOI: `10.1146/annurev-fluid-010313-141357`.

Dahm, W.J.A. and P.E. Dimotakis (1987). 'Measurements of entrainment and mixing in turbulent jets'. *AIAA Journal* 25.9, pp. 1216–1223. DOI: `10.2514/3.9770`.

Dimotakis, P.E. (2000). 'The mixing transition in turbulent flows'. *Journal of Fluid Mechanics* 409, pp. 69–98. DOI: `10.1017/S0022112099007946`.

Eaton, J.K. and J.R. Fessler (1994). 'Preferential concentration of particles by turbulence'. *International Journal of Multiphase Flow* 20, pp. 169–209. DOI: `https://doi.org/10.1016/0301-9322(94)90072-8`.

Elghobashi, S. (1994). 'On predicting particle-laden turbulent flows'. *Applied Scientific Research* 52.4, pp. 309–329. DOI: `10.1007/BF00936835`.

Elsinga, G.E. and C.B. da Silva (2019). 'How the turbulent/non-turbulent interface is different from internal turbulence'. *Journal of Fluid Mechanics* 866, pp. 216–238. DOI: `10.1017/jfm.2019.85`.

Falkinhoff, F., M. Obligado, M. Bourgoin, and P. D. Mininni (2020). 'Preferential Concentration of Free-Falling Heavy Particles in Turbulence'. *Physical Review Letters* 125.6, p. 64504. DOI: `10.1103/PhysRevLett.125.064504`.

Fathali, M. and M.K. Deshiri (2016). 'Sensitivity of the two-dimensional shearless mixing layer to the initial turbulent kinetic energy and integral length scale'. *Physical Review E* 93.4. DOI: `10.1103/PhysRevE.93.043122`.

Frisch, U. (1995). *Turbulence: the legacy of AN Kolmogorov*. Cambridge university press.

Gatignol, R. (1983). 'The Faxén formulae for a rigid particle in an unsteady non-uniform Stokes flow'.

Gerashchenko, S., G.H. Good, and Z. Warhaft (2011). 'Entrainment and mixing of water droplets across a shearless turbulent interface with and without gravitational effects'. *Journal of Fluid Mechanics* 668, pp. 293–303. DOI: `10.1017/S002211201000577X`.

Gerashchenko, S. and Z. Warhaft (2013). 'Conditional entrainment statistics of inertial particles across shearless turbulent interfaces'. *Experiments in Fluids* 54.12. DOI: `10.1007/s00348-013-1631-2`.

Ghosh, S., J. Dávila, J.C.R. Hunt, A. Srdic, H.J.S. Fernando, and P.R. Jonas (2005). 'How turbulence enhances coalescence of settling particles with applications to rain in clouds'. *Proceedings of the Royal Society A: Mathematical, Physical and Engineering Sciences* 461.2062, pp. 3059–3088. DOI: `10.1098/rspa.2005.1490`.

Good, G.H., S. Gerashchenko, and Z. Warhaft (2012). 'Intermittency and inertial particle entrainment at a turbulent interface: The effect of the large-scale eddies'. *Journal of Fluid Mechanics* 694, pp. 371–398. DOI: `10.1017/jfm.2011.552`.

Good, G.H., P.J. Ireland, G.P. Bewley, E. Bodenschatz, L.R. Collins, and Z. Warhaft (2014). 'Settling regimes of inertial particles in isotropic turbulence'. *Journal of Fluid Mechanics* 759.August 2015, R3. DOI: `10.1017/jfm.2014.602`.

Gore, R.A. and C.T. Crowe (1991). 'Modulation of Turbulence by a Dispersed Phase'. *Journal of Fluids Engineering* 113.2, pp. 304–307. DOI: `10.1115/1.2909497`.

Goto, S. and J.C. Vassilicos (2008). 'Sweep-stick mechanism of heavy particle clustering in fluid turbulence'. *Physical Review Letters* 100.5, pp. 1–4. DOI: `10.1103/PhysRevLett.100.054503`.

– (2009). 'The dissipation rate coefficient of turbulence is not universal and depends on the internal stagnation point structure'. *Physics of Fluids* 21.3, p. 035104. DOI: `10.1063/1.3085721`.

– (2015). 'Energy dissipation and flux laws for unsteady turbulence'. *Physics Letters A* 379.16-17, pp. 1144–1148. DOI: `10.1016/j.physleta.2015.02.025`.

– (2016a). 'Local equilibrium hypothesis and Taylor's dissipation law'. *Fluid Dynamics Research* 48.2, p. 21402. DOI: `10.1088/0169-5983/48/2/021402`.

– (2016b). 'Unsteady turbulence cascades'. *Physical Review E* 94.5, pp. 1–3. DOI: `10.1103/PhysRevE.94.053108`.

Hascoët, E. and J.C. Vassilicos (2007). 'Turbulent clustering of inertial particles in the presence of gravity'. *Advances in Turbulence XI: Proceedings of the 11th EUROMECH European Turbulance Conference, June 25-28, 2007 Porto, Portugal*. Springer, pp. 482–484.

Haynes, A.L. and C.E. Parnell (2007). 'A trilinear method for finding null points in a three-dimensional vector space'. *Physics of Plasmas* 14.8. DOI: `10.1063/1.2756751`.

Huck, P. D., C. Bateson, R. Volk, A. Cartellier, M. Bourgoin, and A. Aliseda (2018). 'The role of collective effects on settling velocity enhancement for inertial particles in turbulence'. *Journal of Fluid Mechanics* 846, pp. 1059–1075. DOI: `10.1017/jfm.2018.272`.

Hwang, W. and J.K. Eaton (2004). 'Creating homogeneous and isotropic turbulence without a mean flow'. *Experiments in Fluids* 36.3, pp. 444–454. DOI: `10.1007/s00348-003-0742-6`.

Ireland, Peter J., Andrew D. Bragg, and Lance R. Collins (2016a). 'The effect of Reynolds number on inertial particle dynamics in isotropic turbulence. Part 2. Simulations with gravitational effects'. *Journal of Fluid Mechanics* 796, pp. 659–711. DOI: `10.1017/jfm.2016.227`.

Ireland, P.J., A.D. Bragg, and L.R. Collins (2016b). 'The effect of Reynolds number on inertial particle dynamics in isotropic turbulence. Part 1. Simulations without gravitational effects'. *Journal of Fluid Mechanics* 796, pp. 617–658. DOI: `10.1017/jfm.2016.238`.

Ireland, P.J. and L.R. Collins (2012). 'Direct numerical simulation of inertial particle entrainment in a shearless mixing layer'. *Journal of Fluid Mechanics* 704, pp. 301–332. DOI: `10.1017/jfm.2012.241`.

Kamalu, N., F. Wen, T.R. Troutt, C.T. Crowe, and J.N. Chung (1988). 'Particle dispersion by ordered motion in turbulent mixing layers'. *ASME Cavitation and Multiphase Flow Forum*, pp. 150–154.

Karman, T. and L. Howarth (1938). 'On the statistical theory of isotropic turbulence'. *Proceedings of the Royal Society of London. Series A - Mathematical and Physical Sciences* 164.917, pp. 192–215. DOI: `10.1098/rspa.1938.0013`.

Kolmogorov, A.N. (1941). 'The local structure of turbulence in incompressible viscous fluid for very large Reynolds'. *Numbers. In Dokl. Akad. Nauk SSSR* 30, p. 301.

Lázaro, B.J. and J.C. Lasheras (1989). 'Particle dispersion in a turbulent, plane, free shear layer'. *Physics of Fluids A* 1.6, pp. 1035–1044. DOI: `10.1063/1.857394`.

– (1992). 'Particle dispersion in the developing free shear layer. Part 2. Forced flow'. *Journal of Fluid Mechanics* 235, pp. 143–178. DOI: `10.1017/S0022112092001071`.

Lemarié-Rieusset, P.G. (2018). *The Navier-Stokes problem in the 21st century*. Chapman and Hall/CRC.

Lesieur, M. (2008). *Introduction to Turbulence in Fluid Mechanics*. Dordrecht: Springer Netherlands, pp. 1–23.

Lespinard, G. (1968). 'Contribution à l'étude de la transition en couche limite: effet de l'aspiration pariétale'. Université de Grenoble.

Li, C., K. Lim, T. Berk, A. Abraham, M. Heisel, M. Guala, F. Coletti, and J. Hong (2021). 'Settling and clustering of snow particles in atmospheric turbulence'. *Journal of Fluid Mechanics* 912. DOI: `10.1017/jfm.2020.1153`.

Liepmann, H.W., J. Laufer, and K. Liepmann (1951). *On the spectrum of isotropic turbulence*. Tech. rep.

Liepmann, H.W. and M.S. Robinson (1953). *Counting methods and equipment for mean-value measurements in turbulence research*. Tech. rep. 5, p. 6.

Liu, Y., L. Shen, R. Zamansky, and F. Coletti (2020). 'Life and death of inertial particle clusters in turbulence'. *Journal of Fluid Mechanics* 902, pp. 1–12. DOI: `10.1017/jfm.2020.710`.

Longmire, E. and J.K. Eaton (1992). *Journal of Fluid Mechanics* 236, pp. 217–257. DOI: `10.1017/S002211209200140X`.

Lorenz, E.N. (1963). 'Deterministic Nonperiodic Flow'. *Journal of Atmospheric Sciences* 20.2, pp. 130–141. DOI: `10.1175/1520-0469(1963)020<0130:DNF>2.0.CO;2`.

Mathew, J. and A.J. Basu (2002). 'Some characteristics of entrainment at a cylindrical turbulence boundary'. *Physics of Fluids* 14.7, pp. 2065–2072. DOI: `10.1063/1.1480831`.

Maxey, M.R. (1987). 'The gravitational settling of aerosol particles in homogeneous turbulence and random flow fields'. *Journal of Fluid Mechanics* 174, pp. 441–465. DOI: `10.1017/S0022112087000193`.

Maxey, M.R. and S. Corrsin (1986). 'Gravitational settling of aerosol particles in randomly oriented cellular flow fields'. *Journal of Atmospheric Sciences* 43.11, pp. 1112–1134. DOI: `10.1175/1520-0469(1986)043<1112:GSOAPI>2.0.CO;2`.

Maxey, M.R. and J.J. Riley (1983). 'Equation of motion for a small rigid sphere in a nonuniform flow'. *The Physics of Fluids* 26.4, pp. 883–889. DOI: `10.1063/1.864230`.

Mazellier, N. and J.C. Vassilicos (2008). 'The turbulence dissipation constant is not universal because of its universal dependence on large-scale flow topology'. *Physics of Fluids* 20.1. DOI: `10.1063/1.2832778`.

McFadden, J. (1958). 'The axis-crossing intervals of random functions–II'. *IRE Transactions on Information Theory* 4.1, pp. 14–24. DOI: `10.1109/TIT.1958.1057438`.

Mininni, P.D., D. Rosenberg, R. Reddy, and A. Pouquet (2011). 'A hybrid MPI-OpenMP scheme for scalable parallel pseudospectral computations for fluid turbulence'. *Parallel Computing* 37.6-7, pp. 316–326. DOI: `10.1016/j.parco.2011.05.004`.

Monchaux, R., M. Bourgoin, and A. Cartellier (2012). 'Analyzing preferential concentration and clustering of inertial particles in turbulence'. *International Journal of Multiphase Flow* 40.June 2020, pp. 1–18. DOI: `10.1016/j.ijmultiphaseflow.2011.12.001`.

Monchaux, R. and A. Dejoan (2017). 'Settling velocity and preferential concentration of heavy particles under two-way coupling effects in homogeneous turbulence'. *Physical Review Fluids* 2.10, pp. 1–16. DOI: `10.1103/PhysRevFluids.2.104302`.

Mora, D.O., M. Bourgoin, P.D. Mininni, and M. Obligado (2021a). 'Clustering of vector nulls in homogeneous isotropic turbulence'. *Physical Review Fluids* 6.2, p. 24609. DOI: `10.1103/PhysRevFluids.6.024609`.

Mora, D.O., A. Cartellier, and M. Obligado (2019). 'Experimental estimation of turbulence modification by inertial particles at moderate Reλ'. *Physical Review Fluids* 4.7, pp. 1–10. DOI: `10.1103/PhysRevFluids.4.074309`.

Mora, D.O. and M. Obligado (2020). 'Estimating the integral length scale on turbulent flows from the zero crossings of the longitudinal velocity fluctuation'. *Experiments in Fluids* 61.9, pp. 1–10. DOI: `10.1007/s00348-020-03033-2`.

Mora, D.O., M. Obligado, A. Aliseda, and A. Cartellier (2021b). 'Effect of Reλ and Rouse numbers on the settling of inertial droplets in homogeneous isotropic turbulence'. *Physical Review Fluids* 6.4, pp. 1–19. DOI: `10.1103/PhysRevFluids.6.044305`.

Mora-Paiba, Daniel (2020). 'Clustering and settling dynamics of inertial particles under turbulence'. Theses. Université Grenoble Alpes.

Murray, S.P. (1970). 'Settling velocities and vertical diffusion of particles in turbulent water'. *Journal of Geophysical Research* 75.9, pp. 1647–1654. DOI: `10.1029/jc075i009p01647`.

Nielsen, P. (1993). 'Turbulence effects on the settling of suspended particles'. *Journal of Sedimentary Petrology* 63.5, pp. 835–838. DOI: `10.1306/d4267c1c-2b26-11d7-8648000102c1865d`.

Obligado, M., C. Brun, J.H. Silvestrini, and E.B.C. Schettini (2022). 'Dissipation Scalings in the Turbulent Boundary Layer at Moderate Reθ'. *Flow, Turbulence and Combustion* 108.1, pp. 105–122. DOI: `10.1007/s10494-021-00270-1`.

Obligado, M., T. Teitelbaum, A. Cartellier, P. Mininni, and M. Bourgoin (2014). 'Preferential concentration of heavy particles in turbulence'. *Journal of Turbulence* 15.5, pp. 293–310. DOI: `10.1080/14685248.2014.897710`.

Oseen, C.W. (1910). 'Uber die Stokes' sche Formel und Uber eine verwandte Aufgabe in der Hydrodynamik'. *Arkiv Mat., Astron. och Fysik* 6, p. 1.

Petersen, A.J., L. Baker, and F. Coletti (2019). 'Experimental study of inertial particles clustering and settling in homogeneous turbulence'. *Journal of Fluid Mechanics* 864, pp. 925–970. DOI: `10.1017/jfm.2019.31`.

Pope, S.B. (2001). 'Turbulent flows'. *Measurement Science and Technology* 12.11, pp. 2020–2021.

Puga, A.J. and J.C. Larue (2017). 'Normalized dissipation rate in a moderate Taylor Reynolds number flow'. *Journal of Fluid Mechanics* 818, pp. 184–204. DOI: `10.1017/jfm.2017.47`.

Reynolds, O. (1883). 'XXIX. An experimental investigation of the circumstances which determine whether the motion of water shall be direct or sinuous, and of the law of resistance in parallel channels'. *Philosophical Transactions of the Royal society of London* 174, pp. 935–982.

Rice, S.O. (1944). 'Mathematical Analysis of Random Noise'. *The Bell System Technical Journal* 23.3, pp. 282–332.

Richardson, L.F. (1922). *Weather prediction by numerical process*. University Press.

Rosa, B., H. Parishani, O. Ayala, and L.P. Wang (2016). 'Settling velocity of small inertial particles in homogeneous isotropic turbulence from high-resolution DNS'. *International Journal of Multiphase Flow* 83, pp. 217–231. DOI: `10.1016/j.ijmultiphaseflow.2016.04.005`.

Seoud, E.R. and J.C. Vassilicos (2007). 'Dissipation and decay of fractal-generated turbulence'. *Physics of Fluids* 19.10, pp. 1–11. DOI: `10.1063/1.2795211`.

Shaw, R.A. (2003). 'Particle-turbulence interactions in atmospheric clouds'. *Annual Review of Fluid Mechanics* 35, pp. 183–227. DOI: `10.1146/annurev.fluid.35.101101.161125`.

Simmons, L.F.G. and C. Salter (1934). 'Experimental investigation and analysis of the velocity variations in turbulent flow'. *Proceedings of the Royal Society of London. Series A, Containing Papers of a Mathematical and Physical Character* 145.854, pp. 212–234.

Squires, K.D. and J.K. Eaton (1991). 'Measurements of particle dispersion obtained from direct numerical simulations of isotropic turbulence'. *Journal of Fluid Mechanics* 226, pp. 1–35. DOI: `10.1017/S0022112091002276`.

Sreenivasan, K.R. (1995). 'On the universality of the Kolmogorov constant'. *Physics of Fluids* 7.11, pp. 2778–2784. DOI: `10.1063/1.868656`.

Sreenivasan, K.R., A. Prabhu, and R. Narasimha (1983). 'Zero-Crossings In Turbulent Signals'. *Journal of Fluid Mechanics* 137, pp. 251–272. DOI: `10.1017/S0022112083002396`.

Sumbekova, S., A. Aliseda, A. Cartellier, and M. Bourgoin (2016). 'Clustering and settling of inertial particles in turbulence'. *Springer Proceedings in Physics* 185.August 2018, pp. 475–482. DOI: `10.1007/978-3-319-30602-5_59`.

Sumbekova, S., A. Cartellier, A. Aliseda, and M. Bourgoin (2017). 'Preferential concentration of inertial sub-Kolmogorov particles: The roles of mass loading of particles, Stokes numbers, and Reynolds numbers'. *Physical Review Fluids* 2.2, pp. 1–19. DOI: `10.1103/PhysRevFluids.2.024302`.

Tamai, K. (2016). 'Big whorls, little whorls'. *Nature Physics* 12.3, p. 197. DOI: `10.1038/nphys3697`.

Taylor, G. I. (1935). 'Statistical theory of turbulence'. *Proceedings of the Royal Society of London. Series A-Mathematical and Physical Sciences* 151.873, pp. 444–454. DOI: `10.1098/rspa.1935.0159`.

Tchen, C.M. (1947). 'Mean value and correlation problems connected with the motion of small particles in a turbulent fluid'.

Tennekes, H. and J.L. Lumley (1972). *A first course in turbulence*. MIT press.

Tom, J. and A.D. Bragg (2019). 'Multiscale preferential sweeping of particles settling in turbulence'. *Journal of Fluid Mechanics* 871, pp. 244–270. DOI: `10.1017/jfm.2019.337`.

Tom, J., M. Carbone, and A.D. Bragg (2022). 'How does two-way coupling modify particle settling and the role of multiscale preferential sweeping?' *Journal of Fluid Mechanics* 947, pp. 1–33. DOI: 10.1017/jfm.2022.615.

Vaillancourt, P.A. and M.K. Yau (2000). 'Review of particle-turbulence interactions and consequences for cloud physics'. *Bulletin of the American Meteorological Society* 81.2, pp. 285–298. DOI: 10.1175/1520-0477(2000)081<0285:ROPIAC>2.3.CO;2.

Valente, P. C. and J. C. Vassilicos (2012). 'Universal dissipation scaling for nonequilibrium turbulence'. *Physical Review Letters* 108.21, pp. 1–5. DOI: 10.1103/PhysRevLett.108.214503.

Vassilicos, J.C. (2015). 'Dissipation in turbulent flows'. *Annual Review of Fluid Mechanics* 47, pp. 95–114. DOI: 10.1146/annurev-fluid-010814-014637.

Veeravalli, S. and Z. Warhaft (1989). 'The shearless turbulence mixing layer'. *Journal of Fluid Mechanics* 207, pp. 191–229. DOI: 10.1017/S0022112089002557.

Wang, L.P. and M.R. Maxey (1993). 'Settling velocity and concentration distribution of heavy particles in homogeneous isotropic turbulence'. *Journal of Fluid Mechanics* 256, pp. 27–68. DOI: 10.1017/S0022112093002708.

Wang, Y., K.M. Lam, and Y. Lu (2018). 'Settling velocity of fine heavy particles in turbulent open channel flow'. *Physics of Fluids* 30.9. DOI: 10.1063/1.5046333.

Westerweel, J., C. Fukushima, J. M. Pedersen, and J. C.R. Hunt (2009). 'Momentum and scalar transport at the turbulent/non-turbulent interface of a jet'. *Journal of Fluid Mechanics* 631, pp. 199–230. DOI: 10.1017/S0022112009006600.

Westerweel, J., C. Fukushima, J.M. Pedersen, and J.C.R. Hunt (2005). 'Mechanics of the turbulent-nonturbulent interface of a jet'. *Physical Review Letters* 95.17, p. 174501. DOI: 10.1103/PhysRevLett.95.174501.

Yang, C. Y. and U. Lei (1998). 'The role of the turbulent scales in the settling velocity of heavy particles in homogeneous isotropic turbulence'. *Journal of Fluid Mechanics* 371, pp. 179–205. DOI: 10.1017/S0022112098002328.

Yang, T.-S. and S.) Shy (2021). 'The preferential accumulation and the settling velocity of small heavy particles in Taylor–Couette flows'. *Journal of Mechanics* 37.November, pp. 651–658. DOI: 10.1093/jom/ufab032.

Zimmermann, R., H. Xu, Y. Gasteuil, M. Bourgoin, R. Volk, J.-F. Pinton, and E. Bodenschatz (2010). 'The Lagrangian exploration module: An apparatus for the study of statistically homogeneous and isotropic turbulence'. *Review of Scientific Instruments* 81.5. DOI: 10.1063/1.3428738.

Abstract — Many environmental phenomena involve inertial particles advected in an inhomogeneous turbulent flow. Over the last decades, various studies have focused on the simplified case of homogeneous and isotropic turbulence. Nevertheless, most relevant applications feature non-homogeneous turbulence with a turbulent/non-turbulent interface. This thesis aims to study the motion of small, heavy inertial particles advected by a turbulent/non-turbulent interface. The thesis is divided into three main parts. In a first part, we present a method to analyse experimentally single-phase turbulent flows using solely statistics on points where the fluctuating velocity is equal to zero. We demonstrate that voids of zero crossings primarily control the degree of turbulence and the Taylor Reynolds number, Re_λ. In a second part, we explore the settling velocity modification of inertial particles in homogeneous isotropic turbulence through wind tunnel experiments. Our findings confirm that the settling enhancement decreases significantly with increasing values of the Taylor Reynolds number. Additionally, this study reveals that large-scale structures have a significant impact on the settling rate, even at constant turbulent intensity and Reynolds number. In the third part, we present wind tunnel experiments on the dynamics of inertial particles advected in a turbulent/non-turbulent interface. Only the high-turbulence side is laden with inertial particles, and we are interested in how their properties change as they travel across the interface, particularly their preferential concentration and settling velocity. Our observations confirm that particles tend to oversample high-energetic events within the mixing layer. Finally, the interface is also associated with an increase in clustering intensity and a stronger enhancement of the settling velocity. The work finishes with preliminary results of particle tracking velocimetry measurements.

Keywords: wind tunnel experiments, inertial particles, turbulent/non-turbulent interface

---

Résumé — Un grand nombre de phénomènes environnementaux sont associés au transport de particules inertielles au sein d'un écoulement turbulent inhomogène. Au cours des dernières décennies, la plupart des études se sont concentrées sur le cas simplifié de la turbulence homogène et isotrope. Néanmoins, beaucoup d'écoulements naturels présentent une turbulence non homogène avec une interface turbulente/non turbulente. Cette thèse vise à étudier le mouvement de petites particules inertielles et denses transportées à travers une interface turbulente/non-turbulente. La thèse est divisée en trois parties principales. Dans une première partie, nous présentons une méthode permettant d'analyser expérimentalement les écoulements turbulents monophasiques en se basant exclusivement sur des statistiques concernant les zéros de la vitesse fluctuante. Nous démontrons que les espaces vides de zéros contrôlent le niveau de turbulence et la valeur du nombre de Taylor Reynolds, Re_λ. Dans une seconde partie, nous étudions la modification de la vitesse de chute des particules dans une turbulence homogène et isotrope à l'aide d'expériences en soufflerie. Nous confirmons que l'augmentation de la vitesse de chute diminue significativement avec une augmentation du nombre de Taylor Reynolds. Cette étude dévoile également que les structures de grande échelle ont un effet sur la vitesse de chute, même pour une intensité turbulente et un nombre de Reynolds constants. Dans une dernière partie, nous présentons des expériences en soufflerie sur la dynamique des particules inertielles transportées dans une interface turbulente/non-turbulente. Les gouttes d'eau sont introduites seulement du côté fortement turbulent de l'interface, et nous analysons comment leur propriétés sont modifiées par la présence de l'interface, en se concentrant plus particulièrement sur leur concentration préférentielle et la modification de leur vitesse de chute. Dans la couche turbulente/non-turbulente, nous confirmons que les particules ont tendance à se concentrer dans les portions du fluides présentant de larges fluctuations turbulentes. Enfin, l'interface est également associée à une concentration préférentielle plus intense et à une forte augmentation de la vitesse de chute. En conclusion de ce travail nous présentons des résultats préliminaires sur des mesures de vélocimétrie par suivi de particules.

Mots clés : expériences en soufflerie, particules d'inertie, interface turbulente/non-turbulente

---